Quantum Sensing and Non-Demolition measurements in thermal and ultra-cold atoms

A Thesis

Submitted For The Degree Of

Doctor of Philosophy

by

Sayari Majumder

Enrolment No. RRI/2020/003

Under the Guidance of

Dr. Saptarishi Chaudhuri



In The Light And Matter Physics Department

Raman Research Institute, Bangalore - 560080, India

Jawaharlal Nehru University, New Delhi, India

© Sayari Majumder

All rights reserved

अज्ञानतिमिरान्धस्य ज्ञानाञ्जनशलाकया ।
चक्षुरुन्मीलितं येन तस्मै श्रीगुरवे नमः ॥

"Salutations to the revered Guru, who opens the eyes
of one blinded by the darkness of ignorance with the collyrium of knowledge."

This thesis is dedicated to

my father: Mihir Kumar Majumder, my mother: Sumana Majumder

and to all the taxpayers of India.

Declaration of Original and Sole Authorship

I, **Sayari Majumder**, declare that this thesis entitled *"Quantum Sensing and Non-Demolition measurements in thermal and ultra-cold atoms"* and the data presented in it are original and my own work carried out under the supervision of **Dr. Saptarishi Chaudhuri**. I confirm that the work presented here has not been submitted for the award of any other degree, diploma, membership, associateship, fellowship, etc., of any other university or institute. I further confirm that references to the work of others have been clearly acknowledged. I have also run the thesis through the Drillbit plagiarism software.

.....	.....
(Signature of the student)	(Signature of the supervisor)
Sayari Majumder	**Dr. Saptarishi Chaudhuri**

CERTIFICATE

This is to certify that the work contained in the thesis titled *"Quantum Sensing and Non-Demolition measurements in thermal and ultra-cold atoms"*, submitted by **Sayari Majumder** (Enrollment No. RRI/2020/003) to the **Jawaharlal Nehru University** for the award of the degree of **Doctor of Philosophy** (Ph.D.) in Physical Sciences, is the bonafide record of original research work carried out by **Sayari Majumder** under my guidance and supervision at the **Raman Research Institute** (RRI), Bengaluru, India. The results embodied in the thesis have not been submitted to any other University or Institute for the award of any degree or diploma.

. . . . .	. . . . .
(Signature of the Director)	(Signature of the Supervisor)
Prof. Tarun Souradeep	**Dr. Saptarishi Chaudhuri**
Director & Professor, RRI	Raman Research Institute
Date:	Date: . . . . .

Acknowledgements

This thesis marks the end of a long and transformative journey—one filled with learning, resilience, self-doubt, and quiet breakthroughs. I am grateful to every person who stood by me and made this possible.

First and foremost, I owe my deepest gratitude to my advisor, Dr. Saptarishi Chaudhuri. His calm guidance, sharp scientific insight, and unwavering encouragement have been invaluable. During times when I struggled to believe in myself or in the experiment, he would often remind me, **"Sayari, there's nothing in this world that doesn't work!"**—a simple sentence that gave me hope and reminded me that perseverance is often the missing piece. His mentorship shaped not just my research, but also my way of thinking. He has deeply modified my way of working to bring out the best in me. Secondly, I am always grateful to my parents (Sumana Majumder and Mihir Kumar Majumder) for bringing me to this beautiful world so that I can have some fun with the splendid world of physics. I hope to have some more amazing times tackling physics problems. Thank you for being my pillars. Your sacrifices, love, and unwavering faith in me gave me strength even in the darkest moments. This thesis is a reflection of your dreams as much as mine. I would like to thank my collaborators — Dr. Dibyendu Roy, Dr. Sanjukta Roy, and Rupak Bag — for their insightful discussions, constant encouragement, and invaluable contributions to this research.

I am sincerely thankful to all my labmates, namely Anirban, Gourab, Sagar Da, Neelanjan Da, Shreya Di, Bidyut Da, Subhojit Da, Maheswar Da, Swarnava, Sai Vignesh, Abhishruta in the QuMix group at the Light and Matter Physics (LAMP) department. I also wish to acknowledge all the VSPs and RAs — Nerai, Malavika, Krishnanand, Digvijay, Pranay, Pratik, Naman, Pawni, Bhagyashri, and Varsha — for their assistance and camaraderie. I would like to express my particular gratitude to Mriganka for reading and correcting my entire thesis with great enthusiasm and joy. The lab became a second home, filled with stimulating discussions, occasional chaos, quiet companionship, and shared growth. Whether it was aligning optics, debugging code, or just sharing meals, your presence made the hard days easier and the good days even better. My heartfelt appreciation goes to all my seniors — Sagar da, Shovan da, Silpa di, Sandeep da, Sukanya di, and

Anirban da — for their mentorship and support. I would also like to thank my batchmates — Anirban, Vaibhav, Rupak, Pooja, Shashank, Susovan, Gourab, Kinjal, Mukesh, and Manish — for sharing this journey with me and making it memorable. I am thankful to my committee members, Ranjini Ma'am and Dibyendu Sir, for their constructive feedback and valuable guidance throughout my research journey. I would like to specially thank my seniors, Sukanya Di and Sandeep Da, who were my daily companions, the ones I shared my day-to-day challenges with. They guided and motivated me through the uncertainties of experimental research, and always led by example. They kept my spirits high with entertainment and good food, and soon made my home. To my juniors Aishwarya, Yashica, Arkabrata, Punit, Sovon, Jasim, Soumen, Sayantan, Siddharth, Banamita, Barsa, thank you for your enthusiasm, fresh perspective, and kindness. You reminded me of where I began and why I chose this path. My sincere thanks to the MES section — Ibrahim, Majid, Shiva, and Manju — for their technical assistance and ever-reliable support. I am also grateful to Meena Ma'am and Sujatha Ma'am for their timely help with the electronics.

I would like to acknowledge Savitha Ma'am, our LAMP secretary, for her efficient handling of administrative matters, and extend my thanks to the Library section, RRI Academics section, IT section, and the Security staff for their continuous assistance in keeping things running smoothly. To the technical and administrative staff at Raman Research Institute—thank you for making sure everything ran smoothly and for always being approachable. And to the Institute library—your quiet corners, well-worn pages, and vast resources gave me both refuge and knowledge when I needed them most. I am also thankful to the larger community of hostellers, who became my family away from home. The warmth of shared dinners, late-night conversations, and countless moments of laughter kept me grounded and emotionally strong through this demanding journey.

A heartfelt thanks to the cooks and support staff, whose silent yet consistent efforts ensured I was nourished and cared for, even when I was too consumed by my work to notice. To my friends—thank you for holding space for me in your lives even when I disappeared into deadlines, and for reminding me to breathe, to laugh, and to live outside the lab. Finally, a heartfelt thank you to all the taxpayers of India — your contributions make research like this possible. To everyone who took the time to read my thesis — thank you sincerely. I know it's not easy to take time out for something like this, and I truly appreciate your effort and patience. And finally, to the version of myself who chose to begin this journey with all her fears and uncertainties—thank you for not giving up.

Sayari Majumder

List of Publications

1. Published

(a) **All Optical Broadband Atomic Magnetometer Utilising Raman Driven Spin Noise Spectroscopy**, **Sayari Majumder**, Saptarishi Chaudhuri, *IEEE Transactions on Instrumentation and Measurement*, vol. 74, pp. 1–10, 2025, Art. no. 1503610. doi:10.1109/TIM.2025.3554278

(b) **Quantum Technologies with Cold Rydberg Atoms and Atomic Spins**, Silpa B S, **Sayari Majumder**, Sanjukta Roy, *Phys News*, Vol. 53(1–2), *Bulletin of the Indian Physics Association*, ISSN: 0253-7583, 2023. [link]

(c) **Fast Loaded Dual Species Magneto-Optical Trap of Cold Sodium and Potassium Atoms with Light-Assisted Inter-Species Interaction**, Sagar Sutradhar, Anirban Misra, Gourab Pal, **Sayari Majumder**, Sanjukta Roy, Saptarishi Chaudhuri, *AIP Advances*, vol. 13, 065317, 2023. doi:10.1063/5.0154985

(d) **Real-Time Local Density Probe for Cold Atoms Utilizing Raman Driven Spin Noise Spectroscopy**, **Sayari Majumder**, Bhagyashri Bidwai, Bernadette Varsha, Saptarishi Chaudhuri, *Applied Physics Letters*, vol. 126, 244001, 2025. doi:10.1063/5.0190196 (Editor's Pick, APL SciLight)

(e) **Parametrising Harmonic Strengths in Raman Driven Spin Noise Spectra of Neutral Atoms**, **Sayari Majumder** and Saptarishi Chaudhuri, 2026. Research Square preprint: https://doi.org/10.21203/rs.3.rs-7799231/v1. (under review at *Scientific Reports*)

(f) **Detection of Long-Range Coherence in Driven Hot Atomic Vapors by Spin Noise Spectroscopy**, Rupak Bag, **Sayari Majumder**, Saptarishi Chaudhuri, Dibyendu Roy, arXiv:2509.18036 [quant-ph] (2025). doi:10.48550/arXiv.2509.18036. (under review at *Physical Review Letters*)

2. **In Preparation**

(a) **Probing Inter-Species Interactions in Cold Atoms Using Spin Noise Spectroscopy**, **Sayari Majumder**, Saptarishi Chaudhuri, 2025.

Awards and Media Highlights

- **Applied Physics Letters (APL)** publication on Real-Time Density Probe was selected as:
  - **Editor's Pick**
  - Featured in **APL SciLight** for its impact in atomic physics
  - Press Release by **DST India**
  - Featured on **Raman Research Institute** website
  - Highlighted by **Press Information Bureau (PIB), Govt. of India**
  - Covered in national media: **The Indian Express, Hindustan Samachar and DD News**

    Additional links:

    DD News Coverage

    The Indian Express Article

    GK Today Coverage

    RRI Feature

    RRI Video Feature

    APL SciLight Article

    Kudos Summary Page

    PIB Release

    DST Release

    Hindustan Samachar

- **IEEE Transactions on Instrumentation and Measurement** paper on broadband atomic magnetometry received wide coverage via:
  - Press Release by **DST India**
  - Featured on **Raman Research Institute** website
  - Highlighted by **Press Information Bureau (PIB), Govt. of India**
  - Covered in national media: **The Indian Express**
  - Additional links:

    DST Release

    PIB Release

    The Indian Express Article

    YouTube

Notation and Conventions

Style Conventions

- **Vectors:** bold serif font, e.g. $\mathbf{E}, \mathbf{B}, \mathbf{r}$.
- *Scalars:* italic serif font, e.g. m, K, t (Greek scalars upright, e.g. τ, α).
- Units: roman sans-serif font, e.g. `m`, `s`, `T` (use `\mathrm` or `\textsf` in math).
- Operators: with a hat, e.g. $\hat{H}, \hat{O}, \hat{a}$.
- Quantum states: Dirac notation, e.g. $|\psi\rangle$, $\langle\phi|$, $\langle\phi|\psi\rangle$.

Table 1: Space & Time

Symbol	Quantity	Unit
t	time	s
$r, \mathbf{r}$	position vector	m
x, y, z	Cartesian coordinates	m
θ, ϕ	angular coordinates	rad
$\hat{\mathbf{i}}, \hat{\mathbf{j}}, \hat{\mathbf{k}}$	Cartesian unit vectors	–
f	frequency	Hz
ω	angular frequency	rad/s
k	wavenumber	m^{-1}

Table 2: Mechanics / Dynamics

Symbol	Quantity	Unit
$\mathbf{p}$	momentum	kg m/s
E, U, K	energy (total, potential, kinetic)	J
τ	torque	N m
$\mathbf{L}$	angular momentum	$\mathrm{kg\ m^2/s}$
I	moment of inertia	$\mathrm{kg\ m^2}$

Table 3: Electricity & Magnetism

Symbol	Quantity	Unit
q, Q	charge	C
$\mathbf{E}$	electric field	V/m
$\mathbf{B}$	magnetic flux density	T
Φ_B	magnetic flux	Wb
I	current	A
R	resistance	Ω
μ_0	vacuum permeability	$\mathrm{N/A^2}$
ε_0	vacuum permittivity	F/m
c	speed of light in vacuum	m/s

Table 4: Optics

Symbol	Quantity	Unit
λ	wavelength	m
ν	optical frequency	Hz
ω_L	laser angular frequency	rad/s
I	intensity	$\mathrm{W/m^2}$
P	optical power	W
n	refractive index	–
M	magnification	–
NA	numerical aperture	–
F	focal length	m

Table 5: Quantum Mechanics / Atomic Physics

Symbol	Quantity	Unit
$\psi(\mathbf{r}, t)$	wavefunction	–
$\hat{O}$	operator	–
$\hat{H}$	Hamiltonian	J
$\lvert\psi\rangle, \langle\phi\rvert$	quantum states	–
$\langle\phi\vert\psi\rangle$	inner product	–
$\hat{a}, \hat{a}^\dagger$	annihilation/creation operators	–
Γ	linewidth (decay rate)	$\mathrm{s^{-1}}$
T_1, T_2	relaxation times	s
μ	dipole moment	C·m
$\hbar$	reduced Planck constant	J·s

Table 6: Mathematical Symbols

Symbol	Meaning
$\dot{x}$	time derivative $\frac{dx}{dt}$
$\ddot{x}$	second derivative $\frac{d^2x}{dt^2}$
∂	partial derivative
∇f	gradient of f
$\nabla \cdot \mathbf{A}$	divergence
$\nabla \times \mathbf{A}$	curl
$\nabla^2 f$	Laplacian
$\int f(x)\, dx$	integral
$\sum_i a_i$	summation
δ_{ij}	Kronecker delta
$\delta(x)$	Dirac delta
$\mathbb{R}, \mathbb{C}$	sets of real, complex numbers

Greek Alphabet

α	alpha	β	beta	γ	gamma	δ	delta
ϵ	epsilon	ζ	zeta	η	eta	θ	theta
ι	iota	κ	kappa	λ	lambda	μ	mu
ν	nu	ξ	xi	o	omicron	π	pi
ρ	rho	σ	sigma	τ	tau	υ	upsilon
ϕ	phi	χ	chi	ψ	psi	ω	omega

Physical Constants (SI units)

- Planck's constant: $h = 6.62607015 \times 10^{-34}$ J · s.
- Reduced Planck's constant: $\hbar = \dfrac{h}{2\pi}$.
- Speed of light: $c = 2.99792458 \times 10^{8}$ m/s.
- Boltzmann constant: $k_B = 1.380649 \times 10^{-23}$ J/K.
- Vacuum permittivity: $\epsilon_0 = 8.854187817 \times 10^{-12}$ F/m.
- Vacuum permeability: $\mu_0 = 4\pi \times 10^{-7}$ H/m.
- Elementary charge: $e = 1.602176634 \times 10^{-19}$ C.
- Bohr magneton: $\mu_B = 9.2740100783 \times 10^{-24}$ J/T.
- Nuclear magneton: $\mu_N = 5.0507837461 \times 10^{-27}$ J/T.

Special Conventions

- Unless otherwise stated, all equations are expressed in SI units.
- Angular frequencies are denoted by ω (rad/s), frequencies by f (Hz).
- Magnetic fields are denoted by **B** (Tesla).
- Electric fields are denoted by **E** (V/m).

Contents

Acknowledgements iii

List of Publications v

Awards and Media Highlights vii

Notation and Conventions ix

1 Introduction and Literature Survey 1

1.1 Motivation and Background 1

1.2 Overview of Quantum Sensing 6

1.2.1 Standard Quantum Limit (SQL) 7

1.2.2 Heisenberg Limit 8

1.3 Quantum Non-demolition (QND) Measurements 9

1.3.1 Theoretical Foundation 9

1.3.2 Experimental Methods 10

1.4 Spin Noise Spectroscopy (SNS) 11

1.4.1 Experimental Implementations of SNS 12

1.5 Summary and Transition 15

2 Raman-Driven Spin Noise Spectroscopy 17

2.1 Introduction 17

2.1.1 Spin Noise Power Spectrum 18

2.1.2 Derivation of Spin Noise Signal Strength . . . 20
2.1.3 Quantum statistical treatment of spin-noise spectroscopy . . . 27
2.1.4 Quantum statistical treatment of spin-noise spectroscopy . . . 29
2.2 Experimental Background . . . 33
2.2.1 Experimental Setup . . . 35
2.3 Experimental Results . . . 36
2.3.1 Spin Noise Peaks for ^{85}Rb and ^{87}Rb . . . 36
2.4 Power Spectrum . . . 41
2.4.1 Key Advantages . . . 47

3 Magnetometry using spin noise spectroscopy **49**
3.1 Introduction . . . 50
3.2 Experimental set up . . . 53
3.2.1 Magnetometry Based on Raman-driven spin noise spectroscopy (RDSNS) 58
3.3 Results and Discussion . . . 60
3.3.1 Characterisation and Noise Budget . . . 61
3.3.2 Signal Dependence on Atomic Density . . . 62
3.3.3 Signal Dependence on Magnetic Field . . . 63
3.3.4 Performance of the Magnetometer at Low Magnetic Fields . . . 64
3.3.5 Performance of Magnetometer at High Magnetic Fields . . . 67
3.3.6 Data Analysis . . . 70
3.3.7 AC Magnetometry: Sensitivity and Bandwidth . . . 76
3.4 Conclusion and Outlook . . . 78

4 Dual Species Cold Atomic System **81**
4.1 Overview of the Experimental Apparatus . . . 82
4.1.1 Atomic Sources and Vacuum System . . . 83
4.1.2 Laser Systems . . . 84
4.2 Optical Layout for Dual-Species Operation . . . 88
4.2.1 Magneto-Optical Traps ($2D^+$ and 3D) . . . 88
4.3 Imaging Systems . . . 93

4.3.1 Fluorescence Imaging . . . 93
4.3.2 Absorption Imaging . . . 96
4.4 Magnetic Trap Experiment and Characterization . . . 99
4.4.1 Motivation for Sub-Doppler Cooling . . . 101
4.5 Inter-species Interactions . . . 102
4.5.1 Heteronuclear Collisions in a Dual-Species Na–K 3DMOT . . . 102
4.6 Summary and Outlook . . . 106

5 Real-Time Local Density Probe for Cold Atoms Utilising Raman-Driven Spin Noise Spectroscopy 109
5.1 Introduction . . . 110
5.1.1 Need for Fast, Local, Minimally Invasive Probes . . . 112
5.1.2 Raman-Driven Spin Noise Spectroscopy (RDSNS) as a Technique . . . 113
5.2 Experimental Setup . . . 115
5.3 Theoretical Description . . . 117
5.4 Experimental Implementation . . . 119
5.4.1 Error Estimate . . . 122
5.4.2 Characterisation by varying $3D$ MOT Parameters . . . 123
5.4.3 Characterisation by varying $2D$ Parameters . . . 125
5.4.4 Abel Transform . . . 127
5.5 Image Processing and Abel Inversion . . . 130
5.5.1 Effect of MOT Field Gradient on RDSNS Signal . . . 132
5.5.2 Anti-Helmholtz coil configuration . . . 134

6 Higher Harmonic Generation using Spin Noise Spectroscopy 139
6.1 Motivation and Background . . . 140
6.2 Driven Spin Dynamics and Raman Coupling . . . 141
6.3 Scope and Objectives of the Present Work . . . 141
6.4 Observation of multiple equispaced RDSNS peaks . . . 142
6.5 Multi-level Coupling and Harmonic Generation . . . 146
6.6 Density Dependence of Harmonic Formation . . . 150

6.7 Dependence on Probe Beam Intensity . . . 154
6.8 Magnetic Field Dependence of Harmonic Formation . . . 156
6.9 Detection Sensitivity of External Magnetic field . . . 159
6.10 Conclusion and Outlook . . . 160

7 Conclusion & Outlook **163**
7.1 Outlook . . . 165

A Probe Absorption by Cold Atoms **169**

B Phase Locked Loop **175**

C Image Processing and Abel Inversion **181**
C.0.1 Loading and Scaling the Image . . . 181
C.0.2 Symmetric Cropping and Abel Inversion . . . 182
C.0.3 Conversion to Atom Density . . . 183
C.0.4 Loading Experimental Spin Noise Data . . . 183
C.0.5 Comparison and Data Export . . . 184

D Laser Frequency **187**

E Basics of Laser Cooling and Trapping **195**
E.1 Radiation Pressure and Scattering Force . . . 195
E.2 Doppler Cooling . . . 196
E.2.1 Magneto-Optical Trap (MOT) . . . 197
E.3 Sub-Doppler Cooling . . . 198
E.3.1 Time of Flight Absorption Imaging Derivation . . . 200

F Verification of Higher Harmonics using Raman Driven Spin Noise Spectroscopy **203**
F.1 Experimental Verification . . . 203
F.1.1 Coexistence of Thermal Noise and Coherent Response . . . 203
F.1.2 RF Spectra and Bandwidth of the AOMs . . . 205
F.1.3 Optical Beat-Note Measurement . . . 205

F.1.4 Test of Detection Linearity 206
F.1.5 Conclusion 207

List of Figures

1.1 Illustration of the Faraday effect: as light passes through a magnetised medium, its circular components $\sigma^{\pm}$ experience different phase shifts due to Zeeman splitting, causing the polarisation axis of the output beam to rotate. This rotation encodes information about the instantaneous magnetisation of the atomic ensemble. . . . 12

2.1 Schematic representation of spin precession in the Voigt geometry. The magnetic field **B** (blue) is applied along the $\hat{z}$-axis, perpendicular to the light propagation direction. The magnetization vector **M** (red) precesses around **B** at the Larmor frequency ω_L, forming an angle θ with the field axis. 19

2.2 Spin noise characterization: (a) Two-time autocorrelation function of the spin noise signal. The decay time T_2 is the transverse relaxation time, while the oscillation frequency corresponds to the Larmor precession frequency (ω_L). (b) Spin noise power spectrum showing a Lorentzian peak centered at the Larmor frequency. The linewidth provides a measure of the spin dephasing time T_2, while the area under the peak is related to the atomic number density and probe beam parameters. . . . 20

2.3 Schematic representation of the scattering geometry used in the quantum scattering theory of spin noise. The incident probe beam interacts with the atomic ensemble, and the scattered field is detected at an angle θ relative to the incident direction. The vector $\mathbf{R_k}$ denotes the position vector within the atomic cloud where the scattering event occurs. This configuration captures the momentum transfer and correlation effects central to the derivation of the spin noise spectrum. 30

2.4 Magnetic Circular Birefringence (MCB): (Left) In the absence of an external magnetic field ($B = 0$), the Zeeman sublevels $m_J = -1, 0, +1$ are degenerate. The σ^+ and σ^- transitions therefore have identical resonance frequencies and experience equal refractive indices. As a result, both circular polarization components of the probe field accumulate the same phase, producing no net polarization rotation. The red vertical line represents the probe laser frequency ω_0, which is tuned near (or far-detuned from) the atomic resonance.(Right) When a magnetic field is applied ($B \neq 0$), the Zeeman degeneracy is lifted, shifting the m_J sublevels in opposite directions. Consequently, the σ^+ and σ^- transitions experience different detunings relative to the fixed probe frequency ω_0. This produces unequal dispersive phase shifts for the two circular polarization components, resulting in different real parts of the refractive index ($n_+ \neq n_-$). The accumulated differential phase shift $\Delta\phi \propto (n_+ - n_-)L$ leads to a rotation of the plane of polarization of the transmitted light — the Faraday rotation. In spin noise spectroscopy (SNS), the probe is typically operated far off-resonance, such that the dispersive birefringent response (MCB) dominates over absorptive effects like magnetic circular dichroism (MCD). This ensures minimal spontaneous scattering and enables a weakly perturbative, near quantum non-demolition measurement of the collective spin. 34

2.5 Schematic of the SNS experimental setup, showing the beam-shaping optics, Rubidium vapour cell, magnetic coils in Voigt geometry, and the balanced detection system. This configuration enables non-perturbative probing of intrinsic spin fluctuations via Faraday rotation. 35

2.6 Balanced detection scheme for Faraday rotation: the probe beam is split into two orthogonal polarization components using a PBS. The differential signal between the two photodiodes reflects spin-induced Faraday rotation noise, suppressing common-mode noise. 37

2.7 Spin noise spectrum recorded at $T = 105°C$, probe power = 350 μW, detuning = +7 GHz, and magnetic field $B = 6.31$ G using an ^{87}Rb-enriched vapour cell. Two peaks are observed corresponding to the Larmor precession frequencies of ^{87}Rb and residual ^{85}Rb isotopes. The dominant peak arises from ^{87}Rb due to its higher isotopic concentration in the enriched cell. The smaller peak corresponds to the remaining fraction of ^{85}Rb. The peak frequencies follow $\omega_L = g_F \mu_B B/\hbar$, reflecting the different Landé g_F factors of the two isotopes in the linear Zeeman regime. These spectral features originate from stochastic transverse spin fluctuations of the atomic ensemble, detected through dispersive Faraday rotation of the far-detuned probe beam. 38

2.8 Spin noise spectra for different probe powers. Increasing power leads to stronger signal amplitude and spectral broadening. Parameters: detuning = +8 GHz, $T = 100°C$, $B = 6.31$ G. 39

2.9 (a) FWHM of the SN peak as a function of probe power. The trend indicates increasing power broadening due to enhanced probe interaction. (b) SN signal amplitude versus probe power. The approximately linear dependence is consistent with expectations in the low-saturation regime. 40

2.10 Spin noise spectra at increasing temperatures (70–110°C). Higher temperatures yield stronger signals due to increased atomic density. 41

2.11 (a) Spin-noise amplitude as a function of atomic number density. The fitted slope of 0.53 ± 0.06 indicates a $\sqrt{N}$ dependence, consistent with the expected scaling of spin-noise amplitude for uncorrelated spin fluctuations. (b) Raw spin-noise spectra recorded at different cell temperatures. Increasing temperature raises the vapour pressure and hence the atomic density, resulting in an increase in the observed spin-noise signal amplitude. 42

2.12 Atomic number density of ^{87}Rb atoms as a function of vapor pressure, calculated using the empirical vapor pressure relations from [69] and the ideal gas law. The dashed red line marks the melting point of rubidium at 39.31°C, indicating the transition between the solid and liquid phases. In the solid phase (left of the dashed line), the vapour pressure increases slowly with temperature due to sublimation, while in the liquid phase (right of the dashed line), the rate of increase is much steeper due to vaporisation. 42

2.13 A schematic representation of a three-level atomic system, $|i\rangle$ ($i = 1, 2, 3$), where two Raman beams with frequencies ω_1 and ω_2 couple the states $|1\rangle$ to $|3\rangle$ and $|2\rangle$ to $|3\rangle$, respectively. The diagram also shows the detunings Δ_{13} and Δ_{23} and linewidths γ' (γ) for the ground (excited) states. 43

2.14 Intrinsic spin noise signal from thermal ^{87}Rb atoms. The peak corresponds to the Larmor frequency under a transverse magnetic field of 6.4 Gauss. 44

2.15 Raman-driven spin noise spectroscopy (RDSNS) signal of ^{87}Rb atoms in a vapor cell. The signal peaks when $\omega = \omega_2 - \omega_1 = 2\pi\nu_L$, where ν_L is the Larmor frequency. The red Lorentzian envelope (from Eq. 2.67) represents $|\rho_{21}|^2$ as per Eq. 2.68, while the black spikes are individual Dirac delta contributions. Inset: Three-level atomic system coupled by two Raman beams with detunings Δ_{13}, Δ_{23} and linewidths γ', γ. 45

3.1 Comparison of different atomic magnetometers by operational principles, geometry, and detection methods. The figure shows distinctions between spin-exchange relaxation-free (SERF), RF magnetometers, Bell–Bloom, Mx-type, CPT-based, and NV-center-based sensors. Each platform has unique trade-offs among sensitivity, dynamic range, bandwidth, and applicability. 52

3.2 **Top Left:** Illustration of the 3-level system, $|i\rangle$ ($i = 1, 2, 3$), with two Raman beams with frequencies ω_{s1} and ω_{s2} connecting $|1\rangle$ to $|3\rangle$ and $|2\rangle$ to $|3\rangle$, with Rabi angular frequencies Ω_{13} and Ω_{23}. Detunings Δ_{13} and Δ_{23}, and linewidths (ground sates) γ and (excited state) γ' are indicated. **Bottom Left:** Schematic of the experimental setup. The Raman laser light is divided into two parts: one for the wavelength meter and Saturation Absorption Spectroscopy (SAS) setup, and the other split into two Raman beams whose frequencies and intensities are controlled by NI PXI module through Acousto Optic Modulators (AOMs). Waveplates (WPs) polarise the beams (one circular and the other linear) before entering the measurement setup. The probe laser is also divided into two parts. One part goes into the SAS set up and wavelength meter while the other part enters the measurement set up. Cell temperature and magnetic coil currents are regulated by a PID temperature controller and a stable current controller via PXI module. **Right:** Measurement setup. A linearly polarised (made using a Linear polariser (LP)) probe beam is focused at the cell's center. Raman beams are merged with a non-polarising beam splitter (NPBS). One NPBS output goes to the cell, the other to a photo-detector (PD) to record the beat signal. Polarimetric detection includes a polarising beam splitter (PBS) and a Balanced Photo-Detector (BPD), with the difference signal fed into a Spectrum Analyser (SA) for the power spectrum. 54

3.3 Illustrates the vapor cell set up. The probe beam (red) and the Raman Beams (yellow) passes through a paraffin coated cell (for low field mesurements) or buffer-gas-filled cell (for high field measurements), kept inside a solenoid which is enclosed in a four layer μ-metal casing. 55

3.4 Energy level diagram illustrating the probe and Raman beam configuration used in the experiment. The probe beam is detuned by +1.5 GHz from the $F = 3 \longrightarrow F' = 4$ transition of ^{85}Rb for the paraffin-coated cell, and by +31.5 GHz for the buffer-gas cell. The Raman beams are near-resonant with the same optical transition (one-photon detuning), while their frequency difference is tuned in the MHz range to match the Zeeman splitting (Larmor frequency), thereby driving coherent Raman transitions between ground-state Zeeman sublevels within the $F = 3$ manifold. . 57

3.5 Illustrates the various signal levels. The black line corresponds to the noise when the detector is off. When the detector is turned on, the signal corresponds to the detector's response when no light falls on it, which is represented by the red line. When the probe beam falls on the detector, the signal corresponds to the green line. The orange light represents the intrinsic spin noise signal when the magnetic field is turned on, and we get an intrinsic spin noise peak at the Larmor frequency. In the presence of the Raman beams, the signal spectral amplitude is amplified and is depicted in the pink line. The measurements were taken in a buffer-gas-filled (Neon at 200 Torr) vapour cell maintained at a temperature of 95^oC, which corresponds to a density of 4×10^{12} atoms/cc. The applied magnetic field was approximately 6.9 G. 61

3.6 Signal level variation with atomic density. Experiments were conducted in a Neon (200 Torr) buffer-gas-filled ^{85}Rb vapour cell. The temperature between 70°C and 100°C was varied while keeping the magnetic field constant at about 0.3 mT. Blue, red, and black dots correspond to background, intrinsic SNS, and Raman-driven (RDSNS) signals, respectively. 62

3.7 Dependence of intrinsic and Raman-driven spin noise signals on magnetic field strength. The vapour cell was kept at 95°C. Blue, red, and black dots indicate the background, intrinsic SNS, and Raman-driven (RDSNS) signals, respectively. . . 64

3.8 Illustrates the Raman-driven spin noise spectroscopy signals to calibrate low magnetic fields. The magnetic field was varied from around 0.3 mT to 2.5 mT. The measurements were taken in a paraffin-coated vapour cell at room temperature (20^oC) with a density of $8x10^9$ atoms/cc. (a-e) Corresponds to one of the representative graphs for each magnetic field value. The frequency difference between the two Raman beams (δ_{12}) was varied across the Larmor frequency. Each black peaked signal in every plot corresponds to a particular δ_{12}. We see that the strongest peak appears at the Larmor frequency. Each peak for a particular δ_{12} was recorded by taking 100 spectrum averages and was repeated several times. The blue line is a Lorentzian plot only to act as a line of guide for the envelope. (f) Represents one of the fitting plots for a magnetic field of $\approx$ 1.25 mT. The black dots represent the experimental data points and the red line is the theoretical fit. 65

3.9 (a) Variation of the fitted peak positions (red dots) of the Raman-driven spin noise (RDSNS) envelope with magnetic field showing a near-linear dependence consistent with the theoretical Larmor frequency. (b) Corresponding linewidths (blue dots) extracted from Lorentzian fits. The linewidth increases with magnetic field due to Zeeman broadening and field inhomogeneity. Error bars denote fitting uncertainties. 66

3.10 Illustrates the magnetic field calibration at high field. The magnetic field was varied from around 7.75 mT to 11.25 mT. All the measurements were taken in a buffer-gas-filled (Neon at 200 Torr) vapour cell maintained at a temperature of 95^oC, which corresponds to a density of $4x10^{12}$ atoms/cc. (a-e) Shows one of the representative data for each magnetic field value. The frequency difference between the two Raman beams δ_{12} was varied across the Larmor frequency. Each black peaked signal in every plot corresponds to a particular δ_{12}. We observe that the envelope of the Raman-driven spin noise signal has 6 peaks which correspond to the non-linear Zeeman effect, where the contributions from individual fluctuations between adjacent Zeeman levels start to show independently. For $F = 2$, there are 4 peaks and for $F = 3$ there are 6 such peaks. However, 4 peaks corresponding to $(F = 2, m_F = -1 \rightarrow -2)$ overlaps with $(F = 3, m_F = -1 \rightarrow -2)$, $(F = 2, m_F = 0 \rightarrow -1)$ overlaps with $(F = 3, m_F = 0 \rightarrow -1)$, $(F = 2, m_F = 1 \rightarrow 0)$ overlaps with $(F = 3, m_F = 1 \rightarrow 0)$ and $(F = 2, m_F = 2 \rightarrow 1)$ overlaps with $(F = 3, m_F = 2 \rightarrow 1)$. Hence, overall, we see 6 peaks in the power spectrum. (f) Fig. 3.10f represents one of the fitting plots at a magnetic field of $\approx$10.5 mT. The black points correspond to the experimental points, and the red line is the theoretical fit. 68

3.11 Represents the plot of the peak position of all the 6 peaks with the magnetic field. The peak position error represents the fitting error. We see that this matches the theoretical plot. 70

3.12 Illustrates the energy spacing between adjacent Zeeman levels following the Breit–Rabi formula, Eq. 3.2. 71

3.13 Raman-driven spin noise envelope peaks split due to the non-linear Zeeman effect as the magnetic field increases. The solid lines represent the plot for $F = 2$ state and the dotted lines for $F = 3$ state. 72

3.14 Splitting of $|\rho_{21}|^2$ at a magnetic field of 0.01 T. The solid lines represent the plot for the $F = 2$ state and the dotted lines for the $F = 3$ state. The relative peak strengths here are chosen to make $F = 2$ peaks appear higher than $F = 3$ peaks; in practice, these strengths depend on experimental parameters. 73

3.15 Illustrates the DC magnetic field resolution of the device. The measurement was taken in a paraffin-coated cell at room temperature (20^oC). The magnetic field was changed by 12 μG about 5.989 G, and the change in the signal amplitude was recorded. For each data 10 spectrum averages were taken and repeated several times to estimate the errors. We get an SNR of ≈44 at a drive frequency of 2.795 MHz. The resolution was finally extracted to be 30 pT. 74

3.16 Shows one of the noise spectra with a calibration signal at 120 Hz. The SNR was about 10^3 at the modulation depth of 300 nT. The sensitivity was extracted to be 30 $pT/Hz^{1/2}$ at a magnetic field of around 0.6 mT. 75

3.17 Shows the stitched noise spectrum at various modulation frequencies, varied from 10 Hz to 500 Hz. The magnetic field was modulated by 300 nT_{rms}, and the magnetometer response was recorded at different modulation frequencies. 76

3.18 Illustrates the frequency response of the magnetometer at various modulation frequencies. We get a -3 dB point at around 100 Hz of modulation frequency. . . 77

4.1 Optical layout of the potassium laser system. The figure shows the arrangement of the cooling and repump lasers, optical amplifiers, beam splitters, acousto-optic modulators (AOMs), polarisation optics, and optical fibres used to deliver laser light for trapping and cooling potassium atoms. 84

4.2 Photograph of the TASHG pro system used for generating 589 nm light for the sodium MOT. The system integrates a DL Pro seed laser at 1178 nm, optical isolators, a tapered amplifier, an electro-optic modulator, and a resonant SHG cavity, providing stable high-power output at 589 nm. 86

4.3 Schematic of the sodium optical layout. The 589 nm light from the TASHG pro is split into multiple branches using polarisation optics. Each branch includes an AOM in a double-pass configuration for independent frequency tuning and intensity control. 87

4.4 Schematic diagram of the $2D^+$ MOT. Two transverse cooling beams are retro-reflected using two helicity-preserving right-angled prisms. In addition, a pair of longitudinal cooling beams (pushing and retarding beams) is aligned along the line of the zero magnetic field created due to the configuration of the four race-track-shaped coils. The copper tube with a differential pumping hole connecting the $2D^+$ MOT and the 3D MOT sides, is cut at an angle of 45^o and mirror-polished to facilitate the passage of the retarding beam. An additional pushing beam is used to direct the cold atomic beam to the 3D MOT chamber through the differential pumping hole. 90

4.5 Fluorescence image of a potassium MOT prepared in the chamber used for the 2D-MOT during alignment and optimization of the system. In the normal operating configuration, the 2D-MOT produces a continuous atomic beam that is pushed toward the science chamber using an intensity imbalance between the push and retard beams, which makes direct imaging of the 2D-MOT fluorescence difficult. The image shows the location of the MOT inside the glass cell and the differential pumping tube connecting the source chamber to the 3D-MOT chamber. 91

4.6 Ray-tracing diagram of the three-lens imaging system. The first lens (f = 200 mm) collimates the fluorescence light while focusing the absorption imaging beam. The second lens (f = 75 mm) provides demagnification and re-collimation for the imaging beam while simultaneously focusing the fluorescence. Finally, the third lens (f = 150 mm), placed at a $2f$ distance from the second, relays the image in a $2f$–$2f$ configuration onto the camera plane. 93

4.7 Illustrates the fluorescence image captured by the CCD camera for an atom number of 10^8 Potassium atoms. 94

4.8 Absorption images of the atomic cloud for different time-of-flights (TOF): (a) 0 ms, (b) 5 ms, (c) 10 ms, (d) 15 ms, and (e) 20 ms. The gradual expansion of the cloud reflects the release and ballistic expansion dynamics of the ultracold ensemble. 96

4.9 Magnetic trap efficiency vs. wait time on a short timescale (up to 40 ms). 99

4.10 Magnetic trap efficiency vs. hold time on a long timescale (up to 16 seconds). . . 100

4.11 Fluorescence images of trapped atoms at various times after loading: (left) before transfer, (right) 10 ms, 1 s, 3 s, and 8 s. The gradual decrease in fluorescence indicates a loss of atoms over time. 101

4.12 Photon counts during various stages of the magnetic trapping experiment: (a) background with 2D and 3D molasses beams on, (b) 3D MOT loading phase, (c) fluorescence from atoms trapped in the magnetic field, (d) background with all beams off, (e) magnetic trapping process. 102

4.13 ^{23}Na survival probability as a function of the mixture ratio (ratio of ^{39}K atoms to ^{23}Na atoms). A pronounced reduction in sodium survival is observed with increasing potassium atom number, indicating significant inter-species collisional losses. Inset: Loading dynamics of ^{23}Na atoms in the absence and presence of ^{39}K atoms. 103

4.14 Caption 104

5.1 Schematic of the experimental setup. A $2D^+$ MOT is used as a bright source of cold atoms directed towards the $3D$ MOT. Probe beam (red) and Raman beam (green) intersecting at the $3D$ MOT is shown in the zoomed picture (top left). . . 114

5.2 Optical circuit and detection setup showing Raman laser light, the Saturation Absorption Spectroscopy (SAS) set up, AOMs, control hardware NI PXIe, the probe beam, and the polarimetric set-up. 115

5.3 Raman-Driven Spin Noise Spectroscopy (RDSNS) signals observed in (a) the time domain using an oscilloscope, showing the oscillatory spin noise, and (b) the frequency domain using a spectrum analyzer, highlighting the corresponding spectral features. 116

5.4 MOT loading dynamics measured via RDSNS (a) and total fluorescence counts (b). The RDSNS signal (blue dots) reaches $1/e$ of its saturation density within $\tau \sim 0.85$ s, whereas the fluorescence signal (green squares) shows a slower loading time constant of $\tau \sim 1.96$ s. 118

5.5 (a) RDSNS signals with atoms present and in the absence of atoms. It shows instantaneous signals at three time slices during loading, where black dots are the raw data and green curves are sinusoidal fits. (b) Illustrates the baseline RDSNS signal without atoms in the MOT. 120

5.6 Illustrates the evolution of the RDSNS signal as atoms are captured in the MOT. The signal (blue dots) reaches 1/e of the saturation density within $\tau \sim 1$ s. The corresponding total fluorescence count (green squares) (here, $\tau \sim 1.96$ s) is also shown. 121

5.7 Envelope fitting analysis of the RDSNS signal over a 2 μs measurement window. (a) Residuals from the sine fit to the lower envelope with a standard deviation of 0.0119 and $R^2 = 0.9874$. (b) Residuals from the upper envelope fit with a standard deviation of 0.0127 and $R^2 = 0.9873$. (c) Experimental signal (black dots) overlaid with fitted upper (blue) and lower (red) envelopes. (d) Fitted residuals for both envelopes. The overall fit error in the signal amplitude is estimated to be 3.23%, which translates to an approximate 6% error in the extracted atomic density. Longer measurement durations are expected to reduce this error further by improving the signal-to-noise ratio. 122

5.8 RDSNS signal strength (red dots) and fluorescence data (blue dots) for different beam detunings: (a) $3D$ repump beam detuning varied from -1Γ to 0.8Γ (from $F = 1 \rightarrow F'$ transition of the D_2 line), (b) $3D$ cooling beam detuning varied from -5.5Γ to -10Γ (from $F = 2 \rightarrow F'$ transition of the D_2 line). 123

5.9 RDSNS signal strength (red dots) and fluorescence data (blue dots) for different beam intensities: (a) $3D$ cooling beam intensity varied from $2.7I_{sat}$ to $10.5I_{sat}$, (b) $3D$ repump beam intensity varied from $1.2I_{sat}$ to $5.5I_{sat}$. 124

5.10 RDSNS signal strength (red dots) and fluorescence data (blue dots) for different detunings: (a) $2D$ cooling beam detuning varied from -3.8Γ to -7.4Γ (relative to the $F = 2 \rightarrow F'$ transition of the D_2 line), (b) $2D$ repump beam detuning varied from -3Γ to $+1\Gamma$ (relative to the $F = 1 \rightarrow F'$ transition of the D_2 line). 125

5.11 Dependence of RDSNS and fluorescence signals on (a) the cooling beam intensity (scaled in units of I_{sat}), and (b) the $2D^+$ MOT magnetic field gradient. Saturation of loading efficiency is observed at high intensities, whereas the gradient shows an optimum value beyond which both atom number and density decrease. 126

5.12 Illustrates the variation in the RDSNS signal (red triangles) with the centroid position of the cold cloud which was shifted by applying an additional bias magnetic field. It has been compared with the Inverse Abel transform (blue dots) of the fluorescence image. Inset: Shows the region (x = 0.2 mm and y = 0.45 mm to 3 mm) of the Inverse Abel transform of the fluorescence image. 128

5.13 Schematic of a radially symmetric atomic cloud where $I(y)$ corresponds to the fluorescence intensity recorded by the camera at a transverse distance y from the central axis of the MOT, and $g(r)$ denotes the local atomic number density at a radial distance r from the axis of symmetry which is calculated by doing Abel transform of $I(y)$ as shown in Eq 5.7. 129

5.14 Overview of the analysis pipeline: (a) raw image in pixel, (b) raw image in physical coordinates, (c) image centered using Gaussian centroid, (d) centered and cropped image, (e) result of inverse Abel transform, and (f) comparison between experimental and reconstructed densities. 131

5.15 Illustration of a magnetic field $\mathbf{B}$ lying in the x–z plane at an angle β with respect to the x-axis. The field has a parallel component $\mathbf{B}_{\parallel}$ along the initial magnetization and a perpendicular component $\mathbf{B}_{\perp}$ that induces Larmor precession. This orientation influences the resulting spin dynamics and the shape of the power spectrum. . . . 133

5.16 Magnetic field vector field in the x–z plane for an anti-Helmholtz coil configuration. The tiny arrows indicate the direction of the magnetic field at each point and the color represents the relative field strength. 134

5.17 Magnetic field variation along the x-axis in an anti-Helmholtz coil setup. Left: total field strength $|\mathbf{B}|$ showing a minimum at $x = 0$. Right: angle θ_B between $\mathbf{B}$ and the x-axis, indicating directional variation across the center. 135

6.1 Schematic of the experimental setup used for Raman-driven spin noise measurements, showing the probe and Raman laser paths, acousto-optic modulation, polarisation optics, and balanced detection system in the presence of a transverse magnetic field. 142

6.2 Experimental Set Up. (a) A linearly polarised probe beam (red) is focused at the centre of a Rubidium vapour cell. A pair of coherent beams (yellow) (Raman beams) with particular polarisations (σ^+ and π) is merged and made counter-propagating with respect to the probe beam (red). (b) Scheme of the Experiment. The pair of Raman beams connects the magnetic states of the ground hyperfine Zeeman manifold. Due to the multi-level structure, the atoms are driven to succeeding levels. The excited states are represented by even ket notations, while the ground states are represented by odd ket notations. (c) Illustrates the polarimetric detection setup. The polarisation fluctuation of the probe beam is measured using a PBS (polarising beam splitter) and a balanced photo-detector. 144

6.3 Energy level diagram illustrating Raman-coupled transitions between the Zeeman sublevels of the ^{85}Rb ground hyperfine manifold. The red levels denote the ground-state Zeeman states $|F, m_F\rangle$, while the blue levels represent the excited-state manifold. Optical fields containing σ^+ and π polarization components couple the ground and excited states with Rabi frequency Ω. Spontaneous decay from the excited states occurs at a rate γ, while γ' denotes the ground-state coherence relaxation rate. Two-photon Raman processes mediated by the excited states couple adjacent Zeeman sublevels, forming a ladder of coherently linked spin states. The sequential coupling between multiple m_F states results in oscillations at integer multiples of the Larmor frequency, leading to the higher harmonics observed in the spin noise spectrum. 145

6.4 Shows the observation of multiple peaks in the Raman-driven spin noise spectrum. The probe beam power was 0.64 mW, and the Raman beam power was 4.42 mW. The cell temperature was maintained at 95^oC. The Larmor frequency was 2.38 MHz. 147

6.5 Illustrates the dependence of harmonic peak strength ratios on the total Raman beam intensity at a cell temperature of 95°C, corresponding to a density of 4.5×10^{12} atoms/cc. The total Raman beam power was varied from 0.42 to 4.42 mW. (a) Ratio of the first (light blue circles) and second (green squares) harmonics to the fundamental peak and (b) ratio of the third (dark blue circles) and fourth harmonic (red squares) to the fundamental peak are plotted for various Raman beam intensities. 151

6.6 Shows the dependence of the peak strength on the density of atoms. The density inside the vapour cell was varied by changing the temperature from 80^oC to 105^oC, and the peak strength ratio of the first harmonic (yellow squares) and second harmonic (red circles) to the fundamental peak was measured. The blue lines serve as guides to the eye, illustrating the decreasing peak strength ratio as density increases. 152

6.7 Illustrates dependence of the harmonic peak strength ratio on probe beam power. Increasing probe intensity enhances atom–photon interaction, strengthening both first and higher harmonic peaks. At low power, the signal remains buried in noise, while at higher powers, saturation and dephasing limit further growth. The red lines are guide to eye to illustrate the growth of the peak strength ratio with varying probe power. 153

6.8 Shows the study of the effect of external magnetic field on the harmonic structure of the spin noise peaks. Schematic of Raman coupling between Zeeman sublevels (m_F states) of the ground-state hyperfine manifold (a) at low field and (b) at high field. Red arrows indicate σ^+ transitions and green arrows indicate π^0 transitions, forming cascaded multi-Λ pathways. (c–f) Raman-driven spin noise spectra recorded at different magnetic field strengths (5.38 G, 6.93 G, 8.69 G, and 10.26 G). The fundamental Larmor peak is visible in all cases, while higher-order harmonics weaken progressively with increasing magnetic field due to reduced resonance overlap and detuning of Raman coupling from higher-order transitions. 156

6.9 Illustrates the dependence of drive frequency on the Raman Driven Spin Noise Signals. The temperature is maintained at 95°C. The total Raman beam intensity was kept at 3.75 mW. The probe beam power was 0.7 mW. Each black peak corresponds to a particular Raman driving frequency. In each plot, the red dot-dashed line is drawn as a guide to the eye to trace out the envelope of the entire spectrum. (a) Shows the fundamental peaks when the driving frequency (δ_{12}) is scanned across the Larmor frequency (ν_L). The strongest peak appears when $\delta_{12} = \nu_L$. (b) Shows the occurrence of the first harmonic peaks with the strongest peak appearing at $2\nu_L$. (c) Shows the observation of the second harmonic peaks with the strongest peak appearing at $3\nu_L$. 159

A.1 Shows the LabVIEW program to monitor the number of atoms captured by the MOT using the fluorescence image captured by the camera in continuous acquisition. The plot below shows the frequency position of the Raman laser interpreted using the SAS signal. This light is then made to pass through AOMs in double pass configuration which detunes the light by +220 MHz. 170

A.2 Illustrates the percentage of the probe light being absorbed when an on-resonant probe beam passes through the cold atomic cloud, with changing probe beam intensity. 171

A.3 Shows the absorption of a weak probe beam passing through the cloud. The probe laser has been scanned across resonance ($F = 1$ to F' and $F = 2$ to F' of the D2 transition of potassium atoms). The inset shows the scanning of the laser interpreted using the SAS signal. We see two peaks corresponding to the two resonant transitions. 172

A.4 Illustrates probe absorption signal by the cold atoms in an oscilloscope when the probe laser frequency is swept across resonance.The yellow line represents the piezo scan voltage signal, and the blue line is the absorption signal. 173

B.1 Schematic scan of the PLL implementation. 176

B.2 Frequency drift over time observed on the spectrum analyzer for (a) 10 loops and (b) 50 loops. 177

B.3 RF signal processing chain used for phase locking in the RDSNS setup. Two VCOs drive separate AOMs; their auxiliary outputs are split and mixed to generate a beat signal, filtered, amplified, attenuated, and then sent to the PLL input. Simultaneously, the combined LO and RF outputs are sent to a second mixer and routed to the spectrum analyser. 178

C.1 Overview of the analysis pipeline: (a) raw image in pixel (b) raw image in physical coordinates, (c) image centered using Gaussian centroid, (d) Centered and symmetrically cropped image, (e) result of inverse Abel transform, and (f) comparison between experimental and reconstructed densities. 185

D.1 Represents the hyperfine energy level diagram of Sodium and Potassium. 189

D.2 Represents the hyperfine energy level diagram of Rubidium 190

E.1 Principle of laser cooling and trapping in a magneto-optical trap (MOT). (a) Three orthogonal pairs of counter-propagating, red-detuned laser beams provide velocity-dependent scattering forces that cool atoms. A quadrupole magnetic field, generated by anti-Helmholtz coils (blue loops), ensures a position-dependent restoring force, confining atoms near the trap center (green sphere). (b) Zeeman splitting of the atomic excited state sublevels in the presence of the magnetic field. The σ^+ and σ^- polarized beams preferentially interact with atoms displaced to the left or right, producing a restoring force toward the trap center. 198

E.2 Schematic of Sisyphus cooling in the lin$\perp$lin configuration. (Top) The polarization of the standing wave alternates periodically between σ^+ and σ^- components every $\lambda/2$. (Bottom) The corresponding light shifts create spatially modulated optical potentials for the ground-state Zeeman sublevels $m_g = \pm 1/2$. Atoms moving along z lose kinetic energy by climbing potential hills before being optically pumped to a lower-energy sublevel, leading to cooling below the Doppler limit. 199

F.1 (a) Power spectra measured at low Raman drive power showing the competition between the coherent resonance and the thermal noise background as the Raman detuning $\delta\omega_s$ is varied. (b) Log–log plot of the amplitude of the fundamental peak as a function of atomic density N_0. The slope close to $1/2$ indicates the expected $\sqrt{N_0}$ scaling associated with statistically independent thermal fluctuations. . . . 204

F.2 (a) RF spectra of the oscillators driving the AOMs. (b) Measured diffraction efficiency of an AOM as a function of RF frequency, demonstrating the finite operational bandwidth centered near 110 MHz. 205

F.3 Optical beat-note spectrum between the two Raman beams measured over a wide frequency span. Only the fundamental beat frequency is observed. 206

F.4 Control experiment testing the linearity of the balanced photodetection system. . 206

List of Tables

1 Space & Time ix

2 Mechanics / Dynamics ix

3 Electricity & Magnetism x

4 Optics x

5 Quantum Mechanics / Atomic Physics x

6 Mathematical Symbols x

1.1 Comparison of Major Quantum Sensing Platforms 4

1.2 Comparison of phase uncertainty for different quantum states in interferometry . 8

4.1 Potassium MOT laser parameters. Detunings are given in units of the natural linewidth Γ, and intensities are expressed relative to the saturation intensity I_{sat}. . 85

4.2 Sodium MOT laser parameters. Detunings are given in units of the natural linewidth Γ, and intensities are expressed relative to the saturation intensity I_{sat}. . 88

4.3 Parameters of the Na–3DMOT cooling beams. 98

4.4 Parameters of the K–3DMOT cooling beams. 98

5.1 The table presents optimized $2D$ ($3D$) cooling detuning and intensity values for the $F = 2 \rightarrow F'$ transition of the D_2 line of ^{39}K atoms, along with the repump detuning and intensity parameters corresponding to the $F = 1 \rightarrow F'$ transition. . 117

D.1 Summary of potassium cooling and repumping laser frequency settings. The detuning at the atoms is measured relative to the reference transition. The values provided here are placeholders and should be updated with the actual experimental detunings. 190

E.1 Relevant laser cooling parameters for sodium and potassium D_2 transitions. . . . 200

"I was born not knowing and have had only a little time
to change that here and there."

— Richard Feynman

Chapter 1

Introduction and Literature Survey

1.1 Motivation and Background

The field of precision measurements - Metrology- has always been the foundation for scientific research and technological advancements [1]. As measurement science evolves toward quantum-limited precision, metrology has entered a new era—where measurements are no longer passive but are fundamentally shaped by quantum mechanics, thereby giving rise to the field of Quantum Metrology [2]. The sensitivity and precision enhancement limits achieved by Quantum Metrology [3], by leveraging the principles of Quantum Mechanics, often far exceed the limits achieved by classical measurements. Quantum Sensing [4] exploits phenomena such as quantum entanglement [5], squeezing [6], and quantum coherence [7] to design sensors capable of detecting quantities such as magnetic fields, electric fields, time, temperature, gravitational field which are now transitioning from the controlled laboratory demonstrations to real-world, field-deployable technologies, with applications spanning fundamental science, navigation, medical imaging, and beyond [8, 9]. Some emerging applications include geophysics, brain imaging (e.g.,

magnetoencephalography, MEG) [8], space exploration, probing dark matter, and many more. Quantum sensors have been realized on a variety of physical platforms, such as in atomic vapours [10] (e.g., alkali atoms like Rb, Cs, K, Na), trapped ions [11], cold atoms and quantum gases, superconducting circuits [12], semiconductors and NV centres in diamond [13]. Each platform offers distinct advantages in the quantity to be measured.

Among these, atomic vapours [14] are one of the most mature or developed technologies that have been explored till now. It has been used as atomic clocks [15], magnetometers, and for many other applications. They are usually operable at room temperature and have also been exploited for their good optical readout properties due to strong light-matter interactions. Due to its controllable density, it can ensure a good signal-to-noise ratio (SNR). Another major advantage of atomic vapour systems is their capability for miniaturisation and field deployability [10, 16], which enables these sensors to have immense commercial value. Conversely, it is sensitive to environmental noise, such as thermal and magnetic noise, and therefore requires thermal isolation, which limits its optical access. In table 1.1, a summary of the advantages and disadvantages has been provided for the platforms discussed here.

The platform of ultra-cold atoms has several unique advantages [17, 18]. Due to its ultra-low temperature, it exhibits extremely low thermal noise, making the sensors highly sensitive [10, 19]. As a result, the system has longer coherence times and can therefore be probed for longer durations to extract valuable information [20]. Subsequently, its high controllability and tunability of interactions, such as Feshbach resonances, make it a good candidate for precise measurements and quantum simulations [21, 22]. Despite these advantages, it often involves complex experimental setups involving UHV, laser cooling, and trapping architecture [23, 24]. Moreover, they are often limited by the small number of atoms, leading to lower signal levels. Until now, these have also been mostly lab-based and require improvement for miniaturisation possibilities [25, 26].

Solid-state platforms involving NV centres in diamond [13, 27] can be made compact, but their bulky optics and microwave components need improvement. However, unlike systems that require precise temperature control, NV centre-based magnetometers operate at room temperature. It features high spatial resolution, enabling nanoscale sensing. It is generally limited by a very short coherence time ($\approx \mu s$ and linewidth in $\approx$ MHz). Inefficient readout times, particularly in pulsed Optically Detected Magnetic Resonance (ODMR), are another factor that causes inaccuracies

in the system. Among others, methods such as repetitive readout, spin-to-charge conversion, and Bayesian estimation aim to improve temporal limitations. To overcome the challenges of broad linewidths, super-resolution techniques such as hyperfine splitting and quantum heterodyne detection are being explored [28–30].

The platform of trapped ions has extremely high coherence and good controllability. It has been used for sensing electric/magnetic fields and is mostly suitable for tackling fundamental physics problems. Similar to cold-atom setups, these also involve complex experimental systems and are limited to a few ions. It lacks scalability for enabling large-scale sensing.

Superconducting circuits/qubits [31] make highly sensitive quantum sensors. They are sensitive to electromagnetic signals (RF/MW) and are both fast and tunable. They require cryogenic cooling in order to operate, which makes these setups bulky. Additionally, they are very sensitive to decoherence and noise and are hence largely confined to lab-scale applications.

Photonic quantum sensing platforms exploit quantum properties of light, such as squeezing, entanglement, and single-photon statistics, to precisely measure the quantity of interest [5]. Such systems enable room temperature operations to be feasible. It is possible to make fast detections, and they are generally immune to electromagnetic interference. These benefits make photonic systems a good candidate for chip-scale miniaturisation [32]. The use of squeezed light increases sensitivity by reducing noise in one of the quadratures, enabling measurement precision below the shot-noise limit [33, 34]. Entangled photon pairs can be used to make measurements in noisy environments and are often employed in ghost imaging [35] and quantum-enhanced spectroscopy [36]. Photonic sensors complement matter-based sensing, where speed, portability and optical sensing are critical.

Table 1.1: Comparison of Major Quantum Sensing Platforms

Platform	**Advantages**	**Limitations**
Thermal Atomic Vapours	• Room-temperature operation • Large ensemble size → high signal-to-noise ratio • Mature and robust technology • Long coherence times (e.g., SERF regime) • Strong optical interaction cross-section	• Limited spatial resolution due to atomic diffusion • Spin-exchange relaxation outside SERF regime • Sensitive to magnetic and environmental noise • Optical absorption introduces back-action at high probe power
Ultracold Atoms / BECs	• Suppressed thermal motion • Long interrogation and coherence times • Enables spatially resolved and local probing • Highly tunable interactions and geometry	• Lower atom number compared to vapour systems • Complex vacuum and laser infrastructure • Limited portability • Longer experimental cycle times

(continued on next page)

Platform	Advantages	Limitations
NV Centres in Diamond	• Room-temperature operation • Nanoscale spatial resolution • Sensitive to magnetic, electric, strain and temperature fields • Solid-state and biocompatible platform	• Limited spin coherence at room temperature • Photon shot-noise limited optical readout • Fabrication variability and inhomogeneity • Limited ensemble uniformity
Trapped Ions	• Extremely high coherence times • Precise quantum control and state preparation • High sensitivity to electric fields • Well-understood systematic effects	• Technically complex control systems • Limited scalability for large sensing arrays • Vacuum and laser stability requirements • Slow data acquisition rates
Superconducting Circuits	• On-chip integration • Strong coupling to microwave fields • Quantum-limited amplification • Fast readout	• Requires cryogenic cooling • Material defects limit coherence • Susceptible to flux and charge noise • Engineering complexity

(continued on next page)

Platform	Advantages	Limitations
Photonic Quantum Sensing	• Room-temperature operation • Immune to electromagnetic interference • High bandwidth detection • Chip-scale integration possible • Can surpass shot-noise limit using squeezed or entangled states	• Optical losses degrade quantum advantage • Weak interaction with some matter systems • Requires high-efficiency photon sources and detectors • Shot-noise limited without non-classical light

In quantum sensing, non-destructive measurement techniques are essential whenever long interrogation times, continuous tracking, or repeated sampling of a quantum system is required. This ensures that the state of the system remains unchanged or stable during measurements. Hence, Quantum Non-demolition (QND) measurements become crucial where the state of the system needs to be preserved.

1.2 Overview of Quantum Sensing

Quantum sensing is a branch of quantum metrology that exploits quantum systems, such as atoms, spins, and photons, to measure physical quantities like time, electric fields, and magnetic fields, and has wide-ranging applications [9]. Classical sensors are typically limited by technical noise sources such as thermal fluctuations, electronic noise, and photon shot noise. In contrast, quantum sensors exploit coherent quantum evolution and quantum correlations to approach or surpass the Standard Quantum Limit (SQL), which arises from quantum projection noise when measuring unentangled particles [33]. While quantum sensors are not free from noise, they shift the dominant limitation from classical technical noise to fundamental quantum noise sources. By employing non-classical resources such as squeezing and entanglement, quantum sensors exploit coherent quantum evolution and quantum correlations to reach the Standard Quantum Limit (SQL), which

arises from quantum projection noise when measuring unentangled particles. By employing non-classical resources such as squeezing and entanglement, quantum sensors can surpass the SQL and approach the Heisenberg limit.[2, 19, 37]

Some of the fundamental resources exploited by Quantum sensors are-

Quantum coherence and superposition: Quantum superposition is the property of a quantum system to exist in multiple states simultaneously. Quantum coherence refers to the phase relationship between various states in superposition that a system can exist in simultaneously. It allows interference and relies on superposition of quantum states for sensing [38].

Quantum entanglement: Entangled states in quantum mechanics refer to such a state which can not be further broken down into simpler states. Mathematically, entangled states are those that cannot be decomposed as outer products of more states. It is used for surpassing classical precision bounds [39].

Squeezed State: A state is termed as a Squeezed state when the uncertainty in measuring the observable is less than half of the fundamental limit (say $\Delta x < \sqrt{\hbar/2}$) [40]. It reduces the uncertainty in one variable at the cost of another without violating Heisenberg's uncertainty principle.

1.2.1 Standard Quantum Limit (SQL)

SQL is the precision limit set by the quantum projection noise when measuring unentangled particles [33]. For example, consider an ensemble of N spins in a two-level atomic system. They are prepared in a spin state (say, aligned along the x-direction). Then the angular momentum component along the z-direction will be

$$J_z = \sum_{i=1}^{N} {j_z}^{(i)},$$

with the mean value of $\langle \hat{J}_z \rangle = 0$. The Variance of J_z is $N\left(\frac{\hbar}{2}\right)^2$ and Standard Variation (Quantum projection noise) is $\Delta J_z = \sqrt{N}.\frac{\hbar}{2}$. So, the sensitivity (uncertainty in the estimated phase, $\Delta\theta_{SQL}$) is given by,

$$\Delta\theta_{SQL} \sim \frac{\Delta J_z}{\frac{\partial\langle \hat{J}_z \rangle}{\partial\theta}} \sim \frac{\sqrt{N}}{N} \propto \frac{1}{\sqrt{N}}.$$

So, we see that when we make measurements on unentangled particles, the sensitivity limit scales as $1/\sqrt{N}$. This is the typical measurement limit of most of the classical sensors.

1.2.2 Heisenberg Limit

The Heisenberg limit represents the ultimate bound on measurement precision imposed by quantum mechanics [41]. It scales as:

$$\Delta\theta_{\mathrm{HL}} \sim \frac{1}{N}$$

where N is the number of quantum resources (e.g., photons, atoms, measurements) and $\Delta\theta_{\mathrm{HL}}$ is the measurement uncertainty. This surpasses the SQL by a factor of $\sqrt{N}$.

Let us consider the case of squeezed light being used in detecting gravitational waves by using laser interferometry in the Laser Interferometer Gravitational-Wave Observatory (LIGO) project [42]. When measuring the phase shift (ϕ) in the interferometer, light is sent from one of the input ports, and the phase information is extracted through interference. With coherent light, the phase uncertainty is limited by shot noise, arising from the Poissonian photon statistic, which is the same as the SQL. In the presence of a squeezed light, the variance in one quadrature (phase) is reduced below the vacuum limit, at the cost of an increased uncertainty in the conjugate quadrature (say, electric field amplitude). This reduces the noise in the measurement in the phase, which surpasses the SQL, by achieving:

$$\Delta\phi \sim \frac{1}{N^{\kappa}}, \quad \text{with } \frac{1}{2} < \kappa \leq 1$$

Here, $\kappa = 1$ is the Heisenberg limit.

In summary, the Heisenberg limit sets the fundamental boundary for phase estimation in quantum metrology, representing the maximum possible advantage achievable over classical strategies. While coherent light sources are limited by shot noise to the SQL, quantum states, such as squeezed

Input State & **Phase Uncertainty** & **Scaling**
Coherent State & $\Delta\phi \sim \frac{1}{\sqrt{N}}$ & Standard Quantum Limit (SQL)
Squeezed State & $\Delta\phi \sim \frac{e^{-r}}{\sqrt{N}}$ & Beats SQL
Entangled State (NOON, GHZ) & $\Delta\phi \sim \frac{1}{N}$ & Heisenberg Limit

Table 1.2: Comparison of phase uncertainty for different quantum states in interferometry

or entangled light, enable a substantial reduction in measurement uncertainty.

1.3 Quantum Non-demolition (QND) Measurements

In the pursuit of sensitive quantum sensing, one often encounters difficulty in preserving the state of the system. Quantum measurements tend to collapse the state of the system. Many applications require minimal or no disturbance of the state of the system. Hence, this motivates the development of Quantum Non-Demolition (QND) measurement techniques where the act of measurement does not perturb the observable being measured, allowing repeated measurements and facilitating real-time detection.

1.3.1 Theoretical Foundation

QND measurement mainly requires an operator (say $\hat{O}$) concerning the measured observable that commutes with both the system ($\hat{H}_{\text{sys}}$) and interaction Hamiltonian ($\hat{H}_{\text{int}}$). This is necessary to maintain the stability of the time evolution of the operator. [43, 44] A measurement of an observable $\hat{O}$ is said to be QND if it satisfies the following commutation relations:

$$[\hat{O}, \hat{H}_{\text{int}}] = 0 \tag{1.1}$$

$$[\hat{O}, \hat{H}_{\text{sys}}] = 0 \tag{1.2}$$

These conditions ensure that the measurement interaction does not disturb $\hat{O}$, and the observable remains conserved under the system's time evolution.

However, in practice, some deviation from the ideal QND occurs and can be quantified. Spin-based QND measurements can be done via Faraday rotation. To minimise the perturbation, an off-resonant probe is often employed. This ensures minimal scattering and absorption by the atoms, thereby protecting the state of the system. This also reduces back action, making it a minimally invasive procedure.

$$\hat{H}_{int} \propto \hat{S}_z \hat{J}_z \tag{1.3}$$

Here, $\hat{S}_z$ is the Stokes operator representing the polarisation of the probe light and $\hat{J}_z$ is the collective

spin component of the atomic ensemble along the quantisation axis.

In order to overcome the destructive nature due to the complete collapse of the measured state of the system, QND acts as a powerful strategy. This enables fast and continuous tracking without erasing the information stored in the measured observable. A carefully designed system and interaction Hamiltonian ensure that the measurement observable commutes with both the system and interaction Hamiltonians, allowing one to preserve the system's evolution process. The capability of QND is far-reaching, with fascinating implications in precision metrology, quantum information processing, and fundamental physics experiments, enabling the achievement of ultimate sensitivity and performance.

1.3.2 Experimental Methods

QND measurement techniques have been implemented across a wide variety of experimental platforms, each exploiting different physical interactions to minimise measurement back-action. The central goal of these techniques is to extract information about a quantum system while keeping the observable of interest intact, thereby enabling multiple sequential measurements and preserving coherence. Depending on the physical realisation, QND schemes may involve coupling the system to an ancillary degree of freedom, probing it indirectly via optical or microwave fields, or utilising weak measurements that limit the projection-induced disturbance. The choice of method often depends on the nature of the system (atomic ensemble, trapped ions, solid-state spins, cavity QED systems, etc.), the observable being measured, and the acceptable trade-off between measurement precision and invasiveness. Below, we outline some of the prominent experimental strategies that have been successfully employed to realise QND measurements in practice.

Faraday Rotation: This method detects the Faraday rotation of a probe beam with minimal back-action. [45, 46]. Some of the experiments include the detection of dark field Faraday imaging (DFFI) techniques [47, 48]. When the probe beam interacts with the atomic media in the presence of a magnetic field, the polarisation of the probe beam rotates due to the Magnetic Circular Birefringence (MCB) effect.

State Mapping to an ancillary system: Read out information is first transferred to the ancillary system instead of measuring the state of the system directly. This prevents a complete collapse of the system's state from being measured. Measurement is rather destructively performed on the

ancilla. However, such an experiment requires high-fidelity state transfer in order to preserve the desired quantum information being mapped.

Weak Measurements: Such methods are used to probe state population with the help of weak measurements [49, 50]. Multiple weak measurements restrict the evolution of a quantum state. Such a system requires precise control over the measurement strength and duration. Weak entanglement to an ancilla system (eg, in the quantum Zeno effect) combined with frequent null-result measurements can effectively freeze the atomic evolution.

QND Ramsey Interrogation: This method relies on systematic readout of the phase of atoms in a quantum superposition [51]. It is implemented by Ramsey interference, which doesn't project the atoms into definite states. Since no population measurement is performed, it enables continuous yet non-destructive measurements of the system's phase, which is encoded with the observable of interest. Such interrogation protocol has been commonly explored in atomic clocks.

Dispersive Cavity Probing in the Deep QND Regime: Atoms inside an optical cavity induce a shift in the cavity resonance frequency. This frequency shift is dependent upon their state. A weak probe field whose photon number is low enough such that the spontaneous scattering probability is negligible even while probing, this is the deep QND regime of the cavity. A strong coupling between the cavity and atom ensures high sensitivity. The measurement is performed by detecting the phase/frequency shift via this weak probe [49, 50].

1.4 Spin Noise Spectroscopy (SNS)

Spin noise spectroscopy (SNS) is a particularly intriguing technique within this realm. Unlike conventional spectroscopic methods that require external excitation of the system, SNS leverages the intrinsic quantum fluctuations within a system to extract valuable information. This non-invasive approach makes SNS an excellent candidate for studying delicate quantum systems without perturbing them, thus preserving their natural states.

Despite its potential, several challenges remain in the application and understanding of spin noise spectroscopy. Current research often grapples with issues related to sensitivity, resolution, and the interpretation of complex noise signals. Addressing these challenges is crucial for advancing the capabilities of SNS and unlocking its full potential in applications ranging from

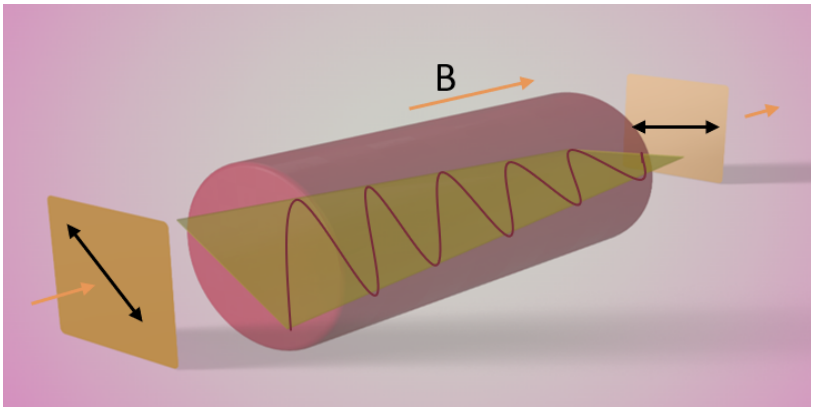


Figure 1.1: Illustration of the Faraday effect: as light passes through a magnetised medium, its circular components $\sigma^{\pm}$ experience different phase shifts due to Zeeman splitting, causing the polarisation axis of the output beam to rotate. This rotation encodes information about the instantaneous magnetisation of the atomic ensemble.

fundamental physics to advanced materials, first discovered by Zapasskii in 1981 [52], where they detected spontaneous spin fluctuations via Faraday rotation noise. Later, in 2004, Crooker et al. extended this concept [53], demonstrating its broad applicability beyond atomic systems. Since then, SNS has evolved into a versatile tool used in semiconductors, quantum dots, ultracold atomic gases, and even solid-state spin systems like nitrogen-vacancy (NV) centres in diamond. The primary objective of this thesis is to enhance the sensitivity and resolution of spin noise spectroscopy and to develop robust methods for the accurate interpretation of noise signals.

Figure 1.1 illustrates how linearly polarised light experiences Faraday rotation as it propagates through a magnetised medium. The σ^{+} and σ^{-} components acquire different phases due to Zeeman shifts, resulting in rotation of the overall polarisation.

1.4.1 Experimental Implementations of SNS

Experimentally, SNS involves measuring the stochastic Faraday rotation (or ellipticity) of a probe beam that interacts with the medium under study. The power spectral density (PSD) of the resulting polarisation noise provides direct access to spin dynamics such as relaxation times, precession frequencies, and g-factors. A variety of physical systems have been explored using SNS, each requiring specific adaptations of the general method.

Atomic vapours : Alkali metal vapours, such as rubidium and caesium, have served as canonical systems for SNS due to their large optical activity and well-understood spin structure [53, 54]. Experiments often employ off-resonant continuous-wave (CW) lasers with balanced polarimetry detection to minimise back-action and achieve long measurement times. These studies have revealed spin-relaxation mechanisms, hyperfine interactions, and magnetic-field-dependent noise spectra.

Semiconductors and quantum wells: In semiconductor systems, SNS has been used to probe itinerant electron spins in n-doped GaAs [55] and related heterostructures. The method provides information on spin coherence without the need for optical pumping, thereby avoiding photocarrier-related perturbations. Careful tuning of probe wavelength and polarisation enables selective sensitivity to conduction-band electrons.

Quantum dots: SNS has also been adapted to study localised spins in self-assembled quantum dots [56], where nuclear spin fluctuations can dominate the noise spectrum. These measurements have shed light on hyperfine coupling, spin dephasing, and dynamic nuclear polarisation processes.

Ultracold atoms: In ultracold alkali gases, SNS provides a minimally invasive probe of spin coherence and collective spin modes [57]. The combination of SNS with optical lattices and Bose–Einstein condensates has enabled studies of many-body spin correlations.

Solid-state spin defects: More recently, SNS has been applied to NV centres in diamond and rare-earth-doped crystals [58], where it can monitor spin relaxation in the presence of complex environmental noise.

Technical developments: Several innovations have enhanced SNS sensitivity and bandwidth, such as heterodyne detection schemes [59], cavity-enhanced probing [60], and time-domain SNS [61]. These approaches enable the detection of sub-nanoradian rotation noise and provide access to fast spin dynamics, surpassing the capabilities of early SNS setups.

The research aims to contribute to a deeper understanding of quantum noise phenomena and to pave the way for new applications of SNS in various scientific fields. This thesis is organised as

follows:

- **Chapter 1: Introduction and Literature Survey**

  Introduces the motivation for quantum sensing, the principles behind it, and an overview of relevant techniques, including Quantum Non-demolition (QND) measurements. It also positions spin noise spectroscopy (SNS) as a key tool within this landscape.

- **Chapter 2: Raman-Driven Spin Noise Spectroscopy (SNS)**

  Discusses the fundamental theory and experimental realisation of SNS. This includes the historical development, physical principles, detection techniques (Faraday rotation, balanced detection), and its role as a QND tool in probing spin dynamics passively.

- **Chapter 3: Magnetometry using Spin Noise Spectroscopy**

  Explores the application of SNS as an atomic magnetometer. Describes how SNS can be used to measure magnetic fields with high sensitivity and bandwidth. Emphasis is placed on the development and calibration of a Raman-driven SNS-based magnetometer.

- **Chapter 4: Dual Species Cold Atomic Machine**

  Details the design and operation of the ultra-cold atom setup. Describes laser cooling, trapping (MOT) and magnetic field control required to prepare cold atomic ensembles suitable for SNS.

- **Chapter 5: Real-Time Local Density Probe for Cold Atoms Utilizing Raman-Driven Spin Noise Spectrscopy**

  Demonstrates the use of SNS to probe local spin and density fluctuations in cold atomic clouds. Discusses spatio-temporal resolution and how SNS can act as a non-invasive, real-time local probe of many-body quantum systems.

- **Chapter 6: Higher Harmonic Generation using Spin Noise Spectroscopy**

  Investigates the phenomenon of higher harmonic generation using Raman-driven SNS. Analyses the experimental conditions under which non-linear spin noise features emerge, and their potential implications for quantum sensing.

- **Chapter 7: Conclusion and Outlook**

  Summarizes the key findings of the thesis. Reflects on the advancement of SNS techniques, their applications in magnetometry and cold atom physics, and discusses future directions, including enhanced squeezing, spatially resolved SNS arrays, and real-time feedback protocols. Presents spin noise measurements in dual-species atomic clouds (e.g., K-Na mixture). Investigates inter-species correlations, differential spin dynamics, and how SNS can uncover interactions in complex quantum mixtures.

1.5 Summary and Transition

In this chapter, we outlined the motivation for exploring quantum sensing, especially in contexts where conventional measurement techniques fall short due to their invasive nature. We introduced key quantum resources such as entanglement, coherence, and spin squeezing that enable enhanced sensing beyond classical limits. The principle of Quantum Non-Demolition (QND) measurement was discussed as a foundation for minimally invasive probing, followed by a brief overview of spin noise spectroscopy (SNS), which serves as the primary technique explored in this thesis.

In the following chapters, we delve deeper into the theoretical framework, experimental setup, and applications of spin noise spectroscopy, beginning with a comprehensive exploration of its principles and historical development.

Through this work, we aim to push the boundaries of what is possible with spin noise spectroscopy, contributing to the broader understanding and application of this powerful technique in the study of quantum systems.

"The fundamental importance of light scattering lies in the fact that it reveals the internal vibrations of the atom itself."

— C. V. Raman

Chapter 2

Raman-Driven Spin Noise Spectroscopy

2.1 Introduction

Motivation

The atomic spins distributed among various Zeeman levels fluctuate over time due to thermal (quantum) noise in the system [59]. Even in thermal equilibrium, atomic spin ensemble exhibits quantum fluctuations [52, 60]. One of the major objective of spin noise spectroscopy (SNS) is that it allows us to observe these fluctuations without disturbing or perturbing the state of the system [53, 55]. This non-perturbative nature makes it a great technique for Quantum Non-Demolition (QND) precision measurements in Quantum Sensing [62, 63]. This enables real-time repeated measurements without destroying the state of the system. One of the crucial advantage of SNS is that the spin noise signal is present even without any external excitation and also carry useful information about the system and its dynamics. Traditional spectroscopy techniques such as optical or microwave spectroscopy rely on absorption or fluorescence and involves excitations

and decoherence [64]. Contrary to this, SNS is based on Magnetic Circular Birefringence (MCB) effect [53, 54] where the probe beam is far detuned from any relevant atomic transitions. This ensures negligible absorption but finite change in the refractive index. To explain this effect, we decompose the linearly polarised probe beam into two orthogonal circular polarisations. When it passes through the atomic medium, it causes subtle changes in the refractive index of these two polarisations. Due to the presence of a magnetic field these fluctuations have signatures relating the noise power spectrum with the magnetic field via the Larmor frequency [52].

2.1.1 Spin Noise Power Spectrum

SNS is often performed in the Voigt geometry where the applied magnetic field is perpendicular to the probe light propagation direction. Suppose the magnetization vector **M** makes an angle θ with a magnetic field **B** applied along the z-axis in the Voigt geometry. A schematic is presented in fig. 2.1. The time dependent magnetization components along the x, y and z direction are-

$$\begin{aligned} M_x(t) &= M_0 \sin\theta \cos(\omega_L t), \\ M_y(t) &= M_0 \sin\theta \sin(\omega_L t), \\ M_z(t) &= M_0 \cos\theta, \end{aligned} \tag{2.1}$$

where M_0 is the magnitude of the magnetization and ω_L is the Larmor frequency.

Following the Bloch equation, we have,

$$\frac{d\mathbf{M}(t)}{dt} = \gamma\, \mathbf{M}(t) \times \mathbf{B} - \frac{M_x\hat{x} + M_y\hat{y}}{T_2} - \frac{(M_z - M_0)\hat{z}}{T_1}, \tag{2.2}$$

where γ is the gyromagnetic ratio, T_2 is the transverse relaxation time constant, and T_1 is the longitudinal relaxation time constant.

For $\mathbf{B} = B_0\hat{\mathbf{z}}$, the equations reduce to:

$$\begin{aligned} \frac{dM_x}{dt} &= \omega_L M_y - \frac{M_x}{T_2}, \\ \frac{dM_y}{dt} &= -\omega_L M_x - \frac{M_y}{T_2}, \\ \frac{dM_z}{dt} &= -\frac{M_z - M_0}{T_1}, \end{aligned} \tag{2.3}$$

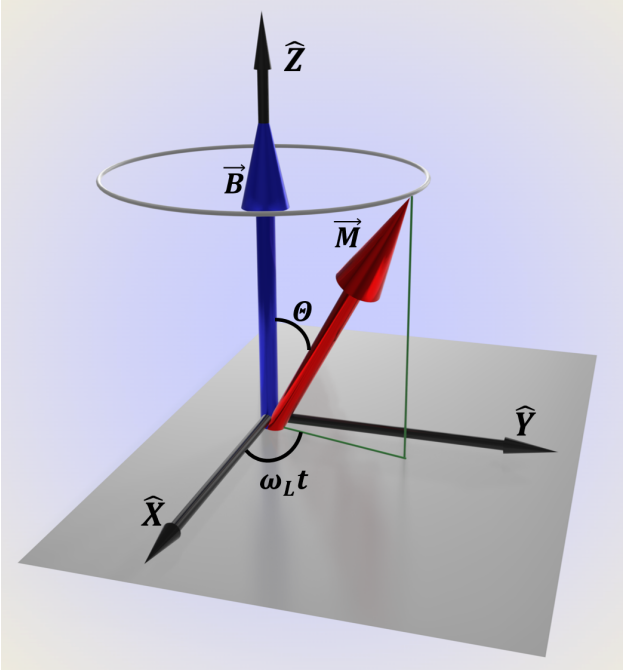


Figure 2.1: Schematic representation of spin precession in the Voigt geometry. The magnetic field **B** (blue) is applied along the $\hat{z}$-axis, perpendicular to the light propagation direction. The magnetization vector **M** (red) precesses around **B** at the Larmor frequency ω_L, forming an angle θ with the field axis.

with $\omega_L = \gamma B_0$.

The two-time autocorrelation function of the transverse magnetization becomes

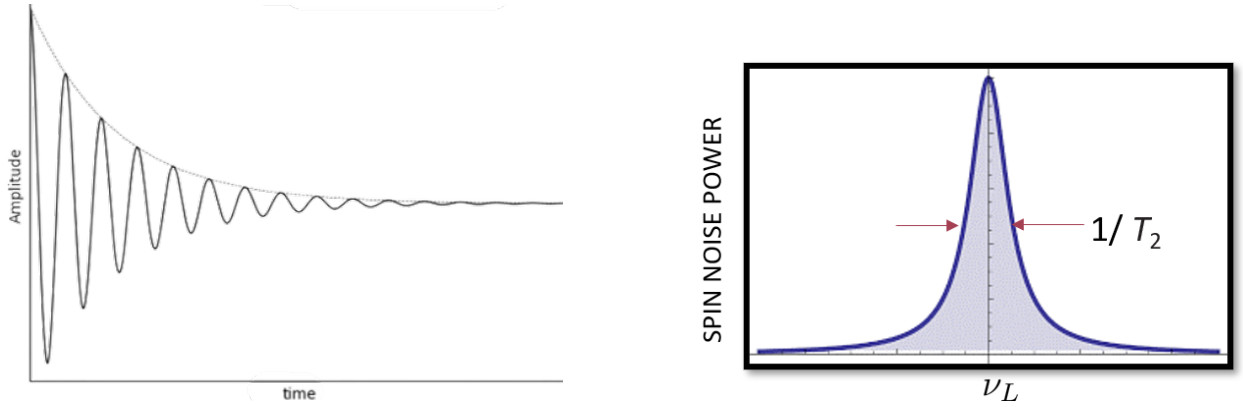
$$\langle M_x(t) M_x(0) \rangle \propto \cos(\omega_L t)\, e^{-t/T_2}, \tag{2.4}$$

which contains an oscillatory term at ω_L and an exponential decay with time constant T_2.

In fig. 2.2a, we have plotted the autocorrelation as a function of time. Using the Wiener–Khinchin theorem [65], the power spectrum is given by the Fourier transform of Eq. (2.4):

$$P(\omega) \propto \int_0^\infty \cos(\omega_L t)\, e^{-t/T_2}\, e^{i\omega t}\, dt = \frac{1}{(\omega - \omega_L)^2 + (1/T_2)^2}. \tag{2.5}$$

Figure 2.2b shows a representative spin noise spectrum. The power spectrum looks like a Lorentzian peak with a finite width proportional to the inverse of the transverse relaxation time T_2, serving as a direct measure of spin coherence. A narrower spectrum indicates a longer coherence time. The peak position at $\nu_L = \frac{2\pi}{\omega_L}$ is determined by the Larmor frequency and can be used for



(a) (b)

Figure 2.2: Spin noise characterization: (a) Two-time autocorrelation function of the spin noise signal. The decay time T_2 is the transverse relaxation time, while the oscillation frequency corresponds to the Larmor precession frequency (ω_L). (b) Spin noise power spectrum showing a Lorentzian peak centered at the Larmor frequency. The linewidth provides a measure of the spin dephasing time T_2, while the area under the peak is related to the atomic number density and probe beam parameters.

precision magnetometry, frequency standards, and other high-resolution measurements and will be discussed in detail in the following chapters.

While the spectral shape encodes the spin dynamics, the amplitude of the spectrum reflects the strength of the spin noise signal itself. In the following section, we derive an expression for the signal strength, highlighting its dependence on atomic density, probe parameters, and detection geometry.

2.1.2 Derivation of Spin Noise Signal Strength

Spin noise spectroscopy (SNS) is based on detecting fluctuations in the Faraday rotation angle of an off-resonant linearly polarized probe beam passing through an atomic ensemble. These fluctuations originate from random statistical spin fluctuations in the atomic sample. We derive below the scaling of the root-mean-square Faraday rotation noise amplitude $\delta\theta_F$ in terms of physical parameters.

Spin Noise Signal Strength: Derivation from Light–Matter Interaction

To derive the scaling of the spin noise signal strength, we start from Maxwell's equations in a medium and connect them to atomic response via the polarization field **P**, which encodes the light–matter interaction [66]. The electric field **E** obeys the wave equation as,

$$\nabla^2\mathbf{E} - \frac{1}{c^2}\frac{\partial^2\mathbf{E}}{\partial t^2} = \mu_0\frac{\partial^2\mathbf{P}}{\partial t^2} \tag{2.6}$$

where c and μ_o are the speed of light and is the magnetic permeability in free space of the atomic medium. Consider an ensemble of non-interacting, stationary atoms, each modeled as a two-level system. The interaction of the atoms with an incident monochromatic electric field, $\mathbf{E}(t) = \mathbf{E}_0 e^{-i\omega t}$ + c.c. induces a dipole moment, and hence a macroscopic polarization **P**, that determines the material's electric susceptibility $\chi(\omega)$. Each atom has a transition dipole matrix element $\mathbf{d} = q_e\langle e|\mathbf{r}|g\rangle$ between the ground $|g\rangle$ and excited $|e\rangle$ states. q_e is the electronic charge. The driven dipole moment $\mathbf{p}(t)$ in frequency space is given by:

$$\mathbf{p}(\omega) = \alpha(\omega)\mathbf{E}(\omega) \tag{2.7}$$

where $\alpha(\omega)$ is the atomic polarizability.

The total Hamiltonian is:

$$\hat{H} = \hat{H}_0 + \hat{H}_{\text{int}}(t) \tag{2.8}$$

where

$$\hat{H}_0 = \hbar\omega_2|e\rangle\langle e| + \hbar\omega_1|g\rangle\langle g|, \quad \hat{H}_{\text{int}} = -\hat{\mathbf{d}}\cdot\mathbf{E}(t)$$

with dipole operator $\hat{\mathbf{d}} = \mathbf{d}_{eg}|e\rangle\langle g| + \mathbf{d}_{ge}|g\rangle\langle e|$, where $\mathbf{d}_{ij}$ is the off-diagonal ij^{th} term of the dipole matrix element, $\hbar\omega_1$ and $\hbar\omega_2$ are the ground and excited state energies respectively. We do energy rescaling by $\hbar\omega_1$, so the free Hamiltonian reduces to,

$$\hat{H}_0 = \hbar\omega_0|e\rangle\langle e|, \tag{2.9}$$

Here, $\omega_o = \omega_2 - \omega_1$.

The time-dependent Schrödinger equation for the wavefunction $|\psi(t)\rangle$ is given as:

$$i\hbar\frac{\partial}{\partial t}|\psi(t)\rangle = \hat{H}|\psi(t)\rangle. \tag{2.10}$$

Let $|\psi(0)\rangle$ be the initial state at the ground state. Expanding the state $|\psi\rangle$ at a time t as,

$$|\psi(t)\rangle = c_g(t)|g\rangle + c_e(t)|e\rangle \tag{2.11}$$

Here, $c_g(t)$ and $c_e(t)$ are the time-dependent coefficients of the ground and excited states respectively. At time $t = 0$, $c_g(t = 0) = 1$ and $c_e(t = 0) = 0$. Substituting into the Schrödinger equation and projecting onto $|g\rangle$ and $|e\rangle$, we obtain:

$$i\hbar\dot{c}_g = -\mathbf{d}_{ge} \cdot \mathbf{E}(t)c_e(t) \tag{2.12}$$

$$i\hbar\dot{c}_e = \hbar\omega_0 c_e(t) - \mathbf{d}_{eg} \cdot \mathbf{E}(t)c_g(t) \tag{2.13}$$

Under Rotating Wave Approximation (RWA), we drop fast oscillating terms $\sim e^{\pm i(2\omega)t}$, and get,

$$\dot{c}_e(t) = -i\frac{\Omega}{2}e^{i\Delta t}c_g(t) \tag{2.14}$$

$$\dot{c}_g(t) = -i\frac{\Omega^*}{2}e^{-i\Delta t}c_e(t). \tag{2.15}$$

Here,

$$\Omega = \frac{\mathbf{d}_{eg} \cdot \mathbf{E}_0}{\hbar} \tag{2.16}$$

is the Rabi frequency. We define, $\Delta = \omega - \omega_0$ as the detuning of the light with frequency ω. For more details on RWA in light-matter interaction, refer to [67]. Assuming weak field (linear response), so that $c_g(t) \approx 1$ and $c_e(t)$ is small. We have,

$$\dot{c}_e(t) = -i\frac{\Omega}{2}e^{i\Delta t}. \tag{2.17}$$

Integrating we get,

$$c_e(t) = -i\frac{\Omega}{2}\int_0^t e^{i\Delta t'}dt' = \frac{\Omega}{2\Delta}\left(1 - e^{i\Delta t}\right).$$

Taking steady-state $t \to \infty$, the oscillating term averages out, and we get:

$$c_e(t) \approx \frac{\Omega}{2\Delta} \tag{2.18}$$

Hence, the expectation value of the induced dipole operator is,

$$\langle \hat{\mathbf{d}} \rangle = c_e^*(t) c_g(t) \mathbf{d}_{eg} + c_g^*(t) c_e(t) \mathbf{d}_{ge} \tag{2.19}$$

$$\approx c_e(t) \mathbf{d}_{ge} + \text{c.c.} \approx \frac{\Omega}{2\Delta} \mathbf{d}_{ge} + \text{c.c.} \tag{2.20}$$

Since $\Omega = \frac{\mathbf{d}_{eg} \cdot \mathbf{E}_0}{\hbar}$, we substitute to obtain:

$$\langle \hat{\mathbf{d}} \rangle = \alpha(\omega) \mathbf{E}_0 \quad \Rightarrow \quad \alpha(\omega) = \frac{|\mathbf{d}_{eg}|^2}{\hbar} \cdot \frac{1}{\omega_0 - \omega} \tag{2.21}$$

To account for spontaneous emission, we modify $\omega_0 \to \omega_0 - i\Gamma/2$, where Γ comes from the dissipation due to spontaneous emission. Then:

$$\boxed{\alpha(\omega) = \frac{|\mathbf{d}_{eg}|^2}{\hbar} \cdot \frac{1}{\omega_0 - \omega - i\Gamma/2}} \tag{2.22}$$

Using the identity from the Einstein's A and B coefficients (refer to chapter 2 of [24]), we have,

$$|\mathbf{d}_{eg}|^2 = \frac{3\pi\varepsilon_0 \hbar c^3}{\omega_0^2} f$$

we finally get:

$$\boxed{\alpha(\omega) = \frac{q_e^2 f}{m} \cdot \frac{1}{\omega_0^2 - \omega^2 - i\omega\Gamma}} \tag{2.23}$$

Here, q_e is the electron charge, m electron mass, f is the oscillator strength of the transition, ω_0 is the atomic resonance frequency and Γ is the decay rate (linewidth) of the transition.

The polarization $\mathbf{P} = N_0 \mathbf{p}$ relates to the susceptibility via $\mathbf{P} = \varepsilon_0 \chi(\omega) \mathbf{E}$. Thus,

$$\chi(\omega) = \frac{N_0 \alpha(\omega)}{\varepsilon_0} = \frac{N_0 e^2 f}{\varepsilon_0 m} \cdot \frac{1}{\omega_0^2 - \omega^2 - i\omega\Gamma} \tag{2.24}$$

Incorporating Zeeman Shifts (Circular Polarization): In the presence of a magnetic field **B**, the energy levels split due to the Zeeman effect. For light with circular polarization $\sigma^{\pm}$ couples $\Delta m = \pm 1$ energy levels. The transition frequency becomes $\omega_0 \mp \Delta E/\hbar$. Here, $\Delta E = \mu_B g_F B$, with g_F being the Landé g-factor.

So for $\sigma^{\pm}$, the resonance frequency is shifted, and we write the susceptibilities as:

$$\chi_{\pm}(\omega) = \frac{N_0 e^2 f}{\varepsilon_0 m} \cdot \frac{1}{(\omega_0 \mp \Delta E/\hbar)^2 - \omega^2 - i\omega\Gamma} \tag{2.25}$$

Approximating for Large Detuning: Assume large detuning $\Delta = \omega - \omega_0 \gg \Gamma$, and expanding the denominator, we get,

$$(\omega_0 \mp \Delta E/\hbar)^2 - \omega^2 \approx \omega_0^2 \mp 2\omega_0 \frac{\Delta E}{\hbar} - \omega^2 \tag{2.26}$$

$$= (\omega_0^2 - \omega^2) \mp 2\omega_0 \frac{\Delta E}{\hbar} \tag{2.27}$$

Substituting into $\chi_{\pm}(\omega)$:

$$\chi_{\pm}(\omega) = \frac{N_0 e^2 f}{\varepsilon_0 m} \cdot \frac{1}{\omega_0^2 - \omega^2 \mp 2\omega_0 \Delta E/\hbar - i\omega\Gamma} \tag{2.28}$$

This leads to the quoted form:

$$\boxed{\chi_{\pm}(\omega) = \frac{N_0 e^2 f}{\varepsilon_0 m} \cdot \frac{1}{\omega_0^2 - \omega^2 \mp \omega\Delta E - i\omega\Gamma}} \tag{2.29}$$

where the $\mp\omega\Delta E$ term encodes the Zeeman shift effect on circular components.

In case of large detuning $\Delta \gg \Gamma$, we expand the denominator and retain the linear Zeeman shift, giving:

$$\chi_+ - \chi_- \approx \frac{2N_0 e^2 f}{\varepsilon_0 m \omega_0} \cdot \frac{S_z}{\Delta_p^2} \tag{2.30}$$

Faraday Rotation Angle: Consider a linearly polarized electromagnetic wave propagating in the z-direction through a medium of length L that exhibits magnetic circular birefringence. This effect rotates the polarization due to the difference in refractive indices for right- and left-circularly

polarized components. The input field can be written as

$$E_+ = \frac{E_0}{2}(\hat{x} + i\hat{y})e^{i(k_+ z - \omega t)}, \tag{2.31}$$

$$E_- = \frac{E_0}{2}(\hat{x} - i\hat{y})e^{i(k_- z - \omega t)}, \tag{2.32}$$

with $k_\pm = \omega n_\pm / c$.

At $z = L$, the total output field is

$$\mathbf{E}_{\text{out}} = \frac{E_0}{2} e^{-i\omega t} \left[\hat{x}(e^{ik_+ L} + e^{ik_- L}) + i\hat{y}(e^{ik_+ L} - e^{ik_- L}) \right]. \tag{2.33}$$

Define the mean and difference wavevectors:

$$\bar{k} = \frac{k_+ + k_-}{2}, \quad \Delta k = k_+ - k_-.$$

Then

$$e^{ik_\pm L} = e^{i\bar{k}L} e^{\pm i\Delta k L/2}.$$

Using $\Delta k L \ll 1$,

$$\mathbf{E}_{\text{out}} \approx E_0 e^{i(\bar{k}L - \omega t)} \left[\hat{x} \cos\left(\tfrac{\Delta k L}{2}\right) - \hat{y} \sin\left(\tfrac{\Delta k L}{2}\right) \right].$$

This corresponds to a linear polarization rotated by a small angle

$$\boxed{\theta_F = \frac{\Delta k L}{2} = \frac{\omega L}{2c}(n_+ - n_-)}. \tag{2.34}$$

Susceptibility and Refractive Index. For weak susceptibility ($|\chi| \ll 1$), the refractive index is $n \approx 1 + \frac{1}{2}\Re[\chi]$, hence

$$n_+ - n_- \approx \tfrac{1}{2}\Re[\chi_+ - \chi_-]. \tag{2.35}$$

In SI units, the susceptibility of a dilute atomic medium near an optical resonance is

$$\chi(\omega) \approx \frac{N_0 e^2 f}{\varepsilon_0 m} \cdot \frac{1}{\omega_0^2 - \omega^2 - i\gamma\omega}, \tag{2.36}$$

with N_0 the atomic number density, f the oscillator strength, ω_0 the resonance frequency, and γ

the linewidth. For large detuning $|\Delta| = |\omega - \omega_0| \gg \gamma$,

$$\chi(\omega) \approx \frac{N_0 e^2 f}{2\varepsilon_0 m \omega_0} \cdot \frac{1}{\Delta}. \tag{2.37}$$

Therefore,

$$n_+ - n_- \approx \frac{N_0 e^2 f}{4\varepsilon_0 m \omega_0} \left(\frac{1}{\Delta_+} - \frac{1}{\Delta_-} \right). \tag{2.38}$$

Spin Fluctuations and Faraday Noise. The expectation value of the electron spin along z is proportional to the population imbalance:

$$\langle J_e \rangle \propto \frac{N^+ - N^-}{N_0}. \tag{2.39}$$

For $N = N_0 A L$ atoms in the probe volume (cross-sectional area A, length L), statistical spin fluctuations have rms size

$$\sqrt{\langle (N^+ - N^-)^2 \rangle} = \sqrt{N} = \sqrt{N_0 A L}. \tag{2.40}$$

The resulting rms Faraday rotation fluctuation is

$$\boxed{\sqrt{\langle \delta\theta_F^2 \rangle} = \frac{e^2 f \beta}{4\varepsilon_0 m c\, \omega_0\, \Delta} \cdot \sqrt{\frac{N_0 L}{A}}}. \tag{2.41}$$

Here β encodes the relative coupling strength of $\sigma^{\pm}$ transitions (for alkali D1 and D2 lines, $\beta = +2$ or -1).

Equation 2.41 gives the *intrinsic* Faraday-rotation variance, independent of probe intensity. In practice, a balanced polarimeter converts a rotation $\theta_F(t)$ into a photocurrent fluctuation $\delta i(t) \approx 2RP\theta_F(t)$, with probe power P and detector responsivity R. Thus the measured electrical spin-noise power scales as $P^2 \langle \delta\theta_F^2 \rangle$. When normalized to photon shot noise ($\propto P$), the integrated spin-noise signal scales linearly with probe power P, in agreement with Crooker *et al.*, Nature 2004 [53].

2.1.3 Quantum statistical treatment of spin-noise spectroscopy

Unlike semiclassical approaches that relate polarization rotation to atomic susceptibility, the quantum statistical framework expresses the observable spin noise in terms of two-time correlation functions of spin operators. This formalism is particularly powerful as it rigorously accounts for quantum fluctuations, thermal averaging, and the full quantum structure of the atom-light interaction. The derivation outlined below follows the treatment of Mihaila et al. [68], starts from the Kramers–Heisenberg scattering amplitude and connects the detected Faraday rotation fluctuations to spin correlation functions.

Field decomposition. The total optical field at the detector is the sum of the strong coherent probe mode and weak fields scattered by individual atoms:

$$\mathbf{A}(\mathbf{r},t) = \mathbf{a}_0(\mathbf{r},t) + \sum_k \delta\mathbf{a}_k(\mathbf{r},t). \tag{2.42}$$

The probe is modeled as a paraxial wave

$$\mathbf{a}_0(\mathbf{r},t) = A_0\, F(\boldsymbol{\rho})\, \hat{\epsilon}_{\text{in}}\, e^{i(kz-\omega t)} + \text{c.c.}, \qquad \int d^2\rho\, |F(\boldsymbol{\rho})|^2 = 1, \tag{2.43}$$

where $F(\boldsymbol{\rho})$ describes the normalized transverse mode profile, $\hat{\epsilon}_{\text{in}}$ is the probe polarization, and $k = \omega/c$.

Single-atom scattering amplitude. An atom at $\mathbf{R}_k$ acts as a localized scatterer, producing a weak outgoing field

$$\delta\mathbf{a}_k(\mathbf{r},t) \;\propto\; \tilde{a}_{\text{in,out}}(\omega,\hat{\mathbf{r}})\, F(\boldsymbol{\rho}_k)\, \frac{e^{i(k|\mathbf{r}-\mathbf{R}_k|-\omega t)}}{|\mathbf{r}-\mathbf{R}_k|}, \tag{2.44}$$

where $\tilde{a}_{\text{in,out}}$ is the scattering amplitude that connects incoming polarization $\hat{\epsilon}_{\text{in}}$ to outgoing polarization $\hat{\epsilon}_{\text{out}}$:

$$\tilde{a}_{\text{in,out}}(\omega) = \frac{r_0^{(\text{SI})}}{m_e} \frac{(\mathbf{P}\cdot\hat{\epsilon}^*_{\text{in}})\, \mathcal{P}_J\, (\mathbf{P}\cdot\hat{\epsilon}^*_{\text{out}})}{\omega_{JR}-\omega}. \tag{2.45}$$

Here $\mathbf{P}$ is the electron momentum operator, $\mathcal{P}_J$ projects onto the intermediate resonance manifold J, and $r_0^{(\text{SI})} = e^2/(4\pi\varepsilon_0 m_e c^2)$ is the classical electron radius in SI units.

Forward detection and mode overlap. In the paraxial forward limit, only the forward-scattered component interferes with the probe to produce measurable polarization rotation. Collecting over the transverse beam profile gives a mode-weighted rotation fluctuation

$$\delta\Theta(t) = C(\omega) \int d^3R \, |F(\boldsymbol{\rho})|^2 \, \hat{s}_z(\mathbf{R}, t), \tag{2.46}$$

where $\hat{s}_z(\mathbf{R}, t)$ is the spin projection density operator and $C(\omega)$ is a frequency-dependent prefactor containing the scattering amplitude and dipole matrix elements.

The effective overlap area of the mode is defined by

$$A_{\text{eff}}^{-1} = \int d^2\rho \, |F(\boldsymbol{\rho})|^4, \qquad \int d^3R \, |F(\boldsymbol{\rho})|^4 = \frac{L}{A_{\text{eff}}}. \tag{2.47}$$

Spin correlation and noise spectrum. The single-sided power spectral density (PSD) of the rotation fluctuations is the Fourier transform of the autocorrelation function:

$$P_\Theta(\omega) = \int_{-\infty}^{\infty} dt \, e^{i\omega t} \langle \delta\Theta(t) \, \delta\Theta(0) \rangle. \tag{2.48}$$

Substituting the expression for $\delta\Theta(t)$ yields

$$P_\Theta(\omega) = |C(\omega)|^2 \, \frac{L}{A_{\text{eff}}} \, n_0 \, S(\omega), \tag{2.49}$$

where n_0 is the atomic number density and

$$S(\omega) = \frac{1}{n_0} \int dt \, e^{i\omega t} \int d^3r \, \langle \hat{s}_z(\mathbf{r}, t) \hat{s}_z(\mathbf{0}, 0) \rangle \tag{2.50}$$

is the normalized spin–spin correlation spectrum. In equilibrium the sum rule

$$\int \frac{d\omega}{2\pi} \, S(\omega) = 1 \tag{2.51}$$

ensures that the total spectral weight per atom is unity.

Detection chain. Finally, a balanced polarimeter converts rotation into photocurrent:

$$\delta i(t) \approx 2RP\,\delta\Theta(t), \tag{2.52}$$

with probe power P and detector responsivity R. The measured photocurrent PSD is then

$$S_i(\omega) = (2RP)^2\,P_\Theta(\omega) + S_{\text{shot}}(\omega) + S_{\text{el}}(\omega), \tag{2.53}$$

where $S_{\text{shot}} \propto RP$ is photon shot noise and S_{el} denotes technical noise. Normalizing the spin-noise area to the shot-noise background reveals the characteristic linear scaling with probe power observed experimentally.

2.1.4 Quantum statistical treatment of spin-noise spectroscopy

Spin noise spectroscopy (SNS) measures intrinsic spin fluctuations of an ensemble via small Faraday rotation fluctuations of an off-resonant probe. A rigorous microscopic description relates the measured optical noise power to a spin–spin correlation function of the atomic ensemble; the derivation below follows the approach of Mihaila *et al.*. [68] [1]

Field decomposition and mode normalization. We work in SI units and write the (transverse) vector potential in the Coulomb gauge as the sum of a strong coherent probe mode and weak scattered contributions:

$$\mathbf{A}(\mathbf{r},t) = \mathbf{a}_0(\mathbf{r},t) + \sum_k \delta\mathbf{a}_k(\mathbf{r},t),$$

where the probe (dominant) mode is written in paraxial form

$$\mathbf{a}_0(\mathbf{r},t) = A_0\,F(\boldsymbol{\rho})\,\hat{\epsilon}\,e^{i(kz-\omega t)} + \text{c.c.}, \qquad \boldsymbol{\rho} = (x,y),$$

and the transverse mode $F(\boldsymbol{\rho})$ is normalized as

$$\int d^2\rho\,|F(\boldsymbol{\rho})|^2 = 1.$$

[1] See the original derivation for more details; here we present a compact, SI-consistent version with transparent assumptions.

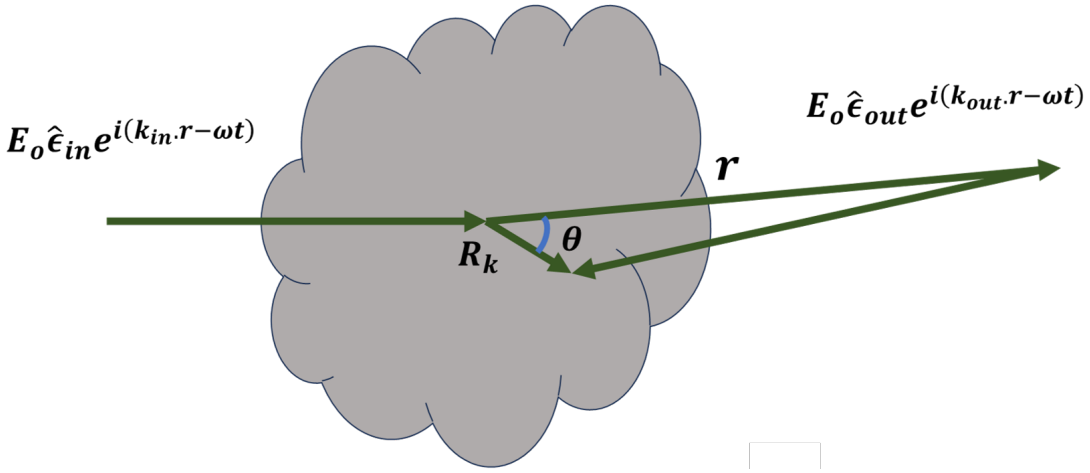


Figure 2.3: Schematic representation of the scattering geometry used in the quantum scattering theory of spin noise. The incident probe beam interacts with the atomic ensemble, and the scattered field is detected at an angle θ relative to the incident direction. The vector $\mathbf{R_k}$ denotes the position vector within the atomic cloud where the scattering event occurs. This configuration captures the momentum transfer and correlation effects central to the derivation of the spin noise spectrum.

(If you prefer a physical beam area, define A_{phys} so that $F \sim A_{\text{phys}}^{-1/2}$.)

Scattered field in the forward approximation. A spin (or atom) at $\mathbf{R}_k = (\boldsymbol{\rho}_k, z_k)$ scatters a weak field. In the weak-scattering, paraxial and forward limits (detector in the far forward direction and $F(\mathbf{r})$ slowly varying on optical wavelength scale) the scattered mode from atom k can be written schematically as

$$\delta\mathbf{a}_k(\mathbf{r}, t) \simeq \mathcal{S}(\omega)\, F(\boldsymbol{\rho}_k)\, \hat{s}_{z,k}(t)\, \frac{e^{ik(z-z_k)}}{z - z_k}\, \hat{\epsilon}' + \cdots ,$$

where $\mathcal{S}(\omega)$ is a (complex) scattering amplitude that contains the atomic matrix elements and resonance denominators, and $\hat{s}_{z,k}$ is the spin-projection operator of atom k (the exact operator structure depends on the atomic level structure and polarization geometry). The forward limit removes the angular integral and replaces the Green's function by a slowly varying function of $z - z_k$; the omitted terms are higher-order in scattering angle and $1/(kz)$.

Intensity difference and Faraday rotation. A polarizing beamsplitter and a balanced photodetector measure the difference of two orthogonal linear polarizations. To first (linear) order in

$\delta\mathbf{a}_k$,

$$\delta I(\mathbf{r},t) \propto \mathrm{Re}\Big[\, \mathbf{a}_0^*(\mathbf{r},t) \cdot \sum_k \delta\mathbf{a}_k(\mathbf{r},t) \,\Big].$$

Integrating the detected difference signal over the beam cross section and evaluating in the forward limit yields an integrated signal proportional to a spatially weighted spin density:

$$\delta\Theta(t) \equiv \int d^2\rho\, \delta I(\boldsymbol{\rho},t) = C(\omega) \int d^3R\, |F(\boldsymbol{\rho})|^2\, \hat{s}_z(\mathbf{R},t), \tag{2.54}$$

where $C(\omega)$ is an experimental prefactor (complex in general) that depends on the probe frequency, the near-resonant intermediate states, and microscopic dipole/momentum matrix elements. Equation (2.54) summarizes the important point: the detected rotation is the optical mode–weighted integral of the spin projection.

Effective area and mode-overlap factor. Define the (noise) effective transverse area

$$A_{\mathrm{eff}}^{-1} \equiv \int d^2\rho\, |F(\boldsymbol{\rho})|^4, \qquad \text{so that} \qquad \int d^3R\, |F|^4 = \frac{L}{A_{\mathrm{eff}}},$$

with L the length of the probed medium. For a uniform (top-hat) beam $A_{\mathrm{eff}} = A$; for a Gaussian beam A_{eff} differs by a numerical factor (e.g. $A_{\mathrm{eff}} = 2\pi R_0^2$ for the usual Gaussian normalization used in Mihaila).

Spin–spin correlations and detected power spectrum. Define the spin density operator $\hat{s}_z(\mathbf{r},t)$ and the (single-point, space-integrated) spin correlation function

$$S(\omega) \equiv \frac{1}{n_0} \int_{-\infty}^{\infty} dt\, e^{i\omega t} \int d^3r\, \langle \hat{s}_z(\mathbf{r},t)\, \hat{s}_z(\mathbf{0},0)\rangle,$$

where n_0 is the atom number density. With the definition $\delta\Theta(t)$ in (2.54), the detected single-sided power spectral density (PSD) of the rotation noise is

$$P_\Theta(\omega) \equiv \int dt\, e^{i\omega t} \langle \delta\Theta(t)\, \delta\Theta(0)\rangle = |C(\omega)|^2 \underbrace{\int d^3R_1\, d^3R_2\, |F(R_1)|^2 |F(R_2)|^2 \langle \hat{s}_z(R_1,t)\hat{s}_z(R_2,0)\rangle}_{= (L/A_{\mathrm{eff}})\, n_0\, S(\omega)}.$$

Hence we obtain the compact and widely used result

$$\boxed{P_\Theta(\omega) \;=\; |C(\omega)|^2 \,\frac{L}{A_{\text{eff}}}\, n_0\, S(\omega)}\,. \tag{2.55}$$

Equation (2.55) is the same structure obtained in Mihaila *et al.* (their Eq. (25) up to unit convention): the measured optical noise is the product of (i) an optical prefactor $C(\omega)$ (microscopic scattering/atomic physics), (ii) a geometric/mode factor L/A_{eff}, and (iii) the intrinsic spin spectral density $n_0 S(\omega)$. :contentReference[oaicite:5]index=5

Expression for the prefactor $C(\omega)$. The complex prefactor $C(\omega)$ can be written in terms of atomic matrix elements and resonance denominators. Following the same approximations as Mihaila (single-electron oscillator, near-resonant intermediate manifold) one finds schematically

$$C(\omega) \;\propto\; \frac{c\, r_0}{m_e}\, \frac{|\langle f|\hat{p}_x|i\rangle|^2}{\omega_J - \omega}$$

where r_0 is the (SI) classical electron radius

$$r_0^{(\text{SI})} = \frac{e^2}{4\pi\varepsilon_0 m_e c^2},$$

and $|\langle f|\hat{p}_x|i\rangle|^2$ denotes the (suitably chosen) momentum (or equivalently dipole) matrix element squared for the optical transition. In practice, it is often convenient to re-express the matrix element in terms of the dipole $d = \langle f|e\hat{x}|i\rangle$ or the oscillator strength f; the exact conversion factors are standard and given in atomic physics texts.

Normalization For a noninteracting classical gas in thermal equilibrium, Mihaila shows that the single-atom (one-particle) spectral weight obeys a sum rule (their Eq. (32)). With our normalisation, the integrated spectral weight per atom is unity:

$$\int \frac{d\omega}{2\pi}\, S(\omega) = 1 \qquad \text{(for the appropriately normalized single-atom correlation).}$$

Use this to relate integrated measured noise area to single-atom matrix elements and occupations, as in Mihaila [68].

Detection chain and probe power. Equation (2.55) gives the intrinsic optical rotation PSD (units rad^2/Hz). A real detector converts rotation into photocurrent: for small rotations a balanced polarimeter gives (to leading order)

$$\delta i(t) \approx 2RP\,\delta\Theta(t),$$

with P the probe power and R the detector responsivity (A/W). Thus the measured electrical PSD scales as $(2RP)^2 P_\Theta(\omega)$. Normalizing the spin-noise area to photon shot noise (which $\propto P$) yields a linear dependence on probe power P, consistent with experiment (Crooker *et al.*). Distinguish carefully between the *intrinsic* rotation variance (independent of probe power) and the *measured electrical* noise (which depends on P).

Conclusion. This SI-consistent formulation reproduces the central result of Mihaila et al. that the detected spin-noise power is proportional to a product of an optical prefactor, a geometric/mode factor L/A_{eff}, and the microscopic spin spectral function $S(\omega)$ [cf. Eq. (25) and (29) of [68].

2.2 Experimental Background

Spectroscopy, the study of matter–radiation interaction, plays a central role in exploring atomic and molecular structure. Among various spectroscopic techniques, Spin noise spectroscopy (SNS) stands out for its non-invasive nature, where the intrinsic fluctuations of spin polarisation are detected without driving transitions.

In SNS, a far-detuned linearly polarised laser beam probes an atomic vapour. Although the ensemble is unpolarized on average, statistical spin fluctuations cause the polarisation axis of the probe beam to randomly rotate, an effect known as Faraday rotation. These fluctuations are picked up as noise on a photodetector.

A related but distinct effect is Magnetic Circular Dichroism (MCD), in which σ^+ and σ^- components are absorbed differently. While MCD is useful in absorption-based studies, SNS relies on birefringence (Faraday rotation), but not on absorption, and thus avoids heating or decoherence.

In the Voigt configuration, the probe light is sensitive to the transverse component of spin

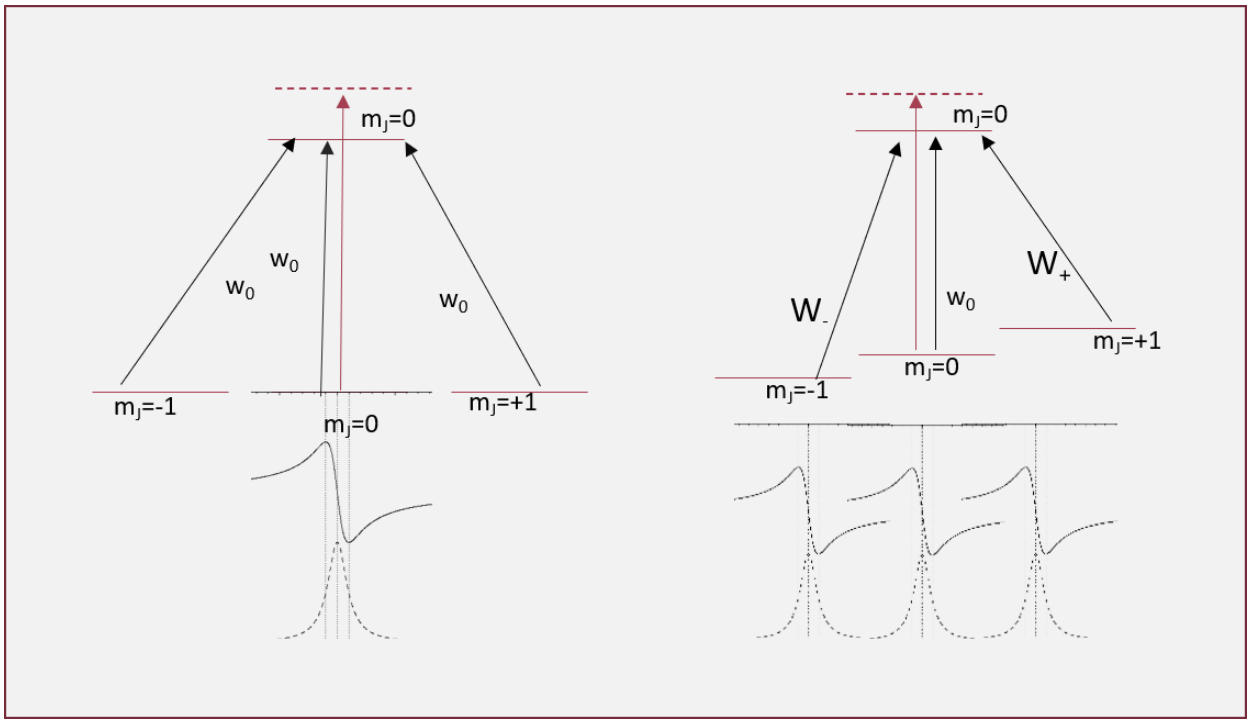


Figure 2.4: Magnetic Circular Birefringence (MCB): (Left) In the absence of an external magnetic field ($B = 0$), the Zeeman sublevels $m_J = -1, 0, +1$ are degenerate. The σ^+ and σ^- transitions therefore have identical resonance frequencies and experience equal refractive indices. As a result, both circular polarization components of the probe field accumulate the same phase, producing no net polarization rotation. The red vertical line represents the probe laser frequency ω_0, which is tuned near (or far-detuned from) the atomic resonance.(Right) When a magnetic field is applied ($B \neq 0$), the Zeeman degeneracy is lifted, shifting the m_J sublevels in opposite directions. Consequently, the σ^+ and σ^- transitions experience different detunings relative to the fixed probe frequency ω_0. This produces unequal dispersive phase shifts for the two circular polarization components, resulting in different real parts of the refractive index ($n_+ \neq n_-$). The accumulated differential phase shift $\Delta\phi \propto (n_+ - n_-)L$ leads to a rotation of the plane of polarization of the transmitted light — the Faraday rotation. In spin noise spectroscopy (SNS), the probe is typically operated far off-resonance, such that the dispersive birefringent response (MCB) dominates over absorptive effects like magnetic circular dichroism (MCD). This ensures minimal spontaneous scattering and enables a weakly perturbative, near quantum non-demolition measurement of the collective spin.

magnetisation (perpendicular to the field). These spin fluctuations behave like a random process whose correlation function exhibits damped oscillations.

Finally, the detection system converts polarisation fluctuations into measurable electrical signals. This is done using a balanced polarimetric detector, which subtracts two orthogonal polarisation channels to enhance sensitivity to spin noise.

2.2.1 Experimental Setup

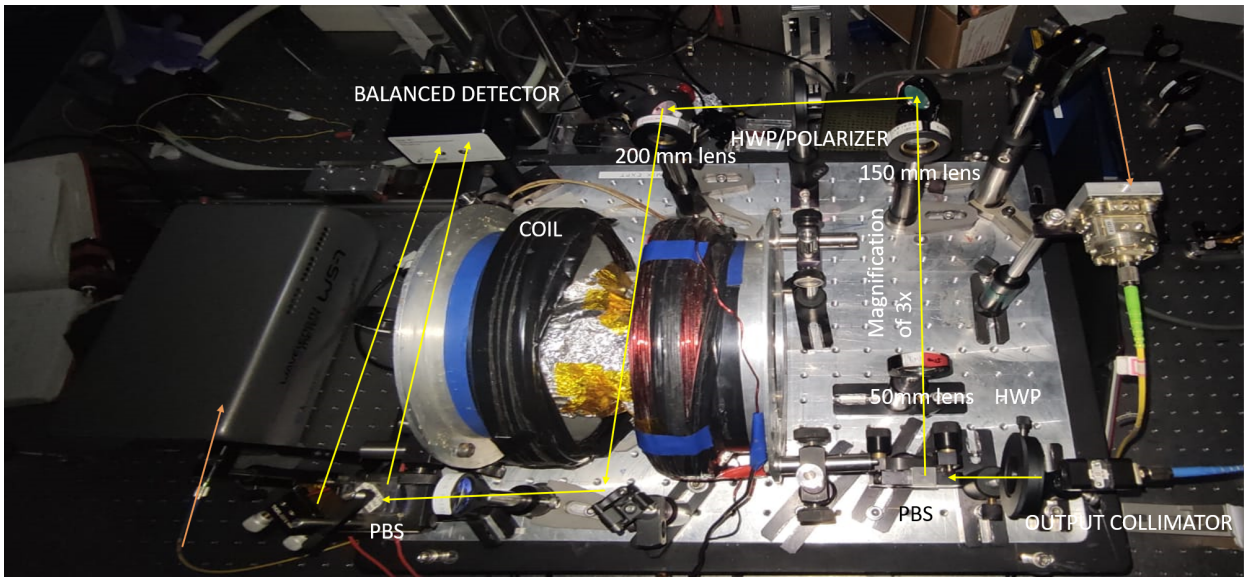


Figure 2.5: Schematic of the SNS experimental setup, showing the beam-shaping optics, Rubidium vapour cell, magnetic coils in Voigt geometry, and the balanced detection system. This configuration enables non-perturbative probing of intrinsic spin fluctuations via Faraday rotation.

Our Spin noise spectroscopy (SNS) experiment is centred around a Rubidium (Rb) vapour cell containing Rb atoms in a Neon buffer gas environment. The cell is enclosed in a temperature-controlled oven regulated via a temperature controller. The temperature governs the vapour pressure, and hence, the atomic number density contributing to the SNS signal. A continuous-wave (CW, Toptica Photonics) 780 nm laser is used as the probe. The beam is focused to a waist of approximately 45 μm at the center of the vapor cell using a lens of 200 mm focal length. This tight focusing enhances the interaction with the atomic ensemble and increases the signal-to-noise ratio (SNR) by probing a small region.

A magnetic field is applied perpendicular to the direction of light propagation. At low field

strengths, a solenoid is used for fine tuning instead of a Helmholtz coil. For higher fields and better homogeneity, a pair of Helmholtz coils is employed. This magnetic field causes Larmor precession of the atomic spins, which is the basis of the SNS signal.

The probe beam's polarization and intensity are adjusted using a combination of optical components. A half-wave plate (HWP) and polarizing beam splitter (PBS) control the intensity of the probe beam sent to the experimental set up. A second HWP and a polarizer set the beam's polarization at 45°, ensuring it contains equal components of σ^+ and σ^- polarizations.

As the beam exits the vapor cell, it enters another PBS, which splits the beam into orthogonal polarization components. These components are directed onto a balanced photodetector, which subtracts the signals to eliminate common-mode noise and isolate the spin-induced polarization fluctuations. The differential signal is processed by a spectrum analyzer that reveals the spin noise power spectrum.

Figure 2.5 illustrates the full experimental layout, from the laser source to the detection system, including optical control elements and magnetic field-generating coils.

The probe is kept detuned by several GHz from the ^{87}Rb $F = 2 \rightarrow F' = 3$ of the D2 transition, allowing for quantum non-demolition (QND) measurements where the probe does not disturb the spin state of the atoms. This detuning also reduces absorption and heating effects.

The resulting spin noise spectrum contains a Lorentzian-shaped peak at the Larmor frequency of the atoms. The width of this peak corresponds to the spin dephasing time T_2.

2.3 Experimental Results

2.3.1 Spin Noise Peaks for ^{85}Rb and ^{87}Rb

At a magnetic field of $B = 6.31$ G and probe detuning of +7 GHz from the $F = 2$ to $F = 3$ transition of the D2 line of ^{87}Rb, two distinct peaks are observed in the spin noise spectrum. These arise due to spontaneous spin fluctuations within the hyperfine ground states of ^{85}Rb and ^{87}Rb.

In the fig. 2.7, the peak at 2.9 MHz corresponds to ^{85}Rb, while the 4.4 MHz peak corresponds to ^{87}Rb. The difference in Larmor frequencies stems from their distinct Landé g_F factors and hyperfine level structures. These peaks originate from spin fluctuations between neighbouring

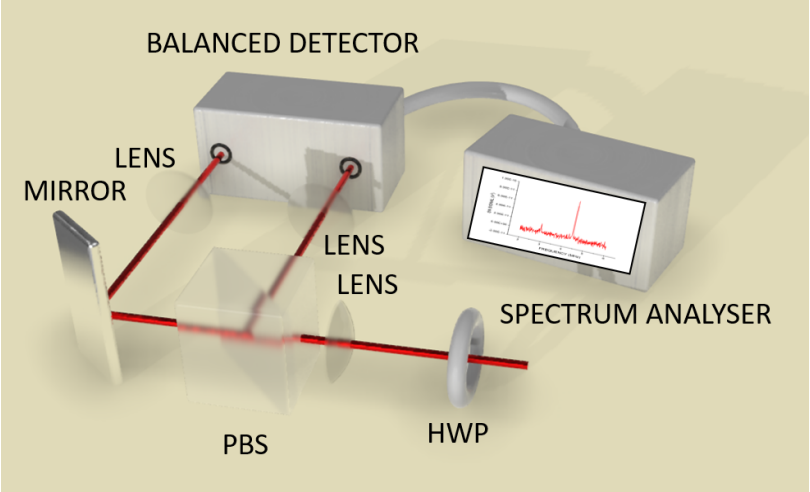


Figure 2.6: Balanced detection scheme for Faraday rotation: the probe beam is split into two orthogonal polarization components using a PBS. The differential signal between the two photodiodes reflects spin-induced Faraday rotation noise, suppressing common-mode noise.

Zeeman sublevels $m_F \leftrightarrow m_F \pm 1$ within a given hyperfine manifold. In the regime of weak magnetic fields, the Zeeman effect is linear, meaning the energy difference between adjacent m_F states is constant. As a result, all such transitions contribute to a single resonance peak per isotope in the spin noise spectrum. The Zeeman splitting for a transition $\Delta m_F = \pm 1$ is given by,

$$h\nu = g_F \Delta m_F \mu_B B \tag{2.56}$$

where μ_B is the Bohr magneton, g_F is the hyperfine Landé g-factor, and B is the applied magnetic field. Since $\Delta m_F = \pm 1$, the splitting is uniform, and fluctuations between all adjacent m_F levels are degenerate in frequency, reinforcing the observed peak. This dual-peak structure confirms that the SNS setup is capable of resolving isotope-specific noise signatures. In addition, we observe that the peak corresponding to the ^{87}Rb isotope is stronger than that of ^{85}Rb. This is due to the higher relative concentration of ^{87}Rb in the enriched vapour cell used for the measurements, resulting in a larger collective spin fluctuation signal from ^{87}Rb compared to the residual ^{85}Rb component.

Dependence on Probe Power: Broadening and Amplification

As the probe power increases, the intensity of the spin noise signal also increases. This is expected, as stronger Faraday rotation fluctuations induce larger differential signals on the photodetector.

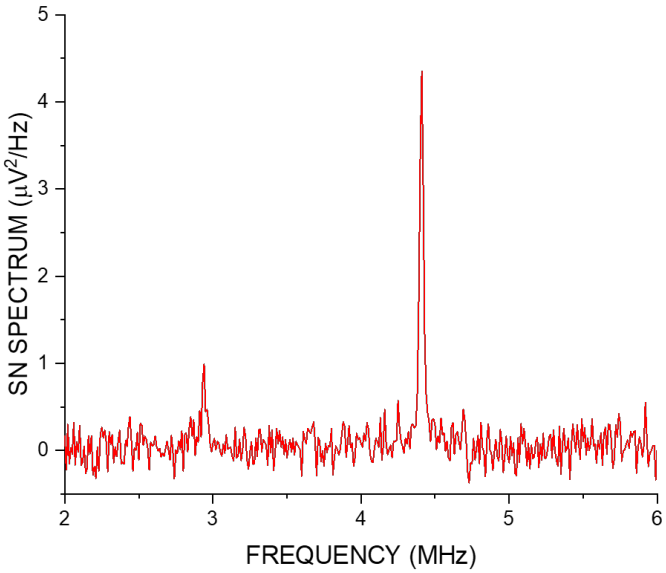


Figure 2.7: Spin noise spectrum recorded at $T = 105°C$, probe power = 350 μW, detuning = +7 GHz, and magnetic field $B = 6.31$ G using an ^{87}Rb-enriched vapour cell. Two peaks are observed corresponding to the Larmor precession frequencies of ^{87}Rb and residual ^{85}Rb isotopes. The dominant peak arises from ^{87}Rb due to its higher isotopic concentration in the enriched cell. The smaller peak corresponds to the remaining fraction of ^{85}Rb. The peak frequencies follow $\omega_L = g_F \mu_B B/\hbar$, reflecting the different Landé g_F factors of the two isotopes in the linear Zeeman regime. These spectral features originate from stochastic transverse spin fluctuations of the atomic ensemble, detected through dispersive Faraday rotation of the far-detuned probe beam.

Figure 2.8 shows how the SNS spectrum evolves with increasing probe power. The signal amplitude rises, and the spectral line broadens. This gives rise to a higher integrated SNS signal.

To quantify this behavior, we extract the linewidth (FWHM) and peak amplitude for each probe power. Together, figs. 2.9a and 2.9b confirm the tradeoff between signal strength and spectral resolution. For optimal sensitivity, moderate probe powers are used to avoid excessive broadening.

Density of Spin Noise Signal

Density influences the amplitude of the spin noise (SN) signal. As the temperature increases, the vapour pressure of the alkali atoms rises, leading to a higher atomic number density. This results in an increased SN signal due to the enhanced number of contributing atoms.

Figure 2.10 shows the SN power spectra recorded at various cell temperatures. A clear increase in peak amplitude is observed with increasing temperature, consistent with the enhanced magneto-

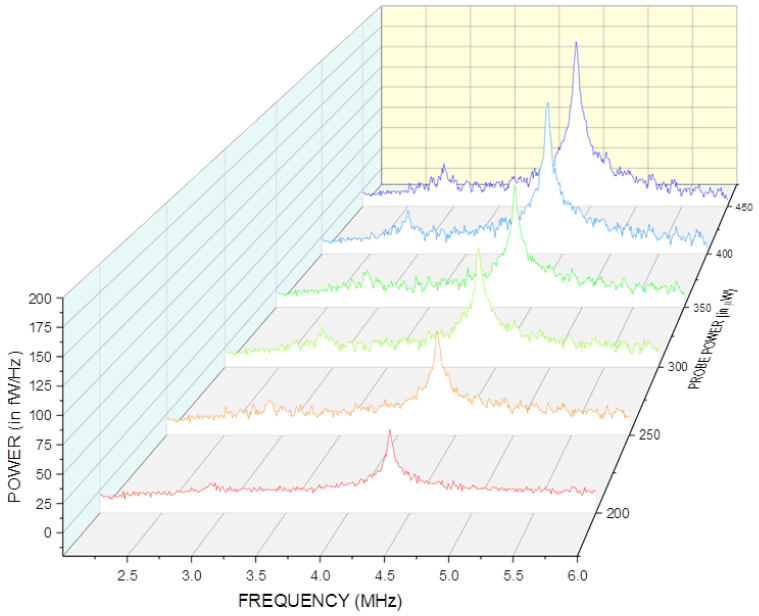


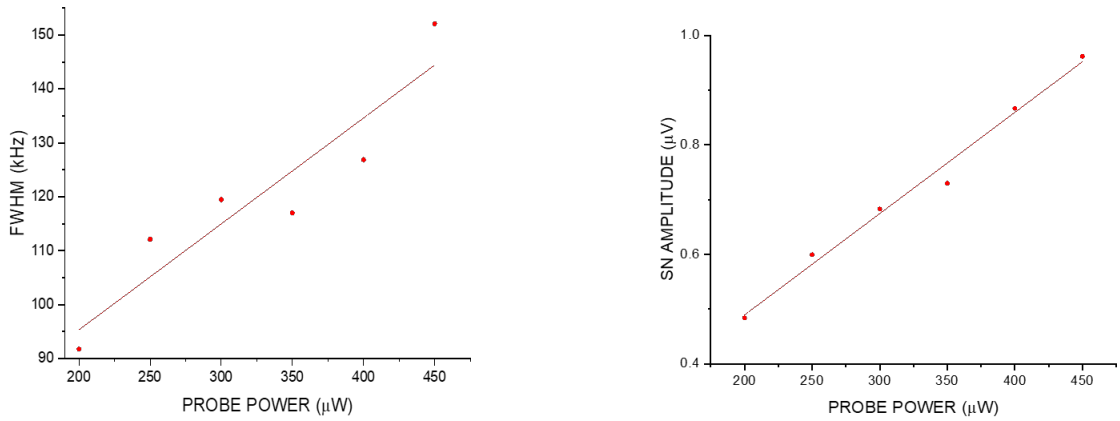
Figure 2.8: Spin noise spectra for different probe powers. Increasing power leads to stronger signal amplitude and spectral broadening. Parameters: detuning = +8 GHz, $T = 100°C$, $B = 6.31$ G.

optical signal from a denser atomic ensemble.

To quantify this trend, we extract the peak amplitude of the SN signal at each temperature and plot it in fig. 2.11(a). The increase is monotonic and reflects the contribution from higher vapour pressure and atom number.

For uncorrelated spin fluctuations, the spin noise amplitude is expected to scale as $A_{\mathrm{SNS}} \propto \sqrt{N}$, where N is the number of atoms. Since atomic density is proportional to N, the expected dependence is $A_{\mathrm{SNS}} \propto \sqrt{n}$. A log–log representation yields a slope close to 0.5, consistent with the expected $\sqrt{N}$ dependence.

Since temperature and atomic density are closely related, it is insightful to examine their interdependence. Figure 2.12 illustrates how the atomic number density varies with vapour pressure, which is a function of temperature for alkali vapours. Consider P_v is the vapor pressure in Torr, T is the absolute temperature in Kelvin, and T_m is the melting point of Rubidium (T_m = 312.46 K, equivalent to 39.31°C). The vapour pressure of rubidium exhibits distinct temperature dependence in the solid and liquid phases due to differences in the enthalpy of sublimation and vaporisation. For temperatures below the melting point (T_m = 39.31°C), Rubidium exists in the solid phase, and the vapor pressure is given by eq. 2.57, which accounts for sublimation. Above



(a) (b)

Figure 2.9: (a) FWHM of the SN peak as a function of probe power. The trend indicates increasing power broadening due to enhanced probe interaction. (b) SN signal amplitude versus probe power. The approximately linear dependence is consistent with expectations in the low-saturation regime.

the melting point, Rubidium transitions to the liquid phase, and the corresponding vapour pressure is described by eq. 2.58, reflecting the energetics of vaporisation. These empirical relations, originally compiled by Steck, are widely used in alkali vapour cell experiments to estimate the atomic number density from the vapour pressure [69]. For the solid phase of rubidium ($T < T_m$):

$$\log_{10} P_v = -94.04826 - \frac{1961.258}{T} - 0.03771687\,T + 42.57526\,\log_{10} T. \tag{2.57}$$

For the liquid phase of rubidium ($T \geq T_m$):

$$\log_{10} P_v = 15.88253 - \frac{4529.635}{T} + 0.00058663\,T - 2.99138\,\log_{10} T. \tag{2.58}$$

Figure 2.11 reiterates the proportional relationship between atomic density and SN amplitude, consolidating the view that both temperature and vapour pressure directly influence the measured SN. Together, these figures provide a consistent and comprehensive picture of how the SN signal grows with temperature, mediated by the increased vapour pressure and atomic number density.

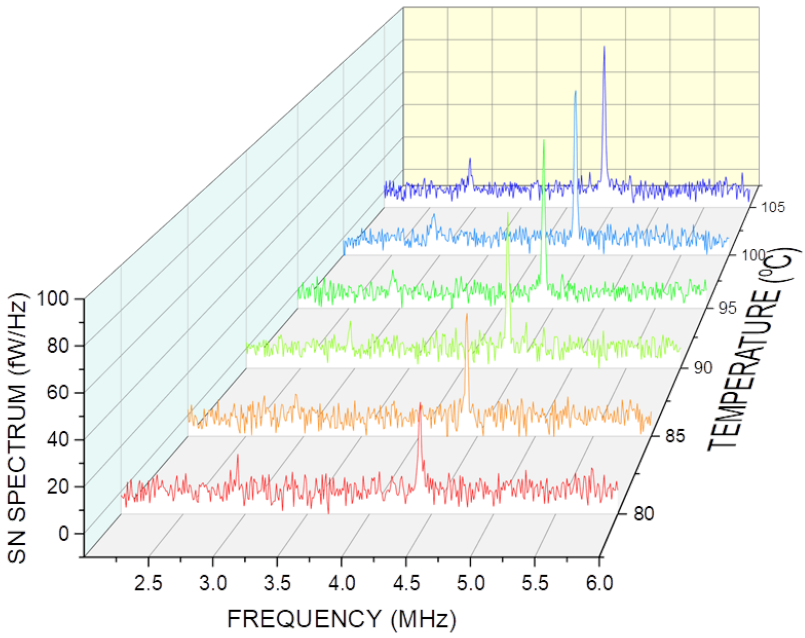


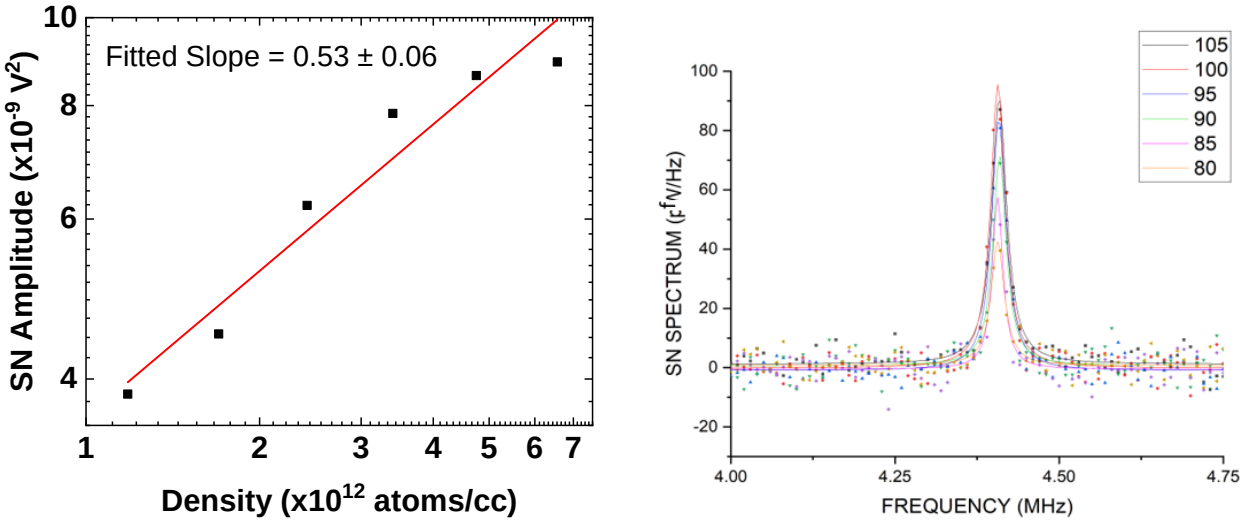
Figure 2.10: Spin noise spectra at increasing temperatures (70–110°C). Higher temperatures yield stronger signals due to increased atomic density.

2.4 Power Spectrum

SNS is a powerful tool to investigate various properties of the system, like relaxation rates, abundance ratios, inter-species spin-spin interactions, etc., in the presence of a transverse magnetic field. This technique has also been used for precise magnetic field detection [70–72]. The polarisation angle ($\theta_F(t)$) of the probe beam fluctuates over time owing to the population redistribution among the Zeeman states due to thermal (and quantum) fluctuations. This fluctuation, $\langle \delta\theta_F{}^2 \rangle^{1/2}$ is a direct measure of $\langle \rho_{21}^{\dagger}(t)\rho_{21}(0) \rangle$ i.e the auto-correlation of the density matrix element ρ_{21} of the ground states $|1\rangle$ and $|2\rangle$ (Fig. 2.13). The Fourier transform of the time correlation of ρ_{12} is the spin noise power spectrum. The time evolution of ρ_{21} is given by,

$$\frac{d\rho_{21}}{dt} = i(\omega_2 - \omega_1 + i\gamma_{21}) + \eta(t) \tag{2.59}$$

where we assume the noise $\eta(t)$ to be a Gaussian white noise with zero mean and $\langle \eta(t')\eta(t'') \rangle = N_2\gamma_{21}\delta(t' - t'')$. N_2 is the number of atoms within the measurement region, ω_2 and ω_1 are the ground state frequencies, and γ_{ij} is the relaxation rate of the spin coherence between states $|i\rangle$ and $|j\rangle$ of the atoms. The power spectrum is given by:



(a) (b)

Figure 2.11: (a) Spin-noise amplitude as a function of atomic number density. The fitted slope of 0.53 ± 0.06 indicates a $\sqrt{N}$ dependence, consistent with the expected scaling of spin-noise amplitude for uncorrelated spin fluctuations. (b) Raw spin-noise spectra recorded at different cell temperatures. Increasing temperature raises the vapour pressure and hence the atomic density, resulting in an increase in the observed spin-noise signal amplitude.

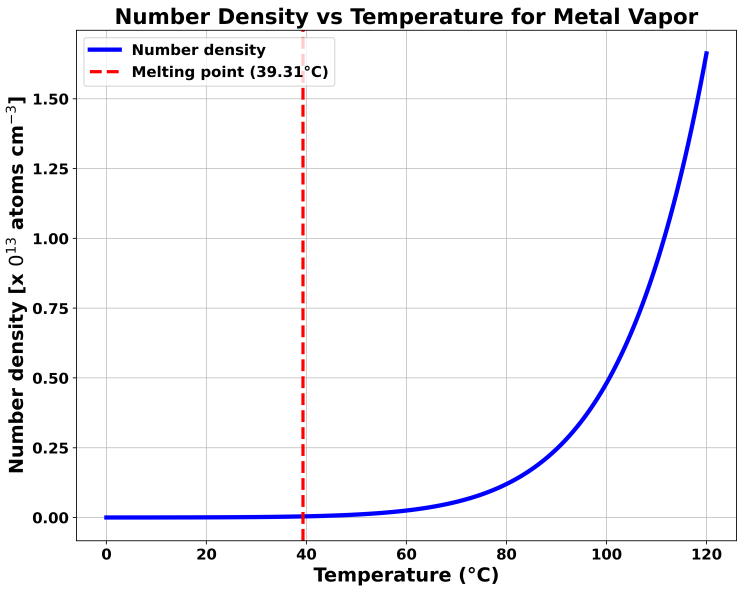


Figure 2.12: Atomic number density of ^{87}Rb atoms as a function of vapor pressure, calculated using the empirical vapor pressure relations from [69] and the ideal gas law. The dashed red line marks the melting point of rubidium at 39.31°C, indicating the transition between the solid and liquid phases. In the solid phase (left of the dashed line), the vapour pressure increases slowly with temperature due to sublimation, while in the liquid phase (right of the dashed line), the rate of increase is much steeper due to vaporisation.

$$P(\omega) = \frac{1}{2\pi}\int_{-\infty}^{\infty} e^{i\omega t}\langle\rho_{21}^{\dagger}(t)\rho_{21}(0)\rangle dt \tag{2.60}$$

$$= \frac{N_2}{2\pi}\left(\frac{\gamma_{21}}{\gamma_{21}^2 + (\omega - (\omega_2 - \omega_1))^2}\right) \tag{2.61}$$

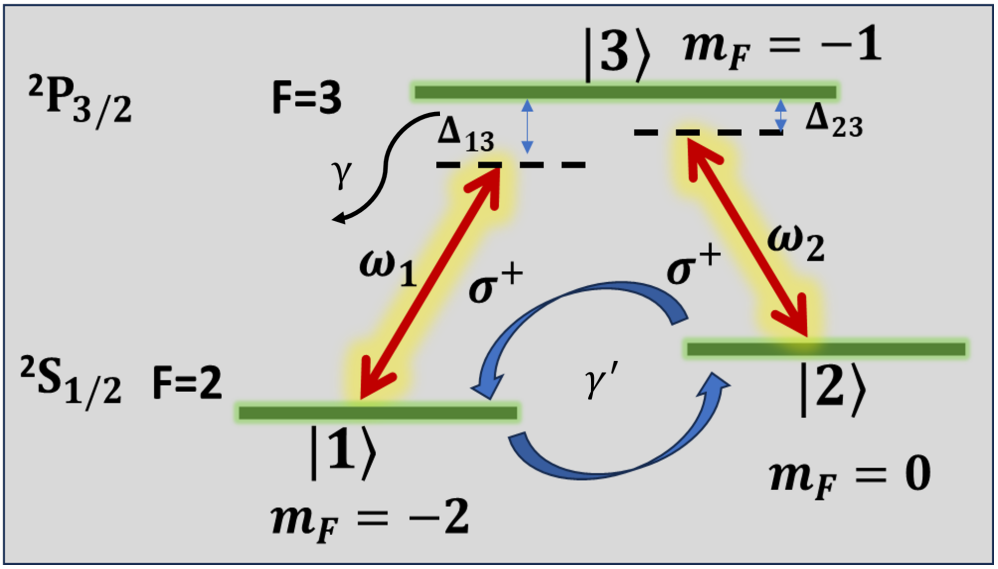


Figure 2.13: A schematic representation of a three-level atomic system, $|i\rangle$ ($i = 1, 2, 3$), where two Raman beams with frequencies ω_1 and ω_2 couple the states $|1\rangle$ to $|3\rangle$ and $|2\rangle$ to $|3\rangle$, respectively. The diagram also shows the detunings Δ_{13} and Δ_{23} and linewidths γ' (γ) for the ground (excited) states.

The power spectrum is a Lorentzian centered at the ($\omega = (\omega_2 - \omega_1) = 2\pi\nu_L$) Larmor frequency with a width of $2\gamma_{21}$. The width of the signal γ_{21} is governed by a number of decoherence factors like spin-destructive collisions, hyper-fine exchange collisions, transit time broadening, etc. These decay channels broaden our intrinsic SNS signals. It has been previously reported that the SNS signal depends on a number of factors like number density (n_o) of atoms being probed, the intensity of the probe beam (I), detuning of the probe beam (Δ), length of the cell (l) and the cross-sectional area of the probe (A). This can be written as a simple equation;

$$\Sigma = \frac{I}{\Delta}\sqrt{\frac{n_o l}{A}} \tag{2.62}$$

where Σ is the area under the curve of $P(\omega)$ which is the spin noise signal amplitude [73]. Intrinsic

SNS signal amplitudes are typically of the order of a few $nV/\sqrt{Hz}$, thereby making it difficult for precision measurements as the Signal-to-Noise ratio (SNR) is low ($\approx$ 100). Hence, we utilise a novel technique [74] in which the intrinsic SNS signal power spectral density is enhanced by a million-fold, leaving the noise level the same. The central theme of this work is the utilisation of this million-fold magnification of the SNR as a precision measurement tool. This relies on coherently driving the population among the adjacent Zeeman states of neutral atoms by utilising a pair of coherent Raman beams and non-invasively measuring this Raman-driven spin ensemble oscillation using the probe beam by employing SNS detection technique. In the Raman-driven power spectrum, the atoms are driven between the level $|1\rangle$ and $|2\rangle$ via level $|3\rangle$ by using a pair of beams connecting these levels. The Hamiltonian of the system can be described as

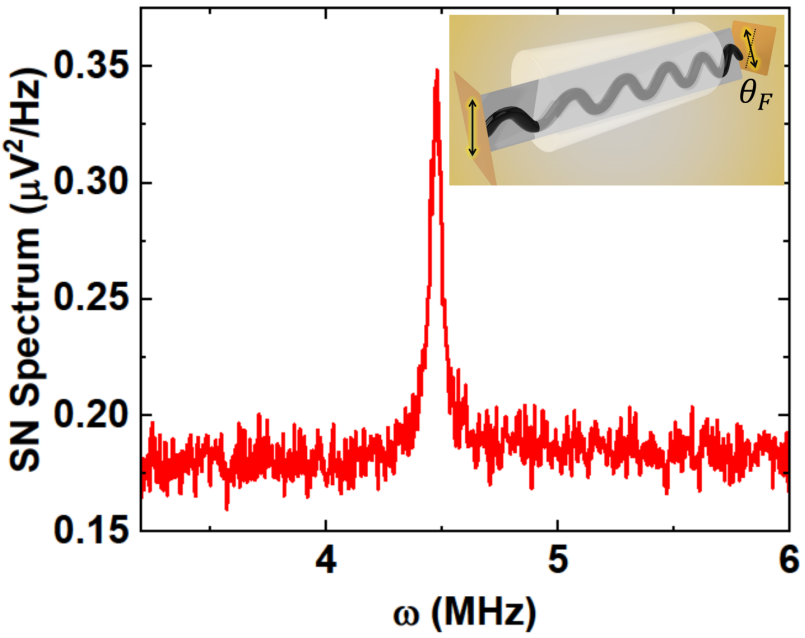


Figure 2.14: Intrinsic spin noise signal from thermal ^{87}Rb atoms. The peak corresponds to the Larmor frequency under a transverse magnetic field of 6.4 Gauss.

$$\begin{aligned}\frac{H}{\hbar} &= \omega_1 |1\rangle\langle 1| + \omega_2 |2\rangle\langle 2| + \omega_3 |3\rangle\langle 3| \\ &+ \frac{\Omega_{13}}{2}\left(|3\rangle\langle 1| e^{-i\omega_1 t} + |1\rangle\langle 3| e^{i\omega_1 t}\right) \\ &+ \frac{\Omega_{23}}{2}\left(|3\rangle\langle 2| e^{-i\omega_2 t} + |2\rangle\langle 3| e^{i\omega_2 t}\right) \end{aligned} \tag{2.63}$$

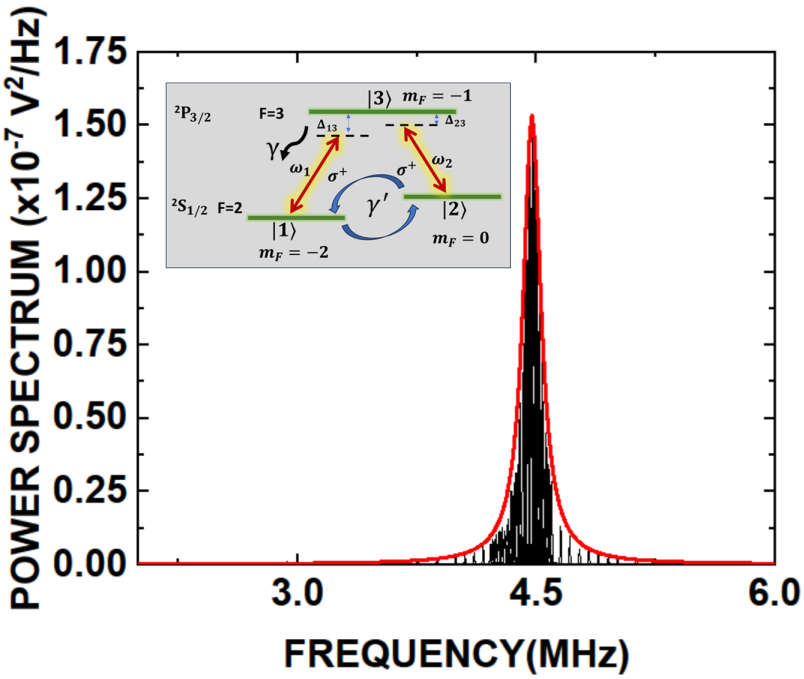


Figure 2.15: Raman-driven spin noise spectroscopy (RDSNS) signal of ^{87}Rb atoms in a vapor cell. The signal peaks when $\omega = \omega_2 - \omega_1 = 2\pi\nu_L$, where ν_L is the Larmor frequency. The red Lorentzian envelope (from Eq. 2.67) represents $|\rho_{21}|^2$ as per Eq. 2.68, while the black spikes are individual Dirac delta contributions. Inset: Three-level atomic system coupled by two Raman beams with detunings Δ_{13}, Δ_{23} and linewidths γ', γ.

where ω_i is the angular frequency of state $|i\rangle$ ($i = 1, 2, 3$). Here, Ω_{13} and Ω_{23} are the resonant Rabi angular frequencies of Raman field 1 (R_1) and Raman field 2 (R_2), respectively. To remove the explicit time-dependence in the Hamiltonian, we need to write the Hamiltonian in the rotating frame by applying the unitary transformation using $R(t) = e^{-i(\omega_1|1\rangle\langle 1|+\omega_2|2\rangle\langle 2|)t}$ followed by an energy scaling $-(\omega_1 + \omega_2)\mathbb{I}$. The final Hamiltonian $\tilde{H}$ of the system in the rotating frame can be written as,

$$\begin{aligned}\frac{\tilde{H}}{\hbar} &= -(\Delta_{12} - \Delta_{23})\,|2\rangle\langle 2| - \Delta_{13}\,|3\rangle\langle 3| + \frac{\Omega_{13}}{2}(|3\rangle\langle 1| + |1\rangle\langle 3|) \\ &\quad + \frac{\Omega_{23}}{2}(|3\rangle\langle 2| + |2\rangle\langle 3|)\end{aligned} \tag{2.64}$$

Here, $\Delta_{13} = \omega_1 - \omega_3 + \omega_1$, $\Delta_{23} = \omega_2 - \omega_3 + \omega_2$, which are related to the frequency detunings of the Raman beams from the relevant optical transitions. The master equation for ρ_{21} in the rotating frame is derived as,

$$\frac{d\rho_{21}}{dt} = i(\Delta_{13} - \Delta_{23} + i\gamma')\rho_{21} - i\Omega_{13}\rho_{23} + i\Omega_{23}\rho_{31} \tag{2.65}$$

Since, there is negligible decay between the states $|2\rangle$ and $|1\rangle$ compared to decay rates from $|3\rangle$ to $|1\rangle$ and $|2\rangle$, we have chosen the following limits on the relaxation rates: $\gamma_{13} = \gamma_{23} = \gamma$, $\gamma_{12} = \gamma_{21} = \gamma'$, and $\gamma' << \gamma$. Here, γ' is the spin coherence relaxation rate between the two Zeeman states. We find $\rho_{21}(t)$ at the steady state. Details of the calculation can be found in [74]. The power spectrum is given by,

$$\begin{aligned}P(\omega) &= \frac{1}{2\pi}\int_{-\infty}^{\infty} e^{i\omega t}\langle\rho_{21}^{\dagger}(t)\rho_{21}(0)\rangle dt \\ &= \delta(\omega + \omega_2 - \omega_1)|\rho_{21}|^2.\end{aligned} \tag{2.66}$$

When the driving is sufficiently strong, the intrinsic fluctuations, which are related to the equilibrium noise, form a broad background in the power spectrum at the steady state. By choosing $\Omega_{13} = \Omega_{23} = \Omega$, $\gamma_{13} = \gamma_{23} = \gamma$, $\gamma_{12} = \gamma_{21} = \gamma'$, $\Delta_{23} = 0$ and $\Delta_{13} = \Delta$, we get

$$\rho_{21} = \frac{-\gamma\Omega^2\left((\gamma' + i\Delta)(2\gamma + i\Delta) + 4\Omega^2\right)}{\gamma(\gamma'^2 + \Delta^2)(2\gamma^2 + \Delta^2) + \left(2\gamma\gamma'(3\gamma' + 4\gamma) + (\gamma' + 2\gamma)\Delta^2\right)\Omega^2 + 4(3\gamma' + 2\gamma)\Omega^4} \tag{2.67}$$

When we consider the Raman resonance limit, that is, i.e $\Delta = 0$ ($\delta_{12} = \nu_L$) in eq. 2.67, we get,

$$|\rho_{21}|^2_{\Delta=0} = \frac{\gamma^2\Omega^4}{(\gamma'\gamma^2 + (3\gamma' + 2\gamma)\Omega^2)^2} \tag{2.68}$$

From eq. 2.66, we see that the power spectrum looks like a dirac delta peak with an envelope as $|\rho_{21}|^2$ which grows with Ω which indicates that the coherence between $|1\rangle$ and $|2\rangle$ also grows and finally saturates at a large value of Ω. The envelope width of the RDSNS signal mimics the width of the intrinsic SNS signal with amplitude 10^6 times enhanced.

2.4.1 Key Advantages

By systematically driving the system into and out of equilibrium, we can uncover physical quantities that are concealed in the intrinsic spin noise (SN) signals. Dynamic perturbation converts the weak, thermally induced spin fluctuations into significantly more exaggerated response, which provides a number of advantageous features. First, the amplitude of the signal is increased by upto six orders of magnitude rendering it easily detectable by standard acquisition electronics without requiring dedicated low-noise preamplifiers. Significantly, this amplification occurs without increasing the background noise floor; rather, the signal-to-noise ratio (SNR) is directly proportional to the gain, maintaining measurement fidelity. In addition, the stronger, modulated signals pave the way for the use of sophisticated lock-in detection methods that are conventionally unsuitable for intrinsic SNS because of its stochastic character, hence facilitating the subtraction of spurious background fluctuations and the selective detection of stray or noisy magnetic fields. A further important benefit is in the spectral behaviour of the Raman-driven spin noise spectroscopy (RDSNS) peaks: each of them possesses a very narrow linewidth, usually just a few hertz, that makes it possible to determine quantities like the Larmor frequency, subtle magnetic field shifts, or resonance splittings with very high accuracy. Effectively, this method converts a normally passive measurement of noise into a high-resolution, actively tunable spectroscopic probe, greatly increasing the range and sensitivity of spin noise experiments.

"The magnetic field is, in a sense, as real as the velocity of a fluid. You cannot see it directly, but you can observe its effects with precision."

— Richard P. Feynman

Chapter 3

Magnetometry using spin noise spectroscopy

This chapter is based on the following publication:

All Optical Broadband Atomic Magnetometer Utilizing Raman-driven spin noise spectroscopy, **Sayari Majumder**, Saptarishi Chaudhuri, *IEEE Transactions on Instrumentation and Measurement*, vol. 74, pp. 1–10, 2025, Art. no. 1503610. doi:10.1109/TIM.2025.3554278

Based on the theoretical foundations of spin noise spectroscopy (SNS) and its extension to Raman-driven spin noise spectroscopy (RDSNS) presented in the previous chapter, the present chapter addresses the experimental implementation and characterisation of an all-optical broadband atomic magnetometer (AM) using the RDSNS method. The RDSNS method allows for the observation of intrinsic spin fluctuations in an atomic vapour under a coherent two-photon Raman drive. The spin noise signal is observed non-invasively using a far-off-resonant, weak probe beam, which is detected through a polarimetric detection scheme. This setup avoids the use of radio-frequency (RF) driving fields in conventional magnetometers, thereby causing

no perturbation to the atomic system. Unlike conventional Optically Pumped Magnetometers (OPMs) and Spin Exchange Relaxation Free (SERF) regime-based magnetometers, which tend to have poor dynamic range and limited bandwidth, the magnetometer based on RDSNS overcomes these limitations while maintaining a similar sensitivity on the order of $30pT/\sqrt{Hz}$.

3.1 Introduction

Atomic magnetometers (AMs) [75–81] have attracted a lot of attention in recent years due to their ultra-high sensitivity and broad applicability across a wide variety of fields including medical imaging [82–86], space exploration [76, 77, 87], and archaeological excavations [88]. Quantum optics has experienced rapid advancement due to advancements in laser and detection technologies, opening up new directions for the improvement of atomic magnetometers with quantum-limited magnetic field sensing. These devices are capable of matching the performance of superconducting quantum interference device (SQUID) magnetometers, which have sensitivities of down to 150 $aT/\sqrt{\text{Hz}}$ [31]. Unlike cryogenically cooled SQUIDs and their associated high operating costs, atomic magnetometers can operate at room temperature, are compact, and can be miniaturised. Atomic magnetometers are categorized based on their mode of operation into a number of classes, including Non-linear Magneto-Optical Rotation (NMOR) magnetometers [89, 90], Coherent Population Trapping (CPT) magnetometers, and Spin Exchange Relaxation Free (SERF) magnetometers. The Optically Pumped Magnetometers (OPMs) [91, 92] form a particularly notable class among them. An OPM generally detects the Faraday rotation of a linearly polarised probe laser propagating through an optically pumped atomic gas. In the presence of a weak magnetic field, the atomic ensemble is populated in different Zeeman sublevels under the Boltzmann distribution. Pumping with a circularly polarised pump beam polarises the atoms in one of the ground-state Zeeman sublevels. This creates a macroscopic magnetisation $\mathbf{M}$ which lags behind the external magnetic field $\mathbf{B}$ at the Larmor frequency. When the pump beam modulation frequency is equal to the Larmor frequency, the optical pumping synchronises with the precession of the spins and the rotation of the probe beam polarisation becomes a maximum. The intensity of this rotation measures the strength of the magnetic field.

Conventional AMs use a modulating radio frequency (RF) field to excite the atomic spins [89,

91–93]. When the RF frequency is equal to the Larmor frequency, magnetic resonance results and the intensity of the probe light transmitted are at a minimum, from which the magnetic field may be calculated. These RF-driven magnetometers are susceptible to external RF interference and therefore require proper shielding. While sensitivities up to 0.3 $fT/\sqrt{\text{Hz}}$ at 0.5 MHz have been reported [94], their bandwidth is restricted by the modulation devices used, for example, electro-optic modulators (EOMs), acousto-optic modulators (AOMs), or mechanical choppers. On the other hand, SERF magnetometers work in a high-density atomic regime at near-zero magnetic fields, where the spin-exchange collisions are significantly faster than the Larmor precession, thus suppressing spin-exchange relaxation and reaching sensitivities as low as the femtotesla level [78, 79, 95, 96]. However, SERF magnetometers have a small dynamic range, usually limited to a few nanotesla. CPT-based magnetometers attain moderate sensitivities, approximately 50 $pT/\sqrt{\text{Hz}}$ at 10 Hz [97], but are very well suited for chip-scale integration. Atomic magnetometry has also been realized based on ultracold atomic gases, e.g., single-domain spinor Bose–Einstein condensates of ^{87}Rb atoms [98] with sensitivities of 78 $fT/\sqrt{\text{Hz}}$.

Figure 3.1 gives a comparative summary of commonly applied magnetometer geometries. **SERF magnetometers** reach sub-femtotesla sensitivity but only function in shielded, near-zero-field conditions. **RF magnetometers** exploit an applied RF field to induce spin precession with broader tunability but the need for stringent shielding from ambient RF noise. **Bell–Bloom magnetometers** utilize amplitude-modulated optical pumping synchronized at the Larmor frequency, with the advantages of compact and portable operation for geomagnetic and space missions. **Mx magnetometers** utilize phase-sensitive detection with RF drive feedback, exhibiting wide dynamic range and are commonly utilized in navigation. **CPT magnetometers** utilize two-frequency optical fields to optically trap atoms in dark states, making chip-scale implementations possible. Even with the variety of available designs, most atomic magnetometers are confronted with an intrinsic tradeoff between dynamic range, bandwidth, and sensitivity. SERF magnetometers, while highly sensitive, are limited to ultra-low-field settings. RF-based systems, while broadband, suffer from electromagnetic interference and usually fall short due to modulation bandwidths. These issues drive the pursuit of alternative, *all-optical* designs that can integrate broadband operation, high sensitivity, and large dynamic range without using RF excitation fields.

One such promising technique is **spin noise spectroscopy (SNS)** [66, 73], an optical, non-

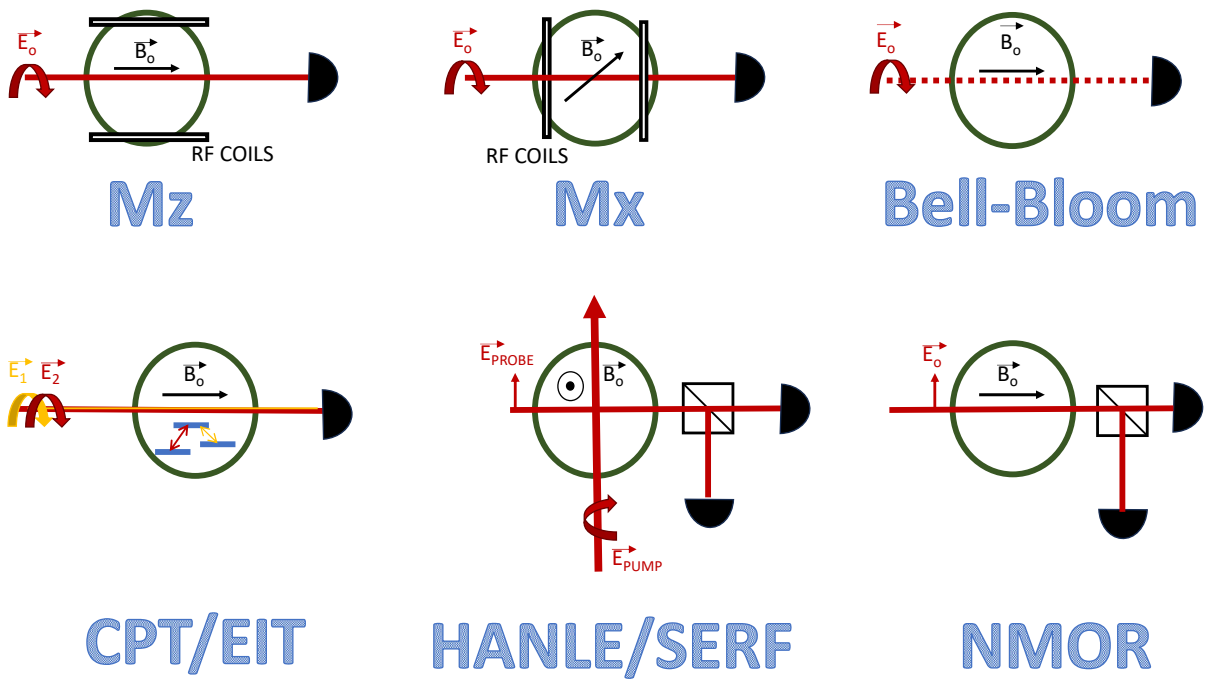


Figure 3.1: Comparison of different atomic magnetometers by operational principles, geometry, and detection methods. The figure shows distinctions between spin-exchange relaxation-free (SERF), RF magnetometers, Bell–Bloom, Mx-type, CPT-based, and NV-center-based sensors. Each platform has unique trade-offs among sensitivity, dynamic range, bandwidth, and applicability.

invasive method that interrogates the stochastic fluctuations of atomic spins at thermal equilibrium. SNS has been successfully used with a broad variety of systems, from alkali vapors [70, 72, 99–101] to multi-electron atoms [102–104], semiconductors [71], and quantum dots [105, 106]. The spin noise spectrum gives direct information on spin relaxation, coherence, and interactions with the environment. But traditional SNS signals are inherently weak, especially in dilute atomic vapors, making the method less optimal for high-precision metrology.

In order to overcome this limitation, the SNS method can be extended by a coherent two-photon Raman drive, giving rise to the newly proposed **Raman-driven spin noise spectroscopy (RDSNS)** [74]. In this setup, two Raman beams induce population oscillations between adjacent

Zeeman sublevels and thereby enhance the intrinsic spin noise and magnetic field sensitivity. The output signal, measurable through a weak far-detuned probe with a polarimetric scheme, allows for precision magnetometry along with the passive, non-perturbative nature of SNS.

In this chapter, we experimentally implement an *all-optical broadband atomic magnetometer* using the RDSNS technique. The RDSNS magnetometer demonstrates a dynamic range of up to 150 G and a sensitivity of less than 30 $pT/\sqrt{\text{Hz}}$ with a paraffin-coated, buffer-gas-filled vapor cell of neutral rubidium atoms. Its all-optical operation offers intrinsic immunity to stray RF interference and the potential for compact, field-deployable quantum sensors.

This chapter is structured as follows: Section 3.2 explains the experimental setup and detection scheme. Section 3.3 addresses the experimental results and performance characterization, and concluding remarks and future prospects in Section 3.4.

3.2 Experimental set up

We used Rubidium atoms in a paraffin-coated glass cell as well as in a buffer gas-filled glass cell to perform all experiments. The probe laser beam was derived from a tunable, narrow-linewidth External Cavity Diode Laser (ECDL) with a center wavelength 780 nm (Toptica Photonics). It was kept far detuned (+1.5 GHz for measurements with paraffin-coated cell and +31.5 GHz for buffer gas filled cell from $F = 3$ to $F' = 4$ transition line of ^{85}Rb) ensuring the non-invasiveness of our measurements. We used a calibrated wavelength meter (WSU 2) from High Finesse GmbH to monitor the frequency detuning of all beams in our set-up. The probe was linearly polarized using a linear polarizer (LPVIS, Thorlabs) with an extinction ratio of 1 part in 10^9 and is focused at the center of the ^{85}Rb-enriched vapor cell with a focal waist of 45μ m.

For measurements at low magnetic fields (less than 2.5 mT), we used a paraffin-coated cylindrical cell with a length 75 mm and a diameter 19 mm. The paraffin coating on the cell plays a crucial role in preserving the spin polarisation from wall collisions, which makes it possible to extract spin noise signals even at room temperature (20^oC) where the density of ^{85}Rb atoms is relatively low ($\approx 10^9$ atoms/cc). The SNS signal strength is proportional to the density of atoms. As will be explained later, the SNS signal strength further decreases at higher fields; therefore, we used a heated buffer-gas-filled cell with a length 75 mm and a diameter 19 mm (Neon buffer gas at 200

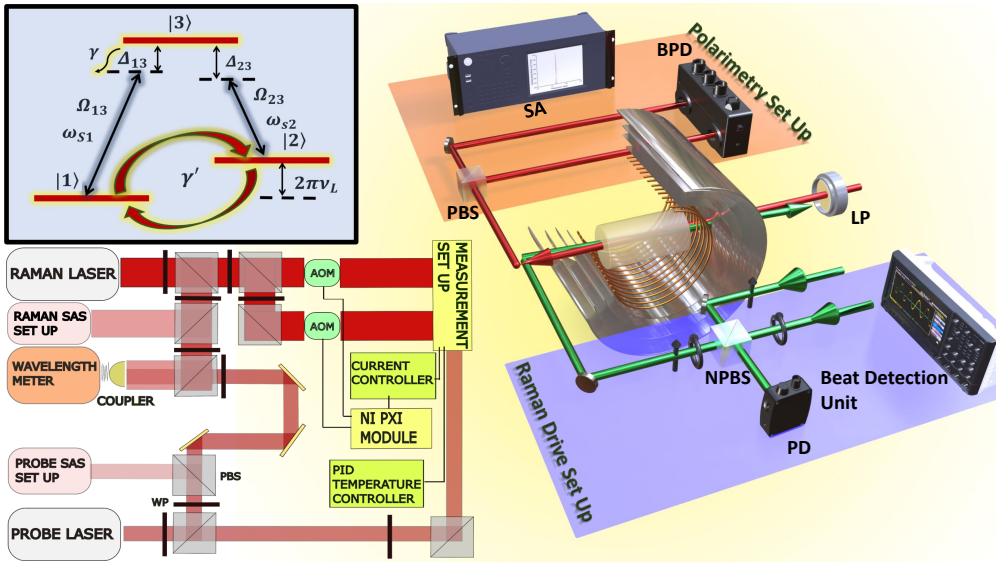


Figure 3.2: **Top Left:** Illustration of the 3-level system, $|i\rangle$ $(i = 1, 2, 3)$, with two Raman beams with frequencies ω_{s1} and ω_{s2} connecting $|1\rangle$ to $|3\rangle$ and $|2\rangle$ to $|3\rangle$, with Rabi angular frequencies Ω_{13} and Ω_{23}. Detunings Δ_{13} and Δ_{23}, and linewidths (ground sates) γ and (excited state) γ' are indicated. **Bottom Left:** Schematic of the experimental setup. The Raman laser light is divided into two parts: one for the wavelength meter and Saturation Absorption Spectroscopy (SAS) setup, and the other split into two Raman beams whose frequencies and intensities are controlled by NI PXI module through Acousto Optic Modulators (AOMs). Waveplates (WPs) polarise the beams (one circular and the other linear) before entering the measurement setup. The probe laser is also divided into two parts. One part goes into the SAS set up and wavelength meter while the other part enters the measurement set up. Cell temperature and magnetic coil currents are regulated by a PID temperature controller and a stable current controller via PXI module. **Right:** Measurement setup. A linearly polarised (made using a Linear polariser (LP)) probe beam is focused at the cell's center. Raman beams are merged with a non-polarising beam splitter (NPBS). One NPBS output goes to the cell, the other to a photo-detector (PD) to record the beat signal. Polarimetric detection includes a polarising beam splitter (PBS) and a Balanced Photo-Detector (BPD), with the difference signal fed into a Spectrum Analyser (SA) for the power spectrum.

Torr) to perform measurements at high magnetic fields. The buffer gas ensures that the atoms stay longer in the probe region, thereby eliminating the transit-time broadening effects. Polymide film flexible heaters [OMEGA KHLVA-105/10-P] and a PID temperature controller [OMRON E5CWL] were employed to uniformly heat the cell to increase the density of ^{85}Rb inside the cell. The cell was thermally isolated from the rest of the set up using ceramic wool blankets. The versatility of our setup indicates that such a magnetometer will work for any kind of cells and atoms.

A uniform magnetic field was created using a solenoid oriented perpendicular to the probe propagation direction. The solenoid was designed to provide a stable and homogeneous magnetic

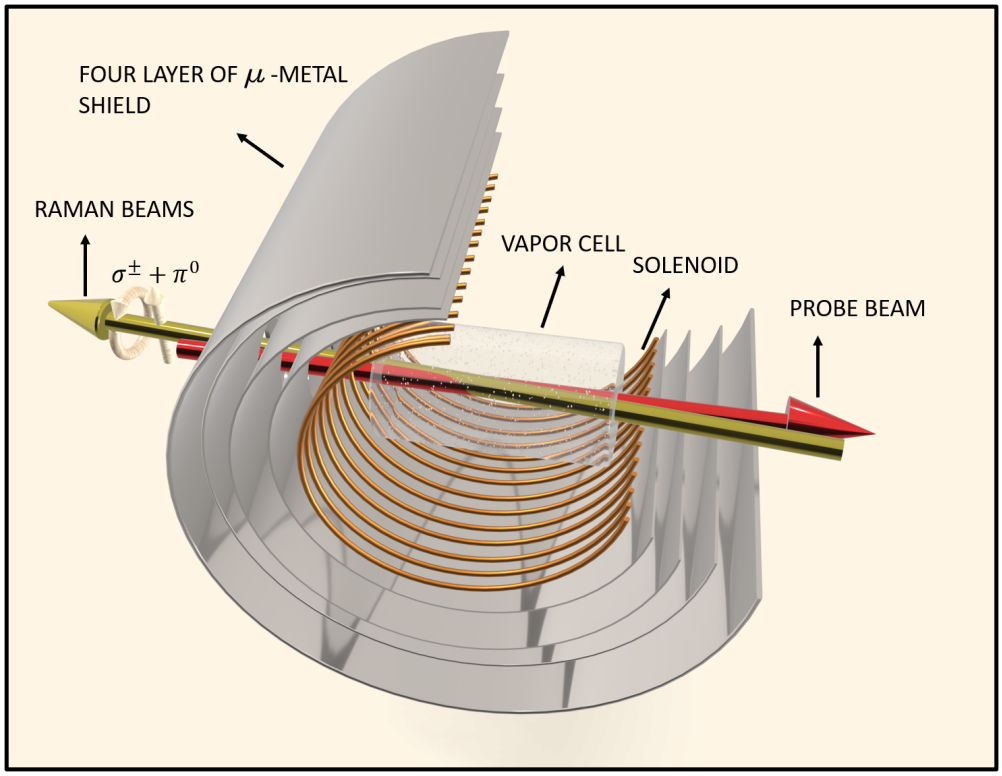


Figure 3.3: Illustrates the vapor cell set up. The probe beam (red) and the Raman Beams (yellow) passes through a paraffin coated cell (for low field mesurements) or buffer-gas-filled cell (for high field measurements), kept inside a solenoid which is enclosed in a four layer μ-metal casing.

field across the vapour cell. The current in the coil was controlled using a very stable current controller (LD3000, Thorlabs) with a stability of $< 1\mu$ A. The maximum spatial variation of the field was measured to be 2 parts in 10^5 over the detection region of 4.5 mm. The temporal variation of the generated field was limited to $< \ pm0.1$ nT over 1 1-second measurement time. To shield the set-up from external stray magnetic fields, the cell and the solenoid were enclosed in a four-layer μ-metal casing as shown in Fig. 3.2, which shields the field by a factor of 10^4 times.

The probe beam passed through a polarimetric detection setup, after passing through the atomic medium. This set-up comprises a polarising beam splitter (PBS122) and a low-noise balanced photodetector with a bandwidth of 80MHz [New Focus 0901]. A balanced detection scheme was chosen to eliminate common-mode noise and to significantly improve the signal-to-noise ratio of our measurements. The detector was further connected to a spectrum analyser [N1996A Agilent Technologies] as well as a home-built spectrum recording unit [107], which captures the power spectrum of the signal. This part of the experimental set-up is similar to the set-up used to perform

the spin noise measurement reported in [108].

To enhance the intrinsic spin noise signal strength, we follow the scheme of Raman-driven spin noise spectroscopy (RDSNS). We used two additional laser beams derived from another ECDL and passed them through two separate acousto-optic modulators (AOMs) in a double-pass configuration for precise frequency and intensity control. The two beams were made σ^+ and π^0 polarised with a polarisation purity of $\geq$ 99% achieved by using a combination of zero-order waveplates. The Raman beams were merged using a non-polarising beam splitter (NPBS). The merged Raman Beams were made to counter-propagate with respect to the probe beam inside the vapour cell. This ensured that no light from the Raman beams was incident on the detector. We took great care, by placing a series of irises, that even a small part of these Raman beams spuriously scattered from the various optical elements did not enter the balanced detector.

As will be discussed later, depending on the frequency difference (δ_{12}) between the two Raman beams and the Larmour frequency, we obtained a distinct marrow (width $\leq$ 1 kHz) Lorentzian peak at a frequency of δ_{12}. It is also important to note that the strongest signal appears exactly at the Larmor frequency, which is proportional to the magnetic field to be sensed. This is the key to our ultra-sensitive magnetic field sensing. The light from one port of the NPBS enters the vapour cell setup, while the light exiting the perpendicular port is used for the Beat Detection Unit (BDU), which shows the interference between the two Raman Beams with a frequency equal to δ_{12}. By simultaneously monitoring the voltage in the AOMs and the beat detection, we ensured that the δ_{12} does not drift more than a few 100 Hz during measurements, providing a consistent reference for our Raman-driven signal.

Overall, the precision and adaptability of our setup allow precise magnetic field measurements over a broad range, utilising spin noise spectroscopy. The optimal conditions for our measurements were determined by combining robust thermal and magnetic shielding, ultra-stable current controllers, PID temperature controllers and modern laser systems. The robustness of the RDSNS technique itself ensures that slight mechanical and electrical noise, as well as minor drifts of laser frequency, do not significantly affect the sensitivity of our device, as will be clear from our statistically significant data presented later.

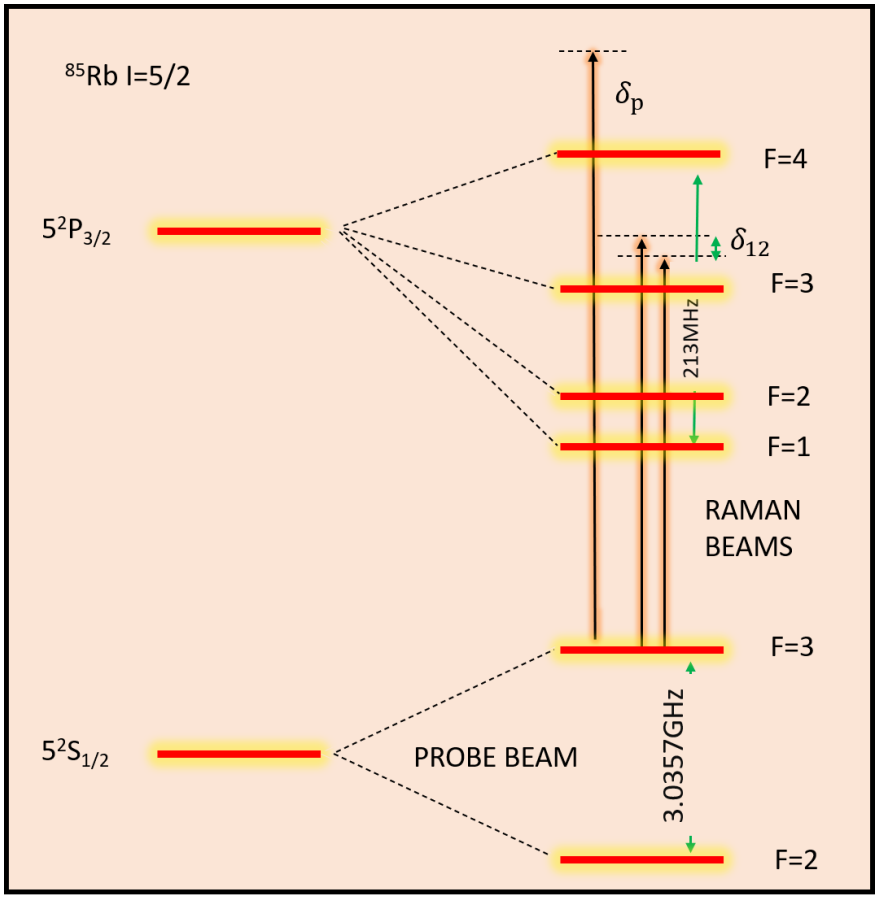


Figure 3.4: Energy level diagram illustrating the probe and Raman beam configuration used in the experiment. The probe beam is detuned by +1.5 GHz from the $F = 3 \rightarrow F' = 4$ transition of ^{85}Rb for the paraffin-coated cell, and by +31.5 GHz for the buffer-gas cell. The Raman beams are near-resonant with the same optical transition (one-photon detuning), while their frequency difference is tuned in the MHz range to match the Zeeman splitting (Larmor frequency), thereby driving coherent Raman transitions between ground-state Zeeman sublevels within the $F = 3$ manifold.

3.2.1 Magnetometry Based on Raman-driven spin noise spectroscopy (RDSNS)

Among the many atomic magnetometer designs, Spin Exchange Relaxation Free (SERF) magnetometers have been well studied for their very narrow resonance linewidths, thus very sensitive to low-intensity magnetic fields [109]. The measurement does not need cryogenic cooling like in superconducting quantum interference devices (SQUIDs) and can easily be miniaturized [110]. But the operating regime of SERF magnetometers is constrained to very low magnetic fields (a few nT) and so are prone to external stray fields with a requirement for magnetic shielding for proper operation.

The broader class of atomic magnetometers is the Optically Pumped Magnetometers (OPMs), which are applied extensively for field sensing across many regimes. In contrast to traditional OPMs, the **Raman-driven spin noise spectroscopy (RDSNS)** magnetometer presented here works across a very wide range of magnetic fields with similar sensitivity and large bandwidth, without any need for cryogenic cooling or RF fields from the outside.

Traditional RF atomic magnetometers utilize an applied RF magnetic field to induce spin precession, allowing for sensitive measurements of magnetic resonances. They are susceptible to interference by ambient RF radiation, such as that from surrounding communication sources. Substituting the RF drive with an *all-optical* Raman excitation renders the RDSNS method free of any requirement for an external RF field. The modulation for excitation of resonance is generated optically alone, and thus it renders immunity from electromagnetic interference as well as dramatically enhancing the device bandwidth. Furthermore, the all-optical setup has simplified the experimental arrangement and facilitates better operational stability. Spin noise spectroscopy (SNS) itself has proved to be a sensitive magnetometer for magnetic field detection [70–72, 99–101].

But the inherent SNS information is usually weak because spontaneous spin fluctuations have small amplitudes, and therefore the precision measurements give low signal-to-noise ratios (SNR). We were able to greatly enhance the spin noise signal by introducing a coherent Raman drive. The power spectral density (PSD) of the RDSNS signal was found to grow by about six orders of magnitude (10^6 times) over the intrinsic SNS signal, which translates to an increase in amplitude

by about a factor of 10^3.

In case the atomic system is excited with a pair of Raman beams, there occurs a narrow resonance peak at the two-photon detuning δ_{12}. Since δ_{12} is swept over the Larmor frequency ν_L, the peak height increases to a maximum at $\delta_{12} = \nu_L$ and decreases symmetrically for larger δ_{12}. This characteristic behavior is a consequence of the Raman resonance condition, wherein the difference in frequencies between the two Raman beams equals the Zeeman splitting between successive ground-state sublevels. At the low-field regime, where the Zeeman splitting is linearly dependent on the applied magnetic field, the magnetic field may be calibrated via

$$\hbar(\omega_{s2} - \omega_{s1}) = g_F \Delta m_F \mu_B B, \tag{3.1}$$

where g_F is the Landé g-factor of ^{85}Rb, μ_B is the Bohr magneton, and Δm_F is the difference in magnetic quantum number between the coupled Zeeman sublevels.

At stronger magnetic fields, the linear Zeeman approximation fails, and the transition frequency vs. magnetic field relation is nonlinear. Here, the magnetic sublevel energies should be characterized by the **Breit–Rabi formula**, which takes into account the coupling of the electronic and nuclear magnetic moments:

$$E_{F,m_F} = -\frac{h\Delta_{hf}}{2(2I+1)} + g_I \mu_B B m_F \pm \frac{h\Delta_{hf}}{2}\sqrt{1 + \frac{4m_F}{2I+1}x + x^2}, \tag{3.2}$$

where

$$x = \frac{(g_J - g_I)\mu_B B}{h\Delta_{hf}}, \tag{3.3}$$

Δ_{hf} is the zero-field hyperfine splitting between $F = 2$ and $F = 3$ ground states, g_J and g_I are the electronic and nuclear g-factors, respectively, and the $\pm$ sign applies to $F = I \pm \frac{1}{2}$ for the $^2S_{1/2}$ ground state of ^{85}Rb.

With the RDSNS scheme, we found fine correspondence between experimentally determined resonance locations and the theoretical Breit–Rabi prediction, which can be seen in Figures 3.8 and 3.10. The envelope of RDSNS signal amplitudes was fitted with Eq. 2.67 to determine the peak locations accurately. As the accuracy of finding these peaks directly determines the accuracy of magnetic field measurement, the technique is highly field sensitive and resolved, making RDSNS

a potential broadband atomic magnetometer.

At extremely high magnetic fields, the envelope of resonance no longer contains a single peak but rather splits into six peaks. This splitting occurs due to the growing effect of the nuclear magnetic moment as the magnetic field increases, making higher-order corrections in the Breit–Rabi energy expression relevant. The multiple resonances offer more information on the hyperfine and nuclear interactions and hold promise for precision spectroscopy at high fields.

The results shown in this section prove that RDSNS can be used as a precision magnetometric method over a broad range of magnetic fields. Its all-optical configuration, large dynamical range, and RF interference immunity make it a good choice for next-generation broadband atomic magnetometers. A thorough description of the experimental observations and related analysis is presented in Section 3.3.

3.3 Results and Discussion

Equilibrium spin noise spectroscopy (SNS) has emerged as a valuable technique for sensing weak magnetic fields and determining intrinsic spin system properties, including spin relaxation rates, isotope abundance ratios, and the Landé g-factors. The measurements are largely indicative of the system's linear response to weak perturbations. Spin noise research has more recently been mapped to non-equilibrium regimes with external drive fields, like AC magnetic fields, creating coherent spin correlations among Zeeman sublevels [111]. These experiments show that periodic driving of the system in and out of equilibrium can provide insights into correlations and dynamical quantities not available in thermal equilibrium. In this chapter, we examine the behaviour of an atomic spin ensemble under a coherent Raman drive, implemented with a pair of phase-coherent Raman laser beams. This setup effectively drives the system into a non-equilibrium steady state, thus changing the inherent spin noise properties. The next sections show the outcomes of our experiments conducted over a broad range of magnetic fields, both in the linear Zeeman regime (low magnetic fields) and the nonlinear Zeeman regime (high magnetic fields). We address these outcomes in the framework of magnetic field sensing with the Raman-driven spin noise spectroscopy (RDSNS) method.

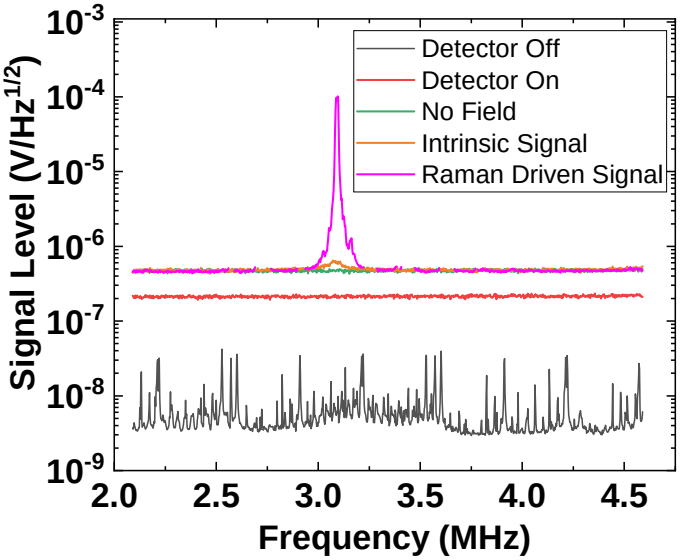


Figure 3.5: Illustrates the various signal levels. The black line corresponds to the noise when the detector is off. When the detector is turned on, the signal corresponds to the detector's response when no light falls on it, which is represented by the red line. When the probe beam falls on the detector, the signal corresponds to the green line. The orange light represents the intrinsic spin noise signal when the magnetic field is turned on, and we get an intrinsic spin noise peak at the Larmor frequency. In the presence of the Raman beams, the signal spectral amplitude is amplified and is depicted in the pink line. The measurements were taken in a buffer-gas-filled (Neon at 200 Torr) vapour cell maintained at a temperature of $95^{o}C$, which corresponds to a density of 4×10^{12} atoms/cc. The applied magnetic field was approximately 6.9 G.

3.3.1 Characterisation and Noise Budget

Prior to reporting the magnetometric measurements, an estimation of the different noise contributions that set a limit to the measurement sensitivity is necessary. Figure 3.5 describes the signal level hierarchy at different experimental conditions.

When the detector was turned off, the signal recorded (black trace) indicated the baseline electronic noise of the system. When the detector was turned on in the dark, the red curve recorded the intrinsic dark noise of the photodiode. When the probe beam was added, the green trace showed the shot-noise background, which is the quantum noise limit of the system. In the presence of an external magnetic field, the intrinsic spin noise signal (orange) emerged as a Lorentzian-shaped peak centered at the Larmor frequency. Lastly, when both the Raman and probe beams were applied, the RDSNS signal (pink) showed a considerable increase in amplitude without any significant rise in the overall noise floor. This measurement illustrates how the Raman driving

mechanism selectively enhances the spin noise spectral amplitude without modifying the detector noise properties. The signals in Figure 3.5 refer to the frequency region from 2.0 MHz to 4.5 MHz, although measurements were pushed as high as 100 MHz to confirm the bandwidth limit of the detector, which showed a 3 dB cutoff at roughly 80 MHz.

3.3.2 Signal Dependence on Atomic Density

The atomic density dependence of intrinsic and Raman-induced spin noise signals was studied systematically by scanning the vapour cell temperature. The background, intrinsic, and Raman-induced signals measured at temperatures between 70°C and 100°C are shown in Figure 3.6.

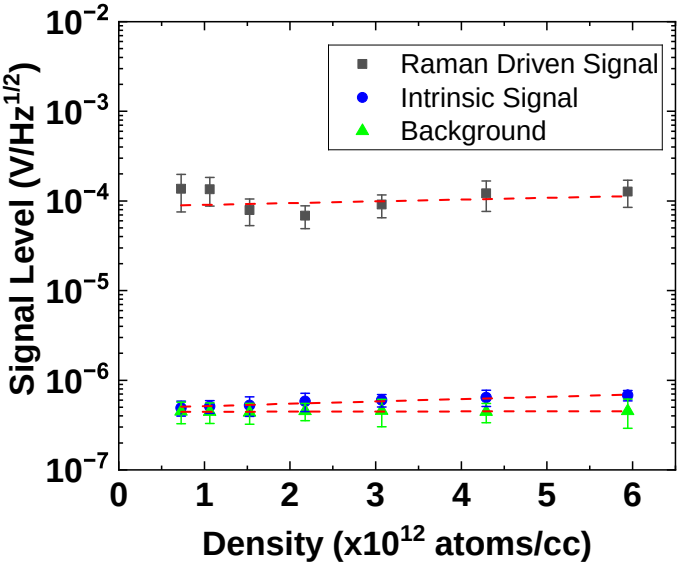


Figure 3.6: Signal level variation with atomic density. Experiments were conducted in a Neon (200 Torr) buffer-gas-filled ^{85}Rb vapour cell. The temperature between 70°C and 100°C was varied while keeping the magnetic field constant at about 0.3 mT. Blue, red, and black dots correspond to background, intrinsic SNS, and Raman-driven (RDSNS) signals, respectively.

The probe beam was 0.8 mW in power and was detuned by +31.5 GHz from the $F = 3 \rightarrow F' = 4$ transition of the ^{85}Rb D_2 line.

The Raman beams were detuned near the same transition at an effective Rabi frequency $\Omega/\gamma \approx 10^{-3}$. The probe detuning δ_p was discovered to be of importance in controlling both the linewidth and the amplitude of the spin noise signals. With increasing detuning, the linewidth of the intrinsic SNS peak decreased because optical perturbation of the ground-state Zeeman populations was diminished, which in turn increased the transverse spin relaxation time T_2. In

order to maximize the signal-to-noise ratio (SNR), probe detuning was selected so that the linewidth was not too broad, but the signal was strong enough. This is especially useful for magnetic field calibration, where spectral accuracy is a function of the sharpness of the resonance peak.

The atomic number density was regulated by changing the cell temperature from 70°C to 100°C in 5°C increments with a PID temperature controller. The data in Figure 3.6 indicates that the intrinsic SNS peak amplitude rises with density, as predicted by Eq. 2.4, which assumes a proportionality to atomic number density.

For low-temperature operation, paraffin-coated cells are beneficial since they reduce spin relaxation caused by wall collisions, maintaining coherence for longer times. But the coating degrades above 60°C, which restricts the vapor density that can be achieved.

Thus, high-density, high-field measurements are best done in buffer-gas-filled cells. The Neon buffer gas (200 Torr) enhances the interaction time of atoms with the probe beam by inhibiting diffusion losses, minimizes transit-time broadening, and reduces spin decoherence, though at the expense of minimal pressure broadening. Each plotted data point is an average over 100 spectra, with multiple runs taken to estimate statistical errors.

3.3.3 Signal Dependence on Magnetic Field

The influence of magnetic field strength on intrinsic and Raman-driven signals was examined by sweeping the external field from 0.1 mT to 1 mT at constant cell temperature 95°C. The results are depicted in Figure 3.7.

At low magnetic fields, the intrinsic SNS signal amplitude and linewidth were almost unchanged. With increasing magnetic field, the intrinsic peak widened and then reduced in amplitude, eventually splitting into several smaller peaks. The RDSNS signal, on the other hand, always showed a far larger amplitude throughout the entire field range, with an average of about three orders of magnitude larger compared to the intrinsic SNS.

One of the important conclusions drawn from Figures 3.6 and 3.7 is that the relative amplification factor of the Raman drive-induced spin noise signal is also almost constant over varying densities and magnetic fields. Such a behaviour indicates that the Raman process increases the sensitivity of the system without the introduction of field-dependent distortions. The RDSNS scheme can thus be viewed as being equivalent to a broadband optical amplifier that preferentially

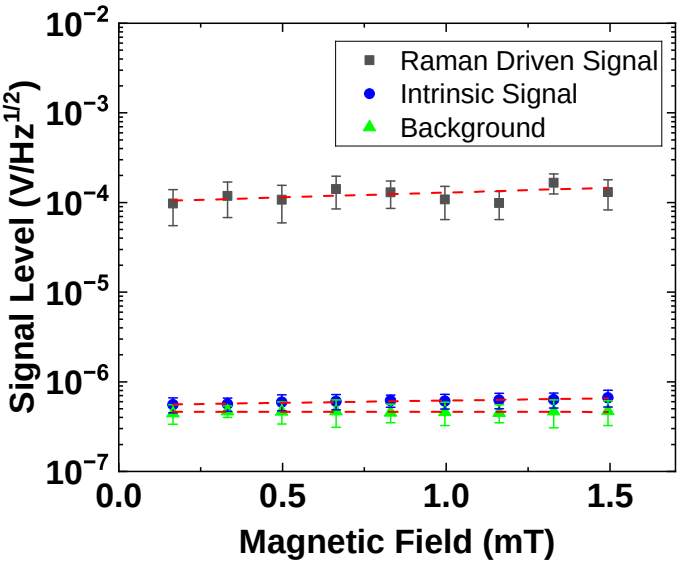


Figure 3.7: Dependence of intrinsic and Raman-driven spin noise signals on magnetic field strength. The vapour cell was kept at 95°C. Blue, red, and black dots indicate the background, intrinsic SNS, and Raman-driven (RDSNS) signals, respectively.

amplifies the spin noise signal while ensuring linearity and stability of the noise floor.

The robustness of the amplification factor over a large dynamic range sets the RDSNS magnetometer as a stable ground for accurate field measurements. The very high signal-to-noise ratio obtained here enables precise measurement of magnetic fields from the positions of the spectral peaks with sub-femtotesla sensitivity. Additional calibration and high-field behaviour are treated in Section 3.2.1.

3.3.4 Performance of the Magnetometer at Low Magnetic Fields

In order to assess the performance of the RDSNS-based magnetometer in the low-field region, we conducted magnetic field calibration measurements in a ^{85}Rb natural abundance paraffin-coated vapour cell. Figure 3.8 shows the measured Raman-driven spin noise (RDSNS) spectra for magnetic fields varying from 0.3 mT to 2.5 mT.

The measurements were conducted at room temperature (20°C), which corresponds to an atomic vapour density of about 8×10^9 atoms/cm^3. The paraffin coating guarantees spin-preserving wall collisions, enabling long spin coherence times and small intrinsic spin noise linewidths even at such low atomic densities. In order to operate in the small-field regime, the probe beam was

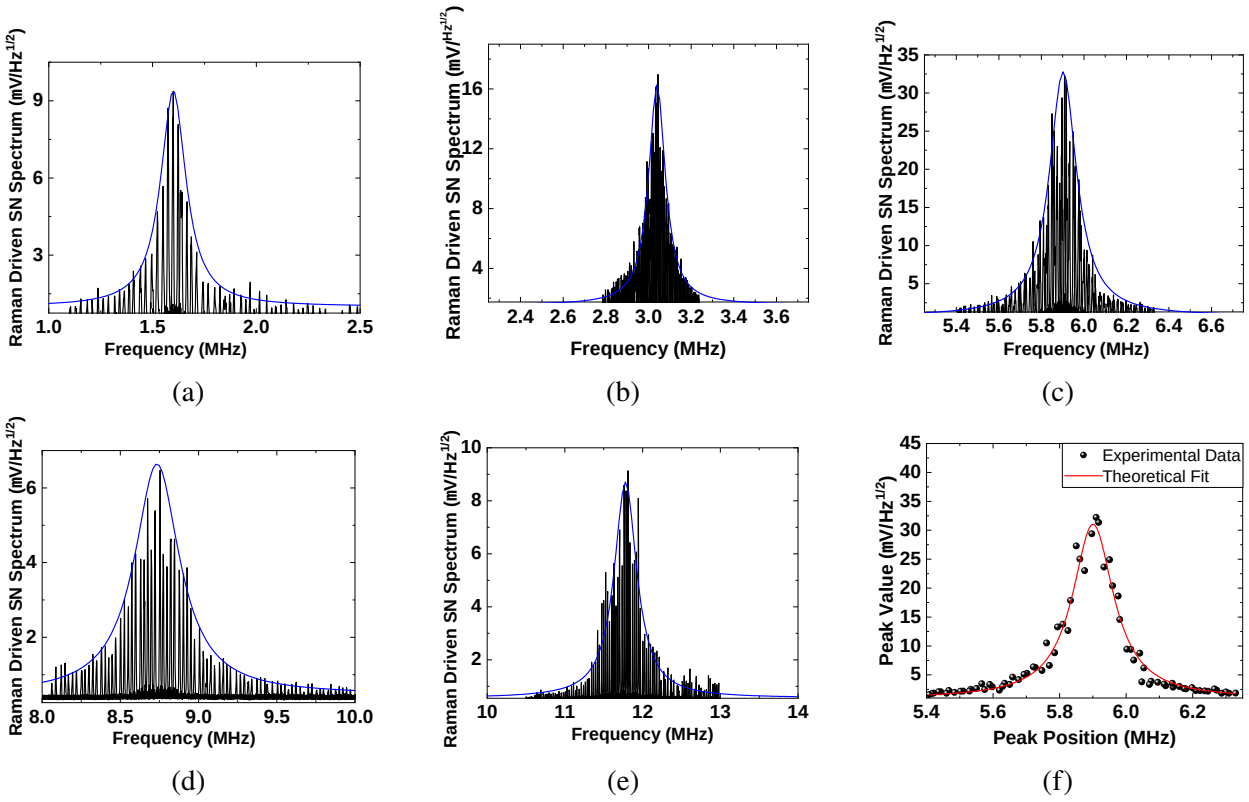
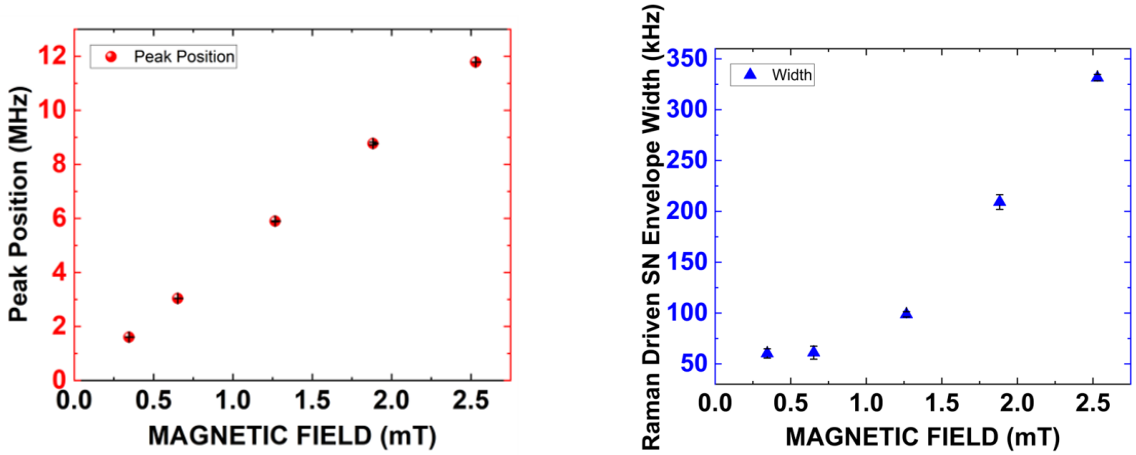


Figure 3.8: Illustrates the Raman-driven spin noise spectroscopy signals to calibrate low magnetic fields. The magnetic field was varied from around 0.3 mT to 2.5 mT. The measurements were taken in a paraffin-coated vapour cell at room temperature (20^oC) with a density of $8x10^9$ atoms/cc. (a-e) Corresponds to one of the representative graphs for each magnetic field value. The frequency difference between the two Raman beams (δ_{12}) was varied across the Larmor frequency. Each black peaked signal in every plot corresponds to a particular δ_{12}. We see that the strongest peak appears at the Larmor frequency. Each peak for a particular δ_{12} was recorded by taking 100 spectrum averages and was repeated several times. The blue line is a Lorentzian plot only to act as a line of guide for the envelope. (f) Represents one of the fitting plots for a magnetic field of $\approx$ 1.25 mT. The black dots represent the experimental data points and the red line is the theoretical fit.

+1.5 GHz detuned from the $F = 3 \rightarrow F' = 4$ transition of the ^{85}Rb D_2 line. The probe detuning δ_p is proportional to the inverse of both the SNS signal amplitude and its linewidth (see Eq. 2.4). Thus, δ_p was selected to strike a balance between non-invasiveness, signal-to-noise ratio (SNR), and spectral sharpness. The probe power remained at 0.8 mW during the experiment.

The Raman beams were obtained with orthogonally circular (σ^+) and linear (π) polarisations, having the same beam waists and equal intensity such that $\Omega/\gamma \approx 10^{-3}$. This allows for uniform optical coupling and maximum overlap of the probe and Raman beams in the vapour cell, facilitating



(a) **Fitted peak positions vs magnetic field.** (b) **Linewidth vs magnetic field.**

Figure 3.9: (a) Variation of the fitted peak positions (red dots) of the Raman-driven spin noise (RDSNS) envelope with magnetic field showing a near-linear dependence consistent with the theoretical Larmor frequency. (b) Corresponding linewidths (blue dots) extracted from Lorentzian fits. The linewidth increases with magnetic field due to Zeeman broadening and field inhomogeneity. Error bars denote fitting uncertainties.

efficient interaction with the same set of atoms.

For calibration, the magnetic field was kept fixed and the two-photon detuning δ_{12} swept through the Larmor frequency ν_L by sharply varying the frequency difference between the two Raman beams using acousto-optic modulators (AOMs). The frequency offset δ_{12} was calibrated from the beat note created by the interference of the two Raman beams, which was measured on an oscilloscope. For every value of δ_{12}, 100 individual spectra were averaged for enhancing SNR, and the procedure was repeated several times in order to maintain statistical consistency.

Representative RDSNS spectra recorded for different magnetic fields are presented in Figures 3.8 a–e. All the spectra show a narrow resonance peak when the two-photon detuning δ_{12} equals the Larmor frequency ν_L, which corresponds to the Raman resonance condition. The envelope of the resonance amplitudes as a function of δ_{12} gives an immediate estimate of the field-dependent spin precession frequency.

Fig. 3.9a and fig. 3.9b presents the envelopes that were fitted to determine the position and linewidth of the resonance peak from the experimental data. All the envelopes were fitted according to Eq. 2.67 to precisely find the Raman-driven resonance peak position. Fig. 3.9a presents the peak positions (red dots) obtained from the experiment and plot of the respective linewidths (blue

dots) as a function of the magnetic field strength. The resonance frequencies extracted adhere to the linear Zeeman dependence at low fields, as expected, and validate the proportionality of the Larmor frequency with respect to the applied magnetic field. The observed width of the Raman-driven spin noise envelope grows with rising field strength, as it indicates the augmented magnetic inhomogeneity and larger precession frequency distribution among the atoms. This behaviour also gives a direct experimental confirmation of the coupling between the intrinsic SNS and RDSNS signals, as explained in Section 3.2.1.

It is worth mentioning that the linewidth may also be regulated by adjusting the probe detuning δ_p. Larger detuning diminishes optical perturbation and gives a narrower envelope, enhancing the accuracy of the field determination. These results all show that the RDSNS-based magnetometer works well in the low-field linear Zeeman regime, allowing for accurate calibration of the magnetic field with high SNR and sub-femtotesla sensitivity.

3.3.5 Performance of Magnetometer at High Magnetic Fields

In order to explore the performance of the RDSNS-based magnetometer in the nonlinear Zeeman regime, we conducted measurements under high magnetic fields with a buffer-gas-filled vapour cell. The cell was filled with ^{85}Rb atoms and the buffer gas Neon at 200 Torr pressure at a temperature of 95°C, yielding a vapor density of about 4×10^{12} atoms/cm^3.

The use of a buffer-gas-filled cell is particularly important in high-field measurements. As the magnetic field strength rises, the spin noise signal becomes wider and weaker as a consequence of larger inhomogeneous broadening and more rapid spin precession. Increased atomic density serves to counter this loss of signal by raising the number of spins involved, which ultimately boosts the overall signal-to-noise ratio (SNR). The buffer gas has two key functions: (i) it traps the atoms in the probe volume for a longer time by inhibiting atomic diffusion, and (ii) it facilitates elastic atom–buffer collisions that maintain the spin polarisation of the ^{85}Rb atoms and ensure spin coherence. Under measurement conditions, the temperature of the cell was actively controlled to within ±0.1°C to maintain uniform density and linewidth. For these experiments, the probe laser was detuned by +31.5 GHz from the $F = 3 \rightarrow F' = 4$ transition of the ^{85}Rb D_2 line. Such large detuning reduces optical pumping and enables non-invasive probing, placing the probe frequency well beyond the pressure-broadened absorption linewidth of approximately 1.9 GHz

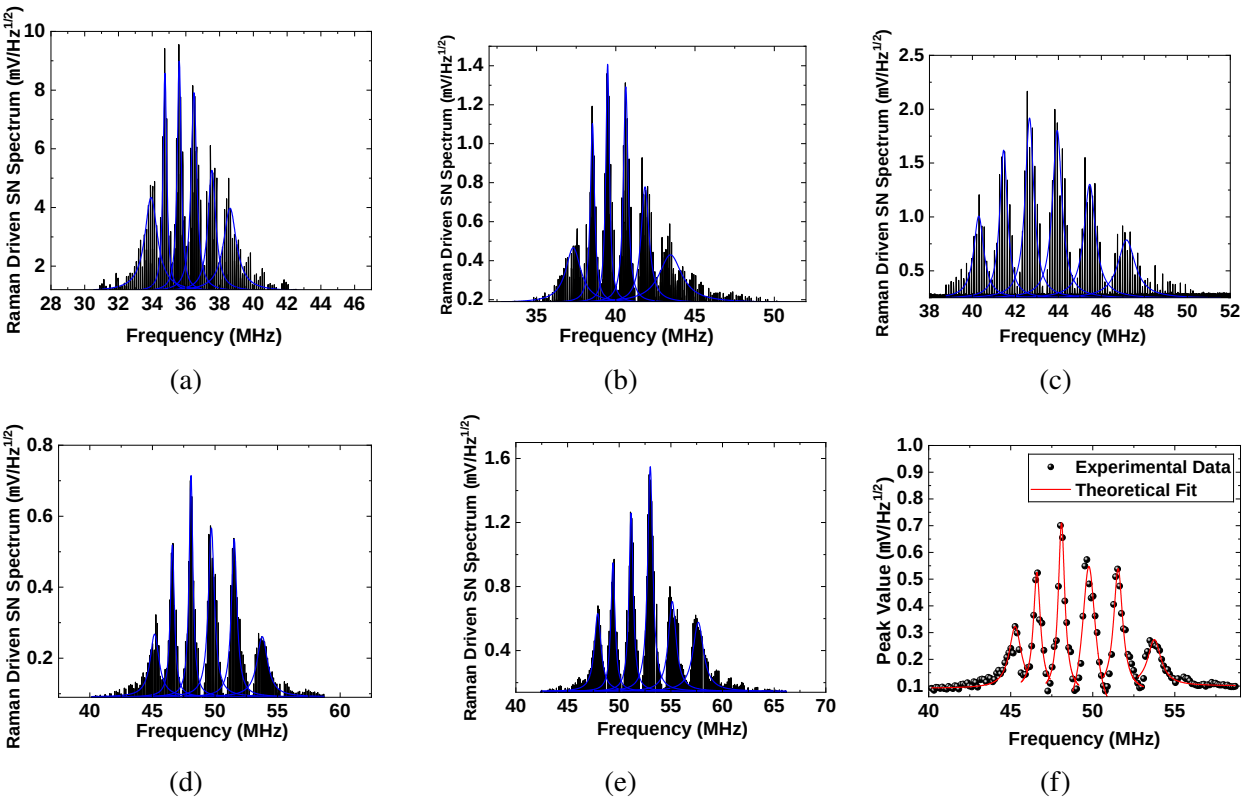


Figure 3.10: Illustrates the magnetic field calibration at high field. The magnetic field was varied from around 7.75 mT to 11.25 mT. All the measurements were taken in a buffer-gas-filled (Neon at 200 Torr) vapour cell maintained at a temperature of $95^{o}C$, which corresponds to a density of $4\text{x}10^{12}$ atoms/cc. (a-e) Shows one of the representative data for each magnetic field value. The frequency difference between the two Raman beams δ_{12} was varied across the Larmor frequency. Each black peaked signal in every plot corresponds to a particular δ_{12}. We observe that the envelope of the Raman-driven spin noise signal has 6 peaks which correspond to the non-linear Zeeman effect, where the contributions from individual fluctuations between adjacent Zeeman levels start to show independently. For $F = 2$, there are 4 peaks and for $F = 3$ there are 6 such peaks. However, 4 peaks corresponding to $(F = 2, m_F = -1 \rightarrow -2)$ overlaps with $(F = 3, m_F = -1 \rightarrow -2)$, $(F = 2, m_F = 0 \rightarrow -1)$ overlaps with $(F = 3, m_F = 0 \rightarrow -1)$, $(F = 2, m_F = 1 \rightarrow 0)$ overlaps with $(F = 3, m_F = 1 \rightarrow 0)$ and $(F = 2, m_F = 2 \rightarrow 1)$ overlaps with $(F = 3, m_F = 2 \rightarrow 1)$. Hence, overall, we see 6 peaks in the power spectrum. (f) Fig. 3.10f represents one of the fitting plots at a magnetic field of $\approx$10.5 mT. The black points correspond to the experimental points, and the red line is the theoretical fit.

(much wider than the 0.5 GHz linewidth typically found in paraffin-coated cells). The Raman beams were adjusted to excite two-photon transitions between neighbouring Zeeman sublevels, and the RDSNS spectra were acquired for magnetic fields between 7.5–11.5 mT.

Figure 3.11 presents the magnetic field calibration results in this high-field regime. As noted earlier in the low-field data (Figure 3.8f), the Raman-driven spin noise spectroscopy (RDSNS)

envelope broadens increasingly with increasing magnetic field, which makes precise peak extraction very difficult at very high fields. However, at higher field strengths, beyond a certain point, the broad resonance envelope begins to split into several distinct peaks. This splitting is the beginning of the **nonlinear Zeeman effect**, in which the separation of adjacent Zeeman sublevels in energy deviates from linear dependence on B because of the growing effect of the nuclear magnetic moment.

In this regime, every pair of neighbouring Zeeman sublevels contributes a single fluctuation component to the spin noise spectrum, resulting in several resonance peaks. For the ^{85}Rb ground hyperfine levels, this leads to several distinct features: four peaks from the $F = 2$ manifold and six from the $F = 3$ manifold. Owing to partial overlap between some transitions—namely, $(F = 2, m_F = -1 \rightarrow -2)$ with $(F = 3, m_F = -1 \rightarrow -2)$, $(F = 2, m_F = 0 \rightarrow -1)$ with $(F = 3, m_F = 0 \rightarrow -1)$, $(F = 2, m_F = 1 \rightarrow 0)$ with $(F = 3, m_F = 1 \rightarrow 0)$, and $(F = 2, m_F = 2 \rightarrow 1)$ with $(F = 3, m_F = 2 \rightarrow 1)$—the resulting spectrum actually has six distinct peaks in total. These are readily apparent in the RDSNS power spectra presented in Figures 3.10a–e.

The presence of these six discrete, well-separated peaks constitutes direct experimental confirmation of the nonlinear Zeeman effect in driven spin noise spectra. In contrast with the broad, single-envelope response observed at smaller fields, the emergence of discrete peaks makes individual Zeeman transitions unambiguously identifiable. This significantly enhances the accuracy of magnetic field determination in the high-field regime, as each distinct peak serves as an individual frequency reference corresponding to a well-defined field value.

The amplitude and position of each peak were characterised by fitting the spectra using Eqs. 3.2 and 2.67, with the peak amplitude and magnetic field as free parameters. One such fitted data set is presented in Fig. 3.10f, illustrating excellent agreement between the experimentally determined resonance positions and the theoretical predictions of the Breit-Rabi model. The fitted results also verify that the nonlinear Zeeman splitting observed in the RDSNS spectra indeed follows the expected quadratic dependence on the magnetic field.

In addition, by manipulating the relative frequencies Δ_{13} and Δ_{23} of the Raman beams, the relative intensities of the six peaks could be controlled, giving a further level of control over the observed spectrum. This can be exploited to maximise SNR or separate out individual transitions, depending on the field range being of interest.

Briefly, RDSNS remains effective in both the nonlinear and linear Zeeman regimes. Under strong magnetic fields, the switch from a single broad resonance to a series of narrow peaks improves spectral resolution and facilitates accurate magnetic field mapping over a wide dynamic range. This makes the RDSNS-based magnetometer a broadband, high-sensitivity, all-optical device for accurate field measurements from sub-millitesla to tens of millitesla.

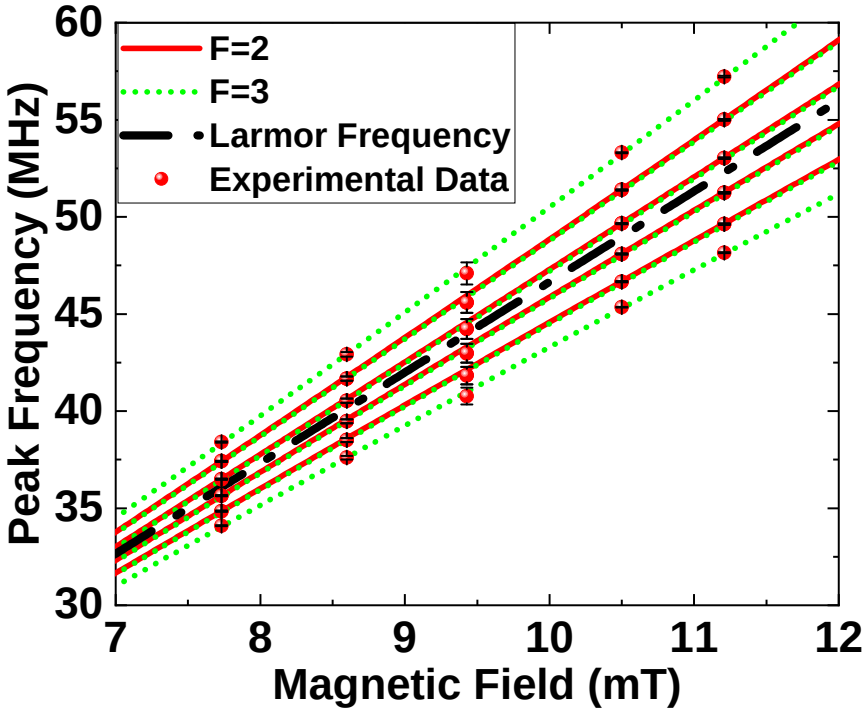


Figure 3.11: Represents the plot of the peak position of all the 6 peaks with the magnetic field. The peak position error represents the fitting error. We see that this matches the theoretical plot.

3.3.6 Data Analysis

The experimental spectra shown above exhibit the increasing splitting of the Raman-induced spin noise envelope with an increasing magnetic field. The splitting occurs because the nonlinear Zeeman effect, which dominates at higher magnetic fields. The calculated energy level splitting of the ^{85}Rb ground hyperfine states versus the magnetic field, obtained from the Breit–Rabi equation (Eq. 3.2), is displayed in Figure 3.12. At weak fields, the Zeeman sublevel splittings are nearly linear, while at strong fields, nonlinear corrections become important, resulting in the emergence of several distinct spectral peaks in the Raman-induced spin noise spectrum.

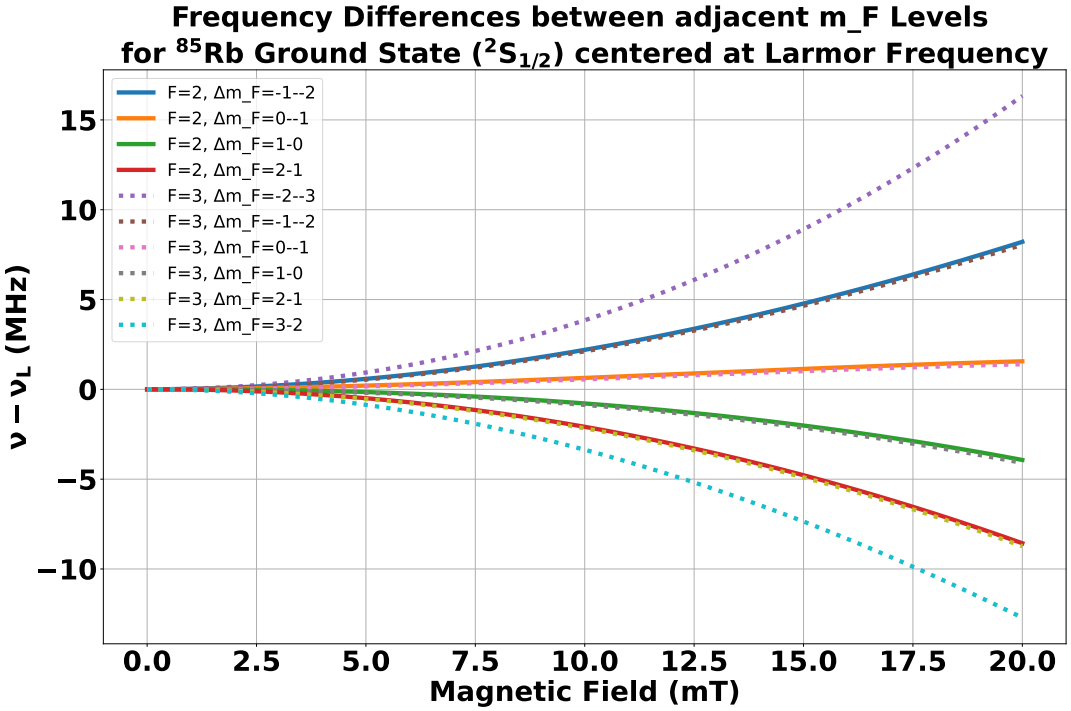


Figure 3.12: Illustrates the energy spacing between adjacent Zeeman levels following the Breit–Rabi formula, Eq. 3.2.

To model the Raman-driven spin noise envelope for different m_F states, we merged the Breit–Rabi equation (Eq. 3.2) with the Raman-driven coherence amplitude $|\rho_{21}|^2$ (Eq. 2.67). During the analysis, the detuning term Δ in Eq. 2.67 was substituted with the frequency difference between adjacent m_F energy levels derived from the Breit–Rabi formula. The resulting spectra are the composite Raman-driven spin noise (RDSNS) envelope to be expected for different magnetic fields.

For ^{85}Rb, the following parameters were employed during the simulation:

- $g_J = 2.00233113$ — electronic Landé g-factor,
- $g_I = -0.000293640$ — nuclear Landé g-factor,
- $\mu_B = 9.274009994 \times 10^{-24}$ J/T — Bohr magneton,
- $\mu_N = 5.050783699 \times 10^{-27}$ J/T — nuclear magneton,
- $\Delta E_{\text{hfs}} = 3.036 \times 10^9 \times 6.62607015 \times 10^{-34}$ J — ground-state hyperfine energy splitting (equivalent to 3.036 GHz).

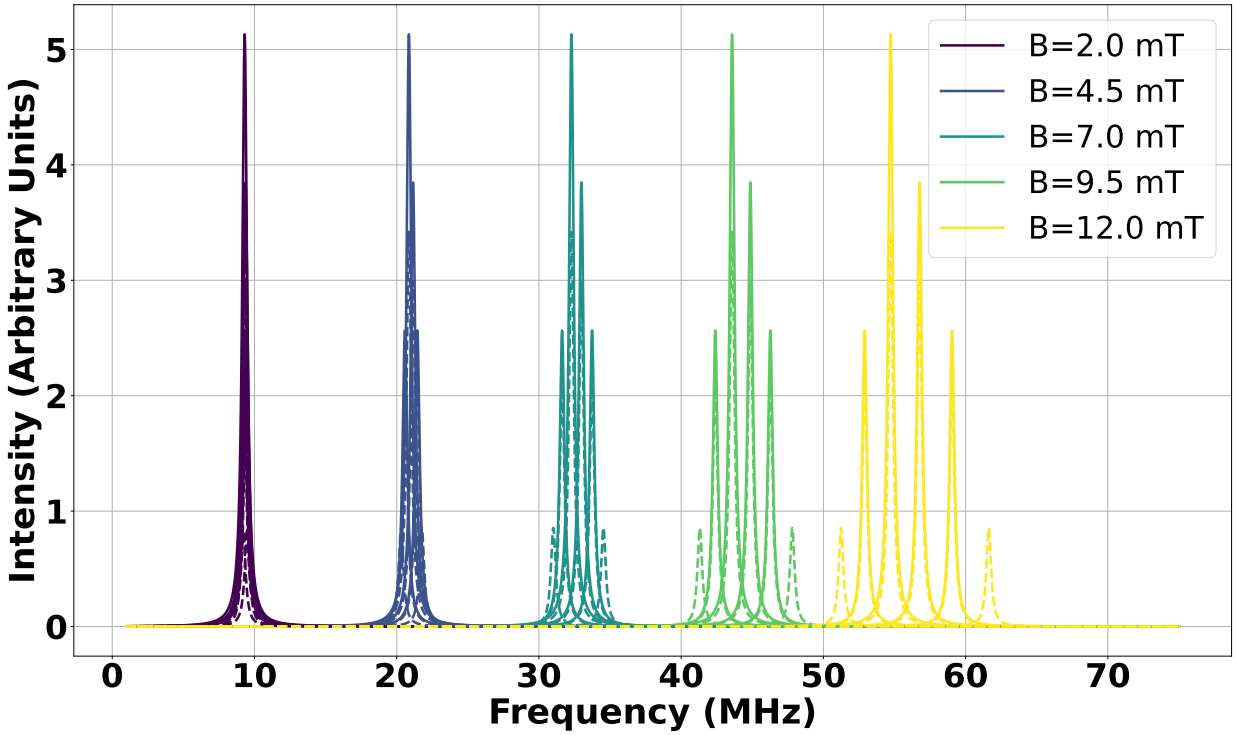


Figure 3.13: Raman-driven spin noise envelope peaks split due to the non-linear Zeeman effect as the magnetic field increases. The solid lines represent the plot for $F = 2$ state and the dotted lines for $F = 3$ state.

Figure 3.13 illustrates the Raman-driven spin noise envelopes simulated as the magnetic field rises from the linear to nonlinear Zeeman regime. The single resonance at low fields progressively develops into a series of multiple peaks, reflecting transitions between adjacent Zeeman sublevels within the $F = 2$ and $F = 3$ ground-state manifolds.

To analyze the data, the measured RDSNS spectra were fitted using the magnetic field, linewidth, and individual peak strengths as free parameters. Relative amplitudes of peaks from the $F = 2$ manifold were assumed to be larger than those from $F = 3$ in the simulation results of Figure 3.13, consistent with the greater equilibrium population in the lower ground-state hyperfine level. Experimentally, these relative amplitudes can be manipulated either by means of optical pumping (which redistributes populations in the hyperfine states) or by adjusting the Raman beam frequencies, which alter the strengths of the couplings and population fluctuations of the Zeeman sublevels. To compare the magnetometric capability of the RDSNS device, we experimentally quantified its magnetic field resolution. The bias magnetic field was created and modulated by a precision current controller (LD3000) controlled by a PXIe system under digital control. For each

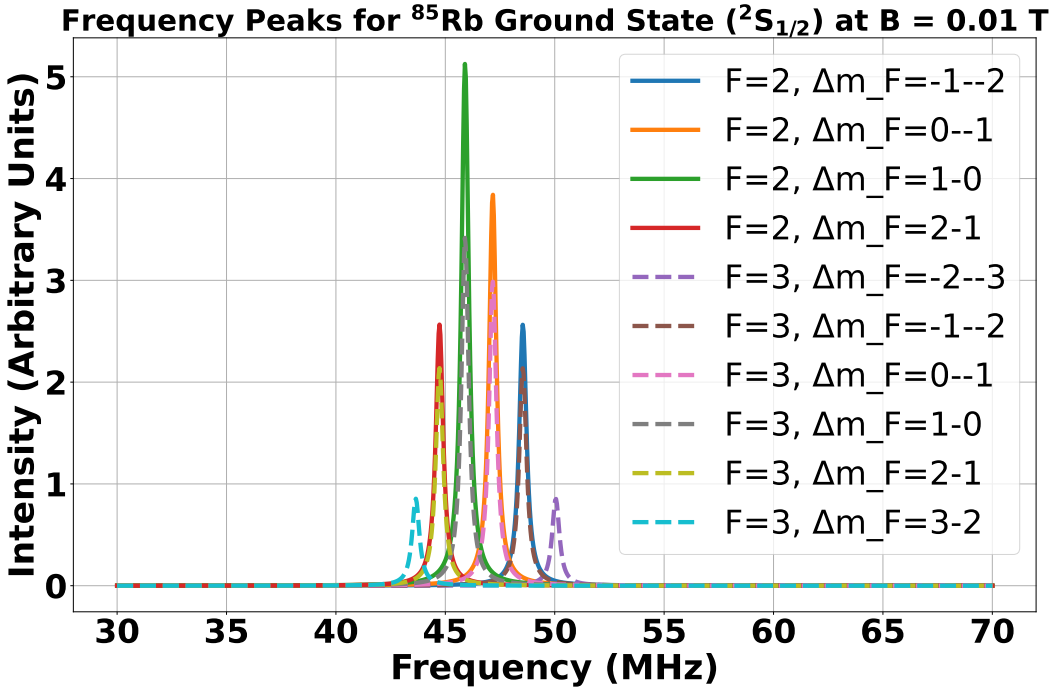


Figure 3.14: Splitting of $|\rho_{21}|^2$ at a magnetic field of 0.01 T. The solid lines represent the plot for the $F = 2$ state and the dotted lines for the $F = 3$ state. The relative peak strengths here are chosen to make $F = 2$ peaks appear higher than $F = 3$ peaks; in practice, these strengths depend on experimental parameters.

value of current, the related Raman-driven spin noise spectrum was averaged over ten iterations to suppress random fluctuations. This process was iterated several times to acquire statistically sound measurements.

The resolution of the field was determined by measuring the variation in signal amplitude with incremental changes in the magnetic field. We determined that a variation of 12 μG in the magnetic field resulted in a noticeable shift in the peak of RDSNS with a signal-to-noise ratio (SNR) of about 44 at a Larmor frequency of 2.795 MHz. Thus, we determined the DC magnetic field resolution of the magnetometer to be about 30 pT. This high-resolution illustration showcases the sensitivity of the RDSNS magnetometer to very small changes in magnetic fields, ranking it among the most sensitive all-optical magnetometric methods.

The sensitivity and broadband character achieved with the RDSNS magnetometer make it exceptionally well suited for use in geomagnetic field research, where sensitive detection of weak field variations is paramount. The geomagnetic field typically varies between 0.025 and 0.065 mT.

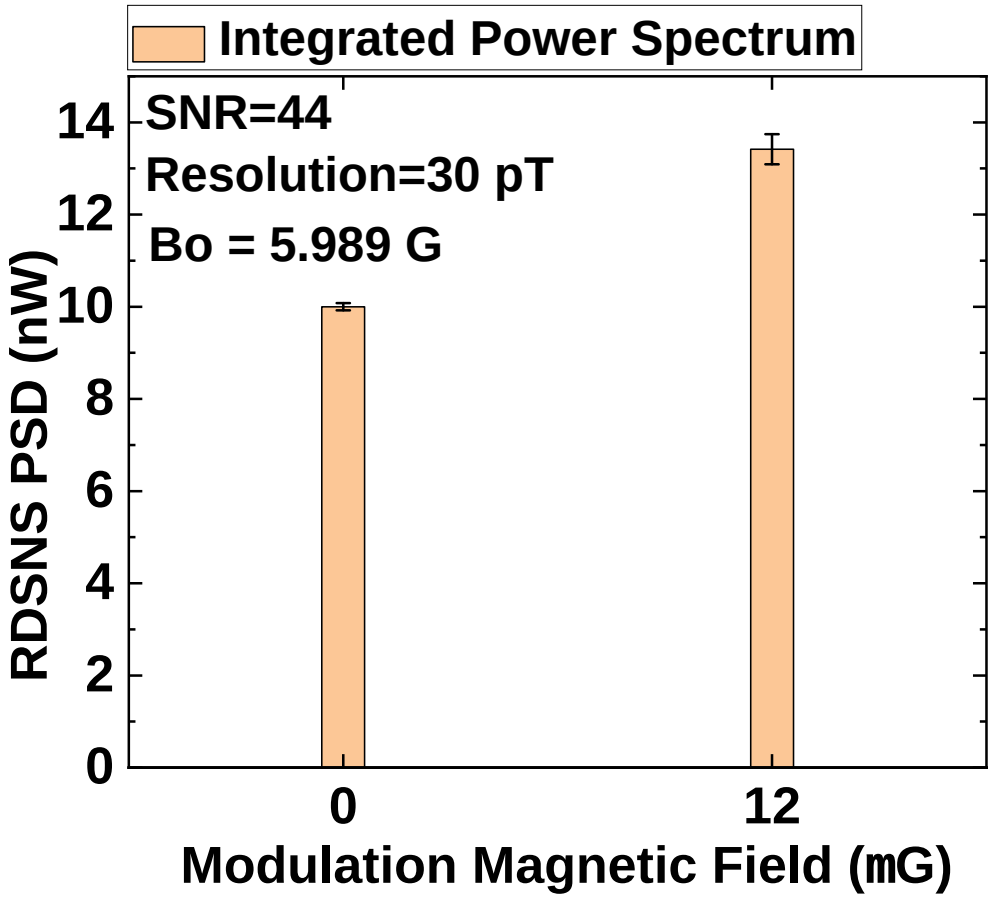


Figure 3.15: Illustrates the DC magnetic field resolution of the device. The measurement was taken in a paraffin-coated cell at room temperature (20^oC). The magnetic field was changed by 12 μG about 5.989 G, and the change in the signal amplitude was recorded. For each data 10 spectrum averages were taken and repeated several times to estimate the errors. We get an SNR of ≈44 at a drive frequency of 2.795 MHz. The resolution was finally extracted to be 30 pT.

The capability to detect changes as small as 30 pT makes it possible to observe fine fluctuations related to geomagnetic storms, seismic precursors, and magnetic anomalies in the environment or archaeology. The all-optical and RF-free design also provides robustness against electromagnetic interference, making this device potentially suitable for application in remote or electromagnetically noisy conditions. Its combination of large dynamic range, high resolution, and field insensitivity makes the RDSNS magnetometer a viable platform for compact, field-deployable quantum magnetic sensing.

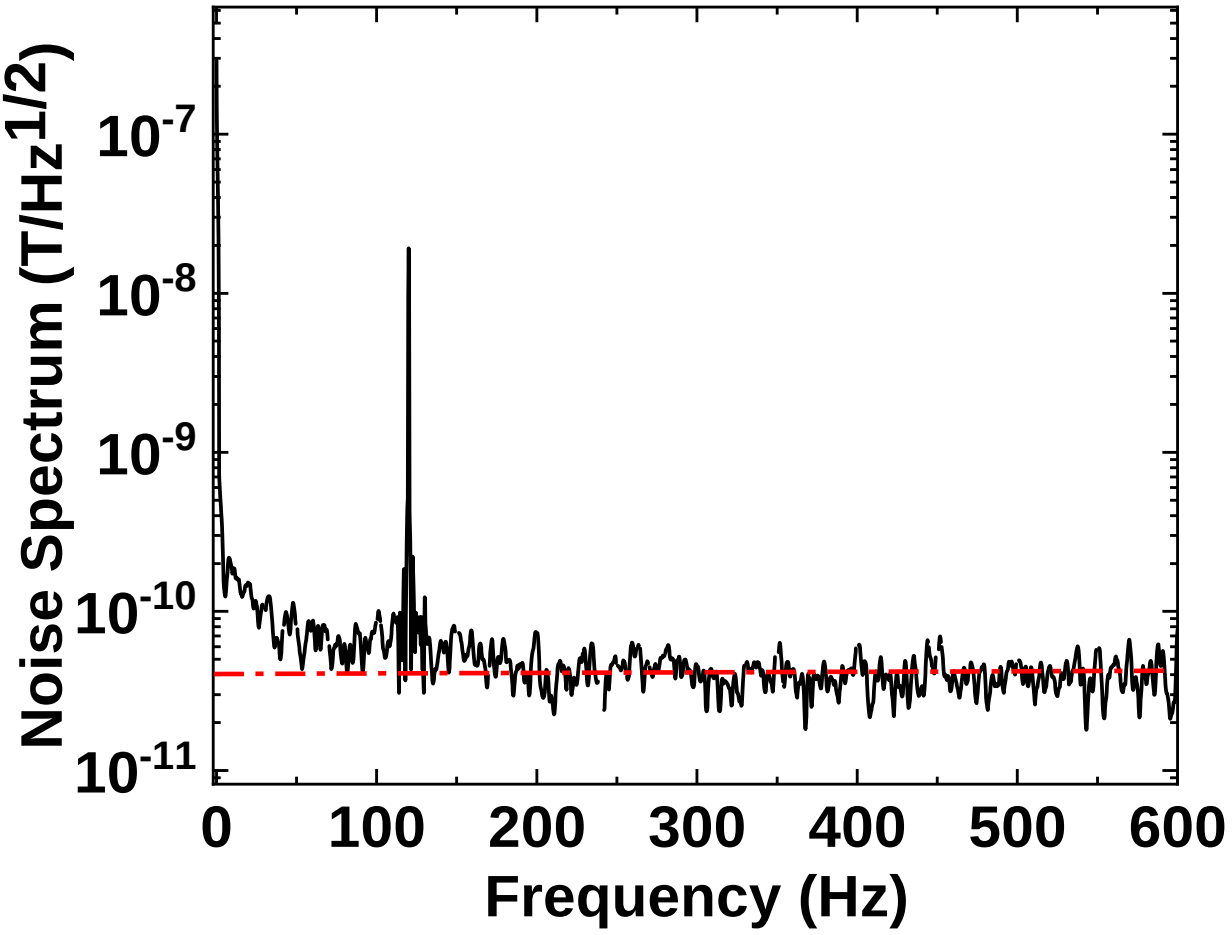


Figure 3.16: Shows one of the noise spectra with a calibration signal at 120 Hz. The SNR was about 10^3 at the modulation depth of 300 nT. The sensitivity was extracted to be 30 $pT/Hz^{1/2}$ at a magnetic field of around 0.6 mT.

3.3.7 AC Magnetometry: Sensitivity and Bandwidth

Along with static field measurements, the capability to measure oscillating magnetic fields over a bandwidth of frequencies is crucial for assessing the **bandwidth** and **sensitivity** of a magnetometer. Sensitivity is the minimum detectable field fluctuation, while bandwidth is the range of frequencies over which the magnetometer responds linearly and efficaciously. Both quantities are very important figures of merit for magnetometric methods comparison [112–116]. In order to test the magnetic noise and dynamic response of the RDSNS magnetometer, a small sinusoidal modulation was introduced into the bias magnetic field, and the output of the magnetometer was measured with varied modulation frequencies.

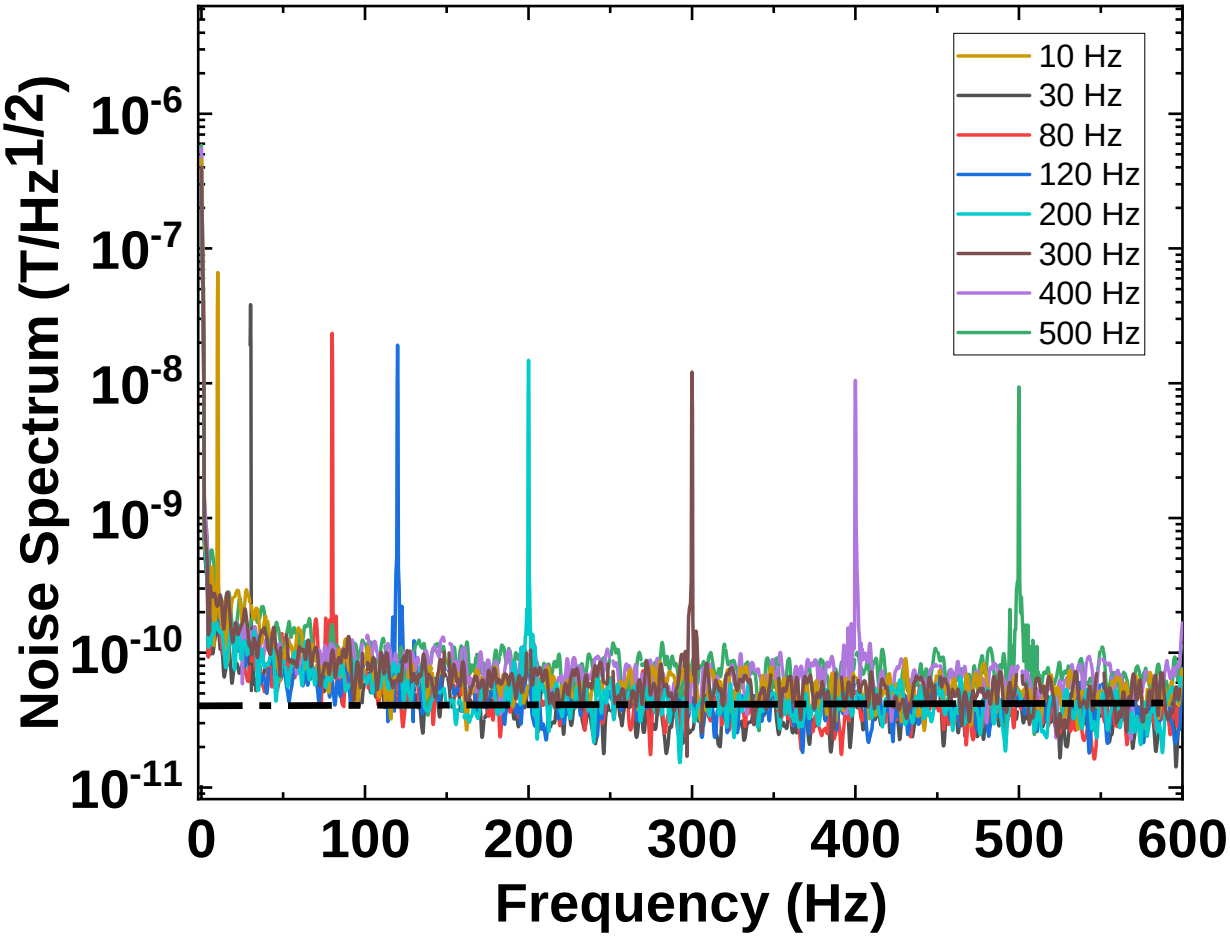


Figure 3.17: Shows the stitched noise spectrum at various modulation frequencies, varied from 10 Hz to 500 Hz. The magnetic field was modulated by 300 nT_{rms}, and the magnetometer response was recorded at different modulation frequencies.

The experiments were performed in a Neon buffer-gas-filled vapour cell (200 Torr) at 95°C

with an applied static bias field of about 0.6 mT produced by a highly stable current controller (LD3000). A 300 nT_{rms} weak sinusoidal magnetic modulation was then superimposed upon the

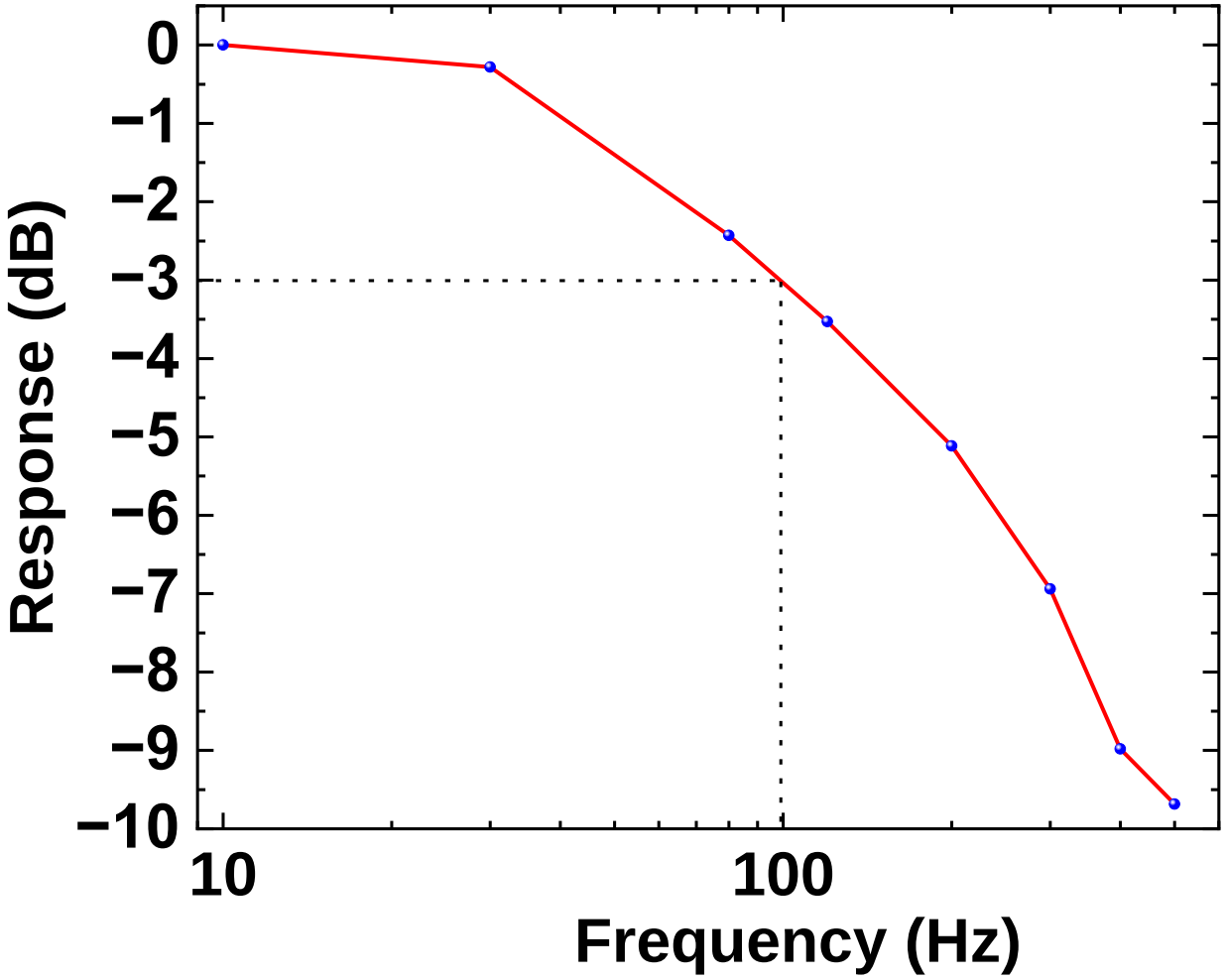


Figure 3.18: Illustrates the frequency response of the magnetometer at various modulation frequencies. We get a -3 dB point at around 100 Hz of modulation frequency.

bias field to create a time-varying total field.

The balanced photodetector differential signal was amplified with a +32 dB gain low-noise amplifier (LNA). The signal was then captured on a high-speed digital oscilloscope, and a Fast Fourier Transform (FFT) was used to achieve the noise power spectrum. The FFT spectrum makes it possible to recognise frequency-dependent features in the magnetometer response and establish the overall noise characteristics within the modulation frequency range. Representative spectra at various modulation frequencies are presented in Figure 3.17.

Figure 3.16 displays a typical noise spectrum for a 120 Hz modulation signal. A well-defined

resonance peak is evident above the noise floor, illustrating the magnetometer's sensitivity to small, time-varying magnetic fields. The signal-to-noise ratio (SNR) of the detected peak was around 10^3 for a modulation amplitude of 300 nT_{rms}. The corresponding sensitivity, characterised by

$$\text{Sensitivity} = \frac{\delta B}{SNR} \times \frac{1}{\sqrt{BW}}, \tag{3.4}$$

was around 30 $pT/\sqrt{Hz}$ at a bias field of 0.6 mT, where δB is the modulation amplitude of the applied field, SNR is the signal-to-noise ratio, and BW is the measurement bandwidth.

The magnetometer response versus modulation frequency is presented in Figure 3.18. The detected signal amplitude is practically independent of frequency up to a certain cutoff frequency, after which it decreases gradually. The -3 dB point of the frequency response curve determines the magnetometer's operational bandwidth, which was around 100 Hz. This bandwidth represents the highest rate at which the RDSNS magnetometer can accurately follow magnetic field changes.

The flat response over a broad range of low frequencies and the comparatively high cutoff frequency show that the RDSNS magnetometer has both high sensitivity and a wide temporal response. The bandwidth is dominated by the inductive response time of the magnetic field coils. By employing fewer turn coils or active compensation methods, the bandwidth can be further extended, making the system more applicable to high temporal resolution requirements.

Combined, these measurements demonstrate that the RDSNS magnetometer achieves a sensitivity of approximately 30 $pT/\sqrt{Hz}$ with a -3 dB bandwidth of 100 Hz at a bias field of 0.6 mT. This figure-of-merit performance is comparable to that of state-of-the-art all-optical magnetometers, but with a considerably wider operational field range.

3.4 Conclusion and Outlook

In this chapter, we have introduced the development, characterisation, and performance analysis of an all-optical broadband atomic magnetometer on the basis of the Raman-driven spin noise spectroscopy (RDSNS) technique. The magnetometer is based on the inherent spin fluctuations of a rubidium atomic ensemble, coherently driven by a pair of Raman beams, and non-invasively measured by a far-detuned probe beam through a polarimetric scheme.

At small magnetic fields, in the linear Zeeman regime, Raman-driven spin noise spectra show

one narrow resonance peak. The position of the resonance gives a very sensitive measurement of the magnetic field, showing higher accuracy than standard spin noise spectroscopy (SNS). With increasing magnetic field, the envelope of the resonance becomes wider and splits into several narrow peaks as a result of the nonlinear Zeeman effect. The field positions of these peaks obey the Breit–Rabi relation, and thus precise field determination is possible even in the high-field limit.

The all-optical design of this magnetometer provides essential advantages over conventional RF-based or SERF magnetometers. It is immune by nature to RF interference, does not require magnetic shielding or cryogenic cooling, and operates stably over a dynamic range of more than 150 G. The device has a DC field resolution of around 30 pT and an AC sensitivity of 30 pT/$\sqrt{\text{Hz}}$ with a bandwidth of 100 Hz, and thus it is an excellent candidate for both low-frequency and broadband magnetic field measurements.

The shown bandwidth and sensitivity are currently limited by the response time of the magnetic field coils. Those might be enhanced by using low-inductance or actively compensated coils. Portability could be further advanced by miniaturisation through MEMS vapour cells [117], laser-based compact systems, and light-induced atomic desorption (LIAD) processes [118]. Phase-locked loop (PLL) feedback for stabilising the Raman frequency might enhance long-term accuracy and insensitivity to drift. In addition, using quantum-amplified probe beams, e.g., linearly polarised squeezed light [119], may further expand the sensitivity frontiers of RDSNS magnetometry.

Aside from precision magnetometry, the RDSNS method may be extended to investigate basic quantum correlations in cold atomic ensembles [120], examine hyperfine spin-exchange interactions among various species, or investigate unusual quantum phases in multi-level systems. From a technology point of view, miniaturised RDSNS magnetometers would be able to offer non-invasive and broadband magnetic sensing for medical diagnostics, geophysical surveys, navigation, and space exploration. The detection of large dynamic range, sub-femtotesla sensitivity, and RF immunity makes the approach a viable candidate to replace present SERF and RF magnetometers for future-generation quantum sensing platforms. In all, this research establishes the Raman-driven spin noise spectroscopy method as a general and scalable paradigm for broadband atomic magnetometry, filling the gap between ultra-sensitive, robust, high-dynamic-range, and field-deployable units.

"Not everything that can be counted counts, and not everything that counts can be counted."

— Albert Einstein

Chapter 4

Dual Species Cold Atomic System

This chapter is based on the following publication:

Fast loaded dual species magneto optical trap of cold sodium and potassium atoms with light-assisted inter-species interaction, Sagar Sutradhar, Anirban Misra, Gourab Pal, **Sayari Majumder**, Sanjukta Roy, Saptarishi Chaudhuri, *AIP Advances*, 1 June 2023; **13**(6): 065317. https://doi.org/10.1063/5.0154985

In this chapter, we explore the construction and working of our cold atomic system. It consists of two species- Sodium and Potassium, which we simultaneously cool and trap in the same 3D trapping field. We discuss in detail our choice of a two-chamber loading scheme for a faster and greater flux of atoms being trapped. We see that we get more than 3×10^{10} potassium atoms and 5.8×10^8 Sodium atoms captured in the $3D$ MOT simultaneously from individual $2D^+$ MOTs with a capture rate of 5×10^{10} and 3.5×10^8 atoms/sec for Potassium and Sodium, respectively. We also explore inter-species interactions in greater detail, which is crucial for such a dual-species cold atom machine, where the effect of one species on the other can alter the loss mechanism for

each species.

Introduction and Motivation

One of the primary motivations behind this thesis is to observe the spin noise signal from cold atoms and to explore the physics of spin-exchange between heteronuclear atomic species. For this purpose, we have designed and constructed a dual-species cold atomic system capable of simultaneously cooling and trapping bosonic ^{23}Na and ^{39}K atoms. The apparatus also allows experiments with fermionic ^{40}K, which is also present in our setup. Developing such a system is important for several reasons. It enables the study of inter-species interactions, such as light-assisted collisions and spin-exchange collisions, which play a central role in multi-species quantum gases. Additionally, it offers a platform for high-precision measurements and quantum sensing applications using dual-species mixtures. Finally, it allows us to prepare cold and dense ensembles suitable for further experiments, such as Spin Noise Spectroscopy (SNS) in mixed atomic samples. The chapter is organised as follows. Sec. 4.1 describes the design of our experimental apparatus, including the vacuum, laser, and magneto-optical trapping systems. In Sec. 4.2, I present the optical layout of our dual-species optical layout. Sec. 4.3, I describe the three lens imaging system which we use to image the magnetically trapped atoms. In Sec. 4.4, I present our studies on magnetic trapping efficiency. Inter-species interaction effects are discussed in Sec. 4.5. Finally, Sec. 4.6 summarises the key results and provides an outlook for future experiments.

4.1 Overview of the Experimental Apparatus

We use a high-flux atomic source to enable fast and efficient loading of atoms into our dual-species sodium–potassium system. The apparatus is designed to prepare, trap, and transport cold atoms in successive stages, starting from atomic sources to culminating in the simultaneous operation of 2D$^+$ and finally loading into the 3D magneto-optical traps (MOTs). In this section, we describe the key subsystems: the atomic sources and the vacuum system, the laser systems, the MOT configurations, and the imaging setup. Each of these subsystems plays a crucial role in ensuring that we can reliably trap and cool both species of atoms, paving the way for further experiments

on inter-species interactions.

4.1.1 Atomic Sources and Vacuum System

Atomic samples of sodium and potassium are contained in separate ovens, each connected to a DN16CF housing equipped with an angled valve to control the flow of atomic vapor at the same time to isolate the oven from the remaining set-up. A temperature gradient is maintained in order to allow the atomic vapours to flow from the source to the 2D glass cells. The ovens are resistively heated, with temperature controlled via dedicated heater controllers to regulate the vapor pressure. Each source is connected to a four-way cross (405002, MDC Vacuum), one port of which leads to a differential pumping tube made of oxygen-free high-conductivity (OFHC) copper. The tube is polished at 45° and has a central hole which primarily allows the atoms in the $2D^+$ MOT to pass through efficiently. The four-way cross also connects to the 3D MOT chamber and to a 20 L/s ion pump (VacIon Plus 20, Agilent), ensuring continuous pumping.

To successfully design and operate experiments with quantum gases, an ultra-high vacuum (UHV) environment is essential. Atoms trapped in a MOT undergo collisions with background gas, leading to significant atom loss and limiting trap lifetimes. Maintaining UHV minimises such collisions, thereby extending the trap lifetime. For instance, to achieve a lifetime of $\sim$ 100 s for potassium, a background pressure of order 10^{-11} mbar is required. Our vacuum system incorporates ion pumps, a differential pumping section, and specialised optical access to meet these requirements. For maintaining a vacuum in the $2D^+$ MOT glass cells of both species, a 20 l/s ion pump is used for each cell. The 3D MOT vacuum is maintained by a 75 l/s ion pump. The differential pumping tube maintains a pressure difference of more than 10^3 between the 2D MOT glass cell (higher pressure for efficient atom loading) and the UHV 3D MOT chamber. This arrangement ensures that a high atomic flux is produced in the 2D MOT, while preserving ultra-high vacuum in the science chamber for long atom lifetimes. Additionally, two ion pumps of pumping speeds 40 l/s and 75 l/s are used to maintain a UHV in the glass cell (science cell) after the transport section. A Titanium sublimation pump is also utilised to maintain the pressure below 10^{-11} mbar. We use an ionisation gauge to monitor the pressure inside the 3D MOT chamber.

4.1.2 Laser Systems

The optical layout is designed by preparing the laser frequencies and intensities separately, and then sending them via polarisation-maintaining optical fibers to the main experimental system containing the 2D and 3D MOT chambers.

Potassium Laser Setup

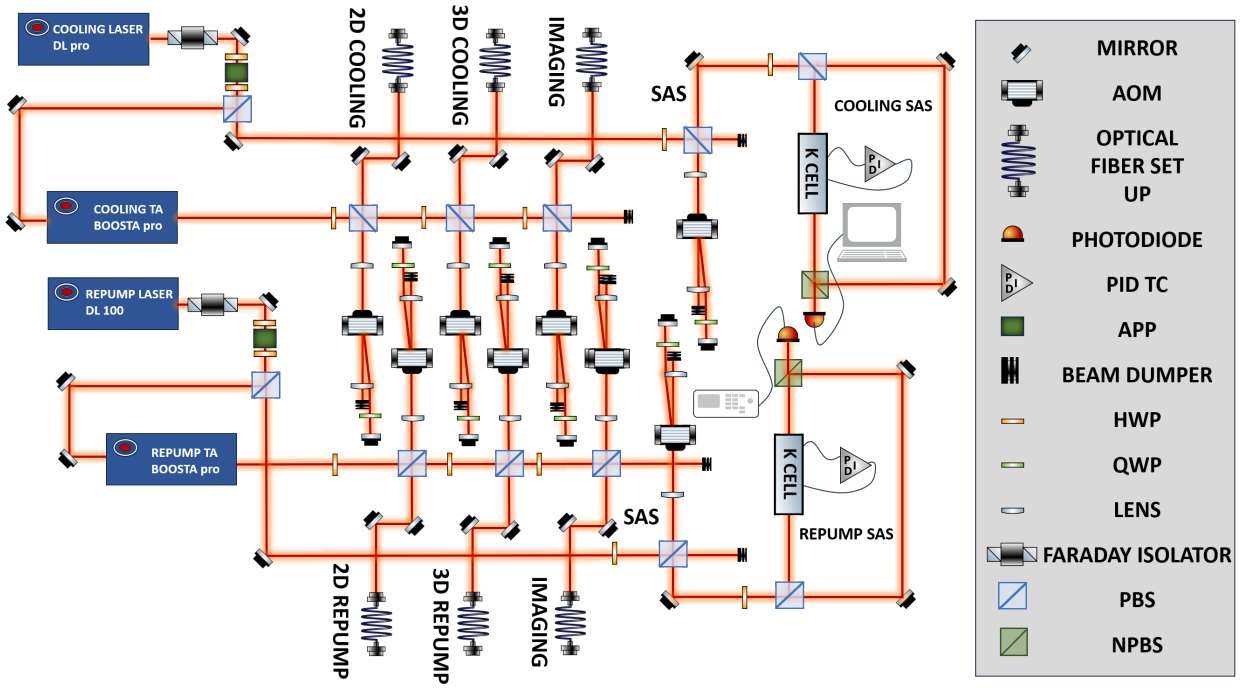


Figure 4.1: Optical layout of the potassium laser system. The figure shows the arrangement of the cooling and repump lasers, optical amplifiers, beam splitters, acousto-optic modulators (AOMs), polarisation optics, and optical fibres used to deliver laser light for trapping and cooling potassium atoms.

In the potassium laser system, we employ two external cavity diode lasers (ECDLs, Toptica Photonics) centred at 767 nm. Light from one of the ECDL, used as the cooling laser (DL pro, laser output $\approx$ 41 mW), is split: one portion (power $\approx$ 5 mW) is directed to a saturation absorption spectroscopy (SAS) setup for precise frequency measurement and laser locking to the cooling transition of ^{39}K. We utilise the Toptica DigiLock module to perform the laser locking of our cooling beams. While the other portion (21 mW) is injected into a tapered amplifier (TA, Toptica BOOSTA pro) to increase optical power. The amplified output (1.4 W) is distributed

to be used for the cooling in the $2D^+$ MOT (441 mW), 3D MOT (268 mW), and imaging (1 mW) setups. For precise frequency and intensity control for each set-up we employ Acousto-Optic Modulators (AOMs) (AA optics, 200 MHz). A similar arrangement is implemented for the repumping transition, using a second ECDL (Toptica Photonics, DL100, output power = 39 mW) and TA (Toptica BOOSTA pro). Similar to the cooling setup, a part of the light from the laser (4 mW) is sent to the SAS setup and a LIR locking scheme is used to lock the repumping laser. While the rest (19 mW) is injected into the TA. The output of the repumping TA is around 528 mW. This output is distributed to the the $2D^+$ MOT (183 mW), 3D MOT (120 mW), and imaging (0.5 mW) setups. Each set-up contains AOMs in the double-pass configuration and this gives us precise control over the power and frequency of the light. Finally, all the light is coupled to polarisation-maintaining optical fibres, which transfer the light to the optical set-up containing the vacuum chamber and trapping fields. For detailed information on the laser frequency settings and intensity distributions, please refer to Appendix D. A detailed optical layout has been provided in the form of a schematic in fig. 4.1.

Table 4.1: Potassium MOT laser parameters. Detunings are given in units of the natural linewidth Γ, and intensities are expressed relative to the saturation intensity I_{sat}.

Beam	Detuning (Γ)	Intensity (I_{sat})
2D MOT cooling	-6.5	11
2D MOT repumper	0 (on resonance)	8.25
3D MOT cooling	-6.8	20
3D MOT repumper	0 (on resonance)	15

Sodium Laser System

For Sodium, we employ a second harmonic generation laser (Toptica Photonics, TASHG pro system), which integrates all the required components for generating high-power, frequency-stable light at 589 nm. The system is seeded by an ECDL (DL Pro) centred at 1178 nm. An optical isolator immediately after the seed laser prevents back reflections and ensures long-term frequency stability. The stabilised light is injected into a TA, boosting the power to 2.2 W. The amplified infrared light passes through another optical isolator and an electro-optic modulator (EOM) for sideband generation, before being frequency-doubled in a resonant second-harmonic generation

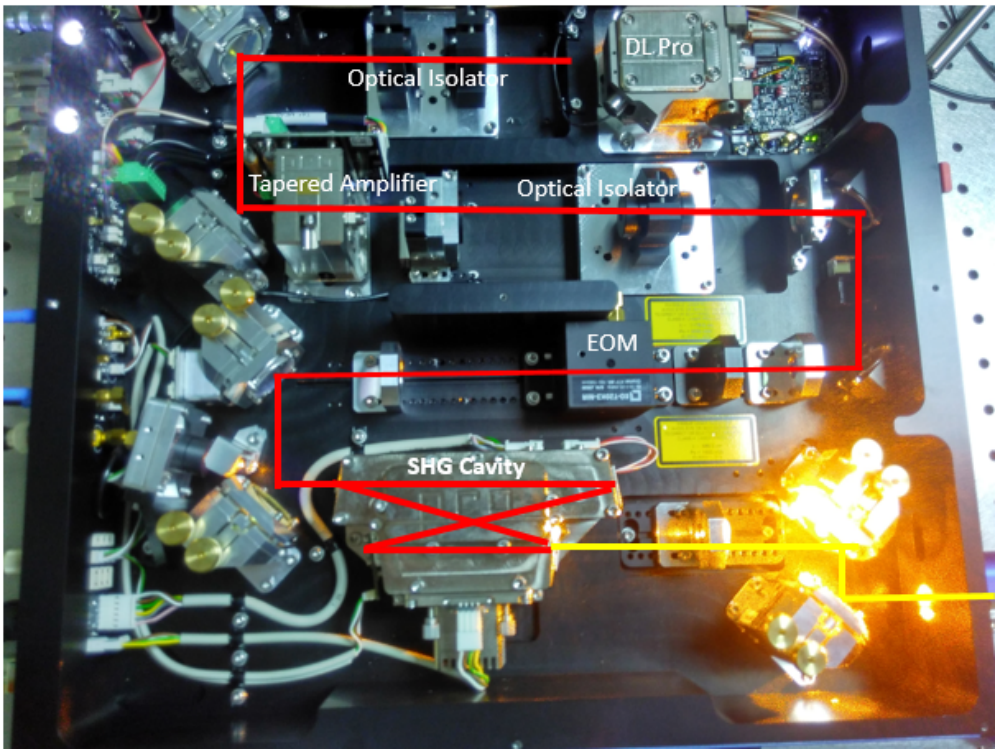


Figure 4.2: Photograph of the TASHG pro system used for generating 589 nm light for the sodium MOT. The system integrates a DL Pro seed laser at 1178 nm, optical isolators, a tapered amplifier, an electro-optic modulator, and a resonant SHG cavity, providing stable high-power output at 589 nm.

(SHG) cavity containing a PPKTP crystal. This cavity is actively stabilised to maintain phase matching in the nonlinear crystal, yielding a stable wavelength of 589 nm with an output power of 1.1 W. The sodium optical layout is organised to provide precise control over frequency and intensity for each beam path. The 589 nm yellow light output from the TASHG pro is first split into separate branches, each containing a double-pass acousto-optic modulator (AOM). This configuration enables independent frequency tuning and power adjustment of each beam. It is subsequently distributed among the $2D^+$ MOT, 3D MOT, additional pushing beam, imaging, and reference setups. Each of these setups contains AOMs in a double-pass configuration. The outputs of the $2D^+$ MOT and 3D MOT after the double-pass from the AOMs are sent through two independent Electro-Optic Modulators (EOMs). The EOMs are phase-modulated, which creates sidebands around the cooling transition at 1.7 GHz. The higher frequency is fed to the 3D repumping transition, while the lower frequency is fed to the cooling transition. We use the Toptica DigiLock locking module for precisely locking the sodium laser at the side of the cooling

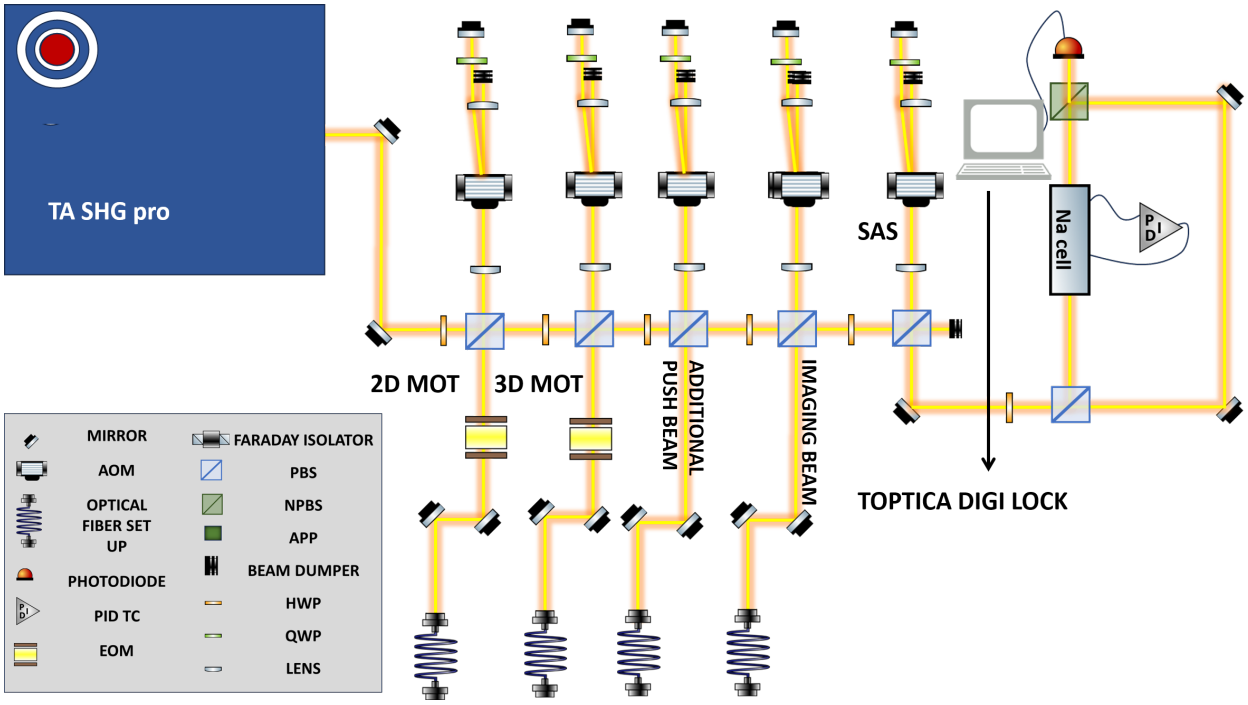


Figure 4.3: Schematic of the sodium optical layout. The 589 nm light from the TASHG pro is split into multiple branches using polarisation optics. Each branch includes an AOM in a double-pass configuration for independent frequency tuning and intensity control.

peak of the Sodium SAS. A detailed schematic of the laser light generation and the optical layout has been presented in fig. 4.2 and fig. 4.3 respectively. For more details regarding sodium laser frequency references, please refer to the information provided in the appendix. D. Typical power levels delivered to each branch are as follows: approximately 118 mW for the 2D MOT, 108 mW for the 3D MOT, 0.5 mW for the imaging setup, and 3 mW directed to the SAS cell for frequency stabilisation. These values ensure efficient loading of the 2D MOT, strong confinement in the 3D MOT, and sufficient probe intensity for absorption imaging, while maintaining a stable frequency reference for laser locking. All beams are coupled into PM fibres for stable and reproducible delivery to the experimental chamber, where they are collimated and shaped into the required geometries.

The intensity of the 2D and 3D cooling beams is set close to the saturation intensity I_{sat}. Operating near I_{sat} ensures a high scattering rate and efficient cooling without introducing excessive power broadening or heating effects. The repump and cooling frequencies are tuned to the respective hyperfine transitions for ^{39}K and ^{23}Na, ensuring efficient laser cooling.

Table 4.2: Sodium MOT laser parameters. Detunings are given in units of the natural linewidth Γ, and intensities are expressed relative to the saturation intensity I_{sat}.

Beam	Detuning (Γ)	Intensity (I_{sat})
2D MOT cooling	−1.5	1.9
2D MOT repumper	0 (on resonance)	0.35
Additional push beam	−2	10
3D MOT cooling	−1.4	10
3D MOT repumper	0 (on resonance)	0.22

4.2 Optical Layout for Dual-Species Operation

The optical layout is designed such that the frequencies and intensities required for the cooling and repumping transitions are prepared separately and subsequently delivered via PM optical fibres to the main experimental system, which houses the 2D and 3D MOT chambers. This modular design enables independent frequency and intensity control for each species, allowing for efficient dual-species operation.

4.2.1 Magneto-Optical Traps ($2D^+$ and 3D)

$2D^+$ Requirement

For performing efficient measurements in quantum gases, a high number of cold atoms in the quantum limit is desirable. To achieve this, it becomes necessary to load and laser cool a large number of atoms initially, so as to compensate for the losses encountered during the magnetic trapping, transport, and evaporative cooling stages. While searching for the most efficient loading schemes, one encounters the most popular technique of vapour-loaded MOT [121–125]. Here, the atoms from the source are heated and directly captured by the 3D trapping field and cooled using the molasses beams. In order to increase the loading rate, one increases the vapour pressure, but it comes at the cost of higher collisional losses from the background. Hence, it has been observed that one can achieve around 10^7 atoms in the MOT using this technique. To overcome such challenges, one has to utilise a setup which is capable of generating a source of atomic beam [126–129] without increasing the losses due to background collisions and at the same time remain well below the capture velocity of the 3D MOT. There are mainly two techniques to do so.

The first is using a Zeeman slower [130–132]. In a Zeeman slower, the inhomogeneous magnetic field compensates the changing Doppler shift experienced by the decelerating atoms, keeping them resonant with the slowing beam. This technique enables deceleration of thermal atomic beams to velocities suitable for MOT capture, with reported fluxes on the order of 10^{11} atoms/s. However, the process is not without limitations. Transverse heating due to spontaneous emission leads to divergence of the slowed beam, reducing the efficiency of MOT loading. Typical loading efficiencies remain only a few per cent unless additional transverse cooling stages are employed. Furthermore, the Zeeman slower only acts on part of the velocity distribution, leaving higher-velocity atoms unaffected; these can collide with the trapped atoms and degrade MOT performance. Additional complications include residual magnetic fields at the end of the slower, which must be carefully compensated to avoid disturbing the MOT gradient fields. From a practical perspective, the high vapour pressures required to operate the Zeeman slower ovens also result in increased material consumption and reduced lifetime of the source.

The second is a two-chamber approach where a pre-cooled source is built separately and the atoms are captured in a separate 3D MOT chamber. This reduces background collisions and also creates an atomic beam with velocities within the capture velocity of the 3D MOT. Here, atoms are first produced in a vapour cell maintained at a moderate background pressure (typically 10^{-6}–10^{-8} mbar), where they are pre-cooled and collimated before being transferred to a second ultra-high vacuum chamber containing the main MOT. Two designs have become standard within this category: the low-velocity intense source (LVIS) and the two-dimensional MOT (2D MOT). In both schemes, atoms are extracted from the vapour and guided along one axis into the science chamber, providing a continuous and well-collimated atomic beam. Comparative studies have shown that the 2D MOT typically provides higher fluxes than the LVIS while requiring an order of magnitude less laser power, making it particularly attractive for experiments where laser power is limited. The 2D MOT has since been implemented across a wide variety of atomic species, from alkali metals to heavier atoms, and has become a reliable alternative to the Zeeman slower for efficient MOT loading.

Hence, using the design inspired by the 2D [131, 133–135] MOT is our approach to create a high flux of a large number of atoms in our 3D MOT chamber. The first stage of cooling is achieved using a $2D^+$ MOT, where a two-dimensional cold atomic beam is generated. The transverse cooling

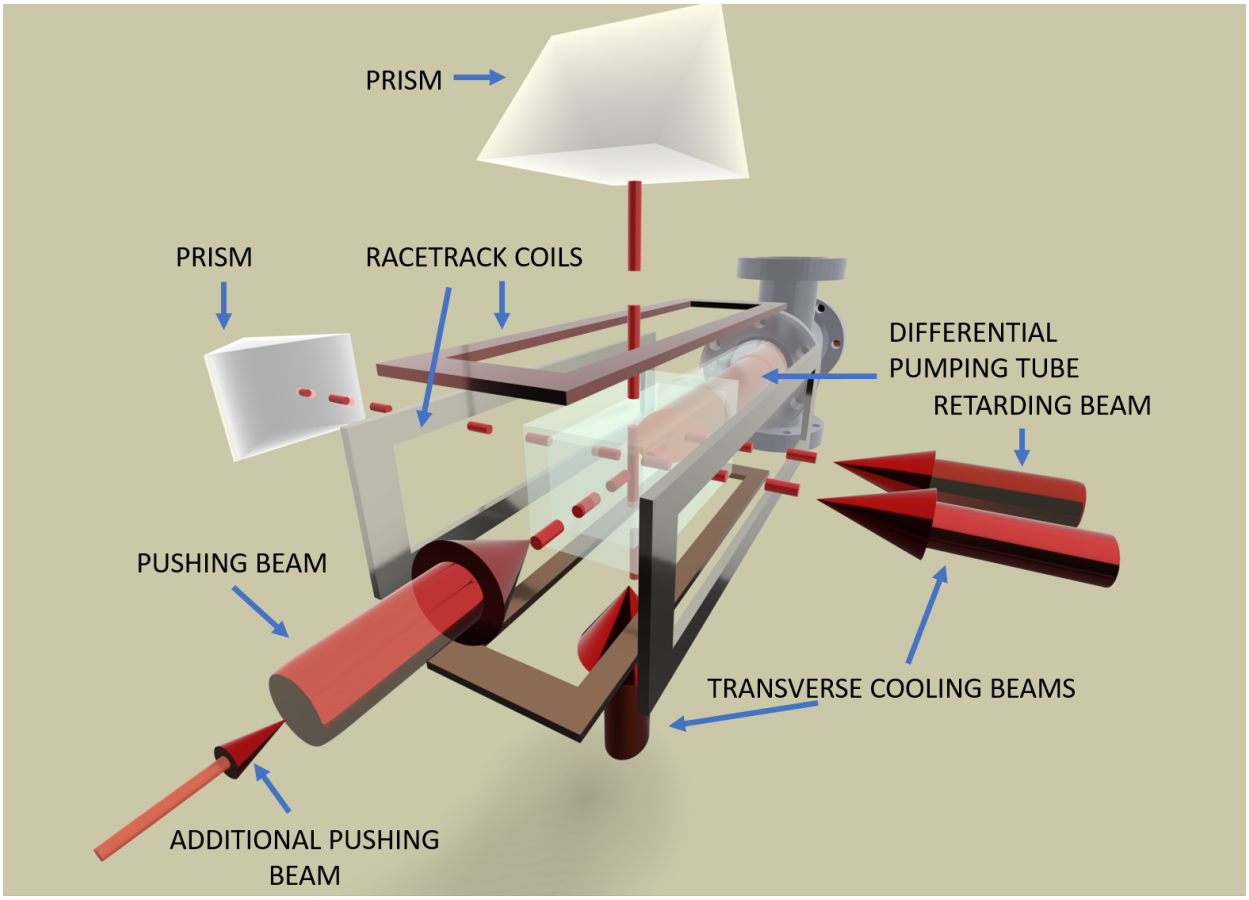


Figure 4.4: Schematic diagram of the $2D^+$ MOT. Two transverse cooling beams are retro-reflected using two helicity-preserving right-angled prisms. In addition, a pair of longitudinal cooling beams (pushing and retarding beams) is aligned along the line of the zero magnetic field created due to the configuration of the four race-track-shaped coils. The copper tube with a differential pumping hole connecting the $2D^+$ MOT and the 3D MOT sides, is cut at an angle of 45^o and mirror-polished to facilitate the passage of the retarding beam. An additional pushing beam is used to direct the cold atomic beam to the 3D MOT chamber through the differential pumping hole.

beams, with suitable polarisations, are retro-reflected using right-angled prisms, providing optical molasses in two directions. A pair of race-track coils in the anti-Helmholtz configuration creates a line of zero magnetic field, allowing atoms to be captured over this line. In the longitudinal direction, a combination of pushing and retarding beams further cools and directs the atomic flux. An additional pushing beam is used to transfer the cold atomic beam into the 3D MOT chamber via the differential pumping tube. The 3D MOT, located in the UHV chamber, captures and traps atoms delivered from the $2D^+$ MOT. Here, a quadrupole magnetic field combined with three pairs of counter-propagating cooling beams provides three-dimensional cooling and confinement. The

3D MOT is capable of simultaneously loading both sodium and potassium, forming the starting point for subsequent experiments.

In a standard 2D MOT, the cooling beams together with the quadrupole magnetic field reduce the atomic velocity components in the transverse plane, thereby collimating the atomic beam. However, the velocity component along the longitudinal axis (the propagation direction of the atomic beam) remains unaffected. This limits both the interaction time of atoms with the cooling region and the overall achievable flux.

The $2D^+$ MOT configuration extends the 2D MOT scheme by introducing two additional counter-propagating beams along the longitudinal direction: a pushing beam and a retardation beam, as illustrated in Fig. 4.4. Since the quadrupole magnetic field in the 2D MOT configuration has no restoring component along the longitudinal axis, the pushing and retardation beams establish an optical molasses along this direction. The pushing beam drives atoms out of the cooling region toward the 3D MOT chamber, while the retardation beam counteracts this acceleration, reducing the average longitudinal velocity. This reduction in velocity increases the interaction time of atoms with the cooling volume, thereby enhancing the efficiency of transverse cooling. As a result, the flux of the atomic beam is significantly higher than that of the conventional 2D MOT.

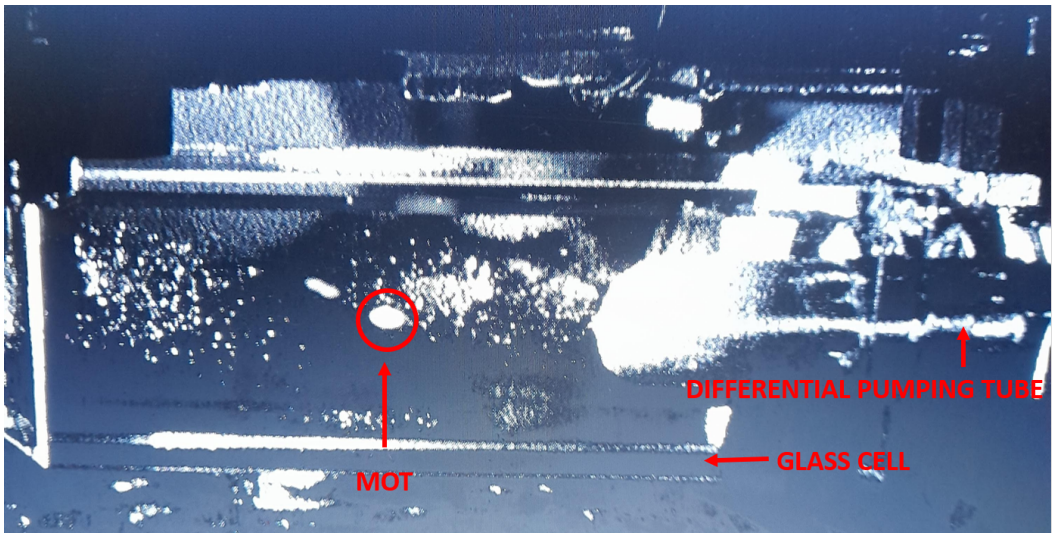


Figure 4.5: Fluorescence image of a potassium MOT prepared in the chamber used for the 2D-MOT during alignment and optimization of the system. In the normal operating configuration, the 2D-MOT produces a continuous atomic beam that is pushed toward the science chamber using an intensity imbalance between the push and retard beams, which makes direct imaging of the 2D-MOT fluorescence difficult. The image shows the location of the MOT inside the glass cell and the differential pumping tube connecting the source chamber to the 3D-MOT chamber.

Although the primary purpose of the 2D-MOT is to produce a collimated atomic beam rather than a stationary cloud, obtaining a clear fluorescence image of the atoms in this configuration is experimentally challenging. In our potassium 2D-MOT, atoms are continuously pushed towards the 3D-MOT chamber by introducing an intensity imbalance between the push and retard beams along the atomic beam axis. As a result, the atoms do not accumulate in the trapping region long enough to produce a strong localized fluorescence signal.

To visualize the trapping region and confirm the optical alignment inside the chamber, we temporarily operated the system in a 3D-MOT configuration within the same chamber used for the 2D-MOT. The fluorescence image obtained in this configuration is shown in Fig. 4.5. The image clearly identifies the location of the MOT within the glass cell as well as the differential pumping tube that connects the source chamber to the ultra-high-vacuum region of the 3D-MOT.

3D MOT

After the atoms are cooled in the 2D MOT glass cell, they are directed to the 3D MOT chamber. The optical layout for the 3D molasses is done carefully to integrate both the IR light of 767 nm for Potassium and the yellow light (589 nm) for Sodium into a single 3D trapping and cooling setup. For Sodium, there is a single fibre output for the 3D MOT light beams. The fibre collimator creates a 12.5 mm of $1/e^2$ Gaussian collimated beam profile, which is then distributed equally between the 3 directions (x, y and z directions) and then expanded by 1.5x magnification using telescope lens combinations (f_1 = 100 mm and f_2 = 150 mm). For the potassium set-up, we have two such fibre collimators (collimation of 12.5 mm $1/e^2$ beam size) to address the cooling and repumping transitions. They are expanded using a telescopic lens set-up (f_1 = 75 mm and f_2 = 150 mm), merged and divided equally in the three directions using combinations of HWP and PBS. The light of Sodium and Potassium is merged using dichroic mirrors, which transmit 767 nm light and reflect the 589 nm light. The dichroic mirror has a cutoff at 650 nm; it reflects light with wavelengths below this cutoff and transmits light with wavelengths above the specified wavelength. We utilised a retro-reflection scheme to generate the 6 MOT beams. This enables a lower power requirement as compared to preparing 6 independent MOT beams. The polarisation of the molasses beams is carefully created using a combination of HWPs and QWPs. At the intersection of these 6 beams of each kind, an optical molasses centre is created. A trapping field is created at the same place where

the optical centre lies with the help of a coil in the anti-Helmholtz configuration. The gradient of this MOT field was carefully measured, which comes out to be about 0.9 G/A.cm. We have also installed another pair of coils in a Helmholtz configuration, which gives a uniform magnetic field. The importance of this coil is more explicitly evident in an experiment on spatial density measurements, which is described in detail in the next chapter.

4.3 Imaging Systems

A high-resolution imaging system is essential for characterising the performance of the MOT and analysing its quantitative and qualitative parameters. We employ two techniques to image our cold atoms and extract useful parameters like size, total number of atoms, temperature of the cloud etc. These include fluorescence and absorption imaging, which are described in detail in the following sections.

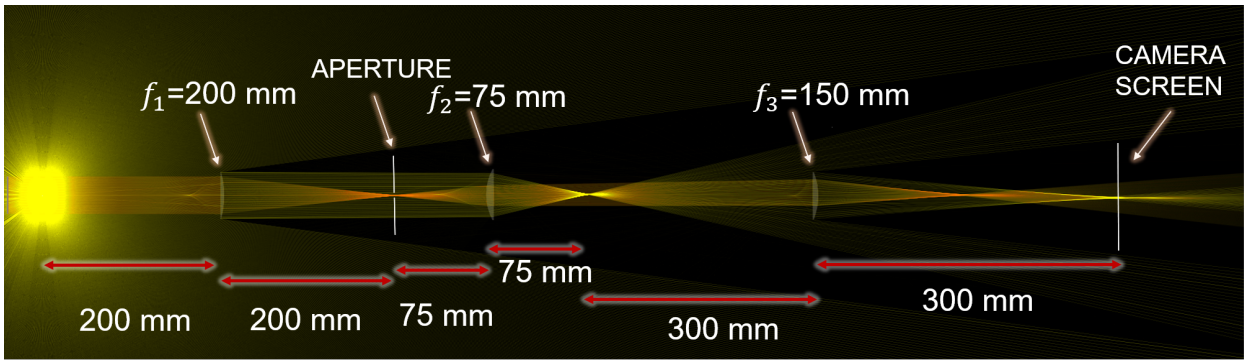


Figure 4.6: Ray-tracing diagram of the three-lens imaging system. The first lens (f = 200 mm) collimates the fluorescence light while focusing the absorption imaging beam. The second lens (f = 75 mm) provides demagnification and re-collimation for the imaging beam while simultaneously focusing the fluorescence. Finally, the third lens (f = 150 mm), placed at a $2f$ distance from the second, relays the image in a $2f$–$2f$ configuration onto the camera plane.

4.3.1 Fluorescence Imaging

When the molasses beams are shone on the atoms, they undergo spontaneous emission in random directions. These atoms fluoresce at a rate which is proportional to Γ and the number of atoms in the excited state. Hence, the total fluorescence is proportional to the total number of atoms. To determine the number of atoms trapped in the MOT, one must consider the collection geometry of

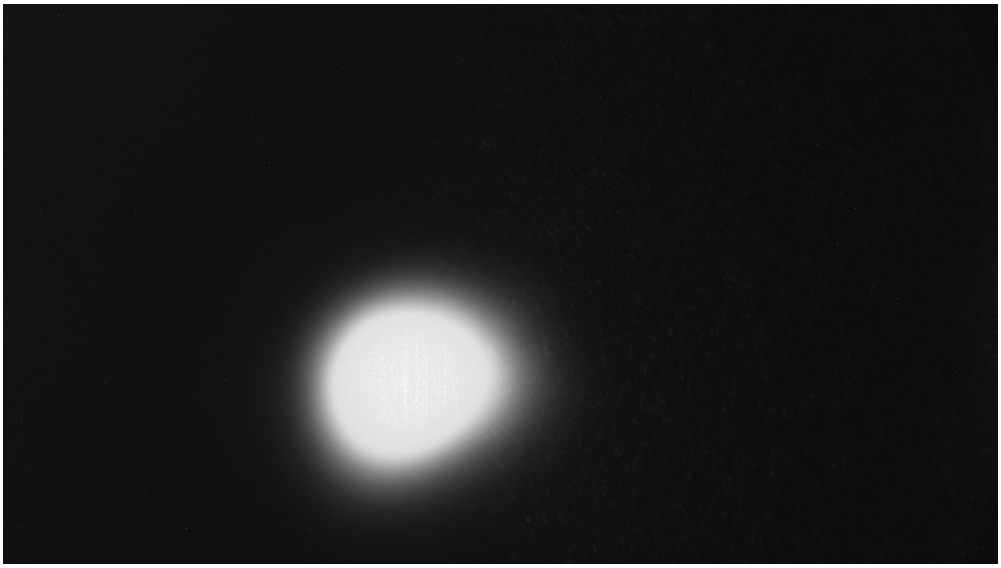


Figure 4.7: Illustrates the fluorescence image captured by the CCD camera for an atom number of 10^8 Potassium atoms.

the emission process. To visualise the fluorescence image, we utilise a CCD camera/photo-detector and a collection lens. Since atoms emit isotropically (4π solid angle), this imaging lens collects a fraction ($\Omega/4\pi$) of the total fluorescence. The solid angle subtended by the first lens to the MOT is given by,

$$\Omega = r^2/f^2. \tag{4.1}$$

Here, r is the radius of the lens and f is the focal length of the lens. Assuming the MOT is at the focal plane of the collection lens, the light from the atom's fluorescence will be collimated. After the collection lens, we have kept a beam splitter, which splits the fluorescence light into 2 paths. One goes to a CCD camera, which enables high-resolution spatial imaging. Another path consists of a photodiode (femtowatt detector). This enables the study of sensitive temporal dynamics of the cloud. Additionally, to display the image on the entire screen of the camera, we magnify the image using a combination of lenses. The number of photon counts per pixel gives us a clear spatial resolution of the cloud. This helps us monitor the size, shape, and number of atoms in the cloud. The integrated pixel count is related to the total number of atoms. In order to derive the relation, we need to modify the scattering equation E.1 for the 3 pairs of counter-propagating laser cooling beams. It can be written as,

$$R_s = \frac{\Gamma}{2}\frac{6s_0}{1 + 6s_0 + (\frac{2\delta}{\Gamma})^2} \tag{4.2}$$

If the atom after excitation emits a photon of energy $h\nu$, the corresponding energy emitted by the atom per second is given by $R_s h\nu$. The total number of photons (N_{ph}) emitted by the entire cloud of atoms (N) is given by,

$$N_{ph} = NR_s. \tag{4.3}$$

Considering the solid angle contribution due to the collection lens, the detector detects N_{ph}^{det} number of photons given as,

$$N_{ph}^{det} = \frac{\Omega}{4\pi} N_{ph} \tag{4.4}$$

$$= \frac{\Omega}{4\pi} NR_s \tag{4.5}$$

The CCD converts the detected photons into counts C_{det} according to

$$N_{ph}^{det} = \frac{C_{\text{det}}}{\eta_{\text{CCD}}}, \tag{4.6}$$

where η_{CCD} is the conversion efficiency (photons per count).

Combining these expressions, the total atom number in the MOT is given by

$$N = \frac{4\pi}{\Omega} \cdot \frac{C_{\text{det}}}{\eta_{\text{CCD}}\, R_{\text{s}}}. \tag{4.7}$$

Equation 4.7 relates the number of atoms in the MOT to the experimentally measured CCD counts, the collection efficiency of the imaging system, and the photon scattering rate for 1 second of exposure time. For an exposure time of τ, we get

$$N = \frac{4\pi}{\Omega} \cdot \frac{C_{\text{det}}}{\eta_{\text{CCD}}\, R_{\text{s}} \tau}. \tag{4.8}$$

In the optical setup, a three-lens system operates in a complementary manner. The fluorescence light emitted by the atomic cloud is collected and collimated by the first lens ($f = 200$ mm). This collimated emission then propagates through the aperture plane. Since the aperture is placed at the probe focus, it has a negligible effect on the fluorescence signal, allowing most of the collected light to pass through.

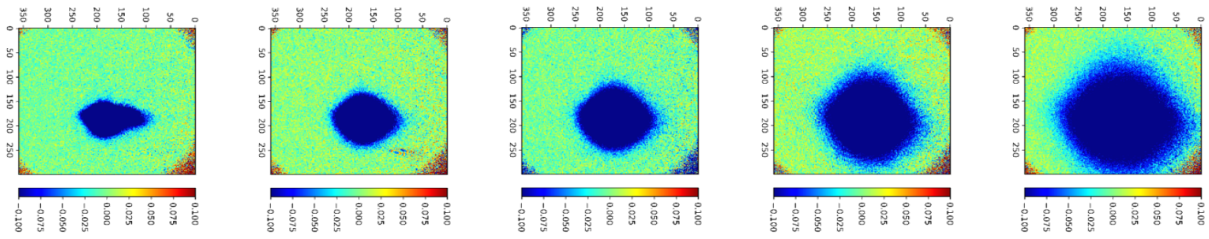
The second lens ($f = 75$ mm) then focuses the collimated fluorescence, creating an intermediate

image. Finally, the third lens (f = 150 mm), placed in the $2f$–$2f$ configuration relative to the second lens, relays this intermediate image onto the detector. In this mode, the optical sequence efficiently collects and images the fluorescence distribution of the atoms.

The number and temperature of trapped atoms are measured using fluorescence and absorption imaging techniques. Fluorescence imaging enables real-time monitoring of atomic number, while absorption imaging, based on the Beer–Lambert law, provides spatial density distributions and column density measurements. The fluorescence image of the trapped potassium cloud recorded on the CCD camera is shown in Fig. 4.7. The image corresponds to an atom number of approximately 10^9. A time-of-flight expansion experiment is employed to determine both the temperature of the atomic cloud and the total number of atoms trapped in the 3D MOT chamber.

4.3.2 Absorption Imaging

In absorption imaging, a resonant probe beam is used to image the cold atomic cloud. The atoms, when probed by this beam, absorb it and create a shadow on the spatial profile of this probe beam. By carefully calibrating the amount of absorption, one can calculate the total number of atoms in the MOT.



(a) (b) (c) (d) (e)

Figure 4.8: Absorption images of the atomic cloud for different time-of-flights (TOF): (a) 0 ms, (b) 5 ms, (c) 10 ms, (d) 15 ms, and (e) 20 ms. The gradual expansion of the cloud reflects the release and ballistic expansion dynamics of the ultracold ensemble.

Another application of this technique is its ability to determine the temperature of the cloud. This is achieved by releasing the atoms from the magnetic trapping field and allowing them to fall freely under gravity. Due to this, the cloud of cold atoms starts to fall and expand simultaneously.

By plotting the size of the cloud with the time of flight, one can easily determine the temperature of the cold atomic cloud. The absorption imaging beam is prepared as a collimated probe before entering the optical system. As shown in Fig. 4.6, the first lens with focal length $f = 200$ mm focuses this probe at its focal plane. At this plane, an aperture is placed to filter out the fluorescence light. This ensures that the isotropically emitted fluorescence from the atoms is effectively blocked, preventing contamination of the absorption image.

After passing through the aperture, the probe beam is intercepted by the second lens with $f = 75$ mm. This lens reduces the beam size and re-collimates it, preparing it for the final relay. The third lens, with $f = 150$ mm, is positioned at twice its focal length ($2f = 300$ mm) from the second lens, forming a standard $2f$–$2f$ imaging system. This configuration relays the image of the atomic cloud onto the camera plane with high fidelity. In this way, the system enables absorption imaging while maintaining suppression of unwanted background fluorescence. After switching off the trapping potential, the atomic cloud undergoes ballistic expansion. The evolution of the spatial distribution for different time-of-flight (TOF) durations is shown in Fig. 4.8. The increasing cloud size with TOF reflects the momentum distribution of the ultracold ensemble.

This dual-purpose arrangement enables the simultaneous performance of absorption and fluorescence imaging within the same optical path, providing both versatility and compactness to the overall experimental setup.

Sodium 3D MOT

For the Na–3DMOT, the relevant cooling beam parameters are summarised in Table 4.3. Using these parameters in Eq. 4.2, the scattering rate is found to be $R_s \approx 1.1 \times 10^7$ s^{-1}. Using the Na–3DMOT parameters from Table 4.3 together with a conversion factor $\eta_{CCD} = 0.37$ (37%) and the collection fraction $\Omega/4\pi = 0.034$. With the tabulated scattering rate of roughly 1.1×10^7 s^{-1}, each atom contributes to the detected counts per exposure when the exposure time is $\tau_{Na} = 5$ ms. Therefore, a measured total CCD signal of $C_{det} \sim 10^{10}$ corresponds to an inferred atom number of approximately 1.5×10^8 atoms under these assumptions.

Table 4.3: Parameters of the Na–3DMOT cooling beams.

Quantity	Value
Cooling beam intensity (I/I_{sat})	7.5
Detuning of the cooling beam (Γ)	-1.4
Scattering rate (R_{s})	1.1×10^7 s^{-1}
$\Omega/4\pi$ (solid angle fraction)	0.034

Potassium 3D MOT

or the K–3DMOT, the cooling beam parameters are listed in Table 4.4. Substituting into Eq. 4.2, the scattering rate is $R_{\text{sc}} \approx 6.2 \times 10^5$ s^{-1}. For the K–3DMOT, using the K table entries with $T_{\text{opt}} = 0.70$, $\eta_{\text{CCD}} = 0.13$ (13%) and $\Omega/4\pi = 0.034$ with the stated scattering rate of approximately 6.17×10^5 s^{-1}, each atom produces roughly 1.9 detected counts per exposure when the exposure time is $\tau_{\text{K}} = 1$ ms. Thus a total CCD signal of $C_{\text{det}} \sim 5 \times 10^9$ implies an atom number on the order of 1.8×10^{10} under these assumptions. The very large potassium number is driven mainly by the combination of short exposure and very large quoted counts; if this conflicts with other diagnostics, re-check the definition and calibration of C_{det}, the camera conversion factor, and any pre-processing applied to the images.

Table 4.4: Parameters of the K–3DMOT cooling beams.

Quantity	Value
Cooling Light intensity (I/I_{sat})	22.7
Detuning of the cooling beam (Γ)	-6.8
Scattering rate (R_{s})	6.17×10^5 s^{-1}
$\Omega/4\pi$ (solid angle fraction)	0.034

In practice, several caveats must be taken into account. Probe saturation and detuning corrections must be applied through σ_{eff}. Optical pumping into dark states and Clebsch-Gordan factors should be included if relevant. For high optical depth (typically OD $\gtrsim$ 2), imaging becomes nonlinear, and one may need to use shorter imaging pulses or off-resonant imaging. Finite imaging resolution must be considered if the cloud size approaches the system's point spread function. Finally, if the apparent atom number changes with TOF, this may indicate atom loss or systematic

imaging errors.

4.4 Magnetic Trap Experiment and Characterization

In this section, we describe our experimental efforts to load sodium atoms into a purely magnetic trap and study their survival over time. The number of atoms remaining in the trap was inferred through fluorescence detection after turning the trapping beams and magnetic fields on and off according to the described sequence. We first measured the survival probability of atoms in the magnetic trap over short timescales (tens of milliseconds). The experimental sequence involved turning on the magnetic quadrupole field to capture atoms in the magnetic trap in the absence of any molasses beams and then probing them with the 3D molasses beam after various wait times. The survival probability as a function of wait time is plotted in Figure 4.9. As seen, the survival probability decays rapidly with time, indicating losses from the trap on this short timescale. The survival probability decreases from approximately 80% at 0 ms to below 10% at 30 ms.

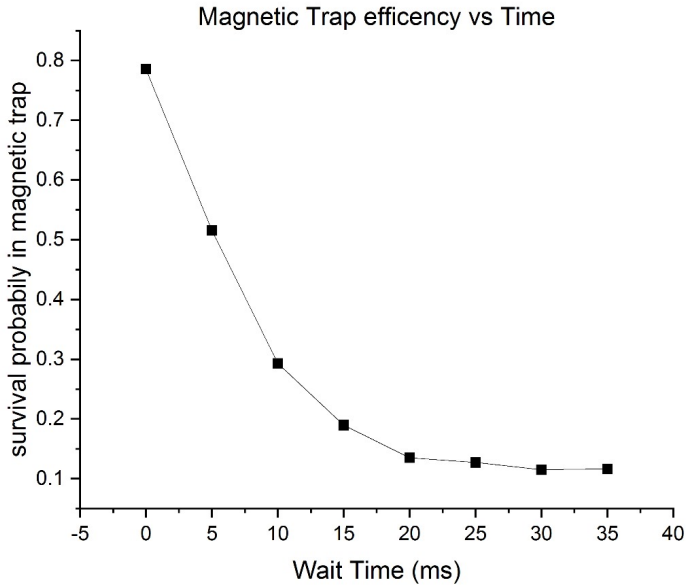


Figure 4.9: Magnetic trap efficiency vs. wait time on a short timescale (up to 40 ms).

A similar experiment was performed for longer timescales (up to 16 seconds). The transfer efficiency of atoms into the magnetic trap was measured as a function of hold time. The results,

shown in Figure 4.10, indicate a gradual decay in the number of trapped atoms, with efficiency decreasing by orders of magnitude over the duration. To visualise atom loss over time, fluorescence

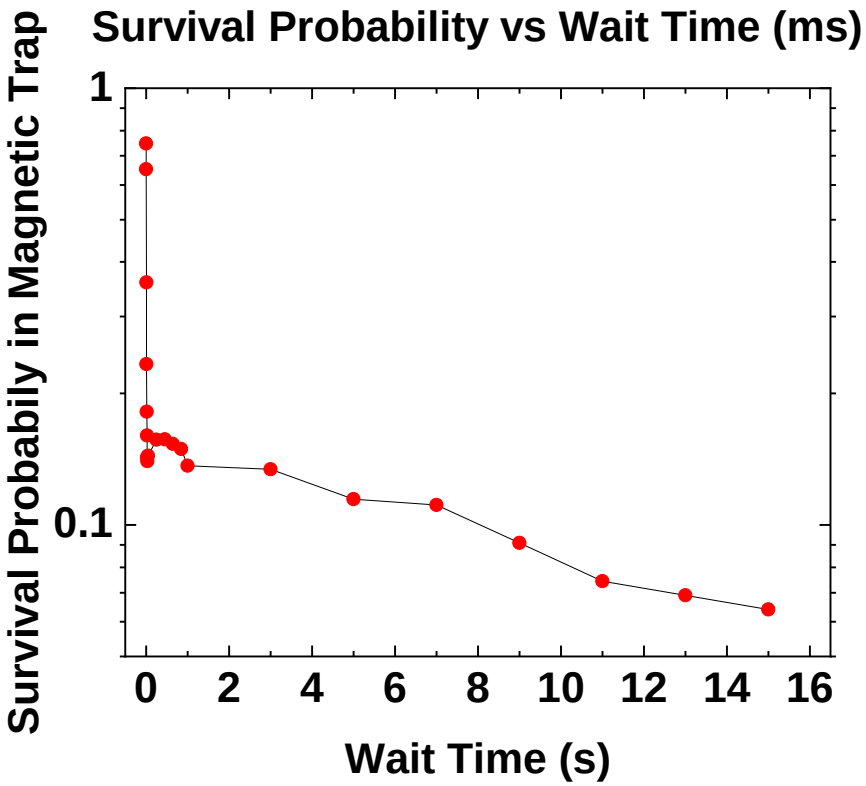


Figure 4.10: Magnetic trap efficiency vs. hold time on a long timescale (up to 16 seconds).

images of the trapped atoms were recorded at different wait times after the magnetic field was turned on. Representative images are shown in Figure 4.11, where decreasing fluorescence clearly illustrates the loss of atoms over time. The fluorescence counts were monitored continuously to analyse the behaviour of atoms during the magnetic trapping process. The experimental sequence and corresponding fluorescence data are shown in Figure 4.12.

The sequence of the magnetic trapping experiment is as follows. Initially, both the 2D and 3D molasses beams were kept on while the magnetic quadrupole field was off. This provided a background fluorescence signal (referred to as Background 1). Subsequently, the 3D MOT magnetic quadrupole field was switched on, allowing the capture of sodium atoms and resulting in a significant increase in fluorescence as atoms were trapped in the MOT. Following this, the 2D molasses beams and the 3D molasses beams were switched off, leaving only the magnetic quadrupole field active. The 3D molasses beams were shone for a brief time again to detect

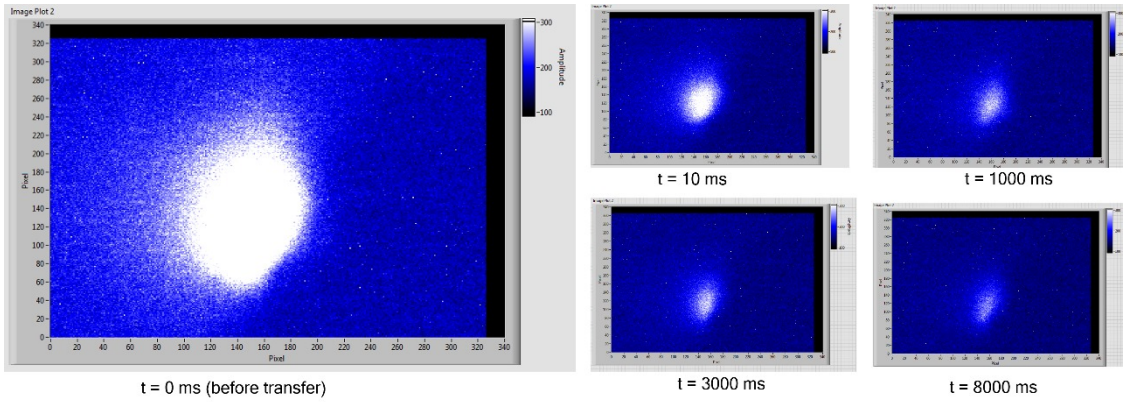


Figure 4.11: Fluorescence images of trapped atoms at various times after loading: (left) before transfer, (right) 10 ms, 1 s, 3 s, and 8 s. The gradual decrease in fluorescence indicates a loss of atoms over time.

the atoms confined in the magnetic potential, providing the fluorescence signal associated with magnetically trapped atoms. After this detection, all fields and beams were turned off to obtain a clean background fluorescence measurement, free from any contribution from trapped atoms. This is referred to as Background 2. Finally, the magnetic quadrupole field was maintained for various durations to observe atoms held purely by magnetic confinement, and the atoms were subsequently probed to measure their survival rates. The transfer efficiency into the magnetic trap was determined by comparing the fluorescence signal from the 3D MOT (after subtracting Background 1) with the fluorescence from the magnetic trap (after subtracting Background 2). The **transfer efficiency** from the MOT to the magnetic trap is calculated as:

$$\text{Transfer Efficiency} = \frac{\text{(3D MOT fluorescence - Background 1)}}{\text{(Magnetic trap fluorescence - Background 2)}} \tag{4.9}$$

This ratio provides a measure of the fraction of atoms successfully transferred into the magnetic trap, corrected for respective background levels.

4.4.1 Motivation for Sub-Doppler Cooling

The motivation for performing this magnetic trapping experiment was to characterise the performance of our current transfer process prior to implementing sub-Doppler cooling techniques. The results clearly show significant atom loss during magnetic trapping, both on short and long timescales. These losses are largely attributable to the relatively high temperatures of the atoms

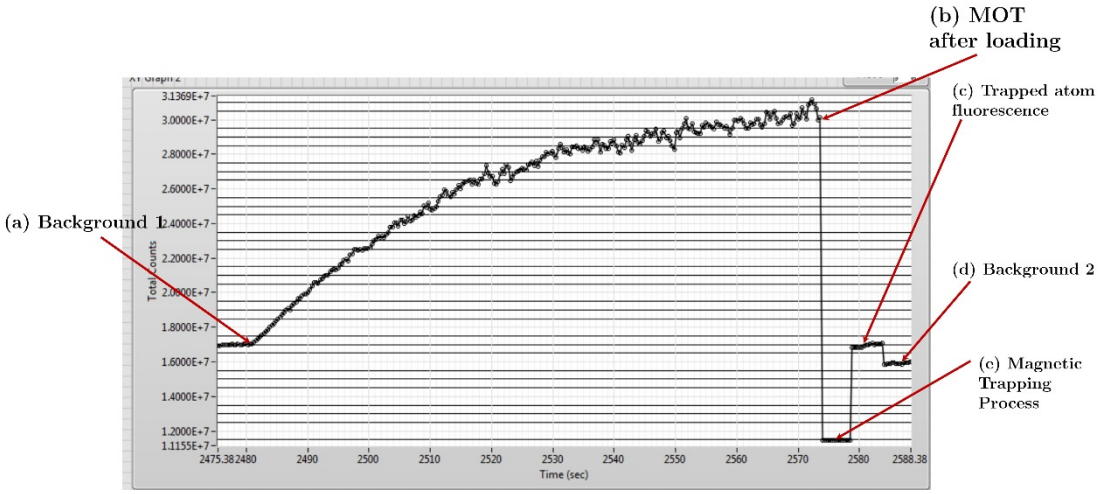


Figure 4.12: Photon counts during various stages of the magnetic trapping experiment: (a) background with 2D and 3D molasses beams on, (b) 3D MOT loading phase, (c) fluorescence from atoms trapped in the magnetic field, (d) background with all beams off, (e) magnetic trapping process.

after 3D MOT loading, which result in rapid escape from the shallow magnetic potential.

In the next stage of the experiment, we employ sub-Doppler cooling methods to further reduce the atomic temperature before transferring the atoms into the magnetic trap. This is expected to drastically improve the loading efficiency and the subsequent lifetime of the trapped atoms, as colder atoms will have lower kinetic energy and remain confined for significantly longer durations.

4.5 Inter-species Interactions

Inter-species cold collisions between spatially overlapping sodium and potassium atomic clouds are a critical consideration in the design and optimisation of dual-species experiments. These interactions can lead to significant atom loss, affecting the efficiency and stability of magnetic and optical trapping schemes. In this study, potassium atoms serve as a bath species, and their influence on sodium atom retention is systematically explored.

4.5.1 Heteronuclear Collisions in a Dual-Species Na–K 3DMOT

In a dual-species three-dimensional magneto-optical trap (3DMOT), inelastic collisions between atoms of different species produce significant interspecies losses [136–138]. In a single-species

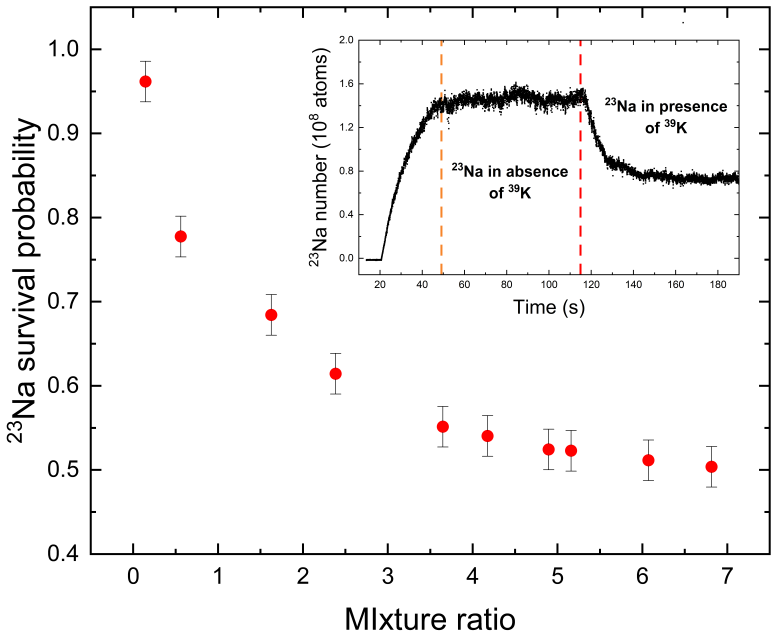


Figure 4.13: ^{23}Na survival probability as a function of the mixture ratio (ratio of ^{39}K atoms to ^{23}Na atoms). A pronounced reduction in sodium survival is observed with increasing potassium atom number, indicating significant inter-species collisional losses. Inset: Loading dynamics of ^{23}Na atoms in the absence and presence of ^{39}K atoms.

sodium 3DMOT, a hyperfine-exchange collision (HCC) [139–141] imparts an increment of approximately 5.5 m/s to each sodium atom's velocity. In a spatially overlapped Na–K 3DMOT, the lighter sodium atoms receive a larger velocity kick of about 6.3 m/s [139], which enhances sodium losses from a shallow trap. Light-assisted collisions represent another important interspecies loss channel. The dominant contribution arises from collisions in which one atom is in the ground state and the other is excited; such ground–excited collisions lead to radiative escape (RE) and fine-structure changing (FSC) processes [141, 142]. Unlike the homonuclear case, where the ground–excited interaction potential scales as $1/R^3$, the heteronuclear ground–excited interaction scales as $1/R^6$. Thus, atoms must approach more closely before RE or FSC occurs. For sodium atoms in a MOT of trap depth $\sim$ 2 K, RE occurs at interatomic separations of about 50 Å, while in Na–K collisions the equivalent distance is only $\sim$ 20 Å [139]. Consequently, light-assisted loss in heteronuclear collisions [136, 137] takes place at shorter distances, and the loss rate is typically smaller than in the homonuclear case.

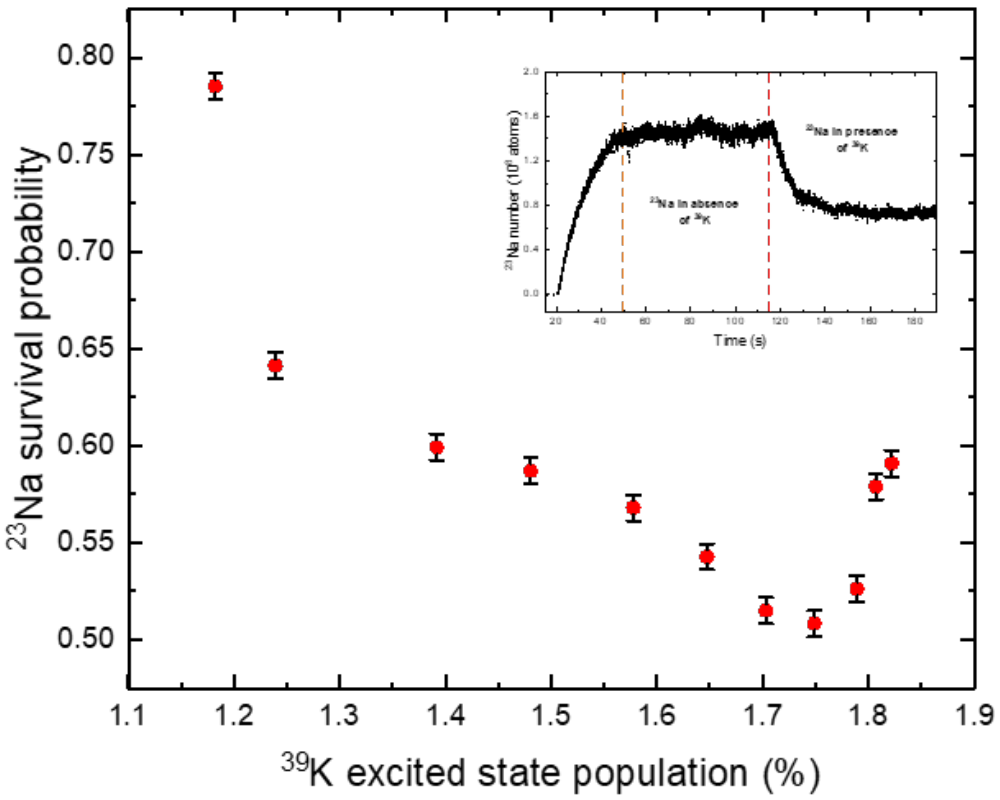


Figure 4.14: Caption

To quantify interspecies losses, we measured the loading dynamics of a sodium MOT in the presence of a potassium MOT. The sodium loading dynamics, including heteronuclear collisions [140]can be written as

$$\frac{dN_{\mathrm{Na}}}{dt} = L_{\mathrm{Na}} - \gamma N_{\mathrm{Na}} - \beta_{\mathrm{NaNa}} \int n_{\mathrm{Na}}^2(\mathbf{r})\, d^3r - \beta_{\mathrm{NaK}} \int n_{\mathrm{Na}}(\mathbf{r})\, n_{\mathrm{K}}(\mathbf{r})\, d^3r, \tag{4.10}$$

where L_{Na} is the sodium loading rate, γ the one-body loss rate, and β_{NaNa} and β_{NaK} the intra- and interspecies two-body loss coefficients. The spatial densities of sodium and potassium are denoted n_{Na} and n_{K}.

For typical alkali MOTs operating in the constant-density regime ($N \gtrsim 10^5$ [122, 143]), the

trapped atom density is well described by a Gaussian distribution,

$$n_{\mathrm{Na}}(\mathbf{r},t) = n_{\mathrm{Na},0}(t)\ \exp\left[-\frac{2r^2}{w_{\mathrm{Na}}^2}\right], \tag{4.11}$$

$$n_{\mathrm{K}}(\mathbf{r},t) = n_{\mathrm{K},0}(t)\ \exp\left[-\frac{2r^2}{w_{\mathrm{K}}^2}\right], \tag{4.12}$$

where w_{Na} and w_{K} are the $1/e^2$ radii of the respective MOTs. Substituting these profiles into the rate equation yields

$$\frac{dN_{\mathrm{Na}}}{dt} = L_{\mathrm{Na}} - \left(\gamma + \beta_{\mathrm{NaK}}\frac{N_{\mathrm{K}}}{\left[2\pi(w_{\mathrm{Na}}^2 + w_{\mathrm{K}}^2)\right]^{3/2}}\right)N_{\mathrm{Na}} - \beta_{\mathrm{NaNa}}\left(\frac{1}{\pi w_{\mathrm{Na}}^2}\right)^{3/2} N_{\mathrm{Na}}^2. \tag{4.13}$$

In steady state, we compare sodium atom numbers in the presence (N_{Na}^0) and absence (N_{Na}) of the potassium MOT. Defining the sodium cloud sizes as w_{Na}^0 (with potassium present) and w_{Na} (without potassium), the interspecies collisional loss coefficient is obtained as

$$\beta_{\mathrm{NaK}} = \frac{\pi^{3/2}(w_{\mathrm{Na}}^{0\,2} + w_{\mathrm{K}}^2)^{3/2}}{N_{\mathrm{K}}N_{\mathrm{Na}}^0}\left[\gamma\left(N_{\mathrm{Na}} - N_{\mathrm{Na}}^0\right) + \beta_{\mathrm{NaNa}}\left(\left(\frac{1}{\pi w_{\mathrm{Na}}^2}\right)^{3/2} N_{\mathrm{Na}} - \left(\frac{1}{\pi (w_{\mathrm{Na}}^0)^2}\right)^{3/2} N_{\mathrm{Na}}^0\right)\right]. \tag{4.14}$$

Using this procedure we obtained $\beta_{\mathrm{NaK}} \approx 2\times10^{-12}\ \mathrm{cm}^3/\mathrm{s}$ for our typical MOT parameters.

To study the dependence on potassium loading, we defined the sodium "survival probability" as $N_{\mathrm{Na}}^0/N_{\mathrm{Na}}$ and the "mixture ratio" as $N_{\mathrm{K}}/N_{\mathrm{Na}}$. Experimentally, the sodium survival probability decreases monotonically with mixture ratio and saturates beyond a ratio of about 5. This saturation occurs because the potassium MOT enters the constant-density regime; therefore, further increases in atom number expand the cloud size without increasing the density. Consequently, each sodium atom interacts with approximately the same average number of potassium atoms.

We also studied the effect of the potassium excited-state fraction. The dominant heteronuclear loss channels are Na–K* and Na*–K. For Na(3s)–K*(4p) collisions the potential curves are attractive, while for Na*(3p)–K(4s) many are repulsive [138]. Increasing the potassium excited fraction, therefore, increases Na–K* loss and reduces sodium survival. We measured the excited-state fraction by probe absorption and varied it by adjusting the K-MOT repumper intensity. The sodium

survival probability decreased with excited-state fraction up to about 1.75%, after which survival increased again. This non-monotonic behaviour arises because for higher excited fractions, homonuclear K–K* collisions dominate. Since these are governed by longer-range $1/R^3$ potentials, they reduce potassium central density and thereby lessen the interspecies loss experienced by sodium.

Finally, we verified the role of potassium excited-state fraction using an optical pumping sequence. A first probe pulse was sent through the K-MOT and detected on a fast photodiode. Then, by extinguishing the cooling light and applying the repumper for $\sim$ 50 μs, atoms were pumped from the $^2S_{1/2}, F = 1$ to the $^2S_{1/2}, F = 2$ state. A second probe pulse applied after $\sim$ 100 μs showed increased absorption, with the change in transmission ΔV proportional to the number of atoms shelved into $F = 2$. This confirmed that the excited-state population correlates directly with the observed sodium survival behaviour.

As illustrated in Fig. 4.13, the survival probability of sodium atoms exhibits a clear dependence on the mixture ratio, defined as the ratio of potassium atoms to sodium atoms in the trap. Specifically, nearly 50% of the trapped sodium atoms are lost as the potassium atom number increases, highlighting the strong inter-species interaction dynamics present in this system.

The inset of Fig. 4.13 provides further insight into the inter-species influence on loading dynamics. It compares the typical loading behaviour of sodium atoms in the absence and presence of potassium. Notably, the presence of potassium alters the steady-state sodium atom number, consistent with increased inelastic collision rates due to overlapping clouds. This observation underscores the necessity of careful density and timing control during dual-species MOT and magnetic trap operation.

4.6 Summary and Outlook

These losses primarily originate from light-assisted cold collisions, where the presence of near-resonant optical fields promotes transient molecular state formation between sodium and potassium atoms [120, 144, 145]. Subsequent spontaneous decay processes release kinetic energy, frequently ejecting atoms from the relatively shallow trapping potentials. Such light-assisted collisions are well-documented in alkali mixtures and have been extensively studied in systems such as Rb–Cs and Rb–K [146, 147]. In addition, density-dependent spin-exchange collisions can contribute

to these losses, especially under conditions of high density and low temperature [148]. These hyperfine-changing collisions lead to atoms being transferred into untrapped magnetic sub-levels, further reducing the sodium atom population.

Beyond their immediate experimental impact, such inter-species interactions are of fundamental importance to a broad range of quantum technology applications, including quantum metrology [149], quantum simulation, and quantum sensing [148, 150]. Understanding and controlling these collisional processes is essential for achieving high phase-space densities and eventual quantum degeneracy in multi-species mixtures. In particular, these results motivate the implementation of sub-Doppler cooling techniques in the subsequent experimental stages [145, 147]. Lower temperatures not only suppress inelastic collisional rates by reducing kinetic energy but also enable tighter confinement and more efficient transfer into magnetic or optical dipole traps.

The findings presented here provide a baseline characterisation of sodium–potassium interactions under MOT conditions. Future work will focus on quantifying the inter-species spin-exchange collision rates through Raman-driven spin noise spectroscopy (RDSNS) and exploring strategies for mitigating these losses, such as species-selective optical potentials or the use of tailored magnetic field gradients [151]. These efforts aim to pave the way toward stable and long-lived dual-species quantum gas platforms.

"Thus, the task is, not so much to see what no one has yet seen; but to think what nobody has yet thought, about that which everybody sees."

— Erwin Schrödinger

Chapter 5

Real-Time Local Density Probe for Cold Atoms Utilising Raman-Driven Spin Noise Spectroscopy

This chapter is based on the following publication:

Real-Time Local Density Probe for Cold Atoms Utilising-Raman Driven Spin Noise Spectroscopy, **Sayari Majumder**, Bhagyashri Deepak Bidwai, Bernadette Varsha FJ, Saptarishi Chaudhuri, *Applied Physics Letters*, **127**(3), July 21, 2025.
doi:10.1063/5.0277027

In this chapter, I present the development of a minimally perturbative detection method for cold atoms. This work builds upon the results published in [57] and expands on the motivation, methodology, and implications of the technique within the broader context of cold atom experiments. This chapter demonstrates a method – Raman-driven spin noise spectroscopy

(RDSNS) – to directly probe the local density of a cloud of cold ^{39}K atoms in real time. This relies on the principle of spin noise spectroscopy, where random spin fluctuations couple to the probe polarisation via the Faraday effect. By introducing Raman coupling between Zeeman states, we enhance the signal to make it measurable. This is an easily implementable scheme with a wide-ranging applicability in detecting cold atoms. Conventional imaging techniques such as absorption and fluorescence imaging have proven to be powerful, but they are inherently perturbative. In particular, these detection schemes are limited by the number of atoms being probed and the detection speed for tracking fast dynamics. These limitations motivate the search for minimally destructive, fast detection methods. Hence, this chapter introduces Raman-driven spin noise spectroscopy (RDSNS) as one such approach. The data can be collected at a MHz refresh rate, allowing for near real-time detection. We validated this technique by monitoring the strength of the RDSNS signal upon varying the key parameters of the 3D magneto-optical trap (MOT) and the cold atom source ($2D^+$ MOT). In order to benchmark our results, we obtained the density profiles from a fluorescence image of a spherically symmetric atomic cloud, reconstructed using an inverse Abel transformation. The two approaches showed excellent agreement, thereby validating the reliability of RDSNS as a minimally perturbative detection method. A significant advantage of this protocol is that it remains applicable to systems without inherent symmetry, for which Abel transformation techniques fail. Furthermore, due to its fast detection time, RDSNS enables real-time monitoring of cold-atom systems, thereby making it a versatile tool for studying dynamical properties like density ripples, expanding clouds, and spin-spin interactions.

5.1 Introduction

Optical detection techniques are a cornerstone of cold atom experiments. They provide a means to measure properties such as density, temperature, and internal state populations, and are essential for both diagnostics and precision measurements [152]. Before describing the method and its results, I begin with a detailed overview of conventional optical detection techniques and their limitations, which motivate the need for new approaches. Conventional imaging methods include absorption imaging[153–155], fluorescence imaging[156, 157], and phase-contrast imaging[158, 159]. In absorption imaging, a resonant probe beam is sent through the atomic cloud and the

attenuation of the beam intensity is recorded on a CCD camera. The transmitted intensity I_t after passing through a column of atoms along the z-direction is related to the incident intensity I_0 via the Beer–Lambert law [160]:

$$I_t(x, y) = I_0(x, y) \exp\left[-\sigma_0 \int n(x, y, z)\, dz\right], \tag{5.1}$$

where σ_0 is the resonant scattering cross section and $n(x, y, z)$ is the atomic number density. The optical density (OD) is then defined as:

$$\mathrm{OD}(x, y) = \ln\left[\frac{I_0(x, y)}{I_t(x, y)}\right]. \tag{5.2}$$

From the OD image, the column density $\tilde{n}(x, y) = \int n(x, y, z)\, dz$ can be inferred. However, in optically thick clouds, the probe beam is strongly attenuated, leading to saturation of the measured OD and underestimation of the true density. This is one such limitation of this technique.

In fluorescence imaging, atoms are illuminated by near-resonant light, and the scattered photons are collected by an imaging system. The number of detected photons per unit time is proportional to the scattering rate Γ_{sc}:

$$\Gamma_{\mathrm{sc}} = \frac{\Gamma}{2} \frac{I/I_{\mathrm{sat}}}{1 + I/I_{\mathrm{sat}} + 4\Delta^2/\Gamma^2}, \tag{5.3}$$

where Γ is the natural linewidth, I is the probe intensity, I_{sat} is the saturation intensity, and Δ is the detuning from resonance. The total signal depends on the solid angle of collection and the quantum efficiency of the camera. Multiple scattering and reabsorption of fluorescence photons can distort the measured spatial profile of the cloud. Imaging methods, including absorption and fluorescence, which uses an on-resonant probe light; depend on parameters such as photon scattering rate, total number of atoms, profile of the probe light, exposure time[161], and quantum efficiency of the camera for a superior signal-to-noise ratio (SNR). Probing a small number of atoms is a challenge, as long exposure time prevents the fast study of dynamical properties. Any measurement performed on an ultracold sample inevitably disturbs it. In minimally destructive imaging techniques, there is always a balance between the signal-to-noise ratio (SNR) and the strength of perturbation. Moreover, in absorption imaging, optically thick clouds cannot be reliably imaged- because of the attenuation of the probe beam intensity, thereby causing inaccuracies in measuring atom

number and structural information. On the other hand, in fluorescence imaging, the image is constructed by collecting the scattered photons from the atomic cloud, where parameters such as photon re-scattering, solid angle corrections, and long exposure times can cause inaccuracies in the measurement. To overcome these problems, methods such as phase-contrast imaging (PCI) [162] and partial transfer absorption imaging (PTAI) have been utilized [163].

PCI is a dispersive imaging method in which an off-resonant probe beam acquires a spatially varying phase shift due to the refractive index of the atomic cloud. A phase plate in the Fourier plane converts this phase modulation into an intensity modulation detectable on a camera. The phase shift is proportional to the column density, but also depends on probe detuning. Increasing detuning reduces absorption (hence less perturbation), but also reduces phase shift and SNR. PTAI attempts to address some of these issues by transferring a fraction of atoms to an auxiliary state and imaging them, but it still involves a compromise between SNR and absorption.

The above methods rely on photon scattering from the atoms, which inevitably perturbs the system. The strength of perturbation is set by the number of scattered photons, which also determines the SNR. Minimally destructive imaging techniques must strike a balance between achieving sufficient SNR and minimizing scattering-induced heating or decoherence.

5.1.1 Need for Fast, Local, Minimally Invasive Probes

Many phenomena in cold atom systems occur on fast time scales and involve spatially localized dynamics, such as thermalization, transport, shock waves, soliton formation, and spin-exchange interactions. For example, inter-species spin-exchange collisions [164], shock wave propagation [165], and charge density wave formation [166] involve rapid spatial density variations that are difficult to capture with conventional imaging techniques.

To study such processes, one requires a detection method that is **local** (sensitive to density in a small volume), is **fast** [167] (MHz refresh rate or higher) and is **minimally perturbative** (negligible heating or decoherence).This has applications in various fields such as cold-atom experiments [47, 74, 168, 169], Quantum Optics [170], and Quantum Sensing [171, 172] etc. Optical measurements that utilize dispersive light-matter interactions, such as detecting the Faraday [173] or Kerr [174] rotation of an off-resonant probe beam, are examples of methods that cause minimal disturbance to the sample being probed.

5.1.2 Raman-Driven Spin Noise Spectroscopy (RDSNS) as a Technique

Spin Noise Spectroscopy (SNS) [175–178] is a non-destructive measurement technique that probes the intrinsic temporal fluctuations of the collective spin of an atomic ensemble. A linearly polarized probe beam, far detuned from any optical transition, passes through the sample. Fluctuations of the atomic spin projection along the probe direction induce small Faraday rotation fluctuations of the probe polarization. These are detected using a balanced polarimeter and analyzed in the frequency domain. The SNS signal is proportional to the spin fluctuation spectrum and scales with the local atomic density within the probe volume. Since the probe is off-resonant, the measurement induces negligible spontaneous emission, making it suitable for continuous, minimally invasive monitoring. In this work, I employ an extension of SNS known as Raman-driven spin noise spectroscopy (RDSNS) [74]. In RDSNS, along with the off-resonant probe, two coherent Raman beams are applied to resonantly couple adjacent Zeeman sublevels within the ground hyperfine manifold. This coherent drive enhances the spin fluctuations at the Raman frequency and generates a strong spin noise signal at that frequency. The presence of the Raman drive increases the signal-to-noise ratio by several orders of magnitude (up to 10^6) compared to intrinsic SNS, enabling real-time detection with high spatial resolution. Importantly, the RDSNS signal is proportional to the local density in the probe volume, not the total atom number. As a result, it is well suited for probing spatially inhomogeneous systems, including those without spherical symmetry where inverse Abel transformation of fluorescence images is not applicable. It exploits the intrinsic spin fluctuations of the atoms as well as an induced two-photon coherent drive to detect the cold atom density in real time. Therefore, it is not limited to the total number of atoms, probe beam intensity attenuation, solid angle considerations, heating effects on the cloud, exposure time, and scattering effects.

Real-time local density measurements are important in studying a wide range of phenomena in cold atomic systems, such as non-equilibrium dynamics, thermalization processes, and transport phenomena. In particular, it enables precise studies of spatially dependent interactions, coherence properties, and density-dependent effects like collisional shifts or optical depth variation. Furthermore, in experiments involving quantum gases out of equilibrium, or those exploring localized phenomena (e.g., shock waves, solitons, or density ripples), temporally resolved spatial density information is vital for unraveling the underlying physics. For example, inter-species spin-exchange

collisions [164], shock wave propagation in atomic media [165], and charge density wave formation [166] etc, which involves detection of rapid spatial density variations that are obscured in traditional imaging techniques. In the next sections, I describe the experimental implementation of RDSNS, present measurements of local density profiles, and compare them to conventional fluorescence imaging with inverse Abel reconstruction for spherically symmetric clouds. The excellent agreement between the two validates RDSNS as a reliable, minimally invasive tool for cold atom density measurements. Moreover, the high temporal resolution of the technique opens the door to studying a wide range of dynamical phenomena in cold atomic ensembles.

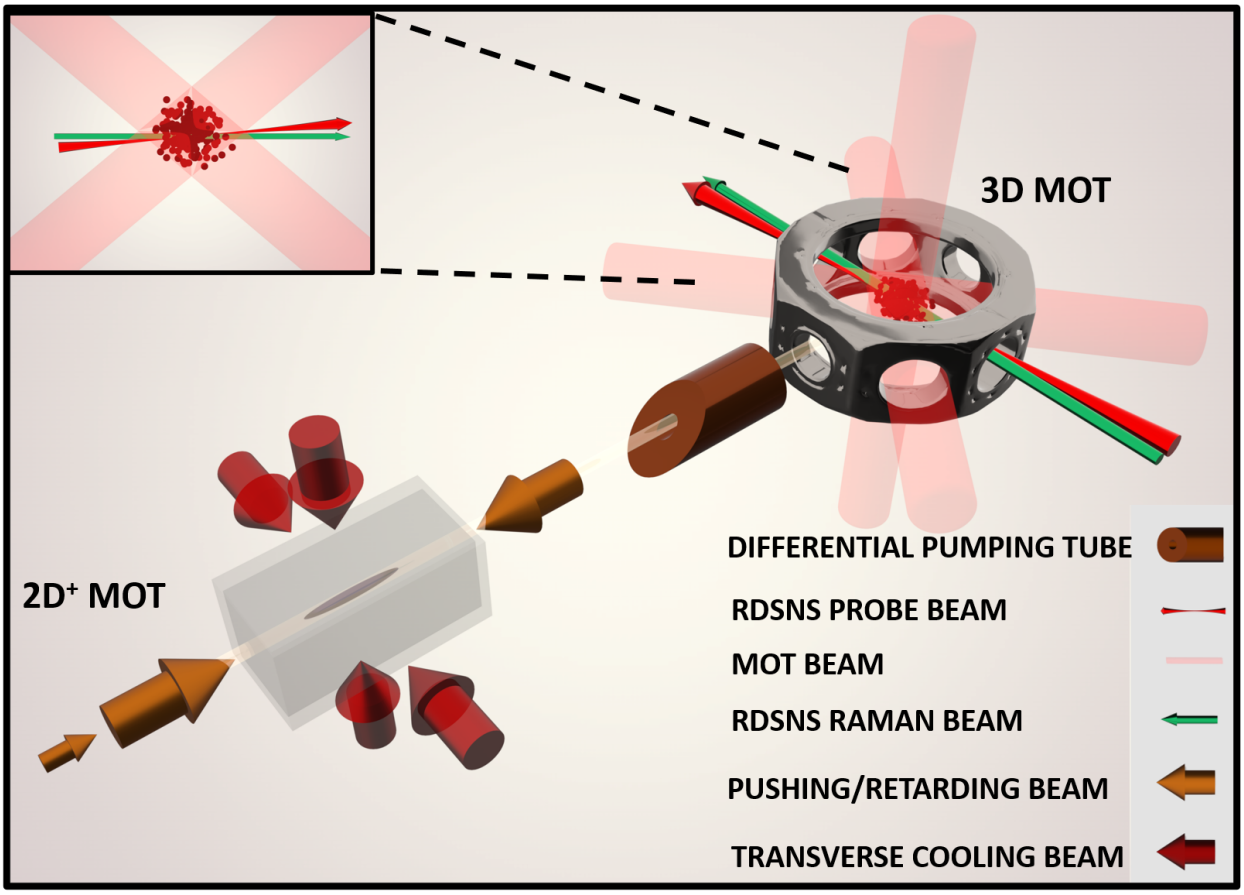


Figure 5.1: Schematic of the experimental setup. A $2D^+$ MOT is used as a bright source of cold atoms directed towards the $3D$ MOT. Probe beam (red) and Raman beam (green) intersecting at the $3D$ MOT is shown in the zoomed picture (top left).

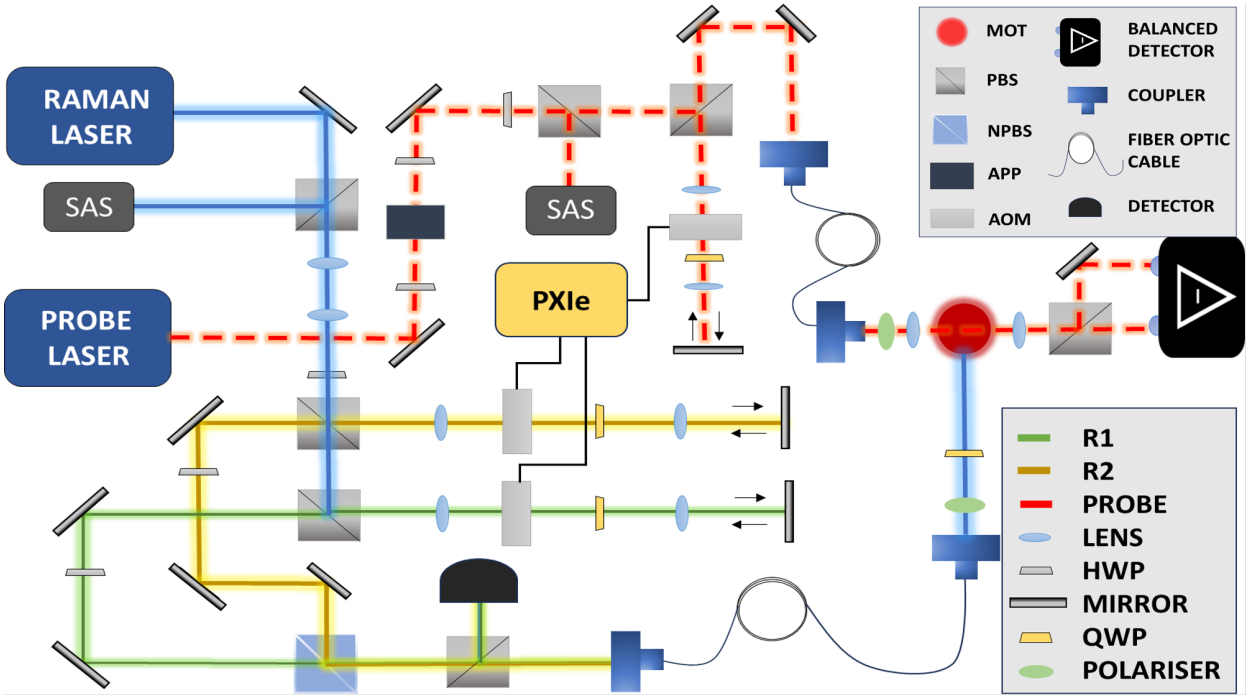
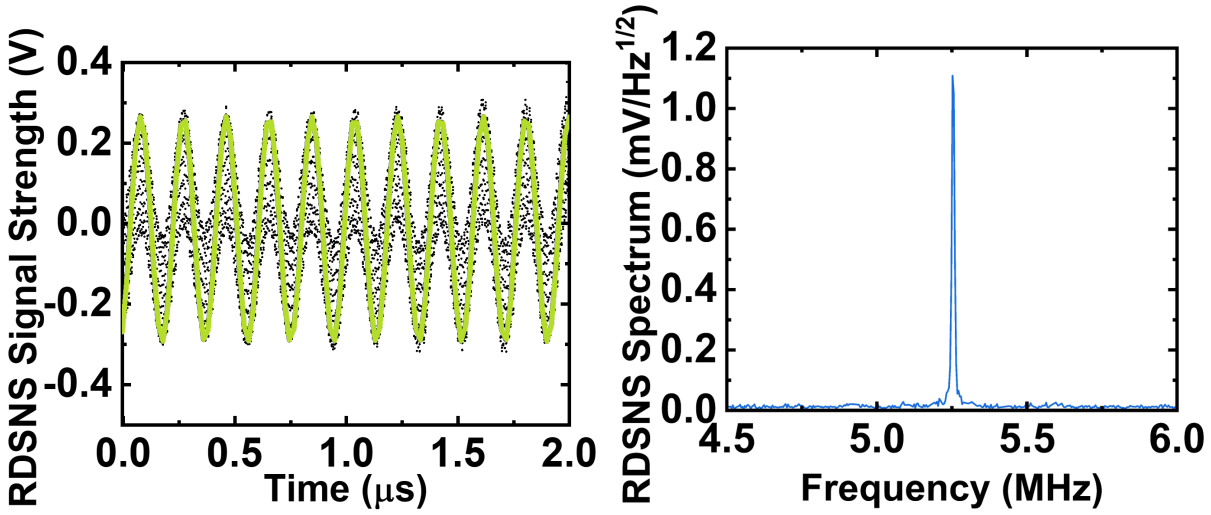


Figure 5.2: Optical circuit and detection setup showing Raman laser light, the Saturation Absorption Spectroscopy (SAS) set up, AOMs, control hardware NI PXIe, the probe beam, and the polarimetric set-up.

5.2 Experimental Setup

The experiment was performed in a cloud of laser-cooled ^{39}K atoms. The experimental procedure involves a two-dimensional Magneto-Optical Trap ($2D^+$ MOT) which acts as a high-flux source of pre-cooled atoms. These cold atoms were directed towards the three-dimensional ($3D$) MOT using a pushing laser beam passing through a differential pumping tube. Details of the experimental setup for the cold atom and its characterization are presented in our previous work [74] and has been described in detail in chapter 4. A schematic of the experimental system used in this work is presented in fig. 5.1. The schematic of the optical layout are shown in fig. 5.2 respectively. The key parameters of the $3D$ MOT and the atomic source are discussed as follows.

We used an External Cavity Diode Laser (ECDL) (Toptica Photonics, DL pro, 767 nm) as the probe beam, blue detuned 140 MHz from the $^2S_{1/2}\ F = 2$ to $^2P_{3/2}\ F' = 2$ transition of ^{39}K, with the help of an Acousto-Optic Modulator (AOM) in double-pass configuration [MT80-B30A1-IR, AA Optics]. The fiber-coupled probe light was focused onto the atoms by a $f = 500$ mm lens, resulting in a waist (Rayleigh range) of 38 μm (2.9 mm). A linear polarizer (LPVIS, Thorlabs) ensured



(a) (b)

Figure 5.3: Raman-Driven Spin Noise Spectroscopy (RDSNS) signals observed in (a) the time domain using an oscilloscope, showing the oscillatory spin noise, and (b) the frequency domain using a spectrum analyzer, highlighting the corresponding spectral features.

$>$ 99.99% probe polarization purity. Additionally, we employed another ECDL to generate a pair of Raman beams 64 MHz red detuned from the $^2S_{1/2}$ $F = 1$ to $^2P_{3/2}$ $F' = 2$ transition. The relative frequency difference (δ_{12}) between the Raman beams were tuned by another set of AOMs. The two beams were merged and fiber-coupled to the same polarisation-maintaining optical fiber. The ouput of the fiber was shone on the cold atom cloud. The δ_{12} was monitored by a Beat Detection Unit (BDU) using a fast photo-detector (DET36A, Thorlabs). The polarisation of the two Raman beams were made $\sigma^+ - \sigma^+$ ($>$ 99.99% purity). The collimated Raman beams and focused probe beam were merged (with a small angle, 1^o) at the cloud center. The transmitted probe beam was re-collimated into the polarimetric setup which consisted of a Polarizing beam splitter [PBS122] and a 100 MHz low-noise Balanced Detector [PDB230A, Thorlabs]. Great care was taken to ensure that no part of the Raman beam fell on the detector. The output of the difference signal from the detector is fed to a low-noise +32 dB amplifier (MAN-1LN from Mini-Circuits), which helps us to detect the signal using an oscilloscope (MSO4034, 350 MHz, 2.5 GS/s). The frequency domain signal is seen using a spectrum analyzer (N1996A, Keysight).

Parameter	Optimized Value of Parameters	Scan Range
$2D$ Cooling Detuning	-5.35 Γ	-3.8 Γ to -7.4 Γ
$2D$ Cooling Intensity	15 I_{sat}	4 I_{sat} to 15 I_{sat}
$2D$ Repump Detuning	-1.17 Γ	-3 Γ to +1 Γ
$2D$ MOT Field Gradient	0.7 G/cm	0 to 1 G/cm
$3D$ Cooling Detuning	-7.8 Γ	-5.5 Γ to -10 Γ
$3D$ Cooling Intensity	10.2 I_{sat}	2.7 I_{sat} to 10.5 I_{sat}
$3D$ Repump Detuning	-0.25 Γ	-1 Γ to 0.8 Γ
$3D$ Repump Intensity	5.5 I_{sat}	1.2 I_{sat} to 5.5 I_{sat}

Table 5.1: The table presents optimized $2D$ ($3D$) cooling detuning and intensity values for the $F = 2 \rightarrow F'$ transition of the D_2 line of ^{39}K atoms, along with the repump detuning and intensity parameters corresponding to the $F = 1 \rightarrow F'$ transition.

5.3 Theoretical Description

The efficiency of atom capture in a MOT is governed by a competition between loading from the atomic source and various loss processes. A quantitative understanding of these processes is essential for optimizing the experimental parameters that determine the steady-state atom number and density. In our experiment, the atoms are subsequently directed from the $2D^+$ MOT into a $3D$ MOT, where they are captured and further cooled. The capture dynamics, addressing various loss processes, are described by the equation 5.4 shown below,

$$\frac{dN}{dt} = L - \alpha N - \beta N^2 - \gamma N^3 \tag{5.4}$$

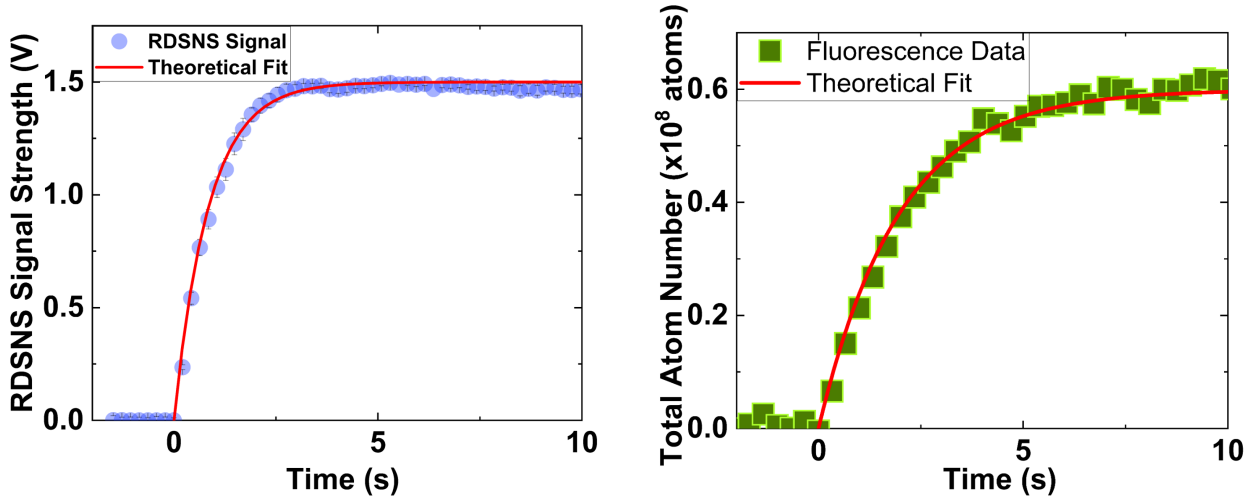
where, L denotes the loading rate, α, β and γ are related to the losses due to collisions with background gas (linear loss), two-body loss — typically from light-assisted collisions (depends on density) and three-body loss respectively.

In our experiment, we optimized the quantities α, β, and γ, as defined in Eq 5.4, by varying several key experimental variables. These included the $2D$ cooling detuning, $2D$ cooling intensity, $2D$ repump detuning, $2D$ MOT field gradient, $3D$ cooling detuning, $3D$ cooling intensity, and $3D$ repump intensity and detuning. The optimized values and their respective scanning ranges are provided in table 5.1.

To probe the spin coherence of the trapped atoms, we measured the Faraday rotation fluctuation $\langle \delta\theta_F{}^2 \rangle^{1/2}$ of the linearly polarized probe, directly giving a two-time correlation of coherence: $\langle \rho_{21}^{\dagger}(t)\rho_{21}(0)\rangle$. The RDSNS signal in the time domain is shown in Fig. 5.3a, where the oscilloscope trace exhibits the characteristic oscillatory spin-noise dynamics. The corresponding frequency-domain representation, obtained using a spectrum analyzer, is presented in Fig. 5.3b, which highlights the spectral features associated with these oscillations. The power spectrum is given by,

$$\begin{aligned} P(\omega) &= \frac{1}{2\pi}\int_{-\infty}^{\infty} e^{i\omega t}\langle \rho_{21}^{\dagger}(t)\rho_{21}(0)\rangle dt \\ &= \delta(\omega + \omega_2 - \omega_1)|\rho_{21}|^2 \end{aligned} \tag{5.5}$$

where ω_1 and ω_2 are the angular frequencies of Raman beams 1 (R_1) and 2 (R_2), respectively. The full power spectrum with an envelope of $|\rho_{21}|^2$ depends upon the spin coherence relaxation rate (γ') between the two Zeeman states, the excited state relaxation rate (γ) and Ω the Rabi frequencies of the Raman fields.



(a) (b)

Figure 5.4: MOT loading dynamics measured via RDSNS (a) and total fluorescence counts (b). The RDSNS signal (blue dots) reaches $1/e$ of its saturation density within $\tau \sim 0.85$ s, whereas the fluorescence signal (green squares) shows a slower loading time constant of $\tau \sim 1.96$ s.

The integrated spin noise signal (Σ) can be written as,

$$\Sigma = \frac{I}{\delta_p}\sqrt{\frac{n_o l}{A}}. \tag{5.6}$$

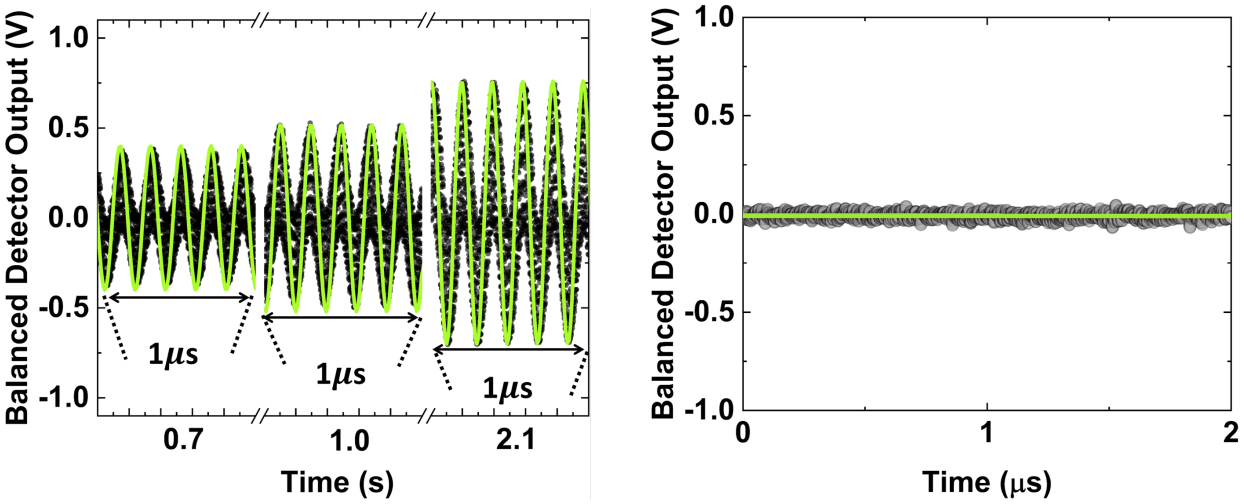
where I, δ_p, A, and l are the probe intensity, detuning, area and length of the probing region, respectively and n_o is the number density of atoms. More details regarding the theoretical description of both the intrinsic SNS and RDSNS signal has been provided in chapter 2. Since the envelope width is constant, the signal strength is directly proportional to $\sqrt{n_o}$. Both the SNS and the RDSNS signals follow this power-law-type plot as verified in our previous work [171]. Focusing the probe in a small region of interest (ROI) of area A, we ensured a larger signal strength. Maintaining a long Rayleigh range enables maximum overlap of the probe with the atom cloud. The major contribution to the RDSNS signal (fig. 5.1) is from the atoms at the focus of the probe, thereby revealing a spatial local density profile with minimal perturbation. Previously, Faraday rotation of a probe has been reported as a dispersive detection technique [47, 179]. The RDSNS signal strength increases with probe intensity. However, to maintain non-invasiveness, low power and large detuning are used to reduce scattering and absorption. This also ensures minimal loss of atoms from the cold atomic cloud. In our dynamic detection technique (RDSNS), signals can be recorded on a much faster ($\sim \mu s$) time scale.

5.4 Experimental Implementation

Having established the theoretical scaling of the RDSNS signal with probe parameters and atomic density, we now turn to its experimental implementation. In the following section, we present measurements of the temporal evolution of the signal during MOT loading and benchmark it against conventional fluorescence detection. This allows us to directly validate the sensitivity, non-invasiveness, and real-time capability of the RDSNS technique.

In Fig. 5.4a we demonstrate how the RDSNS signal evolves as the atom density increases after turning on the trapping field at $t = 0$. The corresponding total fluorescence signal is also shown in the Fig. 5.4b. As shown in Fig. 5.4a, we monitored the SN signal in real time as more atoms get captured in the MOT. A similar trend is observed in both the RDSNS and fluorescence plots. In this particular example, the RDSNS signal reaches $1/e$ of its maximum value within 0.85 s, compared to 1.96 s for the total fluorescence count.

Three representative time slices from this measurement are also shown in Fig. 5.5a. The strength of the signal is a direct measure of the square-root of the local density of atoms ($\sqrt{n_o}$). A reliable



(a) (b)

Figure 5.5: (a) RDSNS signals with atoms present and in the absence of atoms. It shows instantaneous signals at three time slices during loading, where black dots are the raw data and green curves are sinusoidal fits. (b) Illustrates the baseline RDSNS signal without atoms in the MOT.

measure of the local density, can be obtained by averaging over 256 cycles. Remarkably, even five cycles of the oscillatory RDSNS signal—corresponding to just 2 μs of acquisition time—yield density estimates with better than 5% accuracy. To the best of our knowledge, such a fast, real-time, local density measurement in cold atoms has not been reported earlier. We also did not observe any discernible atom loss from the trap during these measurements, confirming that the technique is fairly non-invasive. Finally, fig. 5.5b shows the RDSNS signal recorded in the absence of atoms in the MOT. In this case, the signal is dominated by photon shot noise and electronic noise. The entire RDSNS signal is captured from a probe volume of 0.01 mm^3, containing approximately 10^5 atoms.

Figure 5.6 shows the evolution of the central density and the total atom number after turning on the trapping fields at $t = 0$. The central density is extracted from the RDSNS signal, while the total atom number is obtained from the integrated fluorescence. Both quantities are plotted together for direct comparison. We observe that the central density reaches saturation much faster than the atom number [180]. The central density reaches $1/e$ of its maximum value within 1 s, whereas the fluorescence-derived atom number takes 1.96 s to reach the same fraction of its maximum value.

The faster saturation of the density is a well-known effect in magneto-optical traps, arising from

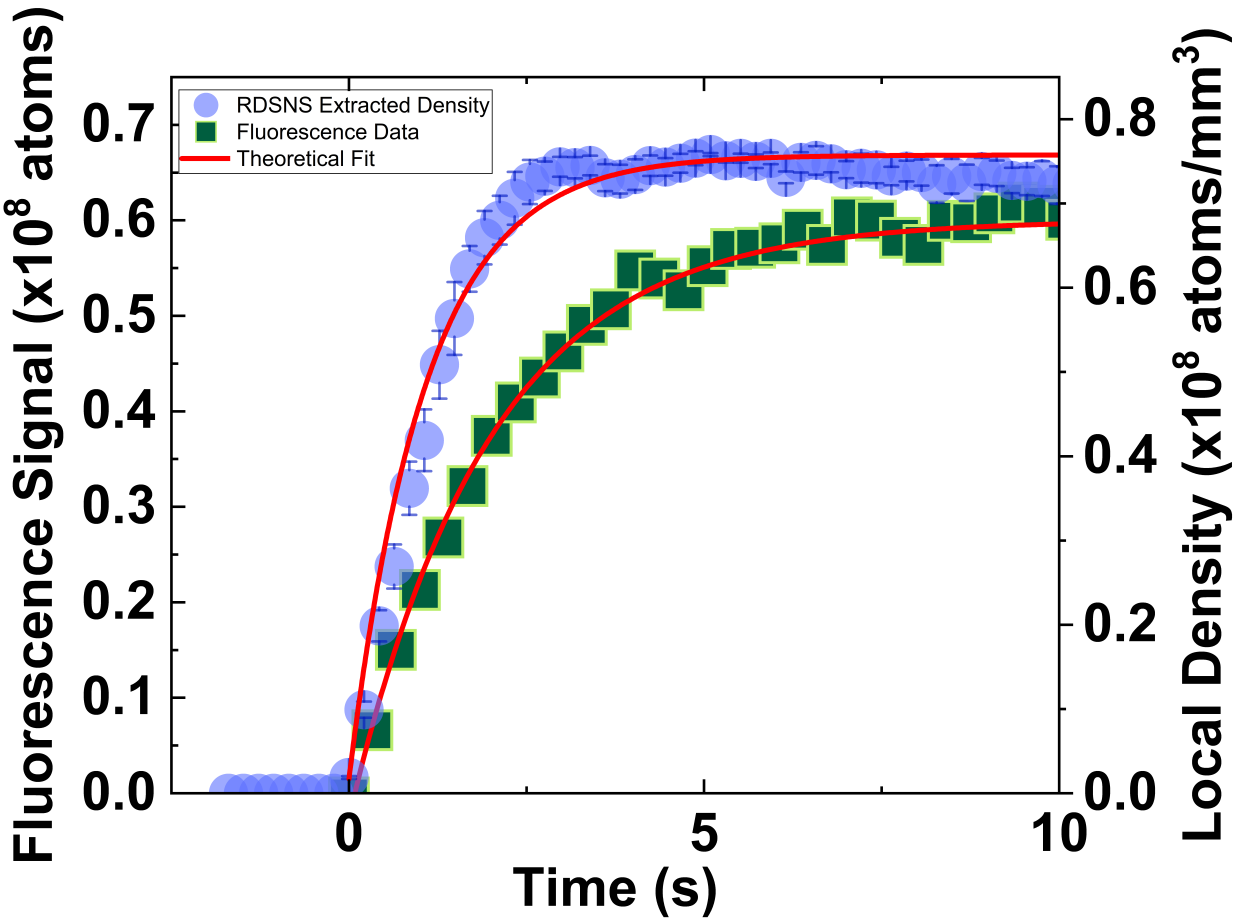


Figure 5.6: Illustrates the evolution of the RDSNS signal as atoms are captured in the MOT. The signal (blue dots) reaches 1/e of the saturation density within $\tau \sim 1$ s. The corresponding total fluorescence count (green squares) (here, $\tau \sim 1.96$ s) is also shown.

several density-limiting mechanisms. First, photons scattered by one atom can be reabsorbed by its neighbors, generating a repulsive radiation pressure force that counteracts further compression of the cloud [181, 182]. This multiple scattering of near-resonant light leads to an effective interatomic repulsion, which prevents the central density from increasing indefinitely even while more atoms are being loaded. Second, at higher densities, inelastic photo-assisted collisions between trapped atoms, such as radiative escape and light-assisted inelastic collisions, become significant and enhance atom loss channels [136, 183]. These processes limit the achievable steady-state density, while the MOT continues to accumulate atoms in its outer regions, thereby increasing the overall atom number but not the peak density.

This behavior highlights the precision of RDSNS in capturing the local density dynamics, as it directly reflects the density-limiting mechanisms, which are often obscured in global fluorescence

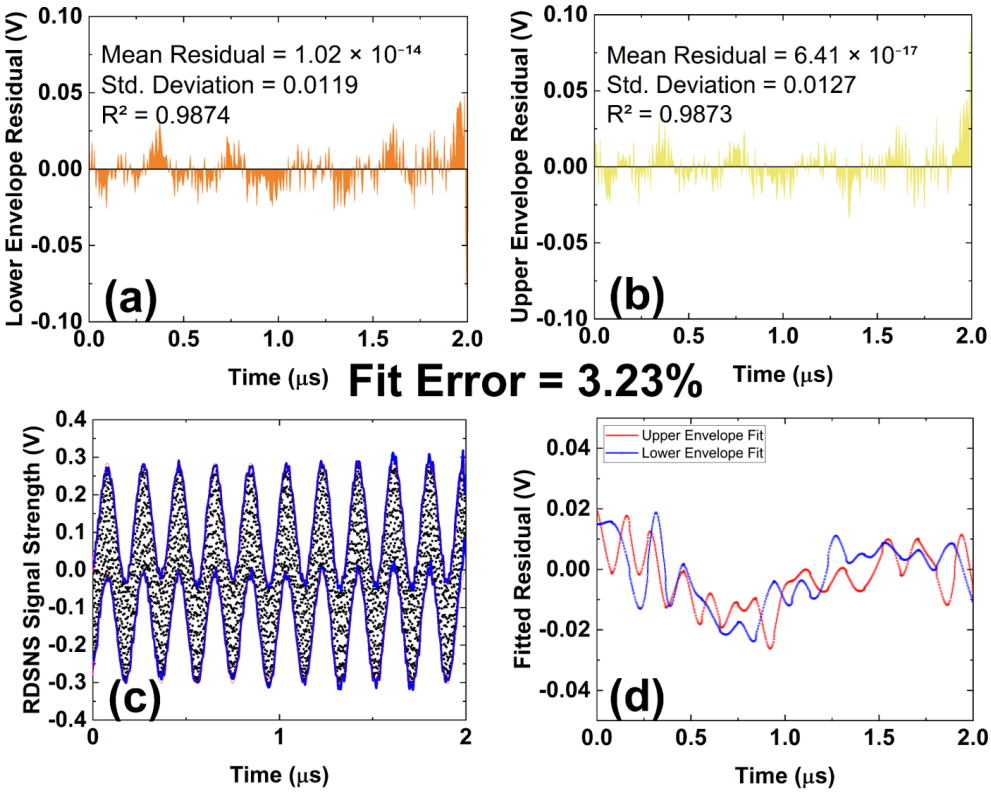
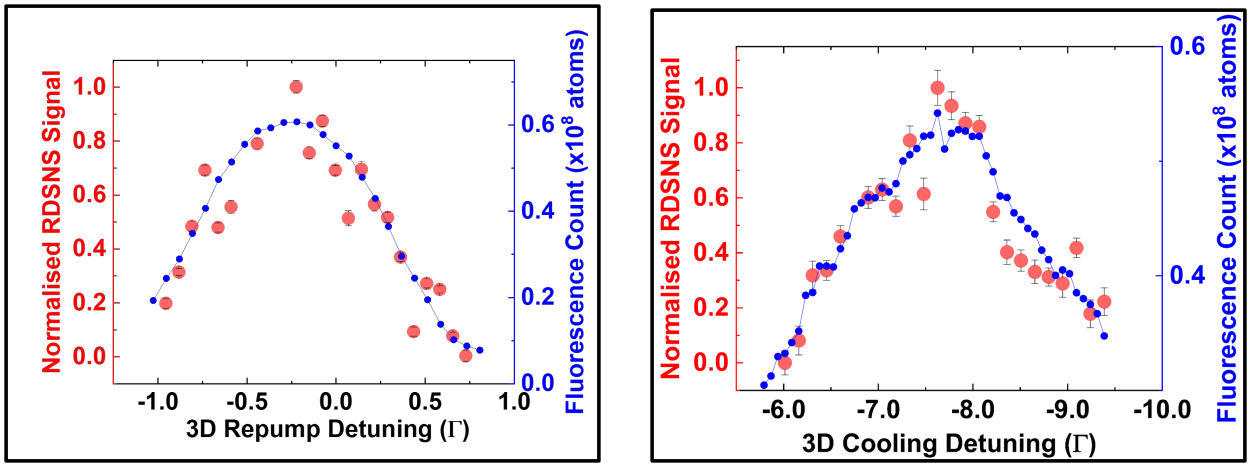


Figure 5.7: Envelope fitting analysis of the RDSNS signal over a 2 μs measurement window. (a) Residuals from the sine fit to the lower envelope with a standard deviation of 0.0119 and $R^2 = 0.9874$. (b) Residuals from the upper envelope fit with a standard deviation of 0.0127 and $R^2 = 0.9873$. (c) Experimental signal (black dots) overlaid with fitted upper (blue) and lower (red) envelopes. (d) Fitted residuals for both envelopes. The overall fit error in the signal amplitude is estimated to be 3.23%, which translates to an approximate 6% error in the extracted atomic density. Longer measurement durations are expected to reduce this error further by improving the signal-to-noise ratio.

measurements. The ability to resolve such effects demonstrates the advantage of local probes in cold-atom experiments.

5.4.1 Error Estimate

In order to accurately determine density values, it becomes necessary to estimate the error budget of our experiment. Figure 5.7 shows the results of the error estimate of the density measurements. We have shown one representative data in fig. 5.7c, of which we have extracted the error (see fig. 5.7a, b and d). This is done by detecting the envelope of the spin noise signal and analyzing its deviation from an ideal sinusoidal fit. The lower and upper envelopes were independently fitted



(a) (b)

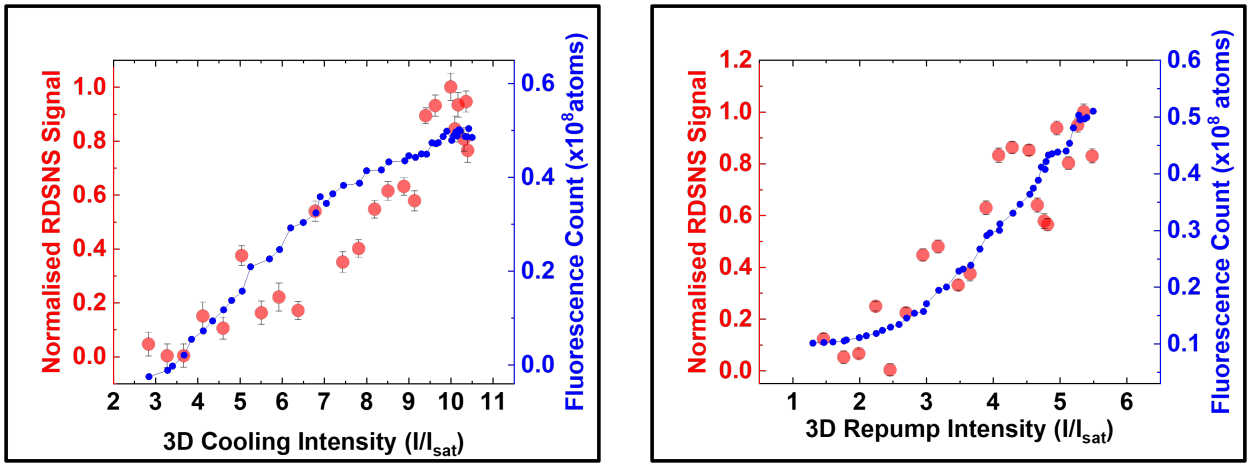
Figure 5.8: RDSNS signal strength (red dots) and fluorescence data (blue dots) for different beam detunings: (a) $3D$ repump beam detuning varied from -1Γ to 0.8Γ (from $F = 1 \rightarrow F'$ transition of the D_2 line), (b) $3D$ cooling beam detuning varied from -5.5Γ to -10Γ (from $F = 2 \rightarrow F'$ transition of the D_2 line).

(fig. 5.7a and b respectively) using sine functions, and the residuals were analyzed to quantify the fit quality. For the lower envelope, $\sigma_{\text{lower}} = 0.01269$, and for the upper envelope, the standard deviation of the residuals was found to be $\sigma_{\text{upper}} = 0.0119$. Given that the total amplitude of the fitted signal was approximately 0.393, the relative error in the fit is estimated to be around 3.23%, based on the lower residual.

This analysis was performed on a dataset corresponding to a short acquisition window of 2 μs. Extending the measurement duration would significantly improve the signal-to-noise ratio, thereby reducing statistical noise and improving the accuracy of the fit. Since the local atomic density is inferred from the total amplitude of the spin noise signal, the associated uncertainty in the density is approximately twice the fit error, leading to a density estimation error of about 6% for this particular signal.

5.4.2 Characterisation by varying $3D$ MOT Parameters

To further validate the RDSNS detection scheme, we characterized the performance of the $3D$ MOT by scanning both the frequency and the intensity of the cooling and repumping beams. Figures 5.8 and 5.9 summarize these results, comparing the steady-state RDSNS signal (proportional to local density, represented by red dots) with the fluorescence measurement (proportional to total atom



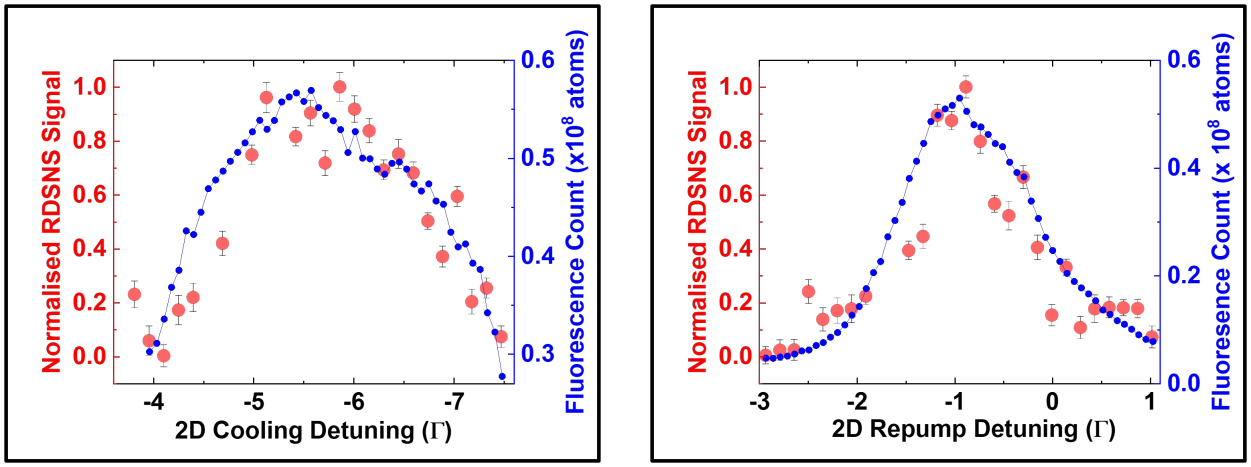
(a) (b)

Figure 5.9: RDSNS signal strength (red dots) and fluorescence data (blue dots) for different beam intensities: (a) $3D$ cooling beam intensity varied from $2.7I_{sat}$ to $10.5I_{sat}$, (b) $3D$ repump beam intensity varied from $1.2I_{sat}$ to $5.5I_{sat}$.

number, represented by blue dots). The closely spaced hyperfine structure of the excited state in ^{39}K makes the MOT particularly sensitive to the repumping conditions. As shown in fig. 5.8a, optimal trapping occurs at a critical repump detuning, where both density and total atom number are maximized. Similarly, in (fig. 5.8b) the detuning of the cooling beam determines the scattering rate and thus the effective trap depth. Near resonance, high scattering rates lead to heating and atom loss, while at large detunings the trap becomes too shallow to capture the atoms effectively. An optimum detuning exists where both density and atom number are highest.

The intensity dependence is demonstrated in fig. 5.9. A higher cooling beam intensity increases both atom number and density up to a saturation level, as expected from scaling of scattering rate with intensity. Similarly, increased repump intensity enables more atoms to be repumped into the cooling cycle, which increases both central density and total atom number. It should be noted that varying the molasses beams' intensities can also cause a minor power imbalance. This imbalance changes the centroid position of the MOT, thus displacing the region of probing relative to the center atomic cloud. Consequently, the locally measured density might change even while the total number of atoms is not affected. Such influences emphasize the spatial profile sensitivity of the RDSNS technique to the MOT and emphasize the need for keeping well-balanced beam intensities in quantitative measurements.

These measurements demonstrate that the RDSNS method provides results in close agreement



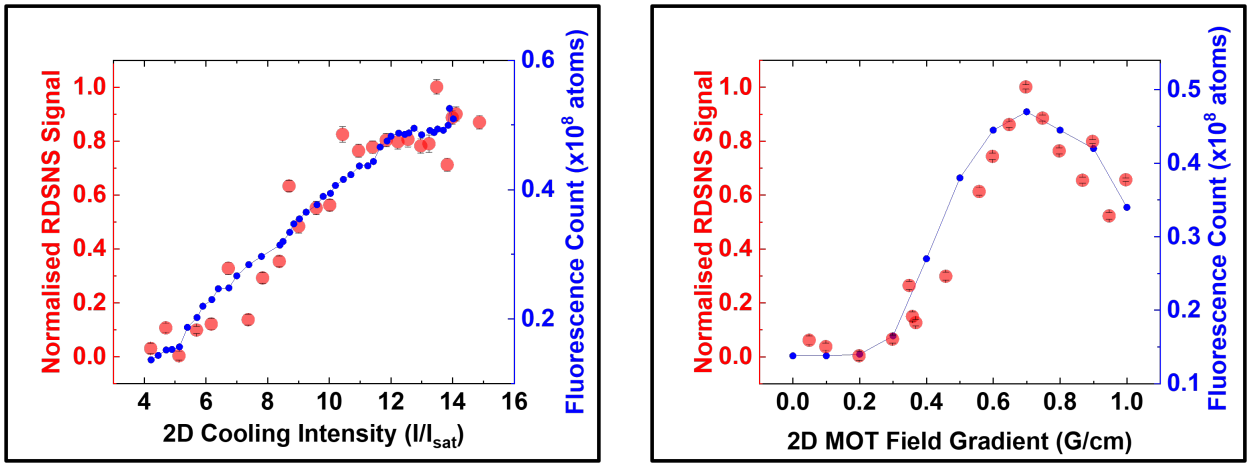
(a) (b)

Figure 5.10: RDSNS signal strength (red dots) and fluorescence data (blue dots) for different detunings: (a) $2D$ cooling beam detuning varied from -3.8Γ to -7.4Γ (relative to the $F = 2 \longrightarrow F'$ transition of the D_2 line), (b) $2D$ repump beam detuning varied from -3Γ to $+1\Gamma$ (relative to the $F = 1 \longrightarrow F'$ transition of the D_2 line).

with conventional fluorescence detection while offering direct access to local density information.

5.4.3 Characterisation by varying $2D$ Parameters

Further comparison of the RDSNS and fluorescence signals are presented in fig. 5.10 and fig. 5.11 by changing the various parameters of cold atom source like the detuning and intensity of the $2D^+$ MOT cooling beams (see fig. 5.10a and fig. 5.11a), the detuning of the repumping beam (see fig. 5.10b) and the magnetic field gradient (see fig. 5.11b). We find a striking agreement between the fluorescence signal and the local density RDSNS signals extracted using our method. The pushing beam plays a crucial role in enhancing the loading efficiency of the $3D$ MOT. It exerts a controlled radiation pressure on the trapped atoms, propelling them out of the $2D$ MOT and into the $3D$ MOT region. This directional force increases the atomic flux and ensures efficient transfer into the capture volume of the $3D$ MOT. By carefully tuning the intensity and detuning of the pushing beam, the velocity and divergence of the atomic beam can be optimised, resulting in significantly improved loading rates for the $3D$ MOT. The scattering force due to the pushing beam depends on the cooling beam's frequency (see fig. 5.10a). A larger confinement of the $2D$ atomic beam in the transverse direction can be achieved by increasing the intensity of the cooling beams resulting from a greater scattering force. This leads to a greater capture rate of the atoms in the $3D$ MOT



(a) (b)

Figure 5.11: Dependence of RDSNS and fluorescence signals on (a) the cooling beam intensity (scaled in units of I_{sat}), and (b) the $2D^+$ MOT magnetic field gradient. Saturation of loading efficiency is observed at high intensities, whereas the gradient shows an optimum value beyond which both atom number and density decrease.

chamber. This is evident from the plot in fig. 5.11a. where we observe that as the intensity of the cooling beams increases, both the fluorescence as well as the density probe signal increase and start to saturate from around $12I_{sat}$.

While the overall trend with the cooling beam detuning is consistent with expectations from Doppler cooling theory—with an optimum detuning around -4Γ to -6Γ [23, 69]—the dependence on the repump beam detuning is particularly striking.

In the case of ^{39}K, the $4^2P_{3/2}$ excited-state hyperfine levels on the D_2 line are separated by only a few MHz, which is comparable to the natural linewidth $\Gamma \approx 6$ MHz [184, 185]. This close spacing leads to strong overlap between transitions, and as a result, the repump beam frequency must be chosen very carefully. Even small deviations from the optimal repump detuning can lead to significant optical pumping of atoms into the dark $F = 1$ ground hyperfine manifold, reducing the effective scattering rate and thereby lowering both the fluorescence and the density signals. This extreme sensitivity is a well-known feature of potassium cooling, and has motivated the use of advanced cooling schemes such as gray molasses and Raman sideband cooling [186, 187].

Our measurements clearly reflect this behavior: as shown in Fig. 5.10b, the RDSNS and fluorescence signals both vary sharply with repump detuning, in agreement with earlier studies of ^{39}K MOT dynamics. The excellent correspondence between the two signals once again confirms

that the RDSNS technique faithfully captures local density variations in regimes where fluorescence alone may not provide complete information. A steeper confinement can also be achieved by increasing the $2D^+$ MOT field gradient. This must also give rise to a higher capture rate which in turn increases the number of atoms being captured in the $3D$ MOT. In fig. 5.11b, we see that as the $2D^+$ MOT field gradient increases, both the density and the fluorescence count increase to an optimum value and then start to decrease. This is because that even though the capture velocity increases of the $2D$ MOT due to a steeper trap, after an optimum point it goes beyond the capture velocity of the $3D$ MOT, thereby decreasing the atom number as well as density in the $3D$ MOT.

5.4.4 Abel Transform

Direct measurement of local density is difficult using standard techniques, however, it is essential to understand the cold atom dynamics. In fig. 5.12, we show the results of a measurement where we shifted the center of the cloud using an external bias magnetic field, thereby changing the probing volume. In regions of higher local atomic density, the spin noise fluctuations are stronger, leading to a higher RDSNS signal. Recording these variations in signal strength, we can effectively map the spatial distribution of the atomic density in real time (red triangles). We independently verified this measurement by performing an inverse Abel transform [188–190] on a fluorescence signal. Since our cloud has spherical symmetry, the inverse Abel transform is an effective mathematical tool for reconstructing the radial density distribution from observed $2D$ fluorescence images.

To find the atomic number density $g(r)$ at different distances from the center, we use a method called the Abel transform which assumes an axial symmetry of the object of interest. This technique transforms the $2D$ intensity distribution data along the line of sight into a $3D$ density profile. The Abel transform is an integral transform commonly employed for functions with spherical or axial symmetry. It is particularly used in projecting an optically thin, axially symmetric profile onto a two-dimensional plane. Conversely, the inverse Abel transform enables the reconstruction of the original emission distribution from such a projection. The Abel transform, $I(y)$ and its inverse, $g(r)$ are given by,

$$I(y) = 2\int_y^\infty \frac{r\, g(r)}{\sqrt{r^2 - y^2}}\, dr \tag{5.7}$$

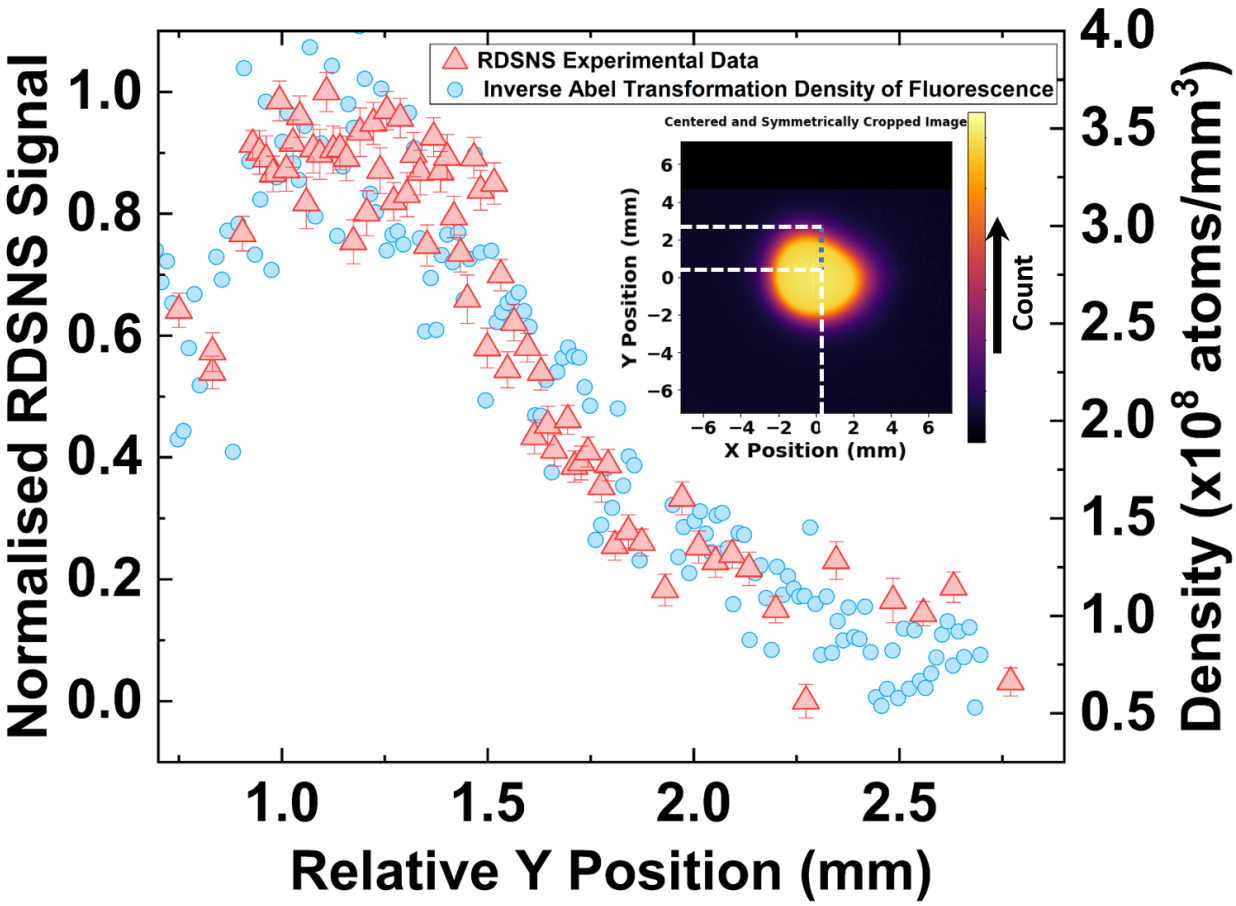


Figure 5.12: Illustrates the variation in the RDSNS signal (red triangles) with the centroid position of the cold cloud which was shifted by applying an additional bias magnetic field. It has been compared with the Inverse Abel transform (blue dots) of the fluorescence image. Inset: Shows the region (x = 0.2 mm and y = 0.45 mm to 3 mm) of the Inverse Abel transform of the fluorescence image.

$$g(r) = -\frac{1}{\pi}\int_r^\infty \frac{dI(y)}{dy}\frac{1}{\sqrt{y^2 - r^2}}\,dy \tag{5.8}$$

Here, the fluorescence intensity $I(y)$ is the light measured by the camera scattered from atoms captured in the MOT along the y direction (see fig. 5.13). We implement the direct integration technique in Python (using python package: hansenlaw). Details of the code can be found in [191].

We employ a bias magnetic field to carry out this experiment. As we vary the bias field, the centre of the MOT shifts vertically, which causes the entire trapped atomic cloud to move accordingly. Since the probe beam interacts with only a specific region of the MOT, this shift changes the probe interaction region with the local density, which in turn affects the RDSNS

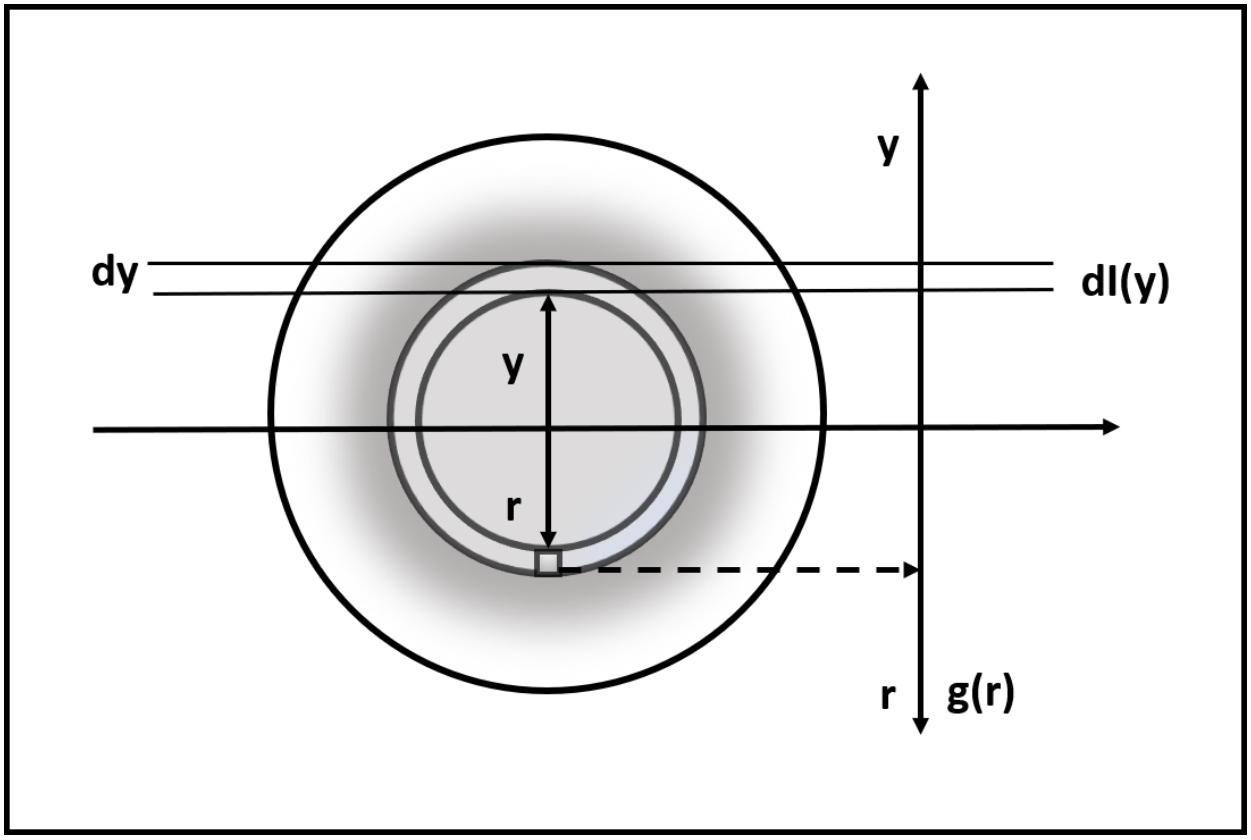


Figure 5.13: Schematic of a radially symmetric atomic cloud where $I(y)$ corresponds to the fluorescence intensity recorded by the camera at a transverse distance y from the central axis of the MOT, and $g(r)$ denotes the local atomic number density at a radial distance r from the axis of symmetry which is calculated by doing Abel transform of $I(y)$ as shown in Eq 5.7.

signal. Since the RDSNS signal is directly proportional to local atomic density, tracking how the signal varies across different positions provides a precise visualisation of the spatial structure of the atomic cloud. To confirm that our measurement is truly a local density probe, we extracted the radial density distribution from the $2D$ fluorescence image of the cloud by implementing an inverse Abel transform. The goal was to reconstruct the local atomic density profile from the fluorescence image recorded by the CCD, leveraging the spherical symmetry of the trap. The original CCD image had a resolution of 1920 × 1080 pixels. We began by converting the image scale from pixels to millimeters, using a known pixel-to-mm calibration factor. The density in per pixel was calculated by multiplying by the scale factor. The pixel size was then converted to mm to extract the density in atoms per mm^3.

We identified the cloud region in the image and performed a $2D$ Gaussian fit. The image was then re-centered and cropped symmetrically around this point to ensure radial symmetry for

accurate Abel inversion. We selected a fixed x-position and computed the inverse Abel transform along the y-axis. Details of the code can be found in [191]. This method effectively reconstructs the density distribution along the probing direction. To convert the inverse Abel transformed data to density values, we mapped the total fluorescence with the total number of atoms (10^8 atoms) and the total Abel transformed signal. The RDSNS data and Abel transformation demonstrated excellent agreement, confirming the effectiveness of our detection scheme. While this was a validation experiment, in several cold atom experiments where there may not be an inherent symmetry of the trap, computing the Abel transformed density profile will be impossible. In that case, our direct RDSNS method will be extremely useful.

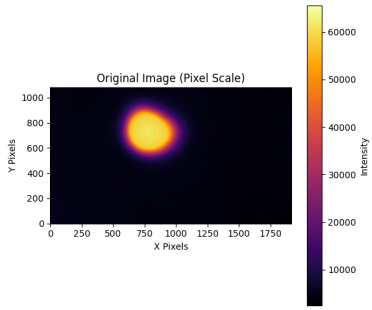
The RDSNS method accounts for contributions from atoms outside the immediate focal waist of the probe region as well, offering a more comprehensive density profile—an aspect nearly impossible to achieve with other in-situ measurement techniques. Since spin fluctuations extend beyond the immediate measurement volume, the detected noise spectrum inherently incorporates information from surrounding atoms, providing a broader yet spatially resolved density profile. This aspect is particularly advantageous when studying weakly trapped or expanding atomic clouds, where traditional in-situ techniques struggle due to their reliance on direct optical absorption or emission from atoms within a fixed probe region.

5.5 Image Processing and Abel Inversion

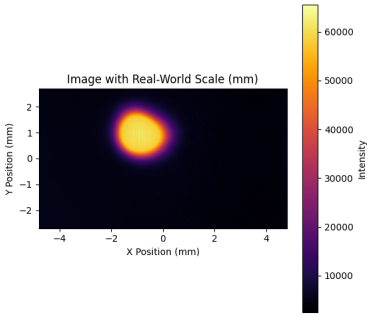
To extract the local atomic density distribution from fluorescence images, we developed a multi-stage image processing pipeline. The complete procedure is illustrated in Fig. 5.14, where each panel highlights a key transformation step.

The starting point is the raw CCD image recorded during the experiment, shown in fig. 5.14a. This image is initially expressed in pixel coordinates. To relate the measured spatial features to real physical units, the pixel values are rescaled using the known CCD pixel size and the optical magnification of the imaging system. The resulting image in real-world coordinates (mm scale) is presented in fig. 5.14b.

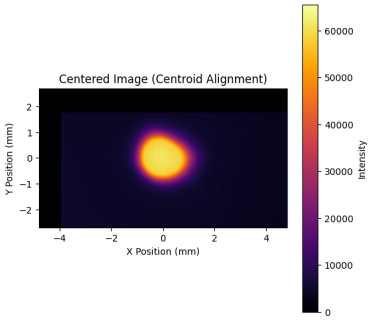
In order to accurately apply the Abel inversion, it is important that the atomic cloud be symmetrically aligned about the central axis. To achieve this, we employ a Gaussian centroiding



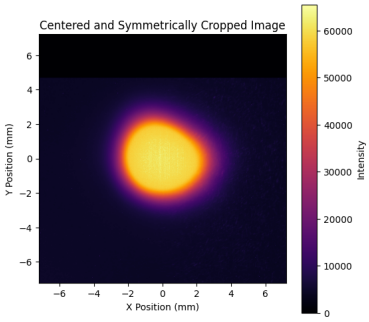
(a) Original Image (in pixel)



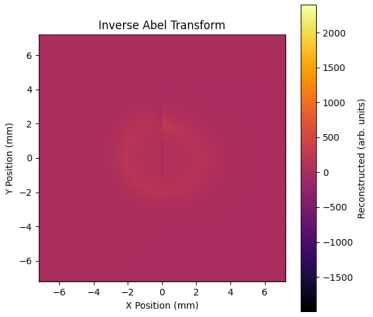
(b) Original Image (in mm)



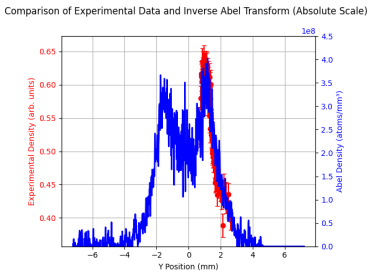
(c) Centered Image



(d) Centered and cropped image



(e) Inverse Abel Transform



(f) Final comparison plot

Figure 5.14: Overview of the analysis pipeline: (a) raw image in pixel, (b) raw image in physical coordinates, (c) image centered using Gaussian centroid, (d) centered and cropped image, (e) result of inverse Abel transform, and (f) comparison between experimental and reconstructed densities.

routine which shifts the image such that the centre of mass of the atomic distribution lies at the origin. The result of this alignment is shown in fig. 5.14c. Once centred, the image is cropped symmetrically to eliminate background regions and edge artefacts, as depicted in fig. 5.14d. This ensures that only the relevant atomic signal is preserved while maintaining cylindrical symmetry.

The next step is the application of the inverse Abel transform, which reconstructs the radial density distribution from the line-integrated fluorescence profile. We employ the Hansenlaw algorithm for numerical stability and efficiency. The outcome of this step is illustrated in fig. 5.14e, where the reconstructed density distribution is clearly resolved.

Finally, we validate the procedure by comparing the reconstructed density profile with the experimentally observed spin noise signals, as shown in fig. 5.14f. The good agreement between the two establishes that the pipeline provides a reliable estimate of the local atomic density under the assumption of cylindrical symmetry.

Thus, the pipeline systematically converts raw experimental CCD images into quantitative

density distributions through a sequence of scaling, centering, cropping, and Abel inversion, as summarized in fig. 5.14.

The technical implementation of each step, including the Python code used for loading, scaling, centering, cropping, and performing the Abel inversion, is provided in Appendix C.

5.5.1 Effect of MOT Field Gradient on RDSNS Signal

SNS is often performed in the Voigt geometry, where the magnetic field is perpendicular to the light propagation direction. Now, by following the Bloch equation,

$$\frac{d\mathbf{M}(t)}{dt} = \gamma\,\mathbf{M}(t) \times \mathbf{B} - \frac{M_x\hat{x} + M_y\hat{y}}{T_2} - \frac{(M_z - M_0)\hat{z}}{T_1}, \tag{5.9}$$

The magnetization $\mathbf{M}(t)$ depends on the following parameters namely the gyromagnetic ratio (γ), precession around the magnetic field $\mathbf{B}$, transverse relaxation (with time constant T_2) and longitudinal relaxation (with time constant T_1). We will now explore what happens when the magnetic field direction is altered. If the field is in the x-z plane and it makes an angle β with the x-axis. It can be written as-

$$\mathbf{B} = B_0\,(\cos\beta\,\hat{x} + \sin\beta\,\hat{z})\,, \tag{5.10}$$

We define, $\omega_L = \gamma B_0$ is the Larmor frequency, B_0 is the magnitude of the magnetic field and β is the angle between the field and the x-axis.

The presence of the magnetic field at an oblique angle introduces both precession and projection effects, leading to a more complex time evolution of the magnetization. The Bloch equations will now involve components of $\mathbf{B}$ along both x and z, and thus the magnetization will precess around the total field direction defined by $\mathbf{B}$. For an arbitrary initial magnetization

$$\mathbf{M}(t = 0) = M_{x_0}\,\hat{x} \tag{5.11}$$

When the magnetic field lies in the x-z plane and makes an angle β with the x-axis, the time evolution of the x-component of the magnetization can be written as,

$$M_x(t) = M_{x_0}\left[\cos^2\beta + \sin^2\beta\cos^2(\omega_L t)\right] e^{-t/T_2}. \tag{5.12}$$

This solution shows that part of the magnetization remains static along x due to the projection of the field along that direction ($\cos^2\beta$), while the remaining part undergoes oscillation at the Larmor frequency due to the perpendicular component ($\sin^2\beta$). The power spectral density $P(\omega)$ of the magnetization noise is given by:

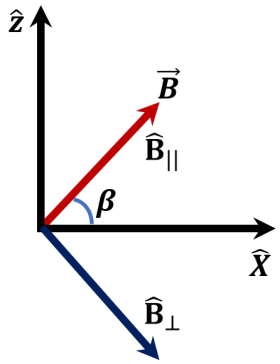


Figure 5.15: Illustration of a magnetic field $\mathbf{B}$ lying in the x–z plane at an angle β with respect to the x-axis. The field has a parallel component $\mathbf{B}_{||}$ along the initial magnetization and a perpendicular component $\mathbf{B}_{\perp}$ that induces Larmor precession. This orientation influences the resulting spin dynamics and the shape of the power spectrum.

$$P(\omega) = \cos^2(\beta)\cdot\frac{1/T_2}{\omega^2 + (1/T_2)^2} + \frac{1}{2}\sin^2(\beta)\cdot\left[\frac{1/T_2}{(\omega-\omega_L)^2 + (1/T_2)^2} + \frac{1/T_2}{(\omega+\omega_L)^2 + (1/T_2)^2}\right] \tag{5.13}$$

This expression shows that the power spectrum consists of a Lorentzian peak centered at $\omega = 0$, whose amplitude is proportional to $\cos^2(\beta)$, a pair of Lorentzian peaks centered at $\omega = \pm\omega_L$, whose combined amplitude is proportional to $\sin^2(\beta)$.

Thus, the orientation of the magnetic field determines the relative weights of the zero-frequency and Larmor-frequency components of the spin noise signal. In particular, for $\beta = 0°$ (field along x axis), all the noise appears at $\omega = 0$, for $\beta = 90°$ (field along z axis), all the noise appears at $\omega = \pm\omega_L$.

5.5.2 Anti-Helmholtz coil configuration

In cold atom experiments, the strength of SNS depends on the orientation and magnitude of the magnetic field **B**. In our setup, the magnetic field lies in the x-z plane and varies across the atomic cloud, particularly along the probe beam direction (x-axis). To understand and control this variation, we calculate the magnetic field at different positions by solving elliptic equations. To verify these calculations, we measure the individual components B_x, B_y, and B_z. The angle $\theta_B(x)$ between the local magnetic field vector and the direction of the probe laser beam also varies with position, influencing the SNS signal.

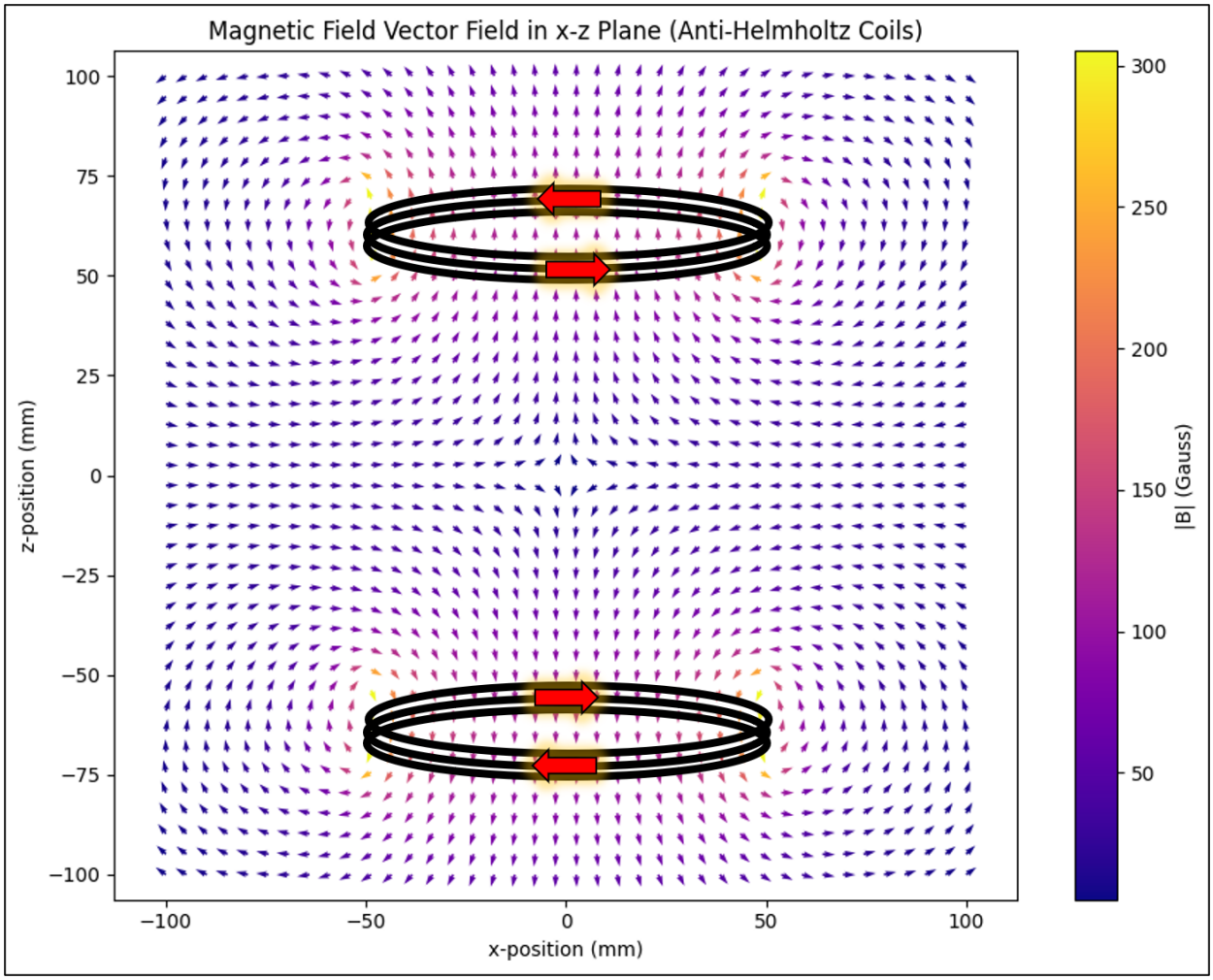


Figure 5.16: Magnetic field vector field in the x–z plane for an anti-Helmholtz coil configuration. The tiny arrows indicate the direction of the magnetic field at each point and the color represents the relative field strength.

For trapping atoms in a MOT, we require a locally uniform magnetic field gradient to provide a

spatially dependent Zeeman shift. This enables spatially selective optical forces on neutral atoms. To achieve this, we use a pair of circular coils carrying equal but opposite currents—known as an anti-Helmholtz configuration. This creates a quadrupole magnetic field with a field minimum at the center. Our MOT use a field gradient of about 18 G/cm along the symmetry axis. While working in the x-z plane and assuming the azimuthal coordinate ϕ is zero, one can identify the cylindrical radial coordinate ρ with the cartesian x-coordinate, i.e., $\rho = x$. Thus, the magnetic field vector can be expressed in Cartesian form as:

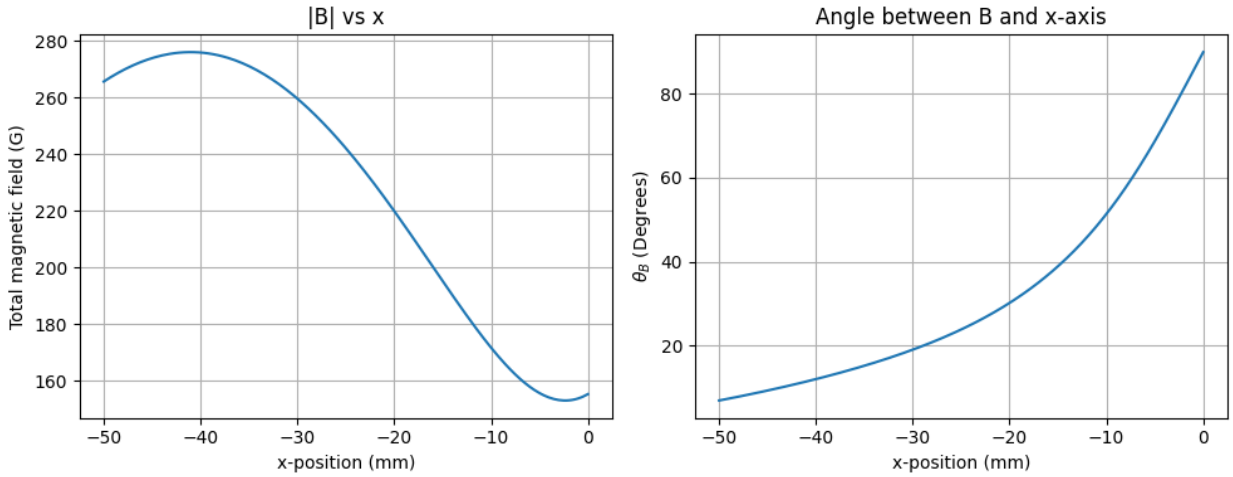


Figure 5.17: Magnetic field variation along the x-axis in an anti-Helmholtz coil setup. Left: total field strength $|\mathbf{B}|$ showing a minimum at $x = 0$. Right: angle θ_B between $\mathbf{B}$ and the x-axis, indicating directional variation across the center.

$$\mathbf{B}(x, z) = B_\rho(x, z)\,\hat{x} + B_z(x, z)\,\hat{z} \tag{5.14}$$

At each point in the x-z plane, the angle $\theta(x, z)$ that the magnetic field vector $\mathbf{B}$ makes with the x-axis is given by:

$$\theta(x, z) = \tan^{-1}\left(\frac{B_z(x, z)}{B_\rho(x, z)}\right) \tag{5.15}$$

Figure 5.16 is a plot of the magnetic field vector field in the x-z plane for an anti-Helmholtz coil configuration. Two identical circular coils are placed symmetrically along the z-axis, one above and one below the origin, and carry equal but opposite currents to generate a magnetic quadrupole field.

The small arrows point in the direction of the magnetic field at every point in space, and color marks the relative field strength. At the middle of the setup ($x = 0, z = 0$), the magnetic field is zero, a characteristic of anti-Helmholtz coils. From the middle, the field gets stronger, and its direction changes based on the superposition of the top and bottom coil fields.

Because of the opposing current directions in the coils, the field lines are curved inward and outward in a symmetric fashion about the center. This produces a linear field gradient along the z-axis close to the origin, which is essential for uses such as magneto-optical trapping, where atoms are trapped in a spatially inhomogeneous magnetic field.

The simulation includes multiple turns per coil and their contributions at each grid point. This produces a highly resolved and physically correct visual representation of the spatial distribution of the magnetic field of an anti-Helmholtz coil pair.

The magnetic field at a point (x, z) in the x-z plane due to a circular current loop of radius a, carrying current I, centered at height z_0, is given using elliptic integrals. Let the radial distance be

$$\rho = |x| \tag{5.16}$$

and the vertical separation from the loop be

$$z_{\text{rel}} = z - z_0 \tag{5.17}$$

Define the modulus squared:

$$k^2 = \frac{4a\rho}{(a+\rho)^2 + z_{\text{rel}}^2} \tag{5.18}$$

The complete elliptic integrals of the first and second kinds are $K(k^2)$, $E(k^2)$.

Then, the axial component B_z of the magnetic field is:

$$B_z = \frac{\mu_0 I}{2\pi \left[(a+\rho)^2 + z_{\text{rel}}^2\right]} \left[K(k^2) + E(k^2) \cdot \frac{a^2 - \rho^2 - z_{\text{rel}}^2}{(a-\rho)^2 + z_{\text{rel}}^2}\right] \tag{5.19}$$

The radial component B_ρ is:

$$B_\rho = \frac{\mu_0 I \cdot z_{\text{rel}}}{2\pi\rho \left[(a+\rho)^2 + z_{\text{rel}}^2\right]} \left[-K(k^2) + E(k^2) \cdot \frac{a^2 + \rho^2 + z_{\text{rel}}^2}{(a-\rho)^2 + z_{\text{rel}}^2}\right] \tag{5.20}$$

To express the radial component in Cartesian coordinates, the x-component is:

$$B_x = \begin{cases} B_\rho, & x > 0 \\ -B_\rho, & x < 0 \\ 0, & x = 0 \end{cases} \tag{5.21}$$

The **maximum field gradient** in the axial direction occurs near $z = a$, and is given by,

$$\left.\frac{\partial B_z}{\partial z}\right|_{z=0} = \frac{48\mu_0 I}{25\sqrt{5}a^2} = 2\left.\frac{\partial B_\rho}{\partial \rho}\right|_{\rho=0}. \tag{5.22}$$

The plot of the magnetic field with the x-axis and the angle $\theta_B(x)$ with the local magnetic field is shown in fig. 5.17. The effect of the local magnetic field on the spin noise signal is rather complex, as it influences both the spectral shape and the relaxation dynamics of the measured fluctuations. In particular, spatial variations in the field gradient across the probing region can lead to inhomogeneous broadening of the noise spectrum, frequency shifts of the spin precession, and modifications of the effective spin–spin correlation times. Therefore, a detailed analysis of the magnetic field profiles within the probing volume is essential not only to interpret the measured spectra correctly but also to optimise the experimental geometry for maximising sensitivity and minimising systematic effects. This consideration provides the basis for the subsequent discussion, where the spatial distribution of the field and its interplay with the probe beam are examined in greater detail.

Conclusion

In conclusion, we have demonstrated a novel, minimally destructive technique based on Raman-driven spin noise spectroscopy (RDSNS) to measure the local density of a cold atomic cloud in real time. Our method allows continuous tracking of density dynamics as atoms are captured by the trapping field, and shows excellent agreement with inverse Abel-transformed density profiles derived from fluorescence image. Unlike conventional absorption- or fluorescence-based techniques, our approach enables local probing without relying on symmetry assumptions or de-

structive measurements. This makes it particularly suitable for studying dynamically evolving or spatially asymmetric atomic systems. We anticipate that this technique will find broad applications in real-time diagnostics of cold atom experiments, especially in contexts involving transport phenomena [192], non-equilibrium dynamics, and quantum simulation platforms [193].

Importantly, this approach can be extended to non-destructive state detection, which is of particular interest for precision metrology and quantum information science. In conventional fluorescence imaging, the measurement process itself perturbs the system by scattering photons and altering both internal and motional states of the atoms. In contrast, spin noise spectroscopy (SNS) provides an intrinsically non-destructive probe since it relies on the detection of spontaneous spin fluctuations via off-resonant Faraday rotation or related mechanisms [52, 53]. With suitable extension, the method presented here could allow for the real-time monitoring of hyperfine F-state populations without significantly disturbing the atoms. This capability would be highly advantageous for experiments where long coherence times and repeated measurements on the same atomic ensemble are required.

Such non-destructive probing techniques are crucial for several frontiers in modern atomic physics. In quantum metrology, the observation of local density and spin population dynamics in real time facilitate better control of atomic clocks and magnetometers, where presently density-dependent shifts and spin-relaxation processes set sensitivity limitations [194]. In quantum simulation, being able to access spatially resolved density information without sample destruction provides the freedom to investigate out-of-equilibrium dynamics, spin-exchange interactions, and correlated many-body states in cold atoms [193]. Last but not least, in quantum computing, non-destructive readout of hyperfine states offers an avenue to quantum non-demolition (QND) measurements [195], a key ingredient for error correction and state initialisation protocols. Having the capability to infer qubit states without causing loss of coherence can find direct applications in neutral-atom quantum computing architectures where hyperfine states are computational basis states [196–199]. For future research, the technique might be optimised to achieve greater spatial resolution and reduced technical noise, perhaps combined with optical cavities or squeezed-light probing to push sensitivity above the standard quantum limit. Such advances would render spin-noise-based detection not only a measurement tool for cold atom experiments but also a central element of scalable quantum technologies.

"If you look closely enough at the world, you'll find that even the simplest things have infinite depth."

— Richard P. Feynman

Chapter 6

Higher Harmonic Generation using Spin Noise Spectroscopy

This chapter is based on the following publication:

Parametrising Harmonic Strengths in Raman Driven Spin Noise Spectra of Neutral Atoms, **Sayari Majumder**, Saptarishi Chaudhuri, 2025. *Scientific Reports* (under review).
Detection of long-range coherence in driven hot atomic vapors by spin noise spectroscopy, Rupak Bag, **Sayari Majumder**, Saptarishi Chaudhuri, and Dibyendu Roy, 2025. https://doi.org/10.48550/arXiv.2509.18036 *Physical Review Letters* (under review).

The study of spin noise correlations in atomic vapours provides a powerful route to explore the intrinsic spin dynamics without the need for active perturbation. In this work, we investigate the emergence of higher-order harmonics in spin noise spectra of hot Rubidium vapour subjected to a strong optical drive using a pair of coherent Raman beams. Under these conditions,

the atomic response gives rise to multiple equi-spaced coherence signals in addition to the fundamental spin noise mode in the frequency spectrum. We observe distinct second, third, and fourth harmonic components with relative amplitude spanning from 10^{-1} to 10^{-4}. By systematically varying the Raman and probe beam intensities, atomic density, magnetic field strength, and drive frequency, we parametrise the evolution of these higher harmonics. This facilitates a precise explanation of the optical driving strength influencing the atomic population dynamics in multi-level Zeeman substructure within the atomic ensemble. The detected harmonic structure facilitates the accurate determination of the energy spacing between magnetic sub-levels and hence acts as an excellent spectroscopic probe of spin coherence in complicated atomic systems. Beyond its fundamental significance, this approach shows promise for precision magnetometry applications in thermal atomic ensembles.

6.1 Motivation and Background

Spin dynamics in atomic vapours is a powerful tool to study coherence, relaxation, and correlations of multi-level quantum systems. These dynamics form the foundation of a wide range of applications from quantum sensing to precision metrology. While there are many techniques conceived to investigate such systems, spin noise spectroscopy (SNS) has become a highly valuable tool given its non-perturbative and sensitivity to intrinsic spin fluctuations. The SNS signal [53, 66, 73, 200–202] originates from spontaneous spin fluctuations projected onto the probe's polarisation axis. Theoretically, this can be expressed through the correlation function of the spin components, which determines the spectral density of the measured Faraday rotation noise. This minimally invasive detection makes SNS suitable for applications in atomic magnetometry [103, 203], biomedical imaging [82], archaeological surveys [204], space exploration [87], and navigation systems [80].

Equilibrium SNS measurements reveal features such as spin-alignment peaks at twice the Larmor frequency [205]. However, in such linear-response regimes, much of the rich dynamics of the system remain hidden.

6.2 Driven Spin Dynamics and Raman Coupling

When an atomic ensemble is driven out of equilibrium using external optical or RF/MW field, the resulting dynamics can amplify spin-noise signals and reveal insightful features. Driving the system generates higher harmonics and higher-order spin correlators, as seen in driven semiconductor SNS [206] and two-photon SNS in alkali vapours [207]. The interplay of optical driving and intrinsic spin fluctuations thus provides a sensitive probe of nonlinear spin responses.

In particular, Raman-driven spin noise spectroscopy (RDSNS) introduces coherent coupling between ground-state Zeeman sublevels via two optical fields. This coupling enables the generation of higher harmonics of the Larmor frequency, whose amplitudes encode the extent of spin coherence induced by the Raman drive [208]. Theoretical models predict that such harmonic generation can be interpreted as signatures of long-range spin correlations within the ground-state manifold.

While electromagnetically induced transparency (EIT) and coherent population trapping (CPT) effects in multi-Λ configurations have demonstrated complex interference phenomena [209–211], the connection between these coherent effects and measurable spin-noise harmonics remains unexplored. Moreover, systematic experimental characterisation of Raman-driven harmonic spin noise in hot multi-atomic vapours has not yet been reported.

6.3 Scope and Objectives of the Present Work

The present work aims to experimentally investigate Raman-driven spin noise spectroscopy in hot vapours of ^{85}Rb atoms. By applying two coherent optical fields, effective Raman couplings are generated between the ground-state Zeeman sublevels. Using dispersive Faraday rotation measurements, higher harmonics of the Larmor frequency are observed in the spin noise spectrum. The amplitudes and spectral widths of these harmonics provide direct information about the degree of coherence established by the Raman drive, thereby linking measurable noise spectra to theoretical models of long-range spin coherence.

Furthermore, the driving scheme presented here demonstrates how harmonic-like behaviour of spin noise can emerge with narrower linewidths than conventional driven oscillations, due to the interplay of stochastic spin fluctuations and coherent driving. This establishes Raman-driven SNS

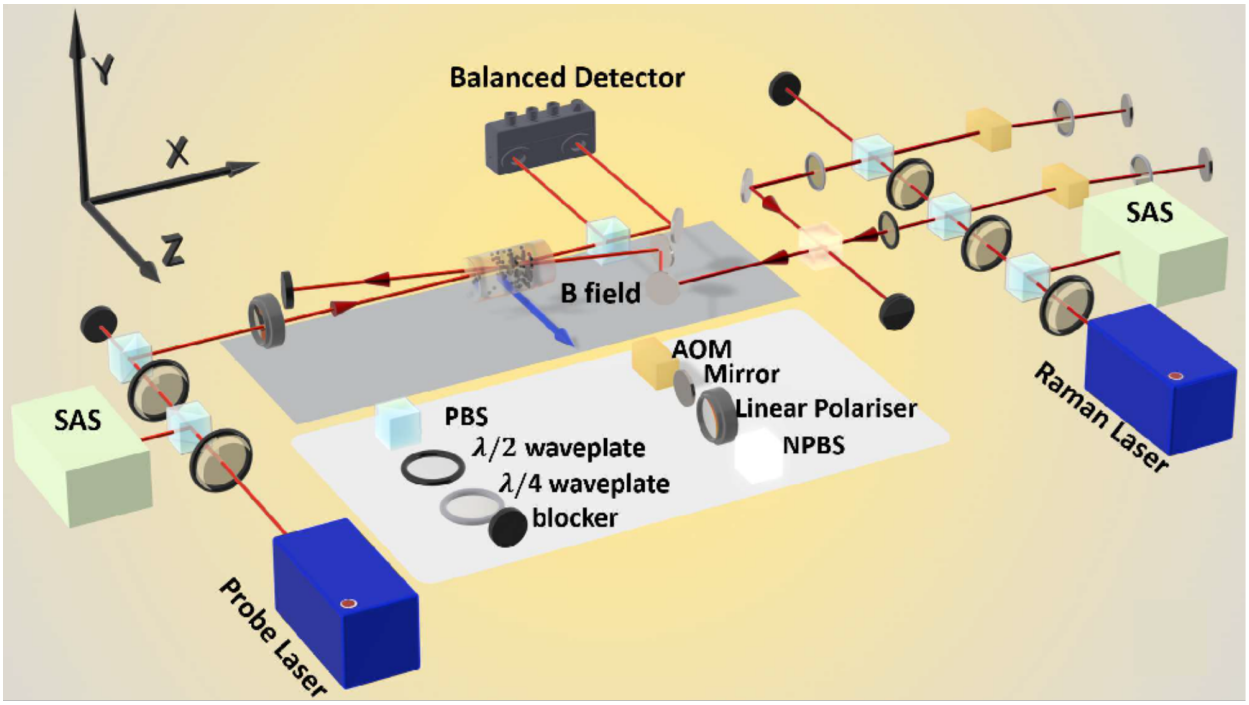


Figure 6.1: Schematic of the experimental setup used for Raman-driven spin noise measurements, showing the probe and Raman laser paths, acousto-optic modulation, polarisation optics, and balanced detection system in the presence of a transverse magnetic field.

as a versatile probe for studying non-equilibrium, multi-level spin systems.

6.4 Observation of multiple equispaced RDSNS peaks

The basic experimental setup, which we previously reported in [171], was used for precision magnetometry. As illustrated in Fig. 6.1, our experimental setup comprises two main laser sources, probe and Raman, derived from two separate External Cavity Diode Lasers (ECDLs) centred at 780 nm (Toptica Photonics DL100). The probe laser is blue detuned by 31 GHz from $^2S_{1/2}$ $F = 3$ to $^2P_{3/2}$ $F = 4$ transition line of ^{85}Rb. It is made linearly polarised before entering the Vapour cell set up with a polarisation purity greater than 99.99 %. The probe light is further focused at the centre of the cell using a lens combination such that the focal waist is 45 μm. After emerging from the vapour cell, the probe beam is collimated again and sent to a polarising beam splitter (PBS122), which splits the light equally between the two ports. The light from two ports of the PBS falls on a balanced photodetector (see Figs. 6.1 and 6.2(c)) having a bandwidth of 100 MHz (Thorlabs, PDB230A). To get the power spectrum of the signal, we further connect the

photodetector output to a Spectrum analyser (Keysight, N1996A). A second ECDL, designated as the Raman laser, is kept on resonance with $^2S_{1/2}$ $F = 3$ to $^2P_{3/2}$ $F = 4$ transition line of ^{85}Rb. The Raman laser output is divided into two beams, which are passed through Acousto-Optic Modulators (AOMs) (ISOMET 1206C and AA OPTICS MT110-A1-IR) in separate double-pass configurations for precise frequency and intensity control. The beam sizes were made identical (waist diameter = 2.2 mm) by suitable lens combinations. Care was taken to make the Raman beams have circular (σ^+) and linear (Π) polarisation with a polarisation purity of above 99.99%. They were merged using a non-polarising beam splitter (BS014). Light from one of the output ports of the NPBS was sent through the vapour cell set-up. Light from the other output port was used to monitor the frequency difference (δ_{12}) between the two Raman beams by detecting the beat frequency of the interfering Raman beams using a photodetector (Thorlabs, DET36A) and an oscilloscope. The merged Raman beams were made to counter-propagate with respect to the probe beam propagation direction (see Fig. 6.1and see Fig. 6.1(a) for a detailed view). This was to ensure that no part of the stray Raman beam falls on the detector. The absolute frequencies of all the light sources were monitored using a wavelength meter (High Finesse GmBh WSU) with a frequency error of ±1 MHz, along with saturation absorption spectroscopy setups. The vapour cell used for this experiment is cylindrical in shape and is made up of Pyrex, having a length of 50 mm and a diameter of 25 mm. It contains both the isotopes of Rubidium in natural abundance. To reduce the effect of spin-destructive collisions, which broaden the linewidth, the cell is filled with a buffer gas of Neon at 200 torr. To control the density of atoms, we heat the cell using strip heaters (OMEGA KHLVA-105/10-P) and a PID temperature controller (OMRON E5CWL). The set-up is thermally insulated using ceramic blankets. We maintain a temperature stability of $\pm 0.05^{\circ}C$. A uniform magnetic field is created using a pair of coils in a Helmholtz configuration. We used a stable current controller (LD3000, Thorlabs) for the magnetic coil with a stability of $<1\ \mu A$. The maximum spatial variation of the field was measured to be 2 parts in 10^5 over the detection region of 4.5 mm. The temporal variation of the generated field was limited to less than ± 0.1 nT over 1 sec of measurement time. To shield the setup from external stray magnetic fields, it was enclosed in a four-layer μ metal casing, which shields the field by a factor of 10^4 times. In the Raman-driven power spectrum, the atoms are driven between the magnetic states (m_F) of the ground hyperfine level via magnetic sub-levels of the excited state by using a pair of laser beams as shown in Fig.

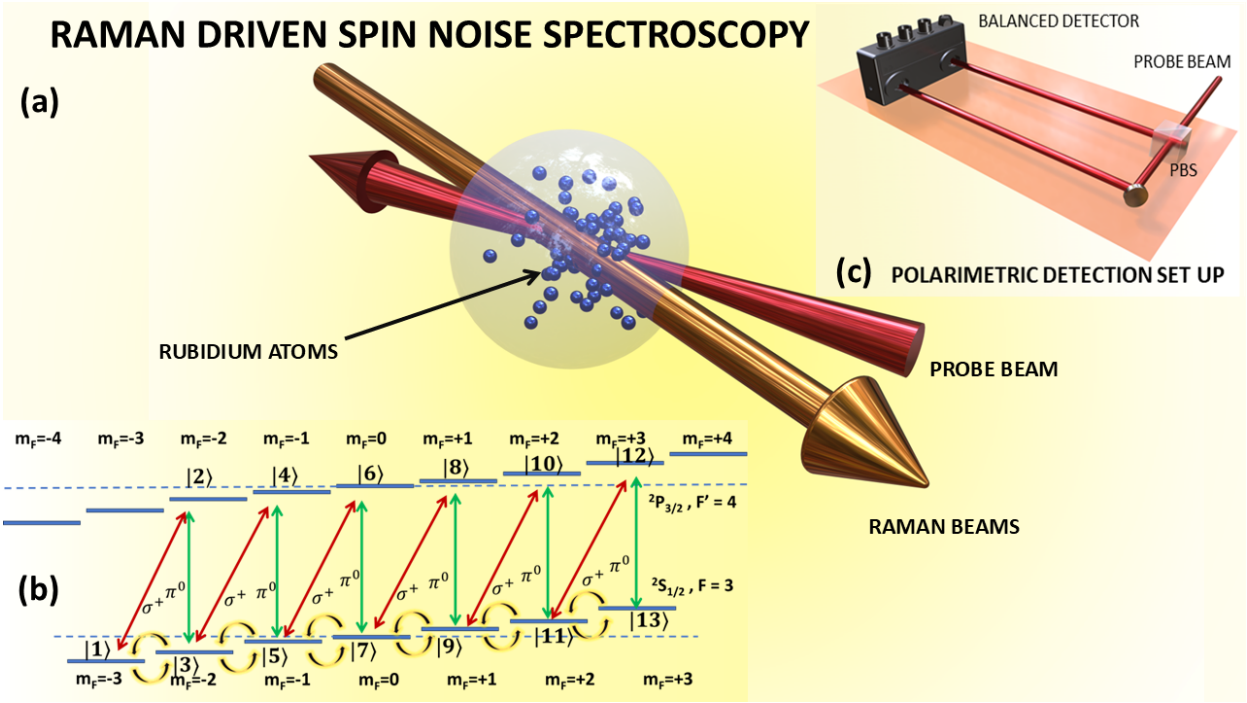


Figure 6.2: Experimental Set Up. (a) A linearly polarised probe beam (red) is focused at the centre of a Rubidium vapour cell. A pair of coherent beams (yellow) (Raman beams) with particular polarisations (σ^+ and π) is merged and made counter-propagating with respect to the probe beam (red). (b) Scheme of the Experiment. The pair of Raman beams connects the magnetic states of the ground hyperfine Zeeman manifold. Due to the multi-level structure, the atoms are driven to succeeding levels. The excited states are represented by even ket notations, while the ground states are represented by odd ket notations. (c) Illustrates the polarimetric detection setup. The polarisation fluctuation of the probe beam is measured using a PBS (polarising beam splitter) and a balanced photo-detector.

6.2. The Hamiltonian of the system can be described as,

$$\begin{aligned}\frac{H}{\hbar} &= \sum_i \omega_i^e \left|i\right\rangle \left\langle i\right| + \sum_j \omega_j^g \left|j\right\rangle \left\langle j\right| \\ &+ \Omega_1 \sum_{\{m,n\}} \left(\left|m\right\rangle \left\langle n\right| e^{-i\omega_{s_1} t} + \left|n\right\rangle \left\langle m\right| e^{i\omega_{s_1} t}\right) \\ &+ \Omega_2 \sum_{\{m,n\}} \left(\left|m\right\rangle \left\langle n\right| e^{-i\omega_{s_2} t} + \left|n\right\rangle \left\langle m\right| e^{i\omega_{s_2} t}\right)\end{aligned}$$

where ω_i is the angular frequency of state $|i\rangle$ and the superscript e or g represents the excited and the ground state. Here, Ω_1 and Ω_2 are the resonant Rabi angular frequencies of Raman field 1 (R_1) and Raman field 2 (R_2), respectively. The states following the selection rule allowed for electric

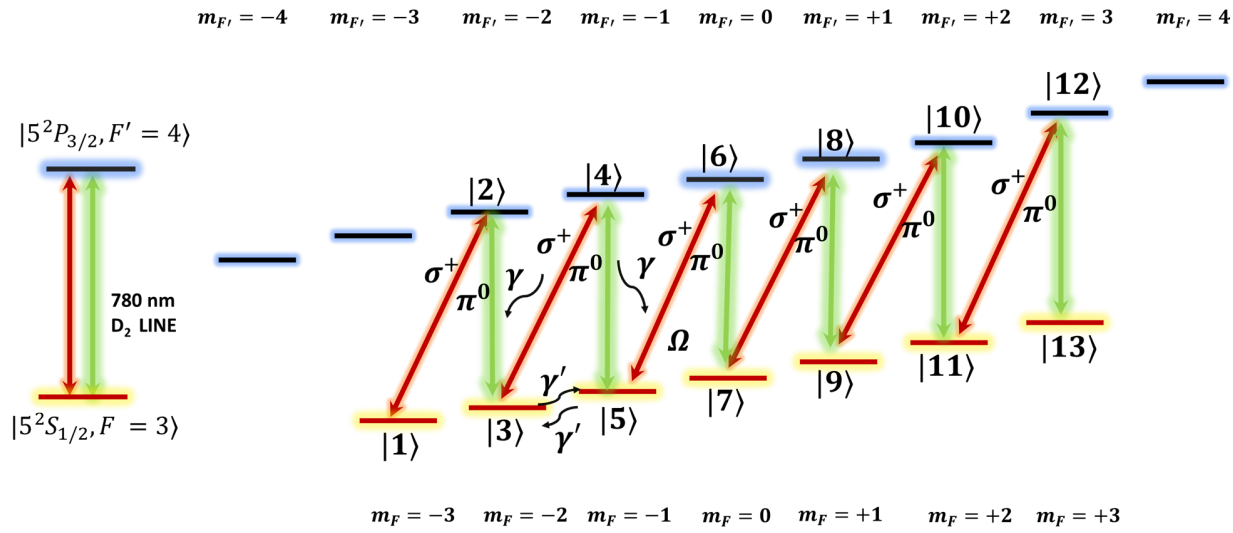


Figure 6.3: Energy level diagram illustrating Raman-coupled transitions between the Zeeman sublevels of the ^{85}Rb ground hyperfine manifold. The red levels denote the ground-state Zeeman states $|F, m_F\rangle$, while the blue levels represent the excited-state manifold. Optical fields containing σ^+ and π polarization components couple the ground and excited states with Rabi frequency Ω. Spontaneous decay from the excited states occurs at a rate γ, while γ' denotes the ground-state coherence relaxation rate. Two-photon Raman processes mediated by the excited states couple adjacent Zeeman sublevels, forming a ladder of coherently linked spin states. The sequential coupling between multiple m_F states results in oscillations at integer multiples of the Larmor frequency, leading to the higher harmonics observed in the spin noise spectrum.

dipole transition is denoted by $\{m, n\}$.

For a simplified 3 level atomic system, for example, the one constituting the ground states $|1\rangle$ and $|2\rangle$ and the excited state $|3\rangle$, there is negligible decay between the states $|1\rangle$ and $|2\rangle$ compared to decay rates from $|3\rangle$ to $|1\rangle$ and $|2\rangle$, we have chosen the following limits on the relaxation rates: $\gamma_{13} = \gamma_{23} = \gamma$, $\gamma_{12} = \gamma_{21} = \gamma'$, and $\gamma' << \gamma$. Here, γ' is the spin coherence relaxation rate between the two Zeeman states, and the relevant correlation function is the auto-correlation of the ground-state coherence $\rho_{21} = \langle 1|\hat{\rho}|2\rangle$. The steady-state expression for ρ_{21} in the Raman resonance limit ($\Delta = 0$, $\delta_{12} = \nu_L$) has been derived in Ref. [74] and was discussed in detail in chapter 2. For the 3 level case, we note that the power spectrum looks like a Dirac delta peak with an envelope as $|\rho_{21}|^2$ which grows with Ω thereby indicating that the coherence between $|1\rangle$ and $|2\rangle$ also grows and finally saturates at a large value of Ω.

In case of a multi-level system, the above discussion can be extended and one can arrive at the generalised form of ρ_{ij} as a function of δ_{ij}. Here, corresponding auto-correlations of the density

matrix elements survive also between $|1\rangle$ and $|3\rangle$, $|1\rangle$ and $|5\rangle$ and, $|1\rangle$ and $|7\rangle$ and so on, via multi-photon resonant couplings (see Figs. 6.2 (b) and 6.3 for nomenclature of states). For clarity, we have named the excited and ground states participating in the long-range coupling as even and odd states, respectively. These additional autocorrelations correspond to the observed higher spin harmonics in the measured Raman-driven spin noise signal, as discussed in the next section. Each higher-order autocorrelation arises from successive Raman couplings through intermediate Zeeman sublevels. Therefore, a coherence between states separated by $\Delta m_F = n$ appears only at n^{th} order in the Raman interaction. Consequently, the amplitude of the n^{th} harmonic scales with increasing powers of the effective Raman coupling strength relative to the relaxation rates, rather than being determined solely by the number of available Zeeman state pairs. For the case of multi-level Raman coupling, the relative transition rate (strength of $(2n-1)^{\text{th}}$ state to that of state $|1\rangle$) is proportional to $(\frac{\Omega^2}{\gamma\gamma'})^{2n-2}$. The details of the mathematical formalism can be found in [208]. We note that this ratio depends mainly on three important parameters, which are γ, γ' and Ω. This ratio increases with Rabi frequency Ω (intensity of the Raman beam) and shows a fall if γ and γ' rise, i.e when the system has faster decay rates.

6.5 Multi-level Coupling and Harmonic Generation

In atomic vapours, the internal structure of atoms introduces a level of complexity far beyond what is captured by simple three-level models such as the Λ- or V-type system. The hyperfine and Zeeman substructure of the ground and excited states gives rise to multiple energy levels that can simultaneously participate in coherent light–matter interactions. As a result, models based solely on three-level approximations often fail to describe the complete dynamics of optically driven atomic ensembles. A more accurate way to model the coupling configurations is instead, by using a cascaded-Λ system (CLS) [212, 213] or ladder-type arrangements [214]. Such a model accounts for the multiple optical pathways and higher-order coherence effects that arise in real atomic systems.

In our experiment, we build upon previous demonstrations showing that a two-photon Raman drive can enhance the intrinsic spin-noise signal by nearly six orders of magnitude [74, 171, 215]. Here, we utilise Raman-driven spin noise spectroscopy (RDSNS) to explore how coherent optical

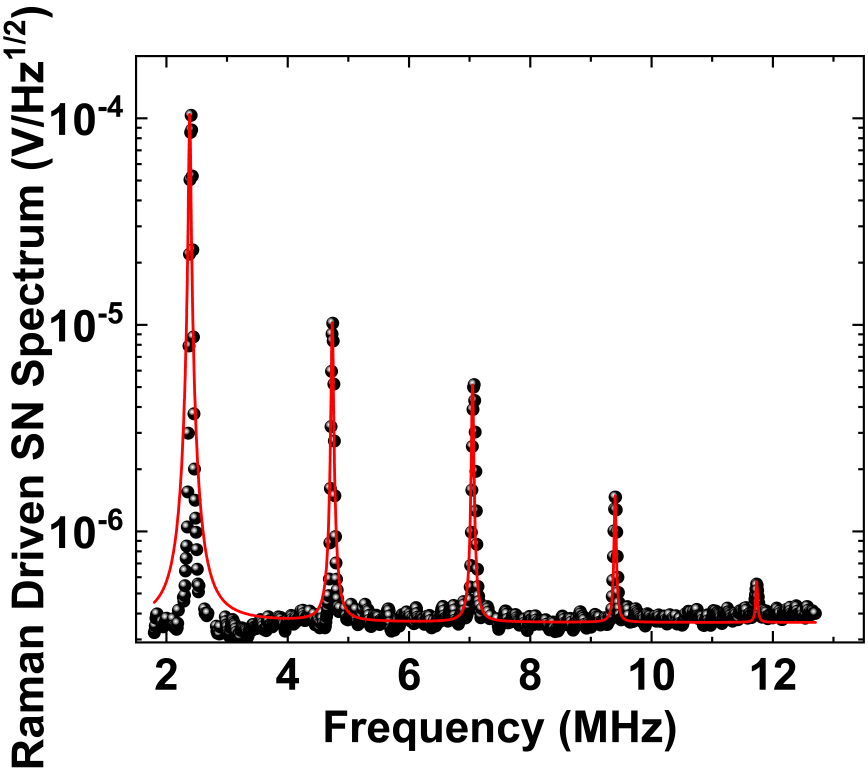


Figure 6.4: Shows the observation of multiple peaks in the Raman-driven spin noise spectrum. The probe beam power was 0.64 mW, and the Raman beam power was 4.42 mW. The cell temperature was maintained at $95^{o}C$. The Larmor frequency was 2.38 MHz.

driving couples the multi-level Zeeman manifold of ^{85}Rb atoms. By systematically varying the experimental parameters—such as atomic density, Raman drive strength, probe beam intensity, and the external magnetic field—we directly observe the formation and evolution of higher harmonics in the spin-noise spectrum.

When a static magnetic field is applied, the degeneracy of the ground- and excited-state hyperfine manifolds ($^2S_{1/2}$, $F = 3$ and $^2P_{3/2}$, $F' = 4$) is lifted, resulting in a set of Zeeman sublevels separated by the Larmor frequency ν_L. Under the action of two coherent Raman fields, multiple transitions between these sublevels become simultaneously accessible. The bichromatic optical drive thus generates a network of coupled states forming a CLS, schematically shown in Figs. 6.2 (b) and 6.3.

The experimentally measured Raman-driven spin-noise spectrum (RDSNS) in Fig. 6.4 exhibits not a single resonance, but a series of well-resolved peaks located at ν_L, $2\nu_L$, $3\nu_L$, $4\nu_L$, and $5\nu_L$. These peaks are evenly spaced by $\nu_L = 2.38$ MHz, forming a distinct frequency comb in the spin

noise signal. Such a comb-like structure clearly indicates that the Raman fields enable long-range coupling across multiple Zeeman sublevels, resulting in multi-photon mixing among the cascaded Raman pathways. The observation of five harmonics is consistent with the Zeeman structure of the $F = 3$ ground state manifold, which contains seven magnetic sublevels ($m_F = -3, \ldots, +3$). The n^{th} harmonic corresponds to coherences between states separated by $\Delta m_F = n$. Since the maximum separation within the manifold is $\Delta m_F = 6$, the number of possible harmonic orders is fundamentally bounded by the available Zeeman structure. In practice, higher-order harmonics beyond the fifth are strongly suppressed by decoherence and finite Raman coupling strength. It is important to distinguish between the structural and dynamical limits governing the observable harmonic order. Structurally, the $F = 3$ ground manifold contains seven Zeeman sublevels, allowing in principle up to six possible coherence orders ($\Delta m_F \leq 6$). However, the amplitude of the n^{th} harmonic arises from an n-photon Raman process and scales approximately as $(\Omega^2/\gamma\gamma')^{n-1}$. Each additional harmonic therefore introduces an extra factor of the effective Raman coupling relative to the relaxation rates. Under our experimental parameters, the sixth-order coherence remains below the detection threshold, resulting in the observation of five harmonics. Increasing Ω could, in principle, make higher-order harmonics visible, although power broadening and enhanced decoherence ultimately impose a practical upper bound. In principle, increasing the Rabi frequency could enhance visibility of additional harmonics up to the structural limit imposed by the manifold.

The origin of these harmonics can be understood in terms of the underlying spin coupling dynamics. At moderate drive strengths, the Raman fields synchronously establish coherence between neighbouring magnetic sublevels at the frequency difference δ_{12}, producing the primary RDSNS peak. When the drive strength is increased, higher-order couplings become significant, establishing coherence between next-nearest and next-next-nearest sublevels. Each of these higher-order processes generates a distinct resonance at integer multiples of δ_{12}—for instance, at $2\delta_{12}$, $3\delta_{12}$, and beyond—manifesting as the observed harmonic series. When δ_{12} matches the Larmor frequency, we get the strongest signal. This is the condition of the resonant spin precession of the atomic ensemble in the applied magnetic field. As expected, the amplitude of the harmonics gradually decreases with increasing order, reflecting the smaller fraction of atoms that can be coherently coupled across larger Zeeman energy separations and the enhanced susceptibility of

these transitions to decoherence.

To characterise this behaviour quantitatively, we define the relative intensity of the n^{th} harmonic as $R_n = I_n/I_1$, where I_n is the spectral amplitude of the n^{th} harmonic and I_1 corresponds to the fundamental peak. Figures 6.5a and 6.5b present the experimentally obtained dependence of R_n on the Raman drive amplitude. We interpret that the harmonic amplitudes are growing with the Rabi frequency Ω, as expected theoretically. Enhanced driving lifts the multi-photon coupling amplitudes, raising the coherence over more widely spaced Zeeman sublevels. However, this growth ultimately saturates as the system reaches a regime in which increased drive strength no longer leads to additional coherent population transfer due to competing relaxation mechanisms.

The ordering of harmonic amplitudes seen in the experiment is straightforward: the first harmonic is always the largest, followed by decreasingly weaker higher orders. Two primary mechanisms explain this systematic decrease. First, the number of atoms that can be coherently driven between increasingly distant magnetic sublevels diminishes rapidly as the coupling order increases. Second, higher-order processes are more sensitive to decoherence, phase instability, and imperfect optical alignment. Consequently, the measured variation of R_n with both Ω and harmonic order reflects a delicate balance between coherent multi-photon coupling and relaxation dynamics, captured by the competing rates Ω, γ, and γ'. The systematic decrease in harmonic amplitude with increasing order has two distinct origins. First, the number of available Zeeman pairs separated by $\Delta m_F = n$ decreases linearly as $(7 - n)$ for the $F = 3$ manifold. This geometric factor contributes to the ordering of harmonic strengths. However, this linear reduction alone cannot explain the observed rapid suppression of higher harmonics. The dominant mechanism arises from the multi-photon nature of the Raman coupling. The n^{th} harmonic corresponds to an n-step coherent Raman process whose amplitude scales approximately as $(\Omega^2/\gamma\gamma')^{n-1}$. Each additional order therefore introduces an extra factor of the effective coupling strength relative to the relaxation rates, leading to a power-law suppression of higher harmonics. The experimentally observed hierarchy thus reflects primarily the nonlinear scaling of multi-photon coherences, with the combinatorial Zeeman factor playing a secondary role.

A particularly interesting feature of these measurements is the existence of a threshold in the drive strength below which higher-order harmonics are essentially absent. The second, third, fourth, and fifth harmonics begin to appear only beyond critical drive strengths of approximately

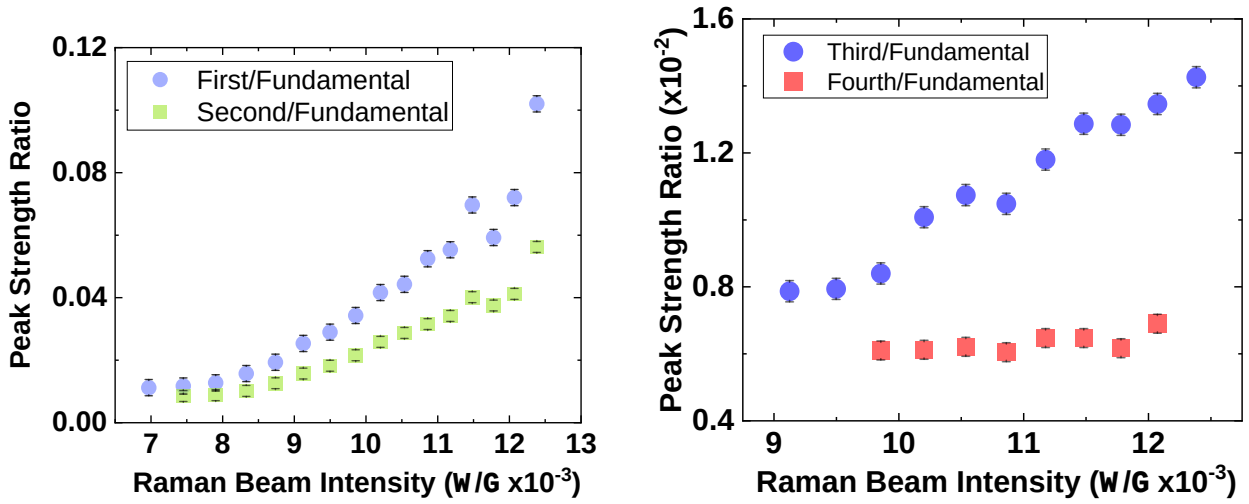
$8.0\times10^{-3}\,\Omega/\Gamma$, $8.5\times10^{-3}\,\Omega/\Gamma$, $9.5\times10^{-3}\,\Omega/\Gamma$, and $12.0\times10^{-3}\,\Omega/\Gamma$, respectively. This progressive increase in the threshold with harmonic order implies that higher-order population transfer requires stronger driving fields to overcome the larger energy gaps between widely separated Zeeman states. Beyond this threshold, the harmonic amplitudes increase rapidly with Ω, confirming their multi-photon origin.

These observations offer several important insights into the nature of coherent light–matter interactions in atomic vapours. First, the emergence of harmonic structures in the spin-noise spectrum demonstrates that the Raman-driven system supports long-range coherences that extend across multiple Zeeman sublevels. Second, the dependence of harmonic amplitudes on the drive strength provides a direct experimental handle for studying multi-photon coupling hierarchies and testing theoretical models of coherence propagation in multi-level systems. Finally, the ability to tune the relative harmonic strengths by varying the optical drive offers a route to optimising the signal-to-noise ratio and to selectively enhance specific coherence pathways. Taken together, these results establish Raman-driven spin noise spectroscopy as a sensitive and quantitative probe of spin dynamics, capable of revealing subtle correlations that are inaccessible in equilibrium spin-noise measurements.

6.6 Density Dependence of Harmonic Formation

Atomic ensemble density is also important in deciding the amplitude and spectral properties of the spin noise signal. The atomic density is directly responsible for determining the number of atoms involved in collective spin fluctuations, and hence it serves as an effective tuning parameter for the general magnitude of the spin-noise response. The density can be finely tuned by varying the vapour cell temperature, which controls the vapour pressure and hence the number of atoms participating. Generally, the overall spin-noise power increases with density since a higher ensemble is responsible for the magnetisation fluctuations detected through the Faraday rotation of the probe beam [53, 66]. But the high-order structure of the spin-noise spectrum, especially the ratio of the strength of higher harmonics to the fundamental, has a more complex and illuminating density dependence.

The experimentally determined ratios of the first and second harmonic peak intensities to the fundamental peak intensity as atomic density is varied by changing the cell temperature from 80°C



(a) (b)

Figure 6.5: Illustrates the dependence of harmonic peak strength ratios on the total Raman beam intensity at a cell temperature of 95°C, corresponding to a density of 4.5×10^{12} atoms/cc. The total Raman beam power was varied from 0.42 to 4.42 mW. (a) Ratio of the first (light blue circles) and second (green squares) harmonics to the fundamental peak and (b) ratio of the third (dark blue circles) and fourth harmonic (red squares) to the fundamental peak are plotted for various Raman beam intensities.

to 105°C are displayed in Fig. 6.6. As the overall spin-noise power increases with density, so do both the harmonic ratios. This trend suggests that, while the driving fields still cause coherent spin oscillations, the higher-order harmonics become increasingly suppressed at higher densities. That is, as more atoms are participating in the spin ensemble, the spectral weight accumulates in the fundamental resonance, while the harmonics are being increasingly washed out.

This behaviour can be explained as a consequence of the increased collisional processes that accompany increased density. In more concentrated vapours, the average free distance between atomic collisions is reduced, resulting in more frequent spin-randomising collisions, as well as atom–atom and atom–wall collisions. These collisions disrupt the coherent spin precession induced by the Raman fields, in effect shortening the time during which an atom can remain phase-coherent with the collective oscillation. The outcome is a more rapid loss of spin correlations and thus a related attenuation of the amplitudes of the higher-order harmonic components, which depend on multi-photon coherence among far-separated Zeeman sublevels.

The relative harmonic intensity ratio $R_n = I_n/I_1$ is expected to fall off, which expresses the sensitivity of higher-order transitions to dephasing. With increasing atomic density, γ' increases

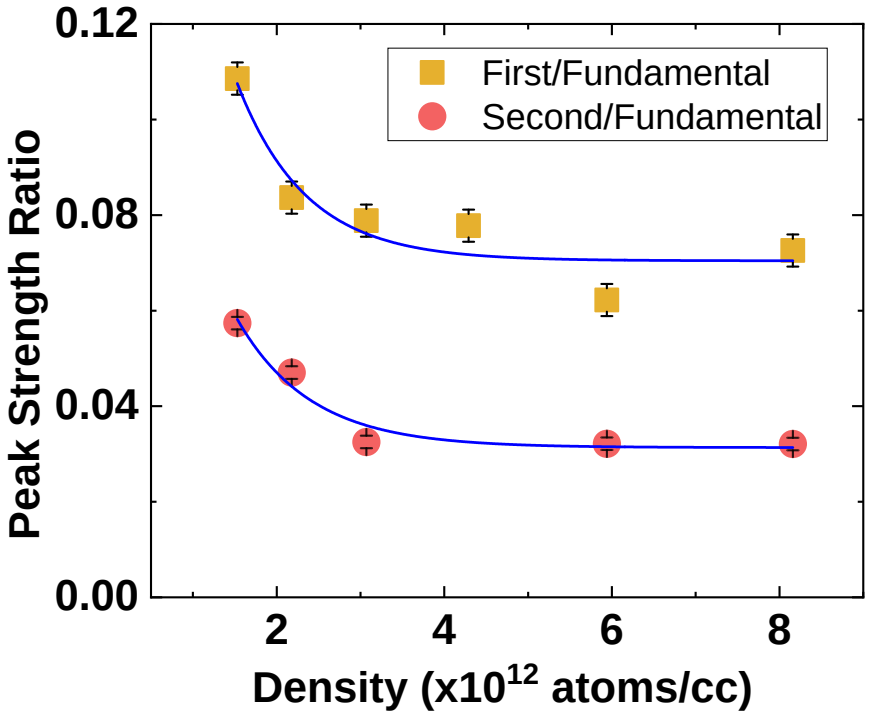


Figure 6.6: Shows the dependence of the peak strength on the density of atoms. The density inside the vapour cell was varied by changing the temperature from 80^oC to 105^oC, and the peak strength ratio of the first harmonic (yellow squares) and second harmonic (red circles) to the fundamental peak was measured. The blue lines serve as guides to the eye, illustrating the decreasing peak strength ratio as density increases.

because of collisional broadening, hence decreasing the coherence lifetime τ_c. The harmonic amplitudes thus decay exponentially more rapidly with increasing density, but the fundamental peak is relatively resilient since it only involves nearest-neighbour spin coherences.

These findings are in agreement with previous measurements [171], wherein the fundamental peak intensity continued to increase with density, while the higher-order harmonics diminished in a systematic manner. The competition between these two divergent trends, the increase in net spin-noise power and the diminution of higher harmonics, demonstrates a characteristic reordering of driving intensity into harmonic orders. Physically, one can view it as a competition between coherent optical driving, which attempts to create long-range spin correlations, and collisional decoherence, which destroys them. At low density, there is enough room for the optical drive to dominate, and higher harmonics will rise forth clearly. At high densities, dephasing will take over the coherent drive, essentially reducing the system back to a largely fundamental response.

This density-dependent redistribution has significant ramifications both for basic research and

applications. Practically speaking, it highlights the need to be within an optimal range of density where coherent effects are robust enough to generate detectable harmonics, without being so dense that collisional broadening takes effect to eliminate them. In quantum metrology and magnetometry applications, control of such a nature is critical to maximising sensitivity. In addition, the systematic variation of harmonic ratios with density indicates a possible diagnostic application: a calibrated vapour cell could, in principle, serve as a noninvasive *density sensor*, in which measured harmonic ratios translate directly into atomic number density or temperature.

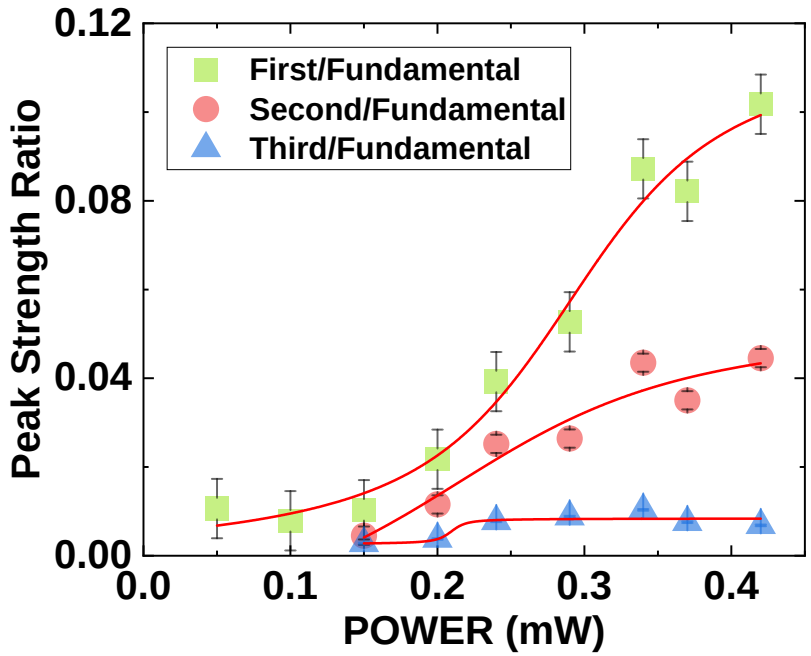


Figure 6.7: Illustrates dependence of the harmonic peak strength ratio on probe beam power. Increasing probe intensity enhances atom–photon interaction, strengthening both first and higher harmonic peaks. At low power, the signal remains buried in noise, while at higher powers, saturation and dephasing limit further growth. The red lines are guide to eye to illustrate the growth of the peak strength ratio with varying probe power.

More generally, these findings underscore that the harmonic structure of the driven spin-noise spectrum contains fine information about the interplay between coherent coupling and decoherence in multi-level atomic systems. From the analysis of the evolution of the harmonic amplitudes with the atomic density, one has direct access to the competing action of optical driving, collisional dynamics, and relaxation processes. This knowledge not only provides a sharper interpretation of Raman-induced spin-noise spectra but also serves as a strong experimental tool for investigating the coherence properties of dense atomic ensembles in non-equilibrium situations.

6.7 Dependence on Probe Beam Intensity

The probe beam intensity plays a decisive role in shaping the measurable spin-noise signal, as it directly determines the strength of atom–photon interactions within the vapour. In spin noise spectroscopy (SNS), the optical probe serves both as a means of interrogating the collective spin state and as a transducer that converts intrinsic spin fluctuations into measurable polarisation fluctuations. The signal strength, therefore, depends not only on the intrinsic spin dynamics of the atomic ensemble but also on the optical response of the medium to the probing field.

At low probe intensities, the weak atom–photon coupling results in very small Faraday rotation fluctuations, often buried below the detector's electronic noise floor. In this regime, the measured power spectrum is dominated by technical noise, making the spin-noise signal indistinguishable from background fluctuations. As the probe intensity increases, the strength of the light–matter interaction grows, thereby enhancing the polarisation fluctuations induced by atomic spin noise. This amplification makes the spin-noise signal progressively more prominent above the detection noise level. The observed increase in signal amplitude with probe intensity is therefore not due to a change in the intrinsic spin dynamics, but rather to an improvement in the optical conversion efficiency of spin fluctuations into detectable polarisation fluctuations.

Figure 6.7 illustrates the plot of the peak strength ratio of the first, second and the third harmonic to that of the fundamental. We see that both the fundamental and higher harmonic components of the spin-noise spectrum increase monotonically with probe intensity up to a certain threshold. Beyond this regime, the signal amplitude tends to saturate, indicating that further increases in probe power do not translate into proportionally larger signals. This saturation behaviour arises because the atomic medium approaches an optical pumping or saturation limit, where the population distribution among magnetic sublevels becomes significantly altered by the probe itself. Once the probe intensity is comparable to or greater than the saturation intensity of the transition, additional power primarily contributes to heating and scattering rather than to coherent probing.

Physically, this behaviour can be understood by considering the probe-induced back-action on the atomic ensemble. At moderate intensities, the probe beam primarily acts as a passive observer, detecting spontaneous spin fluctuations without significantly perturbing the population distribution. This leads to optical pumping, modification of the steady-state populations, and partial

depolarisation of the spin ensemble. As a result, while the overall signal level initially increases, the intrinsic linewidth of the spin-noise resonance can broaden, and the harmonic ratios may no longer reflect purely equilibrium spin fluctuations. At high probe intensities, the additional dephasing mechanisms start to arise, thereby reducing the coherence time. This results in a complete washing out of the higher-order harmonic components.

The enhancement of harmonic content with probe intensity thus reflects a delicate balance between signal amplification and decoherence. At intermediate probe powers, the signal-to-noise ratio is optimal: the polarisation fluctuations are sufficiently strong to be well above the detector noise floor, while the probe-induced perturbations remain minimal. In this range, higher-order harmonics become clearly visible, and their relative amplitudes $R_n = I_n/I_1$ increase steadily with probe intensity. The physical origin of this enhancement lies in the increased effective interaction strength between the collective spin precession and the optical field, which allows the probe to sample a larger fraction of the ensemble's correlated spin motion.

At higher probe intensities, however, this trend reverses. Power broadening and probe-induced collisions become non-negligible, especially in a hot vapour where photon scattering contributes to additional dephasing channels. Excessive probe power may also increase atomic temperature locally, modifying the effective density and collision rate within the interaction region. These effects collectively lead to a degradation of coherence and a reduction in harmonic contrast. Thus, while moderate probe intensities amplify the multi-photon features in the Raman-driven spin noise spectrum, excessively strong probing can obscure them.

From a practical standpoint, the dependence of the harmonic structure on probe intensity provides valuable guidelines for optimising experimental sensitivity. The probe power must be chosen such that it maximises the spin-noise signal without significantly disturbing the spin populations or inducing unwanted optical pumping. The optimal operating regime corresponds to the onset of saturation, where the signal-to-noise ratio is high and the higher harmonics remain discernible without excessive linewidth broadening.

In summary, increasing the probe beam intensity enhances the detectability of spin fluctuations by strengthening atom–photon coupling and improving the optical transduction of spin noise into measurable polarisation noise. The higher harmonic peaks in the Raman-driven spin-noise spectrum grow with probe intensity up to a saturation point, beyond which probe-induced effects

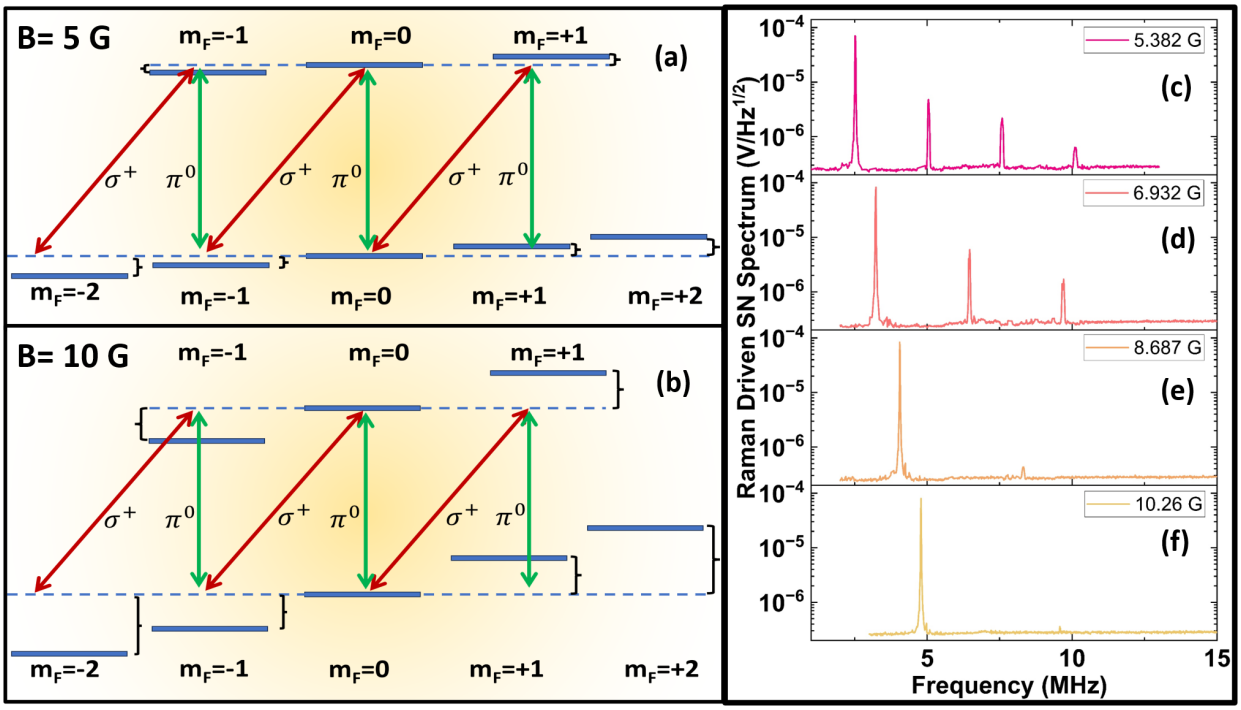


Figure 6.8: Shows the study of the effect of external magnetic field on the harmonic structure of the spin noise peaks. Schematic of Raman coupling between Zeeman sublevels (m_F states) of the ground-state hyperfine manifold (a) at low field and (b) at high field. Red arrows indicate σ^+ transitions and green arrows indicate π^0 transitions, forming cascaded multi-Λ pathways. (c–f) Raman-driven spin noise spectra recorded at different magnetic field strengths (5.38 G, 6.93 G, 8.69 G, and 10.26 G). The fundamental Larmor peak is visible in all cases, while higher-order harmonics weaken progressively with increasing magnetic field due to reduced resonance overlap and detuning of Raman coupling from higher-order transitions.

dominate. Understanding and controlling this balance between amplification and perturbation is essential for accurate spin noise measurements and for exploiting SNS as a precision tool in quantum sensing and nonlinear optical spectroscopy.

Having established how probe intensity affects the harmonic content of the spin-noise spectrum, we now turn to the role of the external magnetic field, which defines the fundamental Larmor precession frequency and governs the spacing and strength of the observed harmonics.

6.8 Magnetic Field Dependence of Harmonic Formation

The applied magnetic field is crucial in determining the structure and spacing of the spin-noise spectrum. By fixing the Larmor precession frequency, the applied magnetic field dictates both

the location of the fundamental resonance and the comparative intensity of its higher harmonics. In Raman-driven spin noise spectroscopy (RDSNS) geometry, the external magnetic field also determines the energy splitting between the Zeeman sublevels of the ground-state hyperfine multiplet, and hence the effective coupling between them. Consequently, changes in the magnetic field alter the level of coherence as well as the relative peak intensity of harmonic order peaks in the spin-noise spectra.

Figure 6.8 displays this dependence. The magnetic field was swept from about 5 G to 10 G, and the resulting spin-noise spectra were measured under otherwise comparable experimental conditions. At lower magnetic fields, a rich harmonic structure is seen; the fundamental Larmor peak, along with its higher-order harmonics, stands out clearly in the observed spectrum. With increasing magnetic field, however, the amplitudes of these higher-order harmonics fall systematically, even when the fundamental peak remains strong. This behaviour shows that the intensity of the coupling among various Zeeman sublevels decreases as the Zeeman splitting increases.

The physical origin of this behaviour is a consequence of the nature of the Zeeman effect. The sublevels in each hyperfine manifold, designated by their magnetic quantum number m_F, suffer an energy shift $\Delta E = g_F \mu_B B m_F$, with B denoting the magnetic field, g_F denoting the Landé g-factor, and μ_B denoting the Bohr magneton. The energy gap between successive m_F states increases linearly with B, making the Zeeman manifold wider. The Raman driving fields, which are resonantly coupled to pairs of m_F states at low fields, are increasingly detuned from these transitions for higher fields. As a result, the effective Raman coupling diminishes, and the coherence between well-separated sublevels is reduced. This leads to a suppression of the amplitudes of higher-order harmonics that rely on effective coherent multi-photon transitions, which are becoming increasingly nonresonant in order to support these harmonic modes.

In weak magnetic fields, the Zeeman splitting is small compared to the Raman detuning, and the optical fields simultaneously couple multiple adjacent m_F levels. This multi-level coupling produces CLS channels, where atoms coherently oscillate between numerous magnetic sublevels. Multiple Raman channels contribute constructively in this regime, generating long-range spin coherences and a dense harmonic structure. The spin-noise spectrum found has peaks of strong intensity at integer multiples of the Larmor frequency, corresponding to collective oscillations among multiple Zeeman transitions.

When the strength of the field is increased, the dynamics alter considerably. The energy gap between successive m_F levels becomes comparable to or greater than the effective Rabi coupling Ω, and thus resonance overlap among Raman transitions decreases. The CLS configuration progressively decomposes into separate Λ systems, each only weakly coupling a small subset of m_F states. The coherence previously spanning multiple levels is now limited to smaller subspaces, and the system is more akin to an ensemble of weakly coupled few-level subsystems. Such a breakdown of coherence appears in the form of a damping of higher-order harmonics in the spin-noise spectrum.

Figure 6.8 illustrates schematically this transition: panels (a) and (b) illustrate the network of couplings at low and high magnetic fields, respectively. At low fields, σ^+ and π^0 transitions both contribute together, creating a dense network of cascaded Λ couplings. At higher fields, detuning of the Raman beams from higher-order transitions decreases overlap between various coupling channels, effectively decoupling the transitions. The spectra measured [Fig. 6.8(c–f)] are clearly indicative of the fact that although the fundamental peak is always present for all field strengths, the higher harmonics decay progressively with increasing B. This is direct experimental evidence for the degradation of multi-level coherence with larger Zeeman splitting.

This behaviour has wider implications for both basic and applied grounds of driven spin-noise spectroscopy. On physical grounds, it emphasises the fine balance between coherent driving and Zeeman detuning in controlling the range of spin correlations in multi-level systems. On practical grounds, such dependence offers an avenue for optimising field sensitivity in magnetometric uses.

In short, a systematic decrease in higher-order harmonic amplitudes in the spin-noise spectrum is caused by a stronger magnetic field strength. This phenomenon arises due to Zeeman-induced detuning of Raman coupling paths, which reduces multi-level coherence and restricts population transfer between distant m_F states. The findings clearly demonstrate how the magnetic field serves as a control parameter for the magnitude of coherence in driven atomic spin systems, thereby providing new insight into the interplay between optical driving, magnetic splitting, and spin dynamics.

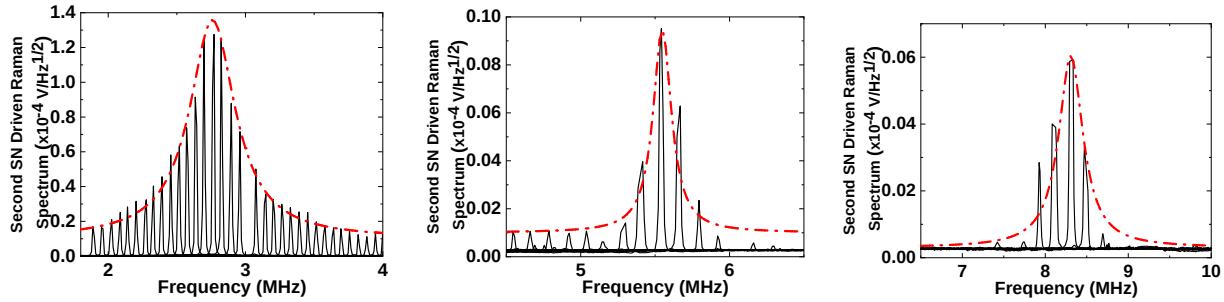


Figure 6.9: Illustrates the dependence of drive frequency on the Raman Driven Spin Noise Signals. The temperature is maintained at 95°C. The total Raman beam intensity was kept at 3.75 mW. The probe beam power was 0.7 mW. Each black peak corresponds to a particular Raman driving frequency. In each plot, the red dot-dashed line is drawn as a guide to the eye to trace out the envelope of the entire spectrum. (a) Shows the fundamental peaks when the driving frequency (δ_{12}) is scanned across the Larmor frequency (ν_L). The strongest peak appears when $\delta_{12} = \nu_L$. (b) Shows the occurrence of the first harmonic peaks with the strongest peak appearing at $2\nu_L$. (c) Shows the observation of the second harmonic peaks with the strongest peak appearing at $3\nu_L$.

6.9 Detection Sensitivity of External Magnetic field

An important parameter governing the strength and spectral position of the spin-noise signal in Raman-driven configurations is the frequency difference between the two Raman fields, denoted by δ_{12}. This frequency difference determines the effective two-photon detuning, which in turn defines the resonance condition for coherent population oscillation between the Zeeman sublevels. In previous work [74, 171], it was shown that as δ_{12} is scanned across the Larmor frequency ν_L, a pronounced resonance appears in the spin-noise power spectrum. The amplitude of this resonance grows as δ_{12} approaches ν_L, reaching a maximum when $\delta_{12} = \nu_L$, where the Raman driving fields are exactly resonant with the Zeeman splitting of the ground-state hyperfine manifold.

This behaviour can be understood as a manifestation of the Raman resonance condition, where the effective Rabi coupling between the two spin states is maximised. At this point, the energy difference between the Raman beams exactly compensates the Zeeman energy splitting between magnetic sublevels, allowing efficient population transfer and sustained coherent spin oscillations. As a result, the spin ensemble exhibits strong collective precession, giving rise to a prominent peak in the spin-noise spectrum. The observed resonance thus marks the condition for maximum coherence between the coupled states.

Interestingly, our measurements reveal that this resonance behaviour is not confined to the

fundamental Larmor peak alone but extends to the higher harmonics as well. Figure 6.9 illustrates that when δ_{12} approaches integer multiples of ν_L, the first and second harmonic peaks also display resonance-like enhancements. Specifically, the first harmonic reaches its maximum at $2\nu_L$ and the second harmonic at $3\nu_L$, mirroring the resonance structure of the fundamental. This demonstrates that the higher harmonics correspond to multi-photon Raman processes that are resonantly enhanced when the drive frequency difference matches integer multiples of the Larmor precession frequency.

A particularly notable feature is the higher sensitivity of the harmonic peaks to detuning. Whereas the fundamental spin-noise peak remains visible even for moderate detuning of δ_{12} from ν_L, the higher-order harmonics appear only when δ_{12} is extremely close to the Larmor frequency. Small deviations from resonance are sufficient to suppress these higher-order features, indicating that multi-photon coherence is highly sensitive to the precise frequency matching of the Raman drive. This pronounced sensitivity implies that the higher harmonics can serve as effective probes for detecting small variations in the magnetic field or in the Raman detuning, since such changes directly shift the resonance condition. The strong dependence of harmonic amplitude on δ_{12} thus offers a pathway for precision magnetometry, where even minute field fluctuations can be detected through changes in harmonic visibility.

This detuning dependence reinforces the interpretation that the harmonic comb observed in the driven spin-noise spectrum originates from coherent Raman coupling across multiple Zeeman sublevels. The resonance of each harmonic at distinct multiples of ν_L highlights the multi-level, multi-photon nature of the underlying dynamics. Together with the previously discussed dependences on atomic density, probe intensity, and magnetic field strength, this behaviour completes a coherent picture of how various experimental parameters influence the formation and strength of the spin-noise harmonics.

6.10 Conclusion and Outlook

In this work, we have experimentally demonstrated the formation of multiple, equally spaced peaks in the spin-noise spectrum of hot ^{85}Rb vapour under Raman driving. By systematically varying key experimental parameters—including the Raman frequency difference, magnetic field,

probe and drive intensities, and atomic density—we have explored the conditions under which these harmonic peaks emerge and evolve. The observation of these harmonics establishes the presence of long-range multi-level coherence within the ground-state Zeeman manifold, induced by the Raman coupling of adjacent magnetic sublevels. The resulting harmonic comb structure represents a distinct signature of nonlinear spin dynamics in optically driven atomic systems.

The dependence of harmonic amplitudes on atomic density and probe intensity reflects the competition between coherent driving and collisional decoherence. At moderate densities and optimal probe intensities, strong multi-photon coupling leads to a well-defined harmonic structure, while higher densities and excessive probe powers introduce dephasing and spectral broadening. Similarly, the suppression of higher-order harmonics with increasing magnetic field reveals how Zeeman-induced detuning disrupts long-range coherence, effectively limiting the number of strongly coupled states. These observations collectively map out a rich interplay between coherence, detuning, and decoherence that governs the harmonic landscape of the Raman-driven spin noise spectroscopy (RDSNS).

Our measurements further confirm that the harmonic intensities exhibit resonant enhancement when the Raman frequency difference δ_{12} matches the Larmor frequency ν_L. This resonance behaviour of higher harmonics provides a direct experimental demonstration of multi-photon Raman coupling processes in a thermal atomic vapour. The higher harmonics are particularly sensitive to small deviations in δ_{12}, suggesting potential applications in precision sensing. In particular, since even minute shifts in magnetic field or optical detuning significantly affect harmonic visibility, the system can function as a high-resolution magnetic-field probe, complementing traditional atomic magnetometry schemes.

More broadly, the observed sequence of harmonic peaks constitutes a driven *spin-noise comb*, analogous in concept to an optical frequency comb [216]. The formation of this comb reflects the periodic modulation of spin fluctuations and opens new possibilities for exploiting SNS in the frequency domain. Incorporating a high-finesse optical cavity could sustain and sharpen higher-order modes, thereby enhancing harmonic resolution. Moreover, the intrinsic shot-noise limit of SNS can be mitigated by employing phase-squeezed light [119, 217], which would reduce the measurement noise floor and improve the visibility of higher harmonics. Such techniques could enable ultra-sensitive detection of magnetic fields, spin correlations, and non-equilibrium

dynamics in atomic and solid-state systems.

In conclusion, Raman-driven spin noise spectroscopy offers a powerful and non-invasive platform for probing coherence, relaxation, and multi-level correlations in atomic vapours. The systematic study of harmonic generation presented here connects experimental observations with theoretical models of driven spin dynamics, providing a bridge between fluctuation-based spectroscopy and nonlinear coherent optics. Beyond its immediate implications for quantum sensing and metrology, this work establishes a foundation for exploring spin-noise phenomena in more complex systems—such as multi-electron atoms, molecules, and condensed-matter environments—where higher-order correlations and long-range coherences play a central role. The extension of these techniques promises to open new avenues in the study of non-equilibrium quantum systems and the development of next-generation quantum sensors.

"The more I learn, the more I realize how much I don't know."

— Albert Einstein

Chapter 7

Conclusion & Outlook

In this thesis, we addressed a broader aim of controlling, probing and understanding atomic systems. We explored a non-destructive way to study the spin dynamics of such systems using a technique known as Spin Noise Spectroscopy (SNS). We observed how it can be used as a precise tool to extract valuable properties of the spin system, such as mixture ratio, gyromagnetic ratio, density of the probing region, and, most importantly, the magnetic field. Despite being an old technique, its applications were numerous, and it paved the way towards Quantum Non-Demolition measurements (QNDs). However, being solely a noise-based measurement, it is often limited to weak signal strengths. In this thesis, we developed a robust yet minimally destructive technique using a two-photon coherent optical driving protocol, specifically Raman-Driven Spin Noise Spectroscopy (RDSNS). Such a driving scheme helped us amplify our signal by a million-fold while maintaining a similar noise floor. Driving a system that has an inherent atomic population oscillation at the Larmor frequency is similar to driving a forced damped harmonic oscillator. When the driving frequency matches the frequency of the inherent oscillation, a resonance condition is reached, resulting in signal amplification. With this, we overcame the detection limitations

posed by traditional SNS techniques. This helped us extend our measurement techniques to sophisticated protocols, such as Phase-Locked Loop-Integrated lock-in detection schemes, signal modulation, and carrier detection methods. This enabled us to build and characterise an extremely precise and fast atomic magnetometer. We were able to achieve a highly sensitive and broadband magnetometer. Such magnetometers have wide applications in Quantum Sensing, metrology, navigation, and medical diagnostics, to name a few. This technique enabled us to study systems in real-time. Such fast detection schemes are always helpful for studying dynamical atomic systems with finer details. We extended the application of our technique to real-time density studies. To achieve this, we needed to build a cold atom machine capable of capturing a high number of atoms and simultaneously laser-cooling them. Beginning from the basic mechanisms governing atom–light interactions, we progressed toward practical realisations of trapping, imaging, and diagnostic tools that are central to modern atomic physics experiments. The design of a $2D^+$ MOT loading into a 3D MOT for both species enabled a high flux of atoms to be captured and cooled into the 3D MOT. Such a design was needed to get a high number of atoms in our quantum gas system. A key part of this work has been the study of heteronuclear cold collisions in a dual-species MOT. We demonstrated that inelastic collisions between trapped atoms of different species result in significant atom loss, thereby reducing trap efficiency. By comparing these processes with the well-understood homonuclear case, we highlighted the role of interspecies interactions in shaping the dynamics of multi-species systems. These insights are directly relevant for experiments seeking to realise ultracold mixtures for quantum simulation, precision metrology, and hybrid atom–molecule studies. My core idea behind building this machine was to explore spin-spin interaction studies using our sophisticated RDSNS scheme, which reveals deeper insights into the spin dynamics of the cold atomic cloud. Extending our work in multi-level atomic studies reveals a comb of spin noise peaks in the frequency domain. We parametrised these peaks by varying key parameters, such as magnetic field, drive frequency, probe beam intensity, and Raman beam intensity. While doing so, we get insights into the long-range coherence that forms and sustains in a strongly driven multi-photon process. We showed that it has wider implications in the field of precision magnetometry. We also demonstrated an analogy where such higher harmonic modes could be enhanced by integrating the system in cavities with high finesse, while sustaining higher-order modes as desired.

The detection of spin relaxation times in physical systems, including cold atoms, leads to a deeper understanding, particularly of the magnetic properties of matter. Moreover, understanding how inter-particle interaction leads to modifications of magnetic properties, such as spin projection noise and Larmor precession frequency, is valuable.

7.1 Outlook

In this work, we have successfully detected spin coherence signals in a Raman-driven cold ^{39}K atomic cloud and observed their modification in the presence of inter-species interactions when overlapped with a cold ^{23}Na ensemble. Using dispersive Faraday rotation fluctuation measurements, we probed the intrinsic spin coherence of potassium atoms in a minimally invasive manner. A significant frequency shift, on the order of several MHz, was observed in the spin coherence peak upon the introduction of sodium atoms, while the nominal unperturbed linewidth of the potassium coherence signal lies in the tens of kHz range—indicating a shift several orders of magnitude larger than the intrinsic width. Additionally, the inter-species coupling leads to enhanced spin relaxation, as reflected by a measurable increase in the coherence linewidth.

These results mark an important step toward understanding inter-species spin-exchange dynamics in dual-species ultracold systems. However, the underlying microscopic mechanisms governing the observed shifts and broadenings — such as spin-exchange collisions, light-assisted processes, and mean-field effects — remain to be explored in greater depth.

In the presence of an external magnetic field, both potassium and sodium atomic spins (S_{K} and S_{Na}) align along the local magnetic field direction. When the two species are spatially overlapped, the local field experienced by the potassium atoms is modified by the spin polarization of the sodium ensemble through interspecies spin–spin coupling. The relevant interaction Hamiltonian can be expressed as

$$H_{\mathrm{int}} = -J \sum_{i} \mathbf{s}_{\mathrm{K},i} \cdot \mathbf{s}_{\mathrm{Na},i}, \tag{7.1}$$

where $J > 0$ denotes the strength of the exchange coupling between the two spin species. This interaction effectively contributes an additional local magnetic field experienced by the potassium

atoms given by

$$\mathbf{B}_{\mathrm{eff,K}} = \mathbf{B}_{\mathrm{ext}} + \frac{J}{g_{\mathrm{K}}\mu_B}\langle \mathbf{S}_{\mathrm{Na}} \rangle, \tag{7.2}$$

where g_{K} is the Landé g-factor of potassium and μ_B is the Bohr magneton. Consequently, when the sodium cloud is introduced, the mean spin polarisation $\langle \mathbf{S}_{\mathrm{Na}} \rangle$ generates an effective field that either adds to or opposes the external bias field depending on the sign and orientation of the sodium spin polarisation. This results in a measurable shift in the Larmor precession frequency and hence the center frequency of the potassium spin coherence signal.

The associated Larmor frequency of the potassium atoms can then be written as

$$\omega_{\mathrm{L,K}} = \frac{g_{\mathrm{K}}\mu_B|\mathbf{B}_{\mathrm{eff,K}}|}{\hbar}. \tag{7.3}$$

Without sodium atoms, the potassium atoms see only the external bias magnetic field $\mathbf{B}_{\mathrm{ext}}$, resulting in the unperturbed spin coherence frequency. The measured frequency shift $\Delta\omega_{\mathrm{L,K}}$ and accompanying linewidth broadening therefore provide direct evidence of the alteration of the local magnetic environment and enhanced spin decoherence mediated through interspecies coupling.

Future studies can build upon these results in several significant ways. One obvious extension would be to systematically vary the interspecies coupling by changing the atomic densities and relative detunings of the probe and Raman beams. Such measurements would help disentangle the coherent and dissipative contributions to the resulting spin dynamics and enable a quantitative determination of the effective shifts in local fields. Moreover, detailed studies of the spin coherence lifetime using spin-echo or Ramsey-type sequences could distinguish between reversible dephasing, arising from fluctuations in the local magnetic field, and irreversible relaxation mechanisms. The inclusion of these techniques would make it possible to extract fundamental timescales associated with interspecies spin transfer and relaxation.

A further step would be to extend the current setup toward QND spin readout in the dual-species configuration. This could allow the observation of correlated spin noise and, in favourable conditions, the generation of entangled or correlated spin states between potassium and sodium atoms. On the theoretical side, it will be essential to develop a coupled spin-dynamics model that incorporates both mean-field local-field effects and stochastic spin-exchange processes. Such a model will help bridge experimental observations with microscopic parameters, such as the cou-

pling constant J, thereby enabling a more comprehensive understanding of the observed frequency shifts and broadenings.

In a broader context, this work demonstrates the capability of Raman-driven spin noise spectroscopy (RDSNS) as a sensitive, non-perturbative probe of multi-species quantum systems. The techniques developed here can be extended to study spin coherence and interaction-induced dynamics in other hybrid atomic ensembles, thereby contributing to the advancement of precision metrology, spin-based sensing, and quantum simulation platforms.

Appendix A

Probe Absorption by Cold Atoms

The probe beam is carefully aligned to pass through the cold atomic cloud. In order to ensure maximum overlap, a collimated 13 mm beam is made to pass through the MOT. The MOT was kicked using the probe being at resonance. This ensured that there was some overlap between the probe and the MOT. A similar strategy was used to align the Raman beams as well. Fig. A.1, represents the kick experiment performed. The left plot shows the decrease in the count of the atoms captured by the MOT when the on-resonant probe beam was allowed. The right side of the image shows the MOT fluorescence image captured by the camera. The bottom plot shows the position of the Raman beams' frequency. Finally, the absorption of the probe beam was monitored by scanning the probe laser and finally monitoring the intensity of the probe absorption on a detector. In fig. A.2, we illustrate how the percentage of absorption changes with the probe intensity. As the intensity of the probe beam was increased, the percentage of absorption was recorded. This is consistent with the following equation of scattering-

Fig. A.3 shows the absorption signal of the probe beam through the cold atomic cloud. The inset in fig. A.3 shows the Saturation Absorption Spectroscopy signal of potassium D2 transition.

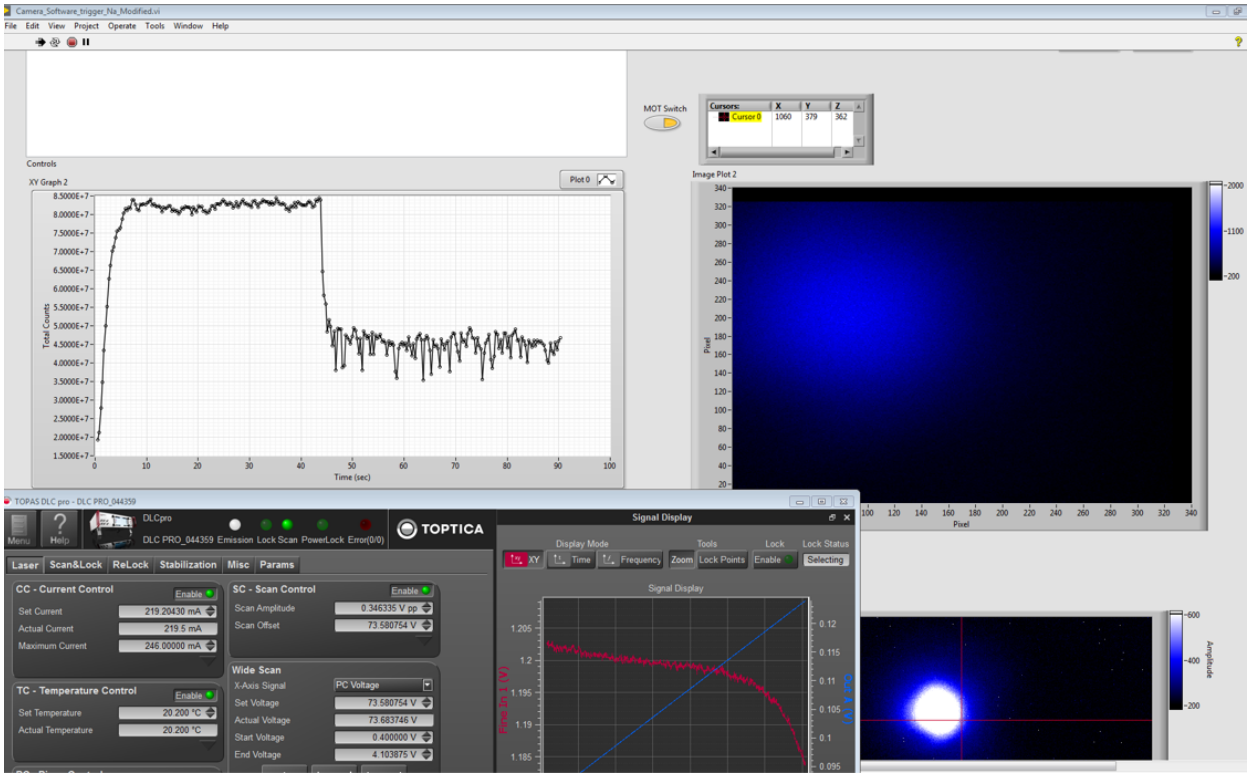


Figure A.1: Shows the LabVIEW program to monitor the number of atoms captured by the MOT using the fluorescence image captured by the camera in continuous acquisition. The plot below shows the frequency position of the Raman laser interpreted using the SAS signal. This light is then made to pass through AOMs in double pass configuration which detunes the light by +220 MHz.

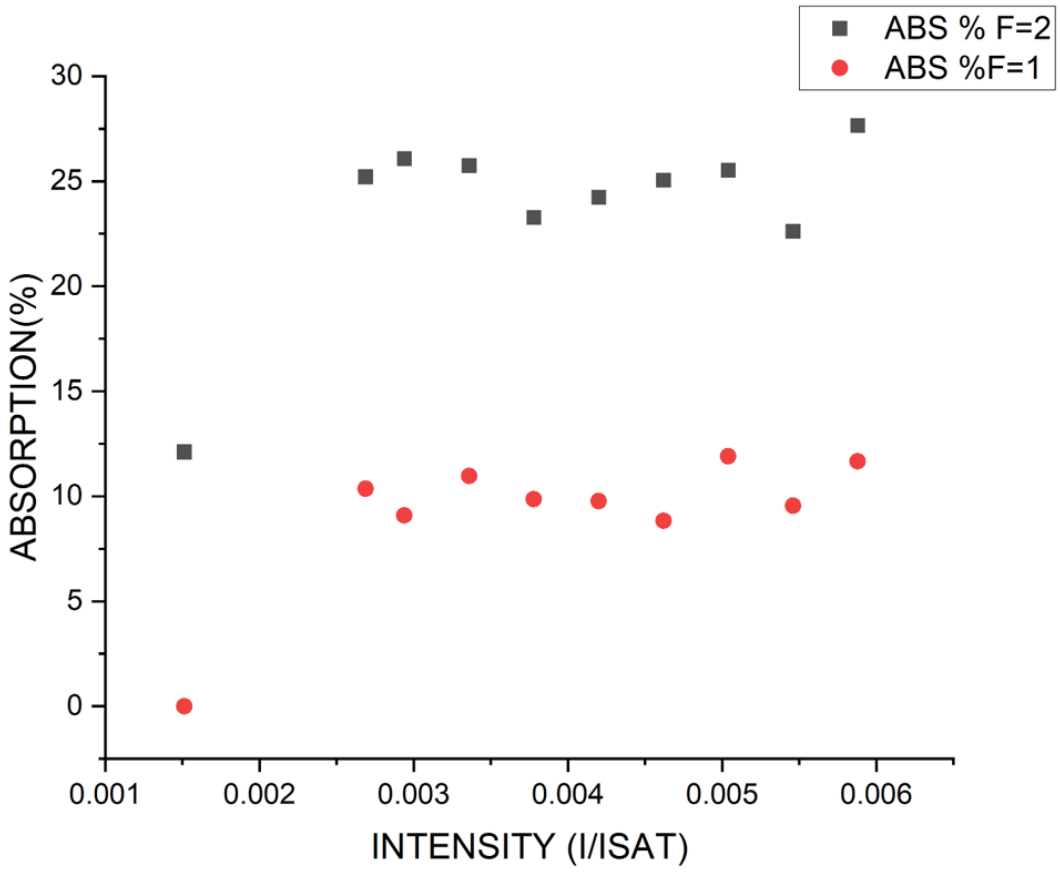


Figure A.2: Illustrates the percentage of the probe light being absorbed when an on-resonant probe beam passes through the cold atomic cloud, with changing probe beam intensity.

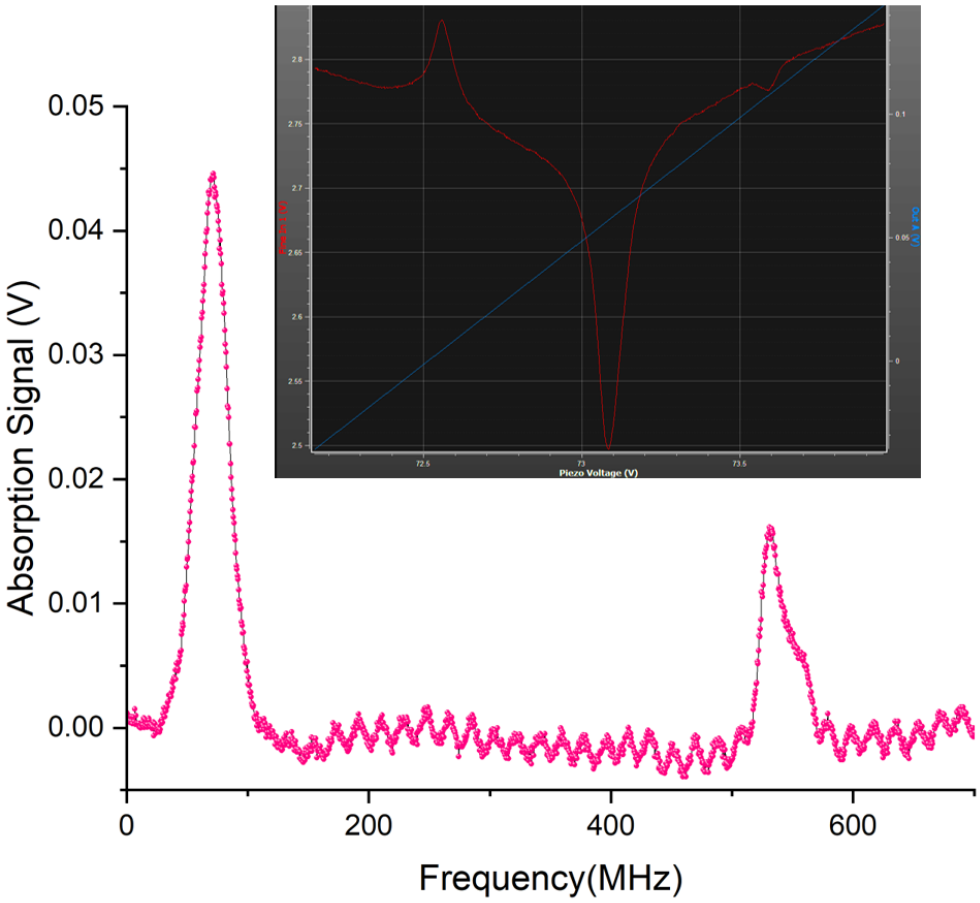


Figure A.3: Shows the absorption of a weak probe beam passing through the cloud. The probe laser has been scanned across resonance ($F = 1$ to F' and $F = 2$ to F' of the D2 transition of potassium atoms). The inset shows the scanning of the laser interpreted using the SAS signal. We see two peaks corresponding to the two resonant transitions.

In fig. A.4, we show the absorption dips corresponding to the two ground hyperfine states of potassium 39 as the piezo voltage of the probe laser is being scanned.

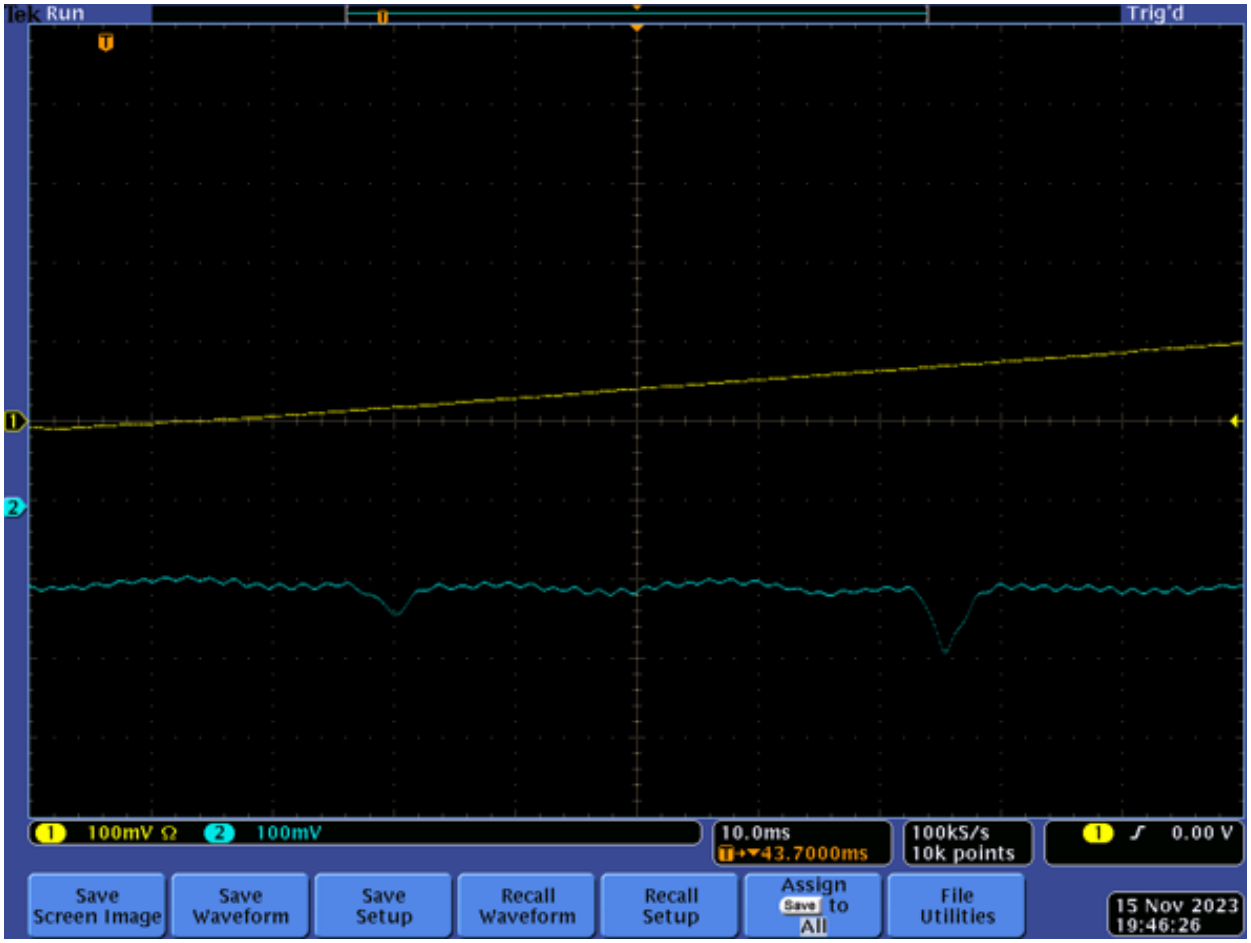


Figure A.4: Illustrates probe absorption signal by the cold atoms in an oscilloscope when the probe laser frequency is swept across resonance.The yellow line represents the piezo scan voltage signal, and the blue line is the absorption signal.

Appendix B

Phase Locked Loop

Motivation

In Raman-Driven Spin Noise Spectroscopy (RDSNS), two laser beams are frequency-shifted via AOMs (Acousto-Optic Modulators) are used to probe spin fluctuations in atoms. These AOMs are driven by independent RF signals generated by separate Voltage-Controlled Oscillators (VCOs). Due to differences in current and phase noise, a relative phase difference arises, causing the Raman detuning to fluctuate. This results in a jittery, unstable signal, making it difficult to extract meaningful information. To overcome this, one VCO is phase-locked to the other using a Phase-Locked Loop (PLL). This stabilizes the frequency difference and significantly improves the clarity of the RDSNS signal.

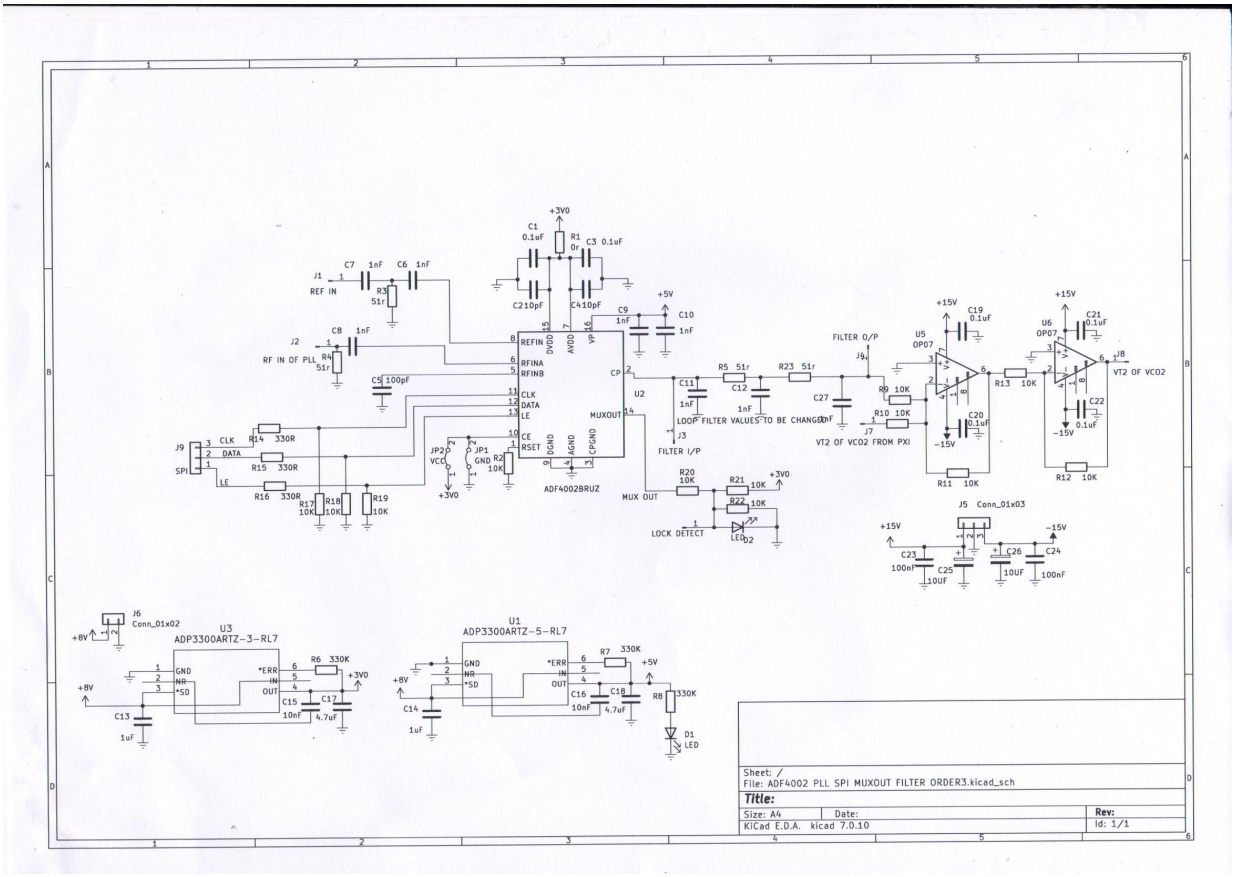


Figure B.1: Schematic scan of the PLL implementation.

Experimental Results

The frequency stability of our phase lock module was evaluated by recording beat signal data from the spectrum analyzer. Two measurement sets were taken: one with 10 loops and another with 50 loops, with each loop recorded at 10-second intervals. A Python program extracted the peak frequency from each spectrum, and the frequency drift was calculated. The total observed drift with PLL was approximately **69 Hz**, whereas without PLL, the drift was in the MHz range.

Implementation of Phase Lock Loop

Two AOMs are each driven by a separate VCO. The auxiliary outputs from both VCOs are fed into RF splitters (GALI-5+), and the outputs are combined in a mixer (ZLW-1H). The intermediate frequency (IF) output, which corresponds to the error signal between both VCOs, is passed through

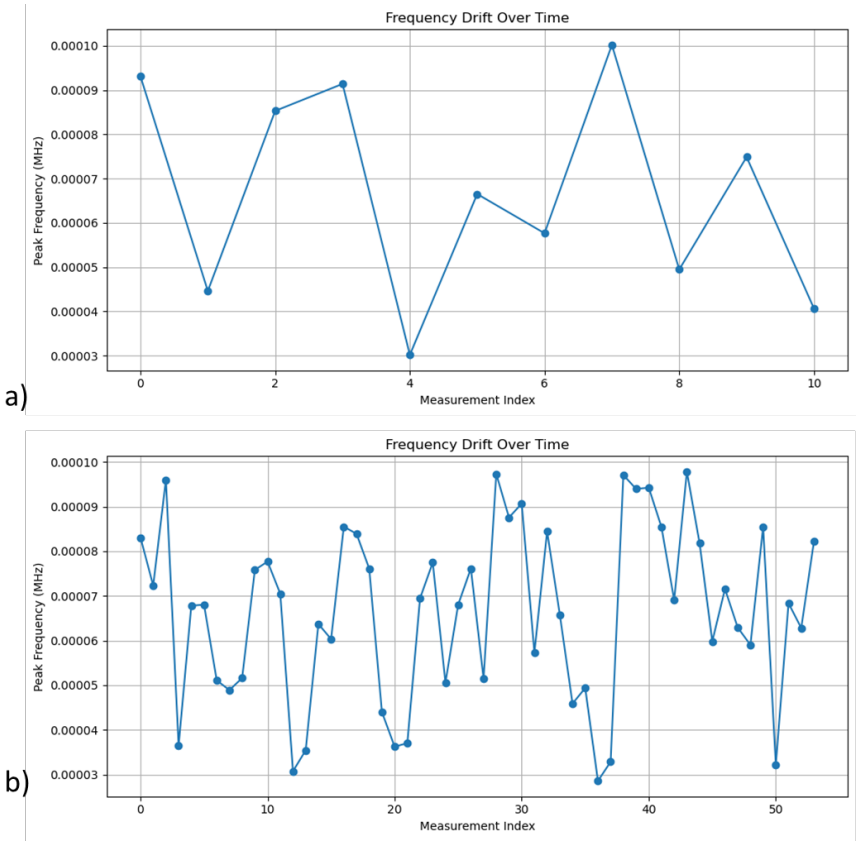


Figure B.2: Frequency drift over time observed on the spectrum analyzer for (a) 10 loops and (b) 50 loops.

low-pass filters (MLP-5) to remove higher-order components. The filtered signal is then passed through an RF switch (SK-2), subsequently amplified using a low-noise amplifier module (TAS 4601V, gain of 10×), attenuated by 10 dB, and finally fed into the PLL circuit ("Jx" input of our Phase Lock Module). Simultaneously, the combined LO and RF outputs from the VCOs are sent to another mixer (ZLW-1H), which acts as a reference for the spectrum analyzer through a 10 dB attenuator.

Power Supply Regulation

The ADF4002 requires two supply rails: +3 V and +5 V. The VP supply (charge pump and VCO interface) must always be greater than or equal to the digital supply (VDD). To satisfy this, the module is powered from a single +8 V input (J6). Two low-dropout regulators are used: U3 (ADP3300ARTZ-3) provides +3.0 V and U1 (ADP3300ARTZ-5) provides +5.0 V. Both rails are

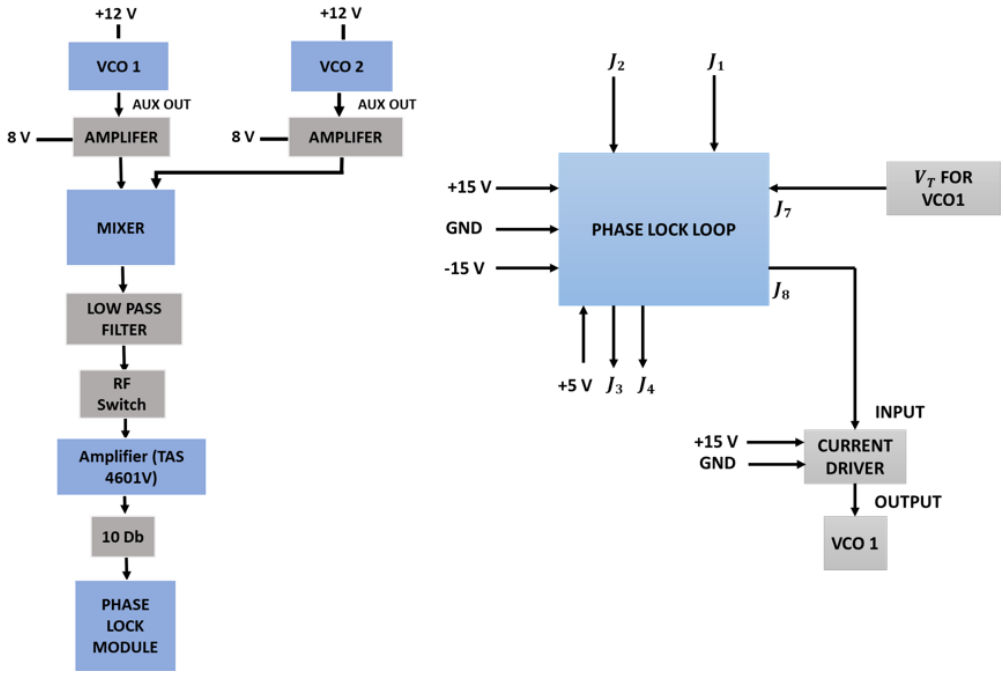


Figure B.3: RF signal processing chain used for phase locking in the RDSNS setup. Two VCOs drive separate AOMs; their auxiliary outputs are split and mixed to generate a beat signal, filtered, amplified, attenuated, and then sent to the PLL input. Simultaneously, the combined LO and RF outputs are sent to a second mixer and routed to the spectrum analyser.

heavily decoupled (C13–C18) to suppress noise, and a simple LED (D1) provides a power-on indicator. The ±15 V rails for the op-amps are supplied externally (J5), with local decoupling (C23–C26).

Reference and VCO Inputs

The PLL requires two inputs: a stable **reference frequency** (J1), typically derived from a laboratory frequency source, and a **feedback frequency** (J2), taken from the auxiliary output of the VCO. Both are AC-coupled through capacitors (C7, C8) and impedance-matched via 51 Ω resistors (R3, R4). Additional capacitors (C5, C6) provide RF bypassing to suppress noise. In our configuration, the REFIN (10 MHz clock) and FINA inputs are used, while FINB remains unconnected.

PLL Core (ADF4002)

The ADF4002 (U2) forms the heart of the circuit. It contains a phase-frequency detector (PFD) and a charge pump (CP). In this setup it is operated as a PFD only. The PFD compares the reference and feedback signals, generating current pulses at the **charge pump output** (Pin 1). These are smoothed into a control voltage by the loop filter. The device is programmed via a three-wire SPI interface (J9), with an Arduino microcontroller as SPI master. The MUXOUT pin drives an LED (LED2) through resistors (R20–R22), providing a visual lock indicator.

Loop Filter

The charge pump output current is converted into a stable DC tuning voltage by the loop filter (C11, C12, C27, R5, R23). This filter determines the bandwidth and stability of the PLL, and its values can be adjusted depending on the VCO's characteristics.

Op-Amp Buffer and VCO Control

The filtered control voltage is buffered and scaled using precision operational amplifiers (U5, U6: OP07). Powered by ±15 V rails, they provide a wide tuning range for the VCO. Resistors (R9–R13) and capacitors (C19–C22) set the gain and suppress noise. The buffered voltage is then delivered to the **VCO tuning inputs** (J7, J8), ensuring stable and low-noise oscillator control.

Overall Operation

In operation, the ADF4002 compares the reference and VCO signals and adjusts the charge pump output until the feedback frequency is phase-locked to the reference. The loop filter and op-amps smooth the correction voltage, ensuring low noise and stability. The MUXOUT LED provides a visual lock indicator. By integrating this PLL into the RDSNS setup, one VCO can be phase-locked to the other, stabilising their relative frequency difference. This ensures a stable Raman detuning and greatly improves the quality of the spin noise spectroscopy signal.

Appendix C

Image Processing and Abel Inversion

C.0.1 Loading and Scaling the Image

The fluorescence image captured by the CCD camera is loaded and converted from pixel units to physical coordinates based on the pixel size of 5 µm. There is a demagnification factor of 2.67 done by using a combination of lenses. The code for this preprocessing is shown in Listing C.1.

```
import numpy as np
import matplotlib.pyplot as plt
import imageio.v3 as iio
import abel

DEMAG_FACTOR = 2.67
PIXEL_SIZE_UM = 5
PIXEL_SIZE_MM = (PIXEL_SIZE_UM * DEMAG_FACTOR) / 1000  # mm

image = iio.imread(r"path_to_image.tif")
```

```
height, width = image.shape
x_extent_mm = width * PIXEL_SIZE_MM / 2
y_extent_mm = height * PIXEL_SIZE_MM / 2

plt.imshow(image, cmap="inferno", origin="lower",
           extent=[-x_extent_mm, x_extent_mm, -y_extent_mm, y_extent_mm
              ])
plt.title("Original Image in Real-World Scale")
plt.xlabel("X (mm)")
plt.ylabel("Y (mm)")
plt.colorbar(label="Intensity")
plt.show()
```

Listing C.1: Loading and scaling the fluorescence image

This image is then centered by using a Gaussian centroiding. This step ensures radial symmetry about the origin, which is crucial for a successful Abel inversion.

```
centered_image = abel.tools.center.center_image(image, method="gaussian
   ")
```

Listing C.2: Centering the image using Gaussian method

C.0.2 Symmetric Cropping and Abel Inversion

To perform a clean Abel inversion, the image is cropped symmetrically about its centre to avoid boundary artifacts. Listing C.3 shows the relevant code. We have used the abel python package to do the transformation by the Hansenlaw method.

```
height, width = centered_image.shape
center_x, center_y = width // 2, height // 2
crop_size = min(center_x, center_y)

cropped_image = centered_image[
    center_y - crop_size:center_y + crop_size,
```

```
    center_x - crop_size:center_x + crop_size
]

x_extent_mm = cropped_image.shape[1] * PIXEL_SIZE_MM / 2
y_extent_mm = cropped_image.shape[0] * PIXEL_SIZE_MM / 2

reconstructed = abel.Transform(cropped_image, method='hansenlaw',
    direction='inverse').transform
```

Listing C.3: Cropping and performing inverse Abel transform

The result of the inverse Abel transform is a 2D image representing the radial atomic density under the assumption of cylindrical symmetry.

C.0.3 Conversion to Atom Density

The inverse Abel signal is scaled using the total number of atoms, assumed here to be $N_{\text{total}} = 10^8$ atoms, to yield the atomic density in units of atoms/mm^3. The code for this is shown in Listing C.4.

```
N_total_atoms = 1e8
total_abel_signal = reconstructed.sum()
scale_factor = N_total_atoms / total_abel_signal

PIXEL_VOLUME_MM3 = PIXEL_SIZE_MM ** 3
density_atoms_per_pixel = reconstructed * scale_factor
density_atoms_per_mm3 = density_atoms_per_pixel / PIXEL_VOLUME_MM3
```

Listing C.4: Conversion from Abel signal to physical density

A vertical lineout is extracted at $x = 0.54$ mm for comparison with experimental spin noise density measurements.

C.0.4 Loading Experimental Spin Noise Data

The experimental data consists of spin noise peak-to-peak values recorded along the y-axis, stored in a CSV file. So the data was recorded by changing the current in the bias coil which shifts the

MOT by 61 pixel per Ampere. The position calibration includes a pixel-to-mm conversion and an offset shift to align with the Abel lineout:

```
import pandas as pd

file_path = 'path_to_peak_to_peak_values.csv'
df = pd.read_csv(file_path)

y_exp = df.iloc[:, 0].values * 61 * 0.005 * 2.67 + 0.6
exp_values = df.iloc[:, 1].values
exp_errors = df.iloc[:, 2].values
```

Listing C.5: Loading and aligning experimental data

C.0.5 Comparison and Data Export

The Abel density profile and experimental spin noise data are plotted on a shared x-axis with dual y-axes. Listing C.6 presents the code.

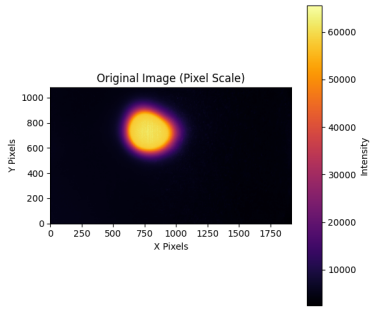
```
fig, ax1 = plt.subplots(figsize=(6, 5))
ax1.errorbar(y_exp, exp_values, yerr=exp_errors, fmt="o", capsize=3,
    color="red")
ax1.set_ylabel("Experimental Density (arb. units)", color="red")
ax1.tick_params(axis="y", labelcolor="red")

ax2 = ax1.twinx()
ax2.plot(y_positions_mm, density_atoms_per_mm3[:, x_indices[3]], color=
    "blue", lw=2)
ax2.set_ylabel("Abel Density (atoms/mm^3)", color="blue")
ax2.tick_params(axis="y", labelcolor="blue")

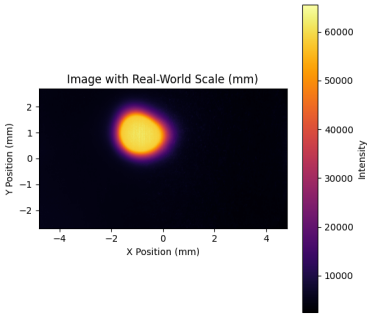
ax1.set_xlabel("Y Position (mm)")
fig.suptitle("Comparison of Experimental and Abel Reconstructed
    Densities")
```

```
ax1.grid(True)
fig.tight_layout()
plt.savefig("comparison_plot.png", dpi=300)
```

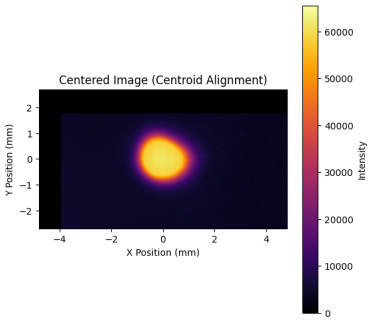
Listing C.6: Dual-axis comparison and data export



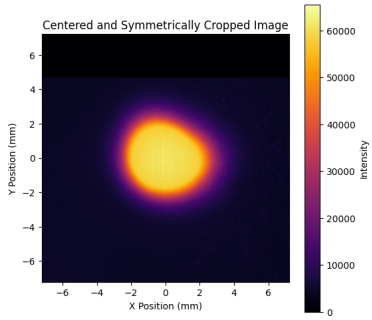
(a) Original Image (in pixel)



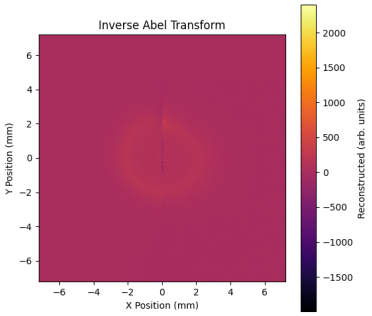
(b) Original Image (in mm)



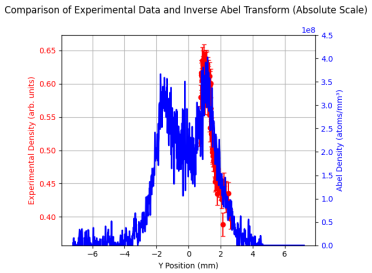
(c) Centered Image



(d) Cenetered and Symmetrically Cropped Image



(e) Inverse Abel Transform



(f) Final Comparison Plot

Figure C.1: Overview of the analysis pipeline: (a) raw image in pixel (b) raw image in physical coordinates, (c) image centered using Gaussian centroid, (d) Centered and symmetrically cropped image, (e) result of inverse Abel transform, and (f) comparison between experimental and reconstructed densities.

Appendix D

Laser Frequency

For potassium (^{39}K), the excited-state hyperfine splittings on the D_2 line (767 nm) are smaller than the natural linewidth, and therefore the individual transitions cannot be spectroscopically resolved in the saturation absorption spectroscopy (SAS). As a result, the cooling laser is side-locked to the blended $F = 2 \rightarrow F'$ manifold feature, while the repump laser is locked to the top of the crossover resonance of the $F = 1 \rightarrow F'$ manifold.

The cooling laser, operating at 767 nm and corresponding to the ^{39}K $F = 2 \rightarrow F'$ transition, is side-locked as described above and then routed through additional double-pass AOM ($\sim$ 200 MHz) to generate the desired frequency detunings for the 2D$^+$ MOT, 3D MOT, and imaging beams. The cooling light, tuned near the $F = 2 \rightarrow F' = 3$ resonance, also off-resonantly couples to nearby transitions such as $F = 2 \rightarrow F' = 2, 1$ because of the small excited-state hyperfine separation. This leads to optical pumping into the $F = 1$ ground state, which is dark to the cooling transition. To optimize trapping, the laser is red detuned by 32.1 MHz for the 2D$^+$ MOT beam, 46.8 MHz for the 3D MOT beam, and 0 MHz for the imaging beam, allowing sequential cooling and efficient atom capture.

$$\omega_{\text{Cooling}} = \omega_{\text{Lock}} - 2\omega_{\text{AOM,Lock}} + 2\omega_{\text{AOM,Laser}} \tag{D.1}$$

$$\omega_{\text{Cooling}} = \omega_{\text{Lock}} - \Delta_{\text{Cooling}}$$

$$\therefore \ \Delta_{\text{Cooling}} = 2\omega_{\text{AOM,Lock}} - 2\omega_{\text{AOM,Laser}}$$

Here, ω_{Cooling} represents the final optical frequency of the cooling beam incident on the atoms, while ω_{Lock} denotes the frequency of the laser when it is locked to the reference transition in the saturation absorption spectroscopy (SAS) setup. The term $\omega_{\text{AOM,Lock}}$ refers to the driving frequency of the Acousto-Optic Modulator (AOM) used in the locking path, operated in a double-pass configuration. Similarly, $\omega_{\text{AOM,Laser}}$ corresponds to the AOM frequency applied in the main laser beam path, also in double-pass configuration, which allows precise control of the detuning required for the $2D^+$ MOT, 3D MOT, and imaging stages. Δ_{Cooling} represents the overall detuning of the cooling laser from the atomic resonance after accounting for the frequency shifts introduced by the AOMs.

The repump laser addresses the $F = 1 \rightarrow F' = 2$ transition to return atoms that have been optically pumped into the dark $F = 1$ ground state back into the cooling cycle. For locking the laser to the repump transition, a 780nm laser is employed and it is stabilized at the crossover point of the derivative of the potassium SAS signal using the Pound–Drever–Hall (PDH) method with PID feedback. Frequency control is achieved with a double-pass AOM ($\sim$ 80 MHz), following the same shifting scheme applied to the cooling beam to obtain the required detunings for the experiment. Because the excited-state hyperfine levels in potassium are closely spaced, the repump beam is run at relatively higher intensity to keep population in the cooling transition and ensure robust operation of both lasers.

$$\omega_{\text{Repump}} = \omega_{\text{Lock}} - 2\omega_{\text{AOM,Lock}} + 2\omega_{\text{AOM,Laser}} \tag{D.2}$$

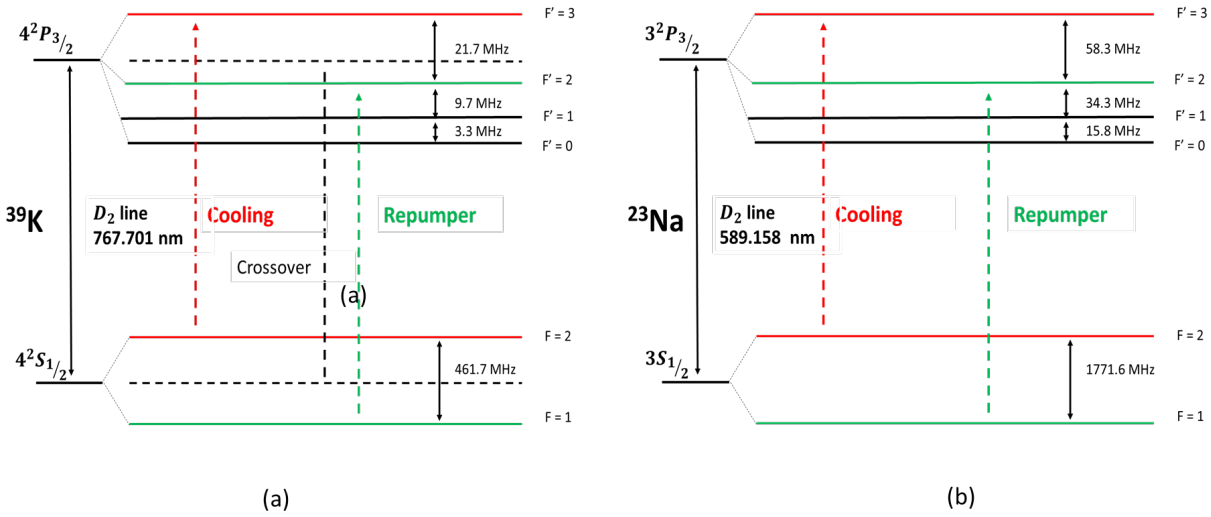


Figure D.1: Represents the hyperfine energy level diagram of Sodium and Potassium.

$$\omega_{\text{Repump}} = \omega_{\text{Lock}} - \Delta_{\text{Repump}}$$

$$\therefore \ \Delta_{\text{Repump}} = 2\omega_{\text{AOM,Lock}} - 2\omega_{\text{AOM,Laser}}$$

Here, ω_{Repump} represents the optical frequency of the repump beam, and Δ_{Repump} denotes its effective detuning from the atomic resonance.

The corresponding detuning values for the repump beams in the $2D^+$ MOT and 3D MOT are listed in Table 1. Since both the SAS and beam paths incorporate double-pass AOMs, the final frequencies of the cooling and repump beams reaching the atoms include the cumulative effects of all AOM-induced shifts, resulting in precisely controlled and stable laser detunings.

Table D.1: Summary of potassium cooling and repumping laser frequency settings. The detuning at the atoms is measured relative to the reference transition. The values provided here are placeholders and should be updated with the actual experimental detunings.

Beam	Target transition	Detuning (Γ)	$\omega_{\text{AOM,Laser}}$ (MHz)
Cooling 2D$^+$ MOT	$F = 2 \rightarrow F'$	-5.35	178.5
Cooling 3D MOT	$F = 2 \rightarrow F'$	-7.8	183.6
Imaging	$F = 2 \rightarrow F'$	0	187.5
Repump 2D$^+$ MOT	$F = 1 \rightarrow F'$	-1.17	193
Repump 3D MOT	$F = 1 \rightarrow F'$	0	90.4

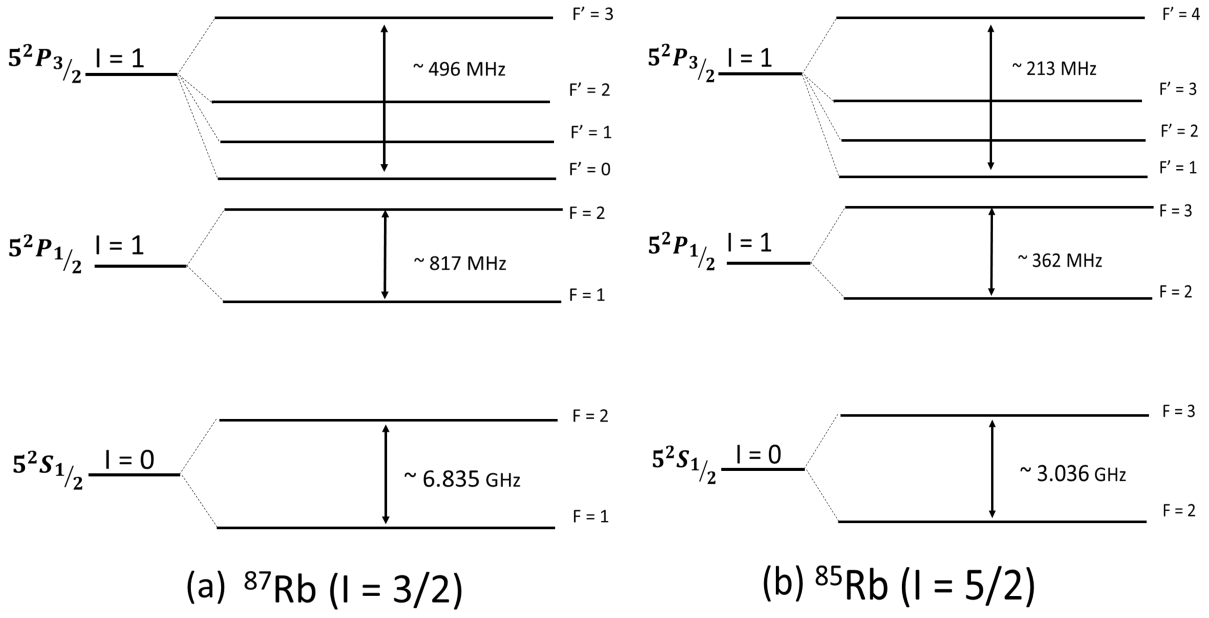


Figure D.2: Represents the hyperfine energy level diagram of Rubidium

Rubidium Energy Levels and Hyperfine Structure

Rubidium (Rb) is an alkali metal with atomic number $Z = 37$, located in Group 1 and Period 5 of the periodic table. It is widely used in atomic physics experiments due to its single valence electron, which allows precise control of its quantum states. Naturally occurring rubidium consists of two isotopes: ^{85}Rb (stable, 72% abundance) and ^{87}Rb (weakly radioactive, 28% abundance).

The ground-state electronic configuration of rubidium is $[\text{Kr}]5S_{1/2}$, corresponding to a single valence electron outside a closed-shell core. The valence electron has orbital angular momentum

$L = 0$ and spin angular momentum $S = 1/2$, giving the total electronic angular momentum

$$\mathbf{J} = \mathbf{L} + \mathbf{S},$$

with $J = 1/2$ for the ground state.

The first excited electronic states correspond to the $5P$ orbital ($L = 1$). Coupling with the electron spin yields two fine-structure levels: $J = 1/2$ and $J = 3/2$, defining the D-lines of rubidium: the D1 line ($5S_{1/2} \rightarrow 5P_{1/2}$) and the D2 line ($5S_{1/2} \rightarrow 5P_{3/2}$). The level labels indicate the principal quantum number n, the multiplicity $2S + 1$, the orbital angular momentum ($S \leftrightarrow L = 0$, $P \leftrightarrow L = 1$), and the total electronic angular momentum J.

The hyperfine interaction represents the coupling between the magnetic dipole moment of the nucleus and the magnetic field generated by the electron at the nucleus. This additional interaction term in the atomic Hamiltonian can be expressed as

$$H_{\mathrm{hf}} = A\,\mathbf{I} \cdot \mathbf{J},$$

where $\mathbf{I}$ is the nuclear spin, $\mathbf{J}$ is the total electronic angular momentum, and A is the magnetic–dipole hyperfine constant, proportional to the product of the nuclear magnetic moment μ_I and the electron probability density at the nucleus $|\psi(0)|^2$. The total angular momentum of the atom is therefore

$$\mathbf{F} = \mathbf{J} + \mathbf{I}, \quad |J - I| \leq F \leq J + I.$$

Each fine-structure level thus splits into several hyperfine components, and the associated energy shift is given by

$$E_F = \frac{A}{2}\,[F(F+1) - I(I+1) - J(J+1)].$$

The sign and magnitude of the interaction depend on the orientation of $\mathbf{I}$ and $\mathbf{J}$ and on the magnitude of μ_I. In physical terms, the nucleus and the electron behave as two coupled magnetic dipoles whose relative orientation modifies the total energy of the atom.

For ^{85}Rb: The nuclear spin is $I = 5/2$. The ground-state hyperfine levels ($5S_{1/2}, J = 1/2$) are

$F = 2, 3$, with a splitting of approximately 3036 MHz. For the D1 excited state ($5P_{1/2}, J = 1/2$), the hyperfine levels are $F = 2, 3$, while for the D2 excited state ($5P_{3/2}, J = 3/2$), F can take values $1, 2, 3, 4$, with splittings ranging roughly from 63 MHz to 120.64 MHz.

For ^{87}Rb: The nuclear spin is $I = 3/2$. The ground-state hyperfine levels ($5S_{1/2}, J = 1/2$) are $F = 1, 2$. The D1 excited state ($5P_{1/2}, J = 1/2$) has $F = 1, 2$, and the D2 excited state ($5P_{3/2}, J = 3/2$) has $F = 0, 1, 2, 3$.

Although ^{85}Rb has the larger nuclear spin ($I = 5/2$), it exhibits a smaller ground-state hyperfine splitting than ^{87}Rb. This difference arises from the nuclear magnetic moment: $\mu_I(^{87}\text{Rb}) = 2.75\,\mu_N$ and $\mu_I(^{85}\text{Rb}) = 1.35\,\mu_N$. The hyperfine constant A is approximately proportional to μ_I, so the larger magnetic moment of ^{87}Rb produces a stronger interaction and consequently a greater energy separation (6.835 GHz compared with 3.036 GHz for ^{85}Rb). The disparity does not result from the value of I itself but from the magnitude of the nuclear magnetic dipole moment.

The hyperfine separations in the excited $5P$ states are substantially smaller than in the $5S$ ground state because the P-orbital electron wavefunction vanishes at the nucleus. The magnetic interaction depends on the electron density at the nucleus, $|\psi(0)|^2$, which is nonzero for S orbitals but nearly zero for P orbitals. Consequently, the $5S_{1/2}$ state exhibits hyperfine splittings on the order of gigahertz, whereas the $5P$ states exhibit splittings of only a few hundred megahertz.

The fine-structure splitting in rubidium ($\sim$ 15 nm between D1 and D2 lines) is large enough to be resolved by common lasers, allowing the two D-line components to be treated independently. The hyperfine splittings are much smaller but crucial for high-precision spectroscopy, laser cooling, and quantum-state manipulation.

The linewidth of an atomic transition reflects the finite lifetime of the corresponding energy level. Ground states ($L = 0$) ideally have no permanent electric dipole moment, resulting in extremely narrow natural linewidths. In practice, however, perturbations such as collisions, stray magnetic fields, and light-atom interactions broaden these levels, causing atoms to undergo random

transitions among the magnetic sublevels within the ground-state manifold. Excited states ($L = 1$) possess a permanent dipole moment and interact with the vacuum electromagnetic field. Temporal fluctuations in this vacuum field make these states unstable, introducing energy uncertainty and natural broadening, eventually leading to spontaneous photon emission and decay back to the ground state.

Understanding the physical origin and quantitative scale of hyperfine structure is essential for experimental design in atomic physics. The ground-state hyperfine transition of ^{87}Rb ($F = 1 \leftrightarrow F = 2$) at 6.835 GHz forms the basis of the rubidium frequency standard used in atomic clocks. In laser-cooling and trapping, optical pumping selectively drives transitions between specific F manifolds (e.g., $F = 2 \rightarrow F' = 3$ and the associated repumping transition $F = 1 \rightarrow F' = 2$), exploiting the hyperfine and Zeeman structure for state control and population cycling. Precise knowledge of the hyperfine constants and transition frequencies thus underpins modern applications in quantum metrology, timekeeping, and quantum information science.

Appendix E

Basics of Laser Cooling and Trapping

In this section I briefly describe the basic principles behind laser cooling and trapping. It also ponders over a few important topics involving Doppler cooling, sub-Doppler cooling, and magnetic trapping.

E.1 Radiation Pressure and Scattering Force

When an atom interacts with near-resonant light, it experiences a recoil momentum $\hbar k$ as it absorbs and spontaneously re-emits photons. Upon averaging over many scattering events, the net force exerted by a single laser beam is given by the *scattering force* ($F_{\mathrm{sc}}(v)$) [218–220]:

$$F_{\mathrm{sc}}(v) = \hbar k \frac{\Gamma}{2} \frac{s_0}{1 + s_0 + \left(\frac{2(\Delta - kv)}{\Gamma}\right)^2}, \tag{E.1}$$

where $\hbar$ is the reduced Planck's constant, $k = 2\pi/\lambda$ is the wavevector of the light field, Γ is the natural linewidth (spontaneous decay rate) of the atomic transition, $\Delta = \omega_L - \omega_0$ is the detuning

of the laser frequency ω_L from the atomic resonance frequency ω_0. v is the velocity of the atom along the beam direction, and $s_0 = I/I_{\text{sat}}$ is the on-resonance saturation parameter defined by the ratio of the laser intensity I to the saturation intensity I_{sat}.

The saturation intensity is given by

$$I_{\text{sat}} = \frac{\pi h c \Gamma}{3\lambda^3}, \tag{E.2}$$

where c is the speed of light, and λ is the transition wavelength.

The saturation intensity I_{sat} represents the characteristic laser intensity at which the transition probability of an atom is significantly modified by the presence of the light field. Physically, it is the intensity at which the excitation rate equals half the maximum possible scattering rate of the atom. For intensities $I \ll I_{\text{sat}}$, the scattering rate increases approximately linearly with I, while for $I \gg I_{\text{sat}}$ the transition becomes power-broadened and the scattering rate saturates at its maximum value $\Gamma/2$. A similar feature was seen in our data discussed in Appendix A, where the intensity of a resonant probe beam was altered and absorption spectroscopy was performed on cold atoms.

E.2 Doppler Cooling

In the presence of two counter-propagating, red-detuned laser beams, atoms experience a velocity-dependent imbalance in scattering forces due to the Doppler effect. An atom moving with velocity v towards one beam sees that the beam is Doppler-shifted closer to resonance, while the counter-propagating beam is shifted further from resonance. As a result, the atom preferentially scatters photons from the beam opposing its motion, producing a net frictional force that damps the velocity.

Expanding the scattering force for small velocities ($kv \ll |\Delta|$) gives a linear friction force:

$$F(v) \approx -\alpha v, \tag{E.3}$$

where the damping coefficient is

$$\alpha = \frac{8\hbar k^2 \Delta s_0}{\Gamma\left(1 + s_0 + \left(\frac{2\Delta}{\Gamma}\right)^2\right)^2}. \tag{E.4}$$

In physical terms, the Doppler cooling limit is the lowest temperature we can reach by using the Doppler effect to slow atoms down. It happens because when we tune the laser frequency just below the atom's resonance, atoms moving towards the laser get a gentle push to slow them down. This process sets a fundamental temperature limit because eventually, the random kicks from spontaneous emission prevent the atoms from getting any colder. The ultimate temperature limit of Doppler cooling arises from this balance between the velocity damping and heating due to random momentum kicks from spontaneous emission. This *Doppler cooling limit* is given by [221]:

$$T_D = \frac{\hbar\Gamma}{2k_B}, \tag{E.5}$$

where k_B is the Boltzmann constant.

For sodium, with $\Gamma/2\pi \approx 10\,\text{MHz}$, the Doppler limit corresponds to $T_D \approx 240\,\mu\text{K}$, while for potassium ($\Gamma/2\pi \approx 6\,\text{MHz}$) it is $T_D \approx 145\,\mu\text{K}$.

E.2.1 Magneto-Optical Trap (MOT)

In a MOT, a quadrupole magnetic field is applied such that the local Zeeman shift depends linearly on position x as:

$$\Delta_{\text{eff}}(x) = \Delta - kv \pm \mu' B' x, \tag{E.6}$$

where B' is the magnetic field gradient and μ' is the effective magnetic moment for the transition. The basic working principle of a MOT is illustrated in Fig. E.1. Counter-propagating, red-detuned laser beams apply a velocity-dependent damping force through the Doppler effect, slowing down atoms. A quadrupole magnetic field introduces position-dependent Zeeman shifts, which make atoms preferentially absorb photons from the beam that pushes them back toward the trap center. By combining the scattering force from near-resonant light with the restoring effect of the magnetic gradient, the MOT achieves simultaneous cooling and trapping of neutral atoms. The resulting force ($F(x)$) is approximately harmonic near the trap center [222]:

$$F(x) \approx -\kappa x - \alpha v, \tag{E.7}$$

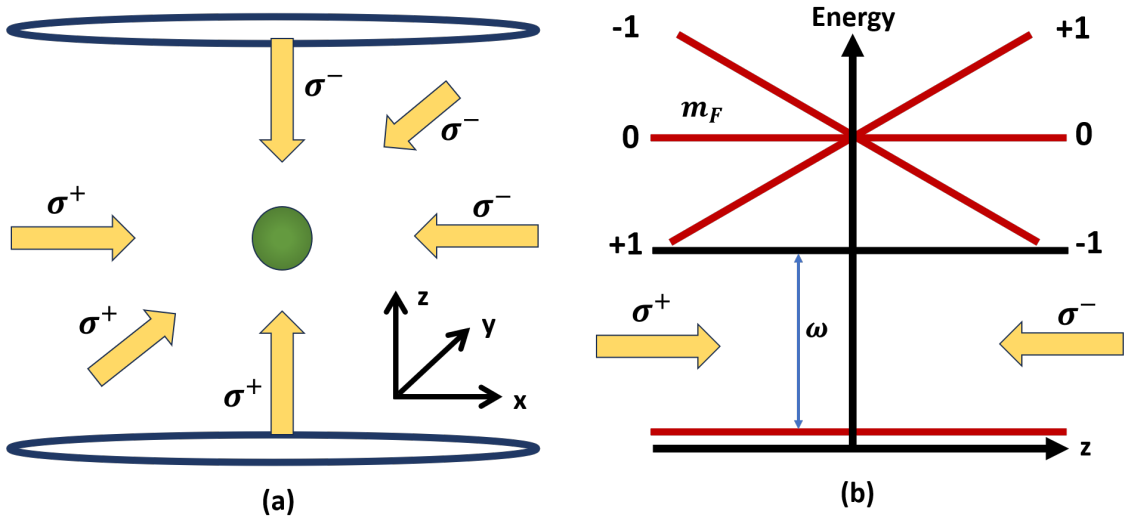


Figure E.1: Principle of laser cooling and trapping in a magneto-optical trap (MOT). (a) Three orthogonal pairs of counter-propagating, red-detuned laser beams provide velocity-dependent scattering forces that cool atoms. A quadrupole magnetic field, generated by anti-Helmholtz coils (blue loops), ensures a position-dependent restoring force, confining atoms near the trap center (green sphere). (b) Zeeman splitting of the atomic excited state sublevels in the presence of the magnetic field. The σ^+ and σ^- polarized beams preferentially interact with atoms displaced to the left or right, producing a restoring force toward the trap center.

where α is the Doppler friction coefficient, and

$$\kappa = \frac{\mu' B' k \, s_0}{1 + s_0 + \left(\frac{2\Delta}{\Gamma}\right)^2} \tag{E.8}$$

is the MOT spring constant. Thus the MOT provides both a restoring force (position-dependent) and a velocity damping force, resulting in stable trapping and cooling.

E.3 Sub-Doppler Cooling

While Doppler cooling sets a fundamental temperature limit, even lower temperatures can be achieved by exploiting the internal structure of atoms and the spatially varying polarization of light. These mechanisms are collectively known as *sub-Doppler cooling* or *polarization gradient cooling*, and they arise from the interplay of optical pumping between Zeeman sublevels and the spatial modulation of light shifts of the ground states.

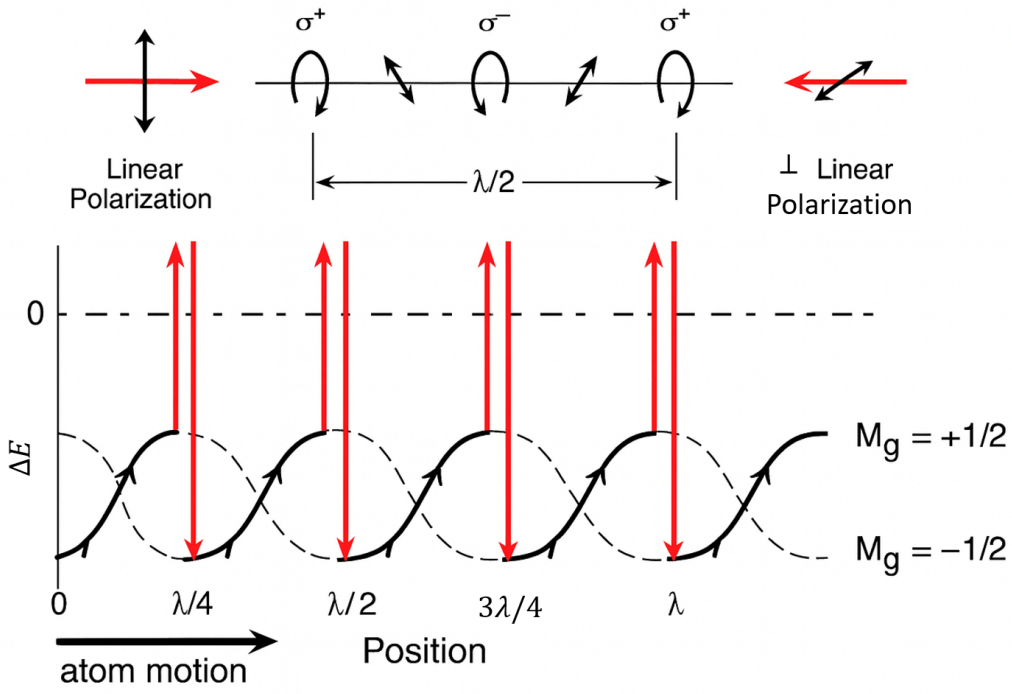


Figure E.2: Schematic of Sisyphus cooling in the lin⊥lin configuration. (Top) The polarization of the standing wave alternates periodically between σ^+ and σ^- components every $\lambda/2$. (Bottom) The corresponding light shifts create spatially modulated optical potentials for the ground-state Zeeman sublevels $m_g = \pm 1/2$. Atoms moving along z lose kinetic energy by climbing potential hills before being optically pumped to a lower-energy sublevel, leading to cooling below the Doppler limit.

A paradigmatic example is *Sisyphus cooling*, first demonstrated in the lin⊥lin configuration [223, 224]. In this geometry, two counter-propagating beams with orthogonal linear polarisations create a standing wave in which the polarisation varies periodically in space, giving rise to alternating σ^+ and σ^- components every $\lambda/2$. The corresponding light shifts produce sinusoidally modulated optical potentials for the ground-state Zeeman sublevels, as shown in Fig. E.2. Atoms moving through this landscape lose kinetic energy as they climb potential hills, and near the top they are optically pumped into another sublevel of lower potential energy. The process then repeats, producing a continuous loss of kinetic energy. This mechanism, reminiscent of the myth of Sisyphus who was condemned to eternally push a boulder uphill, allows cooling well below the Doppler limit. The characteristic temperature scale of sub-Doppler mechanisms is determined not

by the natural linewidth but by the recoil energy,

$$T_{\mathrm{SD}} \sim \frac{E_{\mathrm{rec}}}{k_B} = \frac{\hbar^2 k^2}{2m k_B}, \tag{E.9}$$

where $E_{\mathrm{rec}} = (\hbar k)^2/2m$ is the recoil energy of an atom of mass m. This recoil-limited temperature is typically on the order of a few tens of μK for alkali atoms, significantly lower than the Doppler limit. For sodium, sub-Doppler cooling can routinely reach temperatures of 20–50 μK, while potassium—especially bosonic ^{39}K—presents additional challenges due to its inverted hyperfine structure and requires careful choice of detuning and polarisation to achieve comparable performance. Nevertheless, both species benefit substantially from polarisation gradient cooling, making it a crucial step in preparing dense, ultracold ensembles suitable for magnetic or optical trapping. In summary, laser cooling combines the velocity-dependent force of Doppler cooling

Table E.1: Relevant laser cooling parameters for sodium and potassium D_2 transitions.

Species	**Wavelength** λ (nm)	**Linewidth** $\Gamma/2\pi$ (MHz)	T_D **(**μ**K)**
^{23}Na	589.0	9.8	240
^{39}K	766.7	6.0	145

with position-dependent trapping from magnetic fields in a MOT. While Doppler cooling sets a natural temperature floor (T_D), sub-Doppler mechanisms can push the atomic ensemble to much lower temperatures, enabling the preparation of cold and dense atomic samples. These principles form the basis for our dual-species sodium–potassium apparatus, which we describe in detail in the following sections. For clarity, the relevant parameters for sodium and potassium are summarised in Table E.1.

E.3.1 Time of Flight Absorption Imaging Derivation

In absorption imaging, three raw images are typically recorded for each measurement: the probe with atoms present $I_{\mathrm{atom}}(x, y)$, the probe without atoms (reference) $I_0(x, y)$, and the camera background or dark frame $I_{\mathrm{bg}}(x, y)$. Using these, one defines the corrected intensities as

$$I_{\mathrm{a}}(x, y) = I_{\mathrm{atom}}(x, y) - I_{\mathrm{bg}}(x, y), \qquad I_0(x, y) = I_0(x, y) - I_{\mathrm{bg}}(x, y). \tag{E.10}$$

The optical depth (OD) image is then given by

$$\mathrm{OD}(x, y) = -\ln\left(\frac{I_{\mathrm{a}}(x, y)}{I_0(x, y)}\right). \tag{E.11}$$

On a closed (cycling) transition, the on-resonance cross-section is

$$\sigma_0 = \frac{3\lambda^2}{2\pi}, \tag{E.12}$$

where λ is the probe wavelength. For finite probe intensity and detuning Δ, the effective cross section becomes

$$\sigma_{\mathrm{eff}} = \frac{\sigma_0}{1 + I/I_{\mathrm{sat}} + (2\Delta/\Gamma)^2}, \tag{E.13}$$

where I is the probe intensity at the atoms, I_{sat} is the saturation intensity, and Γ is the natural linewidth. If Clebsch–Gordan factors or optical pumping effects are relevant, they should be incorporated into σ_{eff}.

The column density $n_{\mathrm{col}}(x, y)$, representing atoms per unit area, is related to the optical depth by

$$n_{\mathrm{col}}(x, y) = \frac{\mathrm{OD}(x, y)}{\sigma_{\mathrm{eff}}}. \tag{E.14}$$

The total atom number is then obtained by integrating over the entire image plane. If the camera pixel size is a_{px} and the imaging magnification is M, the physical area per pixel is $(a_{\mathrm{px}}/M)^2$. The atom number is therefore

$$N = \frac{a_{\mathrm{px}}^2}{M^2\,\sigma_{\mathrm{eff}}} \sum_{x,y} \mathrm{OD}(x, y). \tag{E.15}$$

For time-of-flight expansion, assume the trapped cloud has an initial rms width σ_{x_0} and a Maxwell–Boltzmann velocity distribution with rms velocity $\sigma_{v,x} = \sqrt{k_B T/m}$. After a free expansion time t, the rms spatial width evolves as

$$\sigma_x^2(t) = \sigma_{x_0}^2 + \frac{k_B T}{m} t^2. \tag{E.16}$$

A linear fit of σ_x^2 versus t^2 yields the slope $s_x = k_B T/m$, so that the temperature is extracted as

$$T = \frac{m}{k_B} s_x. \tag{E.17}$$

In the limit where σ_{x_0} is negligible compared to the expansion term, one may approximate $\sigma_x(t) \approx \sqrt{\frac{k_B T}{m}}\, t$.

From each absorption image at TOF t, the column density is typically fitted to a two-dimensional Gaussian of the form

$$n_{\mathrm{col}}(x, y) = n_0 \exp\left[-\frac{(x - x_0)^2}{2\sigma_x^2(t)} - \frac{(y - y_0)^2}{2\sigma_y^2(t)}\right] + \text{background}, \tag{E.18}$$

where $\sigma_x(t)$ and $\sigma_y(t)$ are the rms widths along the imaging axes. These widths, initially in pixels, must be converted to meters using the factor a_{px}/M before applying Eq. (E.16).

The practical procedure is as follows. First, calibrate the magnification M and the effective pixel size a_{px}, and determine the effective cross section σ_{eff} from Eq. (E.13). Then acquire images at several time-of-flight values t_i including the three frames I_{atom}, I_0, and I_{bg}. For each TOF, compute the OD map and column density, fit to extract $\sigma_x(t_i)$ and $\sigma_y(t_i)$. Plotting σ_x^2 against t^2 and performing a linear fit gives the temperature, while the atom number can be obtained directly from Eq. (E.15).

Appendix F

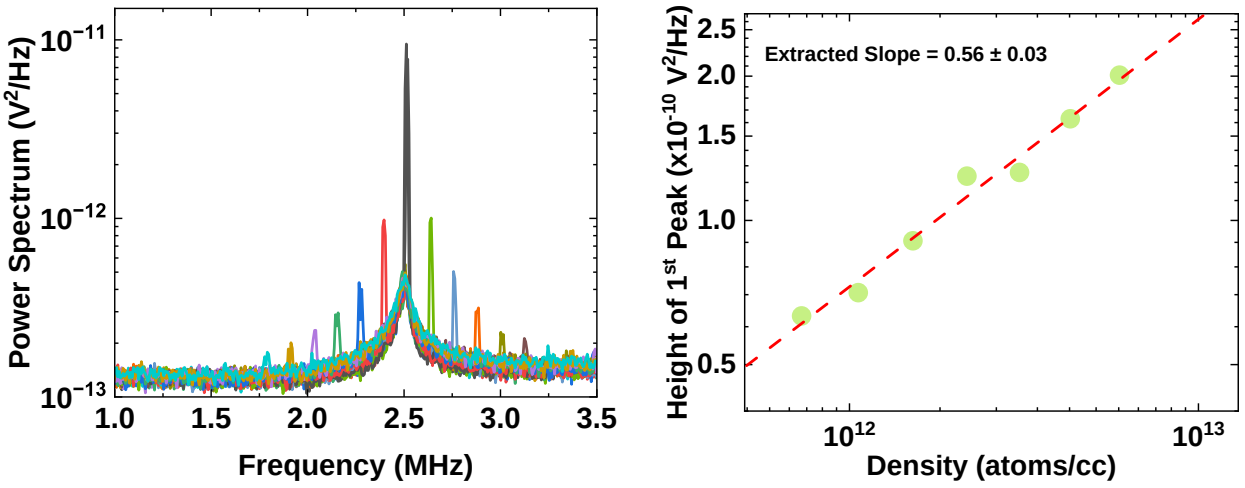
Verification of Higher Harmonics using Raman Driven Spin Noise Spectroscopy

F.1 Experimental Verification

This appendix presents additional experimental measurements that verify the physical origin of the higher-harmonic peaks discussed in Chapter F. These measurements demonstrate that the observed harmonics originate from coherent multi-photon dynamics in the atomic system and are not artifacts arising from the experimental detection scheme or the radio-frequency (RF) sources used to drive the Raman beams.

F.1.1 Coexistence of Thermal Noise and Coherent Response

The experiment is performed using a standard spin noise spectroscopy (SNS) configuration, in which fluctuations of the probe polarization are measured to obtain the power spectrum associated with atomic spin dynamics. In equilibrium, SNS signals originate from thermally induced spin



(a) (b)

Figure F.1: (a) Power spectra measured at low Raman drive power showing the competition between the coherent resonance and the thermal noise background as the Raman detuning $\delta\omega_s$ is varied. (b) Log–log plot of the amplitude of the fundamental peak as a function of atomic density N_0. The slope close to $1/2$ indicates the expected $\sqrt{N_0}$ scaling associated with statistically independent thermal fluctuations.

fluctuations of the atomic ensemble.

In the present experiment, the atomic vapor is driven by Raman beams, placing the system in a nonequilibrium regime. As a result, the measured power spectrum may contain contributions from both intrinsic thermal noise and coherently driven dynamics.

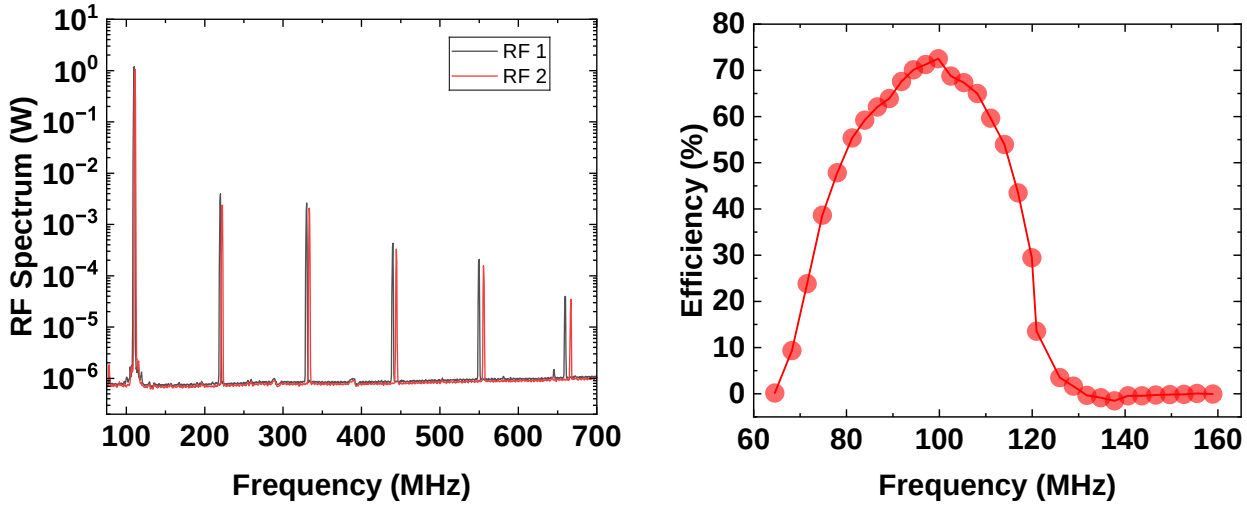
To illustrate this coexistence, measurements were performed at a very low Raman drive power (600 μW). In this regime the coherent response becomes comparable to the intrinsic thermal noise background.

At low Raman power the narrow coherent peak appears on top of a broad thermal noise background. As the Raman detuning $\delta\omega_s$ is varied, the coherent peak shifts while the thermal background remains unchanged.

To further characterize the signal, the amplitude of the fundamental peak was measured as a function of atomic density N_0 by varying the vapor temperature between 70°C and 100°C. The resulting log–log plot shows a scaling close to $\sqrt{N_0}$, which is characteristic of statistically independent fluctuations in an atomic ensemble. These measurements confirm that the SNS setup naturally contains both thermal noise and coherent spectral components.

F.1.2 RF Spectra and Bandwidth of the AOMs

A possible origin of higher harmonics in the measured spectra could be RF harmonics produced by the voltage-controlled oscillators driving the acousto-optic modulators (AOMs). To investigate this possibility, the RF spectra of the oscillators were measured.



(a) (b)

Figure F.2: (a) RF spectra of the oscillators driving the AOMs. (b) Measured diffraction efficiency of an AOM as a function of RF frequency, demonstrating the finite operational bandwidth centered near 110 MHz.

Although weak higher harmonics are present in the RF domain, their amplitudes are strongly suppressed relative to the fundamental frequency. Furthermore, the finite bandwidth of the AOMs strongly attenuates frequency components outside their operational range. As a result, RF harmonics are not efficiently transferred to the optical Raman fields.

F.1.3 Optical Beat-Note Measurement

To directly verify that RF harmonics are not transferred to the optical domain, the optical beat signal between the two Raman beams was measured in the absence of atoms.

The measured spectrum exhibits a single peak corresponding to the beat frequency of the Raman beams. No higher-order harmonics are observed, confirming that RF harmonics are not transferred to the optical signal.

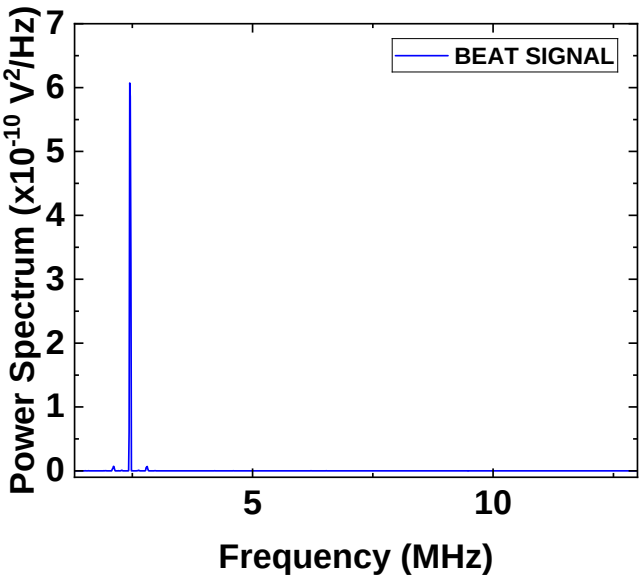


Figure F.3: Optical beat-note spectrum between the two Raman beams measured over a wide frequency span. Only the fundamental beat frequency is observed.

F.1.4 Test of Detection Linearity

Another possible source of spurious harmonics could be nonlinearities in the balanced photodetection system used to measure the probe polarization fluctuations. To test this possibility, a control experiment was performed using the same detector and electronic gain settings as in the main experiment.

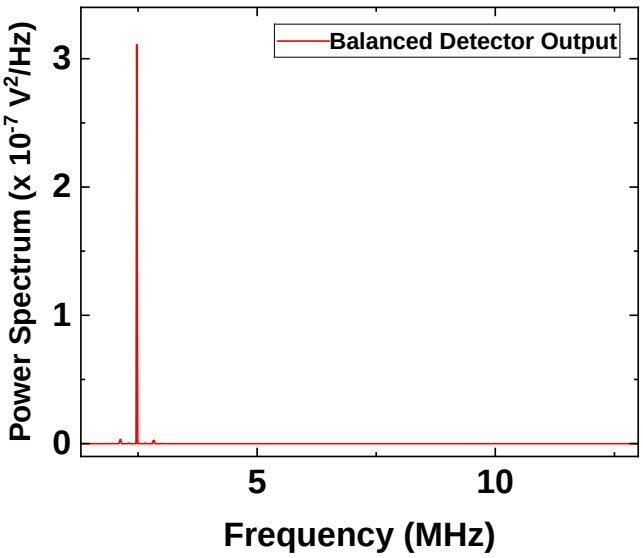


Figure F.4: Control experiment testing the linearity of the balanced photodetection system.

The optical beat signal between the Raman beams was applied to one input port of the balanced detector, while the second port was illuminated with a constant optical field. The total optical power was approximately 700 μW, comparable to that used in the main measurements. The resulting power spectrum shows only the fundamental beat frequency, with no detectable harmonics above the noise floor. This confirms that the higher-harmonic peaks observed in the main experiment do not originate from nonlinearities in the detection electronics.

F.1.5 Conclusion

The combined experimental evidence presented in this appendix—including RF spectral analysis, AOM bandwidth measurements, optical beat-note characterization, and detection linearity tests—demonstrates that the higher-harmonic peaks observed in Raman driven spin noise spectroscopy are not artifacts of the experimental setup. These results support the interpretation that the higher harmonics arise from coherent multi-photon processes in the driven atomic system.

Bibliography

[1] Horst Czichos, Tetsuya Saito, and Leslie Smith, eds. *Springer Handbook of Metrology and Testing*. 2nd ed. Springer Handbooks. Berlin, Heidelberg: Springer, 2011. ISBN: 978-3-642-16640-2. DOI: 10.1007/978-3-642-16641-9. URL: https://doi.org/10.1007/978-3-642-16641-9.

[2] Vittorio Giovannetti, Seth Lloyd, and Lorenzo Maccone. "Advances in quantum metrology". In: *Nature Photonics* 5 (2011), pp. 222–229. DOI: 10.1038/nphoton.2011.35. URL: https://doi.org/10.1038/nphoton.2011.35.

[3] Luca Pezzè et al. "Quantum metrology with nonclassical states of atomic ensembles". In: *Rev. Mod. Phys.* 90 (3 Sept. 2018), p. 035005. DOI: 10.1103/RevModPhys.90.035005. URL: https://link.aps.org/doi/10.1103/RevModPhys.90.035005.

[4] C. L. Degen, F. Reinhard, and P. Cappellaro. "Quantum sensing". In: *Rev. Mod. Phys.* 89 (3 July 2017), p. 035002. DOI: 10.1103/RevModPhys.89.035002. URL: https://link.aps.org/doi/10.1103/RevModPhys.89.035002.

[5] V. Giovannetti, S. Lloyd, and L. Maccone. "Quantum-Enhanced Measurements: Beating the Standard Quantum Limit". In: *Science* 306.5700 (2004), pp. 1330–1336.

[6] Carlton M. Caves. "Quantum-mechanical noise in an interferometer". In: *Phys. Rev. D* 23 (8 Apr. 1981), pp. 1693–1708. DOI: 10.1103/PhysRevD.23.1693. URL: https://link.aps.org/doi/10.1103/PhysRevD.23.1693.

[7] T. Baumgratz, M. Cramer, and M. B. Plenio. “Quantifying Coherence”. In: *Phys. Rev. Lett.* 113 (14 Sept. 2014), p. 140401. DOI: 10.1103/PhysRevLett.113.140401. URL: https://link.aps.org/doi/10.1103/PhysRevLett.113.140401.

[8] Elena Boto et al. “Measuring functional connectivity with wearable MEG”. In: *NeuroImage* 230 (2021), p. 117815. ISSN: 1053-8119. DOI: https://doi.org/10.1016/j.neuroimage.2021.117815. URL: https://www.sciencedirect.com/science/article/pii/S1053811921000926.

[9] Stefano Pirandola et al. “Advances in photonic quantum sensing”. In: *Nature Photonics* 12 (2018), pp. 724–733. DOI: 10.1038/s41566-018-0301-6. URL: https://doi.org/10.1038/s41566-018-0301-6.

[10] John Kitching. “Chip-scale atomic devices”. In: *Applied Physics Reviews* 5.3 (2018), p. 031302. DOI: 10.1063/1.5026238. URL: https://doi.org/10.1063/1.5026238.

[11] Qiuxin Zhang et al. “Precision measurements with cold atoms and trapped ions*”. In: *Chinese Physics B* 29.9 (Sept. 2020), p. 093203. ISSN: 1674-1056. DOI: 10.1088/1674-1056/aba9c6. URL: http://dx.doi.org/10.1088/1674-1056/aba9c6.

[12] Frantisek Janicek et al. “Applications of superconducting quantum interference devices”. In: *2015 16th International Scientific Conference on Electric Power Engineering (EPE)*. 2015, pp. 429–432. DOI: 10.1109/EPE.2015.7161204.

[13] J. M. Taylor et al. “High-sensitivity diamond magnetometer with nanoscale resolution”. In: *Nature Physics* 4 (2008), pp. 810–816. DOI: 10.1038/nphys1075. URL: https://doi.org/10.1038/nphys1075.

[14] H. B. Dang, A. C. Maloof, and M. V. Romalis. “Ultrahigh sensitivity magnetic field and magnetization measurements with an atomic magnetometer”. In: *Applied Physics Letters* 97.15 (2010), p. 151110. DOI: 10.1063/1.3491215. URL: https://doi.org/10.1063/1.3491215.

[15] Andrew D. Ludlow et al. “Optical atomic clocks”. In: *Rev. Mod. Phys.* 87 (2 June 2015), pp. 637–701. DOI: 10.1103/RevModPhys.87.637. URL: https://link.aps.org/doi/10.1103/RevModPhys.87.637.

[16] Peter D. D. Schwindt et al. “Chip-scale atomic magnetometer with improved sensitivity by use of the Mx technique”. In: *Applied Physics Letters* 90.8 (Feb. 2007), p. 081102. ISSN: 0003-6951. DOI: 10.1063/1.2709532. eprint: https://pubs.aip.org/aip/apl/article-pdf/doi/10.1063/1.2709532/14368535/081102_1_online.pdf. URL: https://doi.org/10.1063/1.2709532.

[17] Alexander D. Cronin, Jörg Schmiedmayer, and David E. Pritchard. “Optics and interferometry with atoms and molecules”. In: *Rev. Mod. Phys.* 81 (3 July 2009), pp. 1051–1129. DOI: 10.1103/RevModPhys.81.1051. URL: https://link.aps.org/doi/10.1103/RevModPhys.81.1051.

[18] Immanuel Bloch, Jean Dalibard, and Wilhelm Zwerger. “Many-body physics with ultracold gases”. In: *Reviews of modern physics* 80.3 (2008), pp. 885–964.

[19] Christian L. Degen, Florian Reinhard, and Paola Cappellaro. “Quantum sensing”. In: *Reviews of Modern Physics* 89.3 (2017), p. 035002.

[20] Alexander D Cronin, Jörg Schmiedmayer, and David E Pritchard. “Optics and interferometry with atoms and molecules”. In: *Reviews of Modern Physics* 81.3 (2009), pp. 1051–1129.

[21] Cheng Chin et al. “Feshbach resonances in ultracold gases”. In: *Reviews of Modern Physics* 82.2 (2010), pp. 1225–1286.

[22] Christian Gross and Immanuel Bloch. “Quantum simulations with ultracold atoms in optical lattices”. In: *Science* 357.6355 (2017), pp. 995–1001.

[23] Harold J Metcalf and Peter Van der Straten. “Laser cooling and trapping of neutral atoms”. In: *The Optics Encyclopedia: Basic Foundations and Practical Applications* (2007).

[24] Christopher J Foot. *Atomic physics*. Vol. 7. Oxford university press, 2005.

[25] John Kitching, Svenja Knappe, and Elizabeth A Donley. “Atomic sensors–a review”. In: *IEEE Sensors Journal* 11.9 (2011), pp. 1749–1758.

[26] Peter DD Schwindt et al. “Chip-scale atomic magnetometer”. In: *Applied Physics Letters* 85.26 (2004), pp. 6409–6411.

[27] L. Rondin et al. “Magnetometry with nitrogen-vacancy defects in diamond”. In: *Reports on Progress in Physics* 77.5 (2014), p. 056503. DOI: 10.1088/0034-4885/77/5/056503. URL: https://doi.org/10.1088/0034-4885/77/5/056503.

[28] K. Kim et al. “Quantum sensing with spin defects: principles, progress, and prospects”. In: *Advanced Photonics* 7.6 (2025), p. 064002. DOI: 10.1117/1.AP.7.6.064002. URL: https://www.spiedigitallibrary.org/journals/advanced-photonics/volume-7/issue-6/064002/Quantum-sensing-with-spin-defects--principles-progress-and-prospects/10.1117/1.AP.7.6.064002.short.

[29] H. Babashah et al. “Optically detected magnetic resonance with an open source platform”. In: *Scientific Reports* (2023). Available at SciPost Physics Core. DOI: 10.1038/s41598-023-32235-x. URL: https://app.scholarai.io/paper?paper_id=DOI:10.1038/s41598-023-32235-x&original_url=https%3A%2F%2Fwww.scipost.org%2FSciPostPhysCore.6.4.065%3Facad_field_slug%3Dastronomy.

[30] M. Pfender. “Mitigating the noise of a quantum sensor in single-spin nuclear magnetic resonance”. Doctoral dissertation. PhD thesis. University of Stuttgart, 2018. URL: https://elib.uni-stuttgart.de/server/api/core/bitstreams/dc6ea37f-9814-408b-94a9-6380fa1f1e8b/content.

[31] Jan-Hendrik Storm et al. “An ultra-sensitive and wideband magnetometer based on a superconducting quantum interference device”. In: *Applied Physics Letters* 110.7 (2017), p. 072603. DOI: 10.1063/1.4976823. URL: https://doi.org/10.1063/1.4976823.

[32] A. Politi et al. “Silica-on-silicon waveguide quantum circuits”. In: *Science* 320.5876 (2008), pp. 646–649.

[33] C. M. Caves. “Quantum-mechanical noise in an interferometer”. In: *Physical Review D* 23.8 (1981), p. 1693.

[34] S. Slussarenko and G. J. Pryde. “Quantum metrology with photon pairs and photonic entanglement”. In: *Applied Physics Reviews* 6.4 (2019), p. 041303.

[35] T. B. Pittman et al. “Optical imaging by means of two-photon quantum entanglement”. In: *Physical Review A* 52.5 (1995), R3429.

[36] J. P. Dowling. “Quantum optical metrology–the lowdown on high-N00N states”. In: *Contemporary Physics* 49.2 (2008), pp. 125–143.

[37] Vittorio Giovannetti, Seth Lloyd, and Lorenzo Maccone. “Quantum-enhanced measurements: Beating the standard quantum limit”. In: *Science* 306.5700 (2004), pp. 1330–1336.

[38] Maximilian Schlosshauer. “Quantum decoherence”. In: *Physics Reports* 831 (2019), pp. 1–57.

[39] R. Horodecki et al. “Quantum entanglement”. In: *Reviews of Modern Physics* 81.2 (2009), pp. 865–942.

[40] Masahiro Kitagawa and Masahito Ueda. “Squeezed spin states”. In: *Physical Review A* 47.6 (1993), pp. 5138–5143. DOI: 10.1103/PhysRevA.47.5138.

[41] Vittorio Giovannetti, Seth Lloyd, and Lorenzo Maccone. “Quantum Metrology”. In: *Physical Review Letters* 96.1 (2006), p. 010401.

[42] J. Aasi et al. “Enhanced sensitivity of the LIGO gravitational wave detector by using squeezed states of light”. In: *Nature Photonics* 7 (2013), pp. 613–619. DOI: 10.1038/nphoton.2013.177.

[43] V.B. Braginsky and F.Ya. Khalili. *Quantum Measurement*. Cambridge University Press, 1992. ISBN: 978-0521432241.

[44] A. A. Clerk et al. “Introduction to quantum noise, measurement, and amplification”. In: *Reviews of Modern Physics* 82.2 (2010), pp. 1155–1208. DOI: 10.1103/RevModPhys.82.1155.

[45] J. Appel et al. “Mesoscopic atomic entanglement for precision measurements beyond the standard quantum limit”. In: *Proceedings of the National Academy of Sciences* 106.27 (2009), pp. 10960–10965. DOI: 10.1073/pnas.0901550106.

[46] M. Koschorreck et al. “Sub-projection-noise sensitivity in broadband atomic magnetometry”. In: *Physical Review Letters* 104 (2010), p. 093602. DOI: 10.1103/PhysRevLett.104.093602.

[47] Miroslav Gajdacz et al. “Non-destructive Faraday imaging of dynamically controlled ultracold atoms”. In: *Review of Scientific Instruments* 84.8 (Aug. 2013), p. 083105. ISSN: 0034-6748. DOI: 10.1063/1.4818913. eprint: https://pubs.aip.org/aip/rsi/article-pdf/doi/10.1063/1.4818913/14781030/083105_1_online.pdf. URL: https://doi.org/10.1063/1.4818913.

[48] James Higbie et al. “Non-destructive imaging of an ultracold lattice gas”. In: *Optics Letters* 30.22 (2005), pp. 2640–2642. DOI: 10.1364/OL.30.002640.

[49] I. D. Leroux, M. H. Schleier-Smith, and V. Vuletić. “Implementation of cavity squeezing of a collective atomic spin”. In: *Physical Review Letters* 104 (2010), p. 073602. DOI: 10.1103/PhysRevLett.104.073602.

[50] M. H. Schleier-Smith, I. D. Leroux, and V. Vuletić. “Squeezing the collective spin of a dilute atomic ensemble by cavity feedback”. In: *Physical Review A* 81 (2010), p. 021804. DOI: 10.1103/PhysRevA.81.021804.

[51] O. Hosten et al. “Measurement noise 100 times lower than the quantum-projection limit using entangled atoms”. In: *Nature* 529 (2016), pp. 505–508. DOI: 10.1038/nature16176.

[52] E. B. Aleksandrov and V. S. Zapasskii. “Magnetic resonance in the Faraday-rotation noise spectrum”. In: *Soviet Physics – JETP* 54.1 (1981), pp. 64–67.

[53] S. A. Crooker et al. “Spectroscopy of spontaneous spin noise as a probe of spin dynamics and magnetic resonance”. In: *Nature* 431 (2004), pp. 49–52. DOI: 10.1038/nature02804.

[54] T. Mitsui. “Observation of spin noise in rubidium vapor via Faraday rotation”. In: *Phys. Rev. Lett.* 84 (2000), pp. 5292–5295. DOI: 10.1103/PhysRevLett.84.5292.

[55] M. Oestreich et al. “Spin noise spectroscopy in GaAs”. In: *Phys. Rev. Lett.* 95 (2005), p. 216603. DOI: 10.1103/PhysRevLett.95.216603.

[56] Y. Li, N. A. Sinitsyn, and S. A. Crooker. “Intrinsic spin fluctuations reveal the dynamical response function of holes coupled to nuclear spin baths in (In,Ga)As quantum dots”. In: *Nat. Commun.* 3 (2012), p. 878. DOI: 10.1038/ncomms1880.

[57] Sayari Majumder et al. “Real-time local density probe for cold atoms utilizing Raman driven spin noise spectroscopy”. In: *Applied Physics Letters* 127.4 (July 2025), p. 044004. DOI: 10.1063/5.0277027. URL: https://doi.org/10.1063/5.0277027.

[58] P. Boran, M. Mrozek, and et al. “Spin noise spectroscopy of nitrogen-vacancy centers in diamond”. In: *Phys. Rev. B* 102 (2020), p. 085427. DOI: 10.1103/PhysRevB.102.085427.

[59] V. S. Zapasskii. “Spin-noise spectroscopy: from proof of principle to applications”. In: *Advances in Optics and Photonics* 5.2 (2013), pp. 131–168. DOI: 10.1364/AOP.5.000131.

[60] M. M. Glazov et al. “Spin noise spectroscopy beyond thermal equilibrium and linear response”. In: *Phys. Rev. B* 82 (2010), p. 155325. DOI: 10.1103/PhysRevB.82.155325.

[61] S. A. Crooker et al. “Spin noise of electrons and holes in self-assembled quantum dots”. In: *Phys. Rev. B* 82 (2010), p. 041304. DOI: 10.1103/PhysRevB.82.041304.

[62] G. E. Katsoprinakis et al. “Non-destructive Faraday rotation probing of ultracold atoms in a high-finesse ring cavity”. In: *Phys. Rev. A* 75 (2007), p. 042502. DOI: 10.1103/PhysRevA.75.042502.

[63] J. Appel et al. “Mesoscopic atomic entanglement for precision measurements beyond the standard quantum limit”. In: *Proc. Natl. Acad. Sci. USA* 106.27 (2009), pp. 10960–10965. DOI: 10.1073/pnas.0901550106.

[64] M. D. Lukin et al. “Spectroscopy of dark atomic states”. In: *Opt. Lett.* 23.4 (1997), pp. 295–297. DOI: 10.1364/OL.23.000295.

[65] C. Chatfield. *The Analysis of Time Series—An Introduction*. 4th. London: Chapman and Hall, 1989, pp. 94–95. ISBN: 0-412-31820-2.

[66] Nikolai A. Sinitsyn and Yuriy V. Pershin. “The theory of spin noise spectroscopy: a review”. In: *Reports on Progress in Physics* 79.10 (2016), p. 106501. DOI: 10.1088/0034-4885/79/10/106501.

[67] Claude Cohen-Tannoudji, Bernard Diu, and Franck Laloë. *Quantum Mechanics, Vols. I and II*. New York: Wiley-VCH, 1977. ISBN: 978-0-471-16435-2.

[68] Bogdan Mihaila et al. “Quantitative study of spin noise spectroscopy in a classical gas of ^{41}K atoms”. In: *Phys. Rev. A* 74 (4 Oct. 2006), p. 043819. DOI: 10.1103/PhysRevA.74.043819. URL: https://link.aps.org/doi/10.1103/PhysRevA.74.043819.

[69] Daniel A. Steck. *Rubidium 87 D Line Data*. http://steck.us/alkalidata. revision 2.3.9, available online. 2023.

[70] M. Kozbial et al. “Spin noise spectroscopy of an alignment-based atomic magnetometer”. In: *arXiv preprint arXiv:2312.05577* (2023). URL: https://arxiv.org/abs/2312.05577.

[71] I. Ryzhov, G. Kozlov, D. Smirnov, et al. “Spin noise explores local magnetic fields in a semiconductor”. In: *Scientific Reports* 6 (2016), p. 21062. DOI: 10.1038/srep21062.

[72] Y. Yang et al. “Employing spin noise spectroscopy of rubidium ensemble to calibrate Hall magnetometers when measuring weak magnetic fields”. In: *Optics Communications* (2022). URL: https://www.sciencedirect.com/science/article/pii/S0030401822005132.

[73] Valerii S. Zapasskii. “Spin-noise spectroscopy: from proof of principle to applications”. In: *Adv. Opt. Photon.* 5.2 (June 2013), pp. 131–168. DOI: 10.1364/AOP.5.000131. URL: https://opg.optica.org/aop/abstract.cfm?URI=aop-5-2-131.

[74] Maheswar Swar et al. “Detection of spin coherence in cold atoms via Faraday rotation fluctuations”. In: *Physical Review Research* 3.4 (2021), p. 043171. DOI: 10.1103/PhysRevResearch.3.043171.

[75] Anne Fabricant et al. “How to build a magnetometer with thermal atomic vapor: a tutorial”. In: *New Journal of Physics* 25.2 (2023), p. 025001. DOI: 10.1088/1367-2630/25/2/025001.

[76] H. Korth et al. “Miniature atomic scalar magnetometer for space based on the rubidium isotope 87Rb”. In: *J. Geophys. Res. Space Phys.* 121.8 (2016), pp. 7870–7880. DOI: 10.1002/2016JA022683. URL: https://agupubs.onlinelibrary.wiley.com/doi/10.1002/2016JA022683.

[77] I. Mateos et al. “Noise characterization of an atomic magnetometer at sub-millihertz frequencies”. In: *Sens. Actuat. A Phys.* 224 (2015), pp. 147–155. DOI: 10.1016/j.sna.2015.01.025. URL: https://www.sciencedirect.com/science/article/pii/S0924424715000421.

[78] Jiali Liu et al. “Dynamics of a Spin-Exchange Relaxation-Free Comagnetometer for Rotation Sensing”. In: *Physical Review Applied* 17.1 (Jan. 2022), p. 014030. DOI: 10.1103/PhysRevApplied.17.014030. URL: https://doi.org/10.1103/PhysRevApplied.17.014030.

[79] L. Zhang et al. “A Multi-Pass Optically Pumped Rubidium Atomic Magnetometer with Free Induction Decay”. In: *Sensors* 22.19 (2022), p. 7598. URL: https://www.mdpi.com/1424-8220/22/19/7598.

[80] Y. Lu et al. “Recent Progress of Atomic Magnetometers for Geomagnetic Applications”. In: *Sensors* 23 (2023), p. 5318. DOI: 10.3390/s23115318. URL: https://doi.org/10.3390/s23115318.

[81] Y. A. Hu et al. “Atomic Magnetometers and Their Application in Industry”. In: *Frontiers in Physics* 11 (2023), p. 1212368. DOI: 10.3389/fphy.2023.1212368.

[82] Dmitry Murzin et al. “Ultrasensitive Magnetic Field Sensors for Biomedical Applications”. In: *Sensors* 20.6 (2020). ISSN: 1424-8220. DOI: 10.3390/s20061569.

[83] O. Alem et al. “Fetal magnetocardiography measurements with an array of microfabricated optically pumped magnetometers”. In: *Phys. Med. Biol.* 60.12 (2015), pp. 4797–4811. DOI: 10.1088/0031-9155/60/12/4797. URL: https://iopscience.iop.org/article/10.1088/0031-9155/60/12/4797/meta.

[84] T.H. Sander et al. “Magnetoencephalography with a chip-scale atomic magnetometer”. In: *Biomed. Opt. Express* 3.5 (2012), pp. 981–990. DOI: 10.1364/BOE.3.000981. URL: https://www.osapublishing.org/boe/abstract.cfm?uri=boe-3-5-981.

[85] K. Kamada et al. “Human magnetoencephalogram measurements using newly developed compact module of high-sensitivity atomic magnetometer”. In: *Jpn. J. Appl. Phys.* 54.2 (2015), p. 026601. DOI: 10.7567/JJAP.54.026601. URL: https://iopscience.iop.org/article/10.7567/JJAP.54.026601/meta.

[86] M.J. Brookes et al. “Magnetoencephalography with optically pumped magnetometers (OPM-MEG): the next generation of functional neuroimaging”. In: *Trends in Neurosciences* (2022). URL: https://www.cell.com/trends/neurosciences/fulltext/S0166-2236(22)00102-3?dgcid=raven_jbs_aip_email.

[87] M. Jiang et al. “Search for axion-like dark matter with spin-based amplifiers”. In: *Nature Physics* 17 (2021), pp. 1402–1407. DOI: 10.1038/s41567-021-01348-7.

[88] Lisa Hodgetts, Peter Dawson, and Edward Eastaugh. “Archaeological magnetometry in an Arctic setting: a case study from Maguse Lake, Nunavut”. In: *Journal of Archaeological Science* 38.7 (2011), pp. 1754–1762. ISSN: 0305-4403. DOI: https://doi.org/10.1016/j.jas.2011.03.007. URL: https://www.sciencedirect.com/science/article/pii/S0305440311000823.

[89] Sushree S. Sahoo et al. “Nonlinear magnetoelectric effect in atomic vapor and its application to precision radio-frequency magnetometry”. In: *Phys. Rev. A* 105 (6 June 2022), p. 063509. DOI: 10.1103/PhysRevA.105.063509. URL: https://link.aps.org/doi/10.1103/PhysRevA.105.063509.

[90] K.K. George Kurian et al. “Single-Beam Room-Temperature Atomic Magnetometer with Large Bandwidth and Dynamic Range”. In: *Phys. Rev. Appl.* 19 (5 May 2023), p. 054040. DOI: 10.1103/PhysRevApplied.19.054040. URL: https://link.aps.org/doi/10.1103/PhysRevApplied.19.054040.

[91] Cameron Deans, Luca Marmugi, and Ferruccio Renzoni. “Sub-picotesla widely tunable atomic magnetometer operating at room-temperature in unshielded environments”. In: *Review of Scientific Instruments* 89.8 (Aug. 2018), p. 083111. ISSN: 0034-6748. DOI: 10.1063/1.5026769. eprint: https://pubs.aip.org/aip/rsi/article-pdf/doi/10.1063/1.5026769/13566656/083111_1_online.pdf. URL: https://doi.org/10.1063/1.5026769.

[92] W. Chalupczak et al. “Room temperature femtotesla radio-frequency atomic magnetometer”. In: *Applied Physics Letters* 100.24 (2012), p. 242401. DOI: 10.1063/1.4729016. URL: https://doi.org/10.1063/1.4729016.

[93] O. Alem, K. L. Sauer, and M. V. Romalis. "Spin damping in an rf atomic magnetometer". In: *Physical Review A* 87.1 (2013), p. 013413. URL: https://journals.aps.org/pra/abstract/10.1103/PhysRevA.87.013413.

[94] David A. Keder et al. "An unshielded radio-frequency atomic magnetometer with sub-femtoTesla sensitivity". In: *AIP Advances* 4.12 (2014), p. 127159. DOI: 10.1063/1.4905449. URL: https://doi.org/10.1063/1.4905449.

[95] Jiali Liu et al. "Dynamics of a Spin-Exchange Relaxation-Free Comagnetometer for Rotation Sensing". In: *Phys. Rev. Appl.* 17 (1 Jan. 2022), p. 014030. DOI: 10.1103/PhysRevApplied.17.014030. URL: https://link.aps.org/doi/10.1103/PhysRevApplied.17.014030.

[96] H. Zhang et al. "On-site monitoring of atomic density number for an all-optical atomic magnetometer based on atomic spin exchange relaxation". In: *Optics Express* 24.15 (2016), pp. 17234–17243. DOI: 10.1364/OE.24.017234. URL: https://opg.optica.org/abstract.cfm?uri=oe-24-15-17234.

[97] A. Pollinger et al. "Control loops for a Coupled Dark State Magnetometer". In: *Proceedings of the SENSORS, 2010 IEEE*. [Google Scholar] [CrossRef]. IEEE. Waikoloa, HI, USA, Nov. 2010, pp. 779–784. DOI: 10.1109/ICSENS.2010.5690214.

[98] S. Palacios Alvarez et al. "Single-domain Bose condensate magnetometer achieves energy resolution per bandwidth below $\hbar$". In: *Proceedings of the National Academy of Sciences* 119.6 (Feb. 2022), e2115339119. DOI: 10.1073/pnas.2115339119.

[99] V. G. Lucivero et al. "Squeezed-light spin noise spectroscopy". In: *Physical Review A* 93.5 (2016), p. 053802. URL: https://journals.aps.org/pra/abstract/10.1103/PhysRevA.93.053802.

[100] V. Guarrera, R. Gartman, and G. Bevilacqua. "Spin-noise spectroscopy of a noise-squeezed atomic state". In: *Physical Review Research* 3.3 (2021), p. L032015. URL: https://journals.aps.org/prresearch/abstract/10.1103/PhysRevResearch.3.L032015.

[101] W. Chalupczak and R. M. Godun. "Near-resonance spin-noise spectroscopy". In: *Physical Review A* 83.3 (2011), p. 032512. URL: https://journals.aps.org/pra/abstract/10.1103/PhysRevA.83.032512.

[102] S. Liu et al. "Interplay between atomic alignment and orientation fluctuations in the spin noise spectroscopy of metastable helium". In: *New Journal of Physics* 24 (2022), p. 113047. DOI: 10.1088/1367-2630/aca428.

[103] J Delpy et al. "Creation and dynamics of spin fluctuations in a noisy magnetic field". In: *New Journal of Physics* 25.9 (Oct. 2023), p. 093055. DOI: 10.1088/1367-2630/acfb30.

[104] L. Yang et al. "Two-colour spin noise spectroscopy and fluctuation correlations reveal homogeneous linewidths within quantum-dot ensembles". In: *Nature Communications* 5 (2014), p. 4949. DOI: 10.1038/ncomms5949.

[105] Y. Li et al. "Intrinsic spin fluctuations reveal the dynamical response function of holes coupled to nuclear spin baths in (In,Ga)As quantum dots". In: *Phys Rev Lett* 108.18 (May 2012), p. 186603. DOI: 10.1103/PhysRevLett.108.186603.

[106] Tian-Jiao Sun et al. "Non-equilibrium spin noise spectroscopy of a single quantum dot operating at fiber telecommunication wavelengths". In: *J. Appl. Phys.* 131.6 (Feb. 2022), p. 065703. DOI: 10.1063/5.0079070.

[107] V. Mugundhan et al. "A Real-Time Digital Receiver for Correlation Measurements in Atomic Systems". In: *IEEE Transactions on Instrumentation and Measurement* 70 (2021), pp. 1–8. DOI: 10.1109/TIM.2020.3026843.

[108] Maheswar Swar et al. "Measurements of spin properties of atomic systems in and out of equilibrium via noise spectroscopy". In: *Optics Express* 26.25 (2018), pp. 32168–32183. DOI: 10.1364/OE.26.032168.

[109] Jundi Li et al. "SERF Atomic Magnetometer–Recent Advances and Applications: A Review". In: *IEEE Sensors Journal* 18.20 (2018), pp. 8198–8207. DOI: 10.1109/JSEN.2018.2863707.

[110] Renjie Li et al. “Parameter optimisation of miniaturised SERF magnetometer below relaxation rate saturation region”. In: *Measurement* 214 (2023), p. 112733. ISSN: 0263-2241. DOI: 10.1016/j.measurement.2023.112733. URL: https://www.sciencedirect.com/science/article/pii/S026322412300297X.

[111] P. Glasenapp et al. “Spin Noise Spectroscopy Beyond Thermal Equilibrium and Linear Response”. In: *Physical Review Letters* 113.15 (2014), p. 156601. DOI: 10.1103/PhysRevLett.113.156601.

[112] Y. Kim and I. Savukov. “Ultra-sensitive Magnetic Microscopy with an Optically Pumped Magnetometer”. In: *Scientific Reports* 6 (2016), p. 24773. DOI: 10.1038/srep24773. URL: https://doi.org/10.1038/srep24773.

[113] Fei Lu et al. “Scanning multi-channel spin-exchange relaxation-free atomic magnetometer with high spatial and time resolution”. In: *Optics Letters* 47.15 (2022), pp. 3908–3911. DOI: 10.1364/OL.465276. URL: https://doi.org/10.1364/OL.465276.

[114] Yang Li et al. “Optimization of the alkali-metal density ratio in a hybrid optical pumping atomic magnetometer”. In: *Measurement Science and Technology* 30.1 (Dec. 2018), p. 015005. DOI: 10.1088/1361-6501/aaefe2. URL: https://dx.doi.org/10.1088/1361-6501/aaefe2.

[115] I. K. Kominis et al. “A subfemtotesla multichannel atomic magnetometer”. In: *Nature* 422 (2003), pp. 596–599.

[116] J. C. Allred et al. “High-sensitivity atomic magnetometer unaffected by spin-exchange relaxation”. In: *Physical Review Letters* 89.13 (2002), p. 130801.

[117] Sylvain Karlen et al. “Lifetime assessment of RbN_3-filled MEMS atomic vapor cells with Al_2O_3 coating”. In: *Optics Express* 25 (2017), pp. 2187–2194.

[118] L. Torralbo-Campo et al. “Light-induced atomic desorption in a compact system for ultracold atoms”. In: *Sci Rep* 5 (2015), p. 14729. DOI: 10.1038/srep14729.

[119] Lele Bai et al. “Enhancement of spin noise spectroscopy of rubidium atomic ensemble by using the polarization squeezed light”. In: *Opt. Express* 30 (2022), pp. 1925–1935.

[120] Sagar Sutradhar et al. “Fast loaded dual species magneto optical trap of cold sodium and potassium atoms with light-assisted inter-species interaction”. In: *AIP Advances* 13.6 (2023), p. 065317. DOI: 10.1063/5.0154985.

[121] Umakant D. Rapol, Ajay Wasan, and Vasant Natarajan. “Loading of a Rb magneto-optic trap from a getter source”. In: *Physical Review A* 64 (June 2001), p. 023402.

[122] Carl Wieman, Gwenn Flowers, and Sarah Gilbert. “Inexpensive laser cooling and trapping experiment for undergraduate laboratories”. In: *American Journal of Physics* 63.4 (1995), pp. 317–330.

[123] J. Fortagh et al. “Fast loading of a magneto-optical trap from a pulsed thermal source”. In: *Journal of Applied Physics* 84.12 (1998), pp. 6499–6501.

[124] K. Moore et al. “Collimated, single-pass atom source from a pulsed alkali metal dispenser for laser-cooling experiments”. In: *Review of Scientific Instruments* 76 (2004), p. 023106.

[125] S. Bartalini et al. “Full characterization of the loading of a magneto-optical trap from an alkali metal dispenser”. In: *European Physical Journal D* 36.1 (2005), pp. 101–104.

[126] K. Stam et al. “Large atom number Bose–Einstein condensate of sodium”. In: *Review of Scientific Instruments* 78 (Feb. 2007), p. 013102.

[127] J. Catani et al. “Intense slow beams of bosonic potassium isotopes”. In: *Physical Review A* 73 (Mar. 2006), p. 033415.

[128] Sean Ravenhall, Benjamin Yuen, and Chris Foot. “High-flux, adjustable, compact cold-atom source”. In: *Optics Express* 29.14 (July 2021), pp. 21143–21159.

[129] G. Lamporesi et al. “Compact high-flux source of cold sodium atoms”. In: *Review of Scientific Instruments* 84.6 (2013), p. 063102.

[130] Michael A. Joffe et al. “Transverse cooling and deflection of an atomic beam inside a Zeeman slower”. In: *Journal of the Optical Society of America B* 10.12 (Dec. 1993), pp. 2257–2262. DOI: 10.1364/JOSAB.10.002257.

[131] E. Pedrozo-Peñafiel et al. “Direct comparison between a two-dimensional magneto-optical trap and a Zeeman slower as sources of cold sodium atoms”. In: *Laser Physics Letters* 13.6 (May 2016), p. 065501. DOI: 10.1088/1612-2011/13/6/065501.

[132] Dallin Durfee. “Dynamic Properties of Dilute Bose-Einstein Condensates”. PhD thesis. Massachusetts Institute of Technology, 1999.

[133] Saptarishi Chaudhuri, Sanjukta Roy, and C. S. Unnikrishnan. “Realization of an intense cold Rb atomic beam based on a two-dimensional magneto-optical trap: Experiments and comparison with simulations”. In: *Physical Review A* 74 (Aug. 2006), p. 023406.

[134] Armin Ridinger et al. “Large atom number dual-species magneto-optical trap for fermionic ^{6}Li and ^{40}K atoms”. In: *The European Physical Journal D* 65 (Mar. 2011).

[135] T. G. Tiecke et al. “High-flux two-dimensional magneto-optical-trap source for cold lithium atoms”. In: *Physical Review A* 80 (July 2009), p. 013409.

[136] M. Prentiss et al. “Light-induced collisions between optically trapped atoms”. In: *Optics Letters* 13.6 (1988), pp. 452–454. DOI: 10.1364/OL.13.000452.

[137] D. Sesko et al. “Collisional losses from a light-force atom trap”. In: *Physical Review Letters* 63 (Aug. 1989), pp. 961–964.

[138] Béatrice Bussery, Yamina Achkar, and Monique Aubert-Frécon. “Long-range molecular states dissociating to the three or four lowest asymptotes for the ten heteronuclear diatomic alkali molecules”. In: *Chemical Physics* 116.3 (1987), pp. 319–338.

[139] M. S. Santos et al. “Hyperfine-changing collision measurements in trap loss for mixed species in a magneto-optical trap”. In: *Physical Review A* 60 (Nov. 1999), pp. 3892–3895.

[140] M. W. Mancini et al. “Trap loss rate for heteronuclear cold collisions in two species magneto-optical trap”. In: *The European Physical Journal D* 30.1 (July 2004), pp. 105–116.

[141] John Weiner et al. “Experiments and theory in cold and ultracold collisions”. In: *Reviews of Modern Physics* 71 (Jan. 1999), pp. 1–85.

[142] G. D. Telles et al. “Trap loss in a two-species Rb–Cs magneto-optical trap”. In: *Physical Review A* 63 (Feb. 2001), p. 033406.

[143] C. G. Townsend et al. “Phase-space density in the magneto-optical trap”. In: *Physical Review A* 52 (Aug. 1995), pp. 1423–1440.

[144] Z. Hadzibabic et al. “Two-species mixture of quantum degenerate Bose and Fermi gases”. In: *Physical Review Letters* 88 (2002), p. 160401. DOI: 10.1103/PhysRevLett.88.160401.

[145] A. Mosk et al. “Mixture of ultracold lithium and cesium atoms in an optical dipole trap”. In: *Applied Physics B* 73 (2001), pp. 791–799. DOI: 10.1007/s003400100743.

[146] S. Z. Hassan. “Dynamics of anions and ultracold atoms in a hybrid atom-ion trap”. PhD thesis. Heidelberg University, 2022. DOI: 10.11588/heidok.00031692.

[147] E. Neri et al. “Realization of a cold mixture of fermionic chromium and lithium atoms”. In: *Physical Review A* 101 (2020), p. 063602. DOI: 10.1103/PhysRevA.101.063602.

[148] S. L. Cornish, M. R. Tarbutt, and K. R. A. Hazzard. “Quantum computation and quantum simulation with ultracold molecules”. In: *Nature Physics* (2024). DOI: 10.1038/s41567-024-02453-9.

[149] C. L. Holloway et al. “Atom-based quantum radio-frequency field sensing”. In: *IEEE Transactions on Antennas and Propagation* 65.3 (2017), pp. 1115–1128. DOI: 10.1109/TAP.2016.2633336.

[150] C. L. Degen, F. Reinhard, and P. Cappellaro. “Quantum sensing”. In: *Reviews of Modern Physics* 89.3 (2017), p. 035002. DOI: 10.1103/RevModPhys.89.035002.

[151] R. P. Bhatt. “Developing tools for cold atom research: an ultracold Na-K experiment, proposals for unitary k-designs, and a web interface”. PhD thesis. Heidelberg University, 2022. DOI: 10.11588/heidok.00031968.

[152] M. Koschorreck et al. “High resolution magnetic vector-field imaging with cold atomic ensembles”. In: *Applied Physics Letters* 98.7 (Feb. 2011), p. 074101. ISSN: 0003-6951. DOI: 10.1063/1.3555459. eprint: https://pubs.aip.org/aip/apl/article-pdf/doi/10.1063/1.3555459/14445431/074101_1_online.pdf. URL: https://doi.org/10.1063/1.3555459.

[153] David A. Smith et al. “Absorption imaging of ultracold atoms on atom chips”. In: *Opt. Express* 19.9 (Apr. 2011), pp. 8471–8485. DOI: 10.1364/OE.19.008471. URL: https://opg.optica.org/oe/abstract.cfm?URI=oe-19-9-8471.

[154] G. Reinaudi et al. “Strong saturation absorption imaging of dense clouds of ultracold atoms”. In: *Opt. Lett.* 32.21 (Nov. 2007), pp. 3143–3145. DOI: 10.1364/OL.32.003143. URL: https://opg.optica.org/ol/abstract.cfm?URI=ol-32-21-3143.

[155] K. S. Hardman et al. “Time-of-flight detection of ultra-cold atoms using resonant frequency modulation imaging”. In: *Opt. Lett.* 41.11 (June 2016), pp. 2505–2508. DOI: 10.1364/OL.41.002505. URL: https://opg.optica.org/ol/abstract.cfm?URI=ol-41-11-2505.

[156] Gordon E. Lott, Michael A. Marciniak, and John H. Burke. “Three-dimensional imaging of trapped cold atoms with a light field microscope”. In: *Appl. Opt.* 56.31 (Nov. 2017), pp. 8738–8745. DOI: 10.1364/AO.56.008738. URL: https://opg.optica.org/ao/abstract.cfm?URI=ao-56-31-8738.

[157] D. B. Hume et al. “Accurate Atom Counting in Mesoscopic Ensembles”. In: *Phys. Rev. Lett.* 111 (25 Dec. 2013), p. 253001. DOI: 10.1103/PhysRevLett.111.253001. URL: https://link.aps.org/doi/10.1103/PhysRevLett.111.253001.

[158] D. V. Sheludko et al. “Non-iterative imaging of inhomogeneous cold atom clouds using phase retrieval from a single diffraction measurement”. In: *Opt. Express* 18.2 (Jan. 2010), pp. 1586–1599. DOI: 10.1364/OE.18.001586. URL: https://opg.optica.org/oe/abstract.cfm?URI=oe-18-2-1586.

[159] A. R. Perry et al. “Multiple-camera defocus imaging of ultracold atomic gases”. In: *Optics Express* 29.11 (May 2021), p. 17029. ISSN: 1094-4087. DOI: 10.1364/oe.422981. URL: http://dx.doi.org/10.1364/OE.422981.

[160] Peter Atkins and Julio de Paula. *Atkins’ Physical Chemistry*. 10th ed. Oxford: Oxford University Press, 2014. ISBN: 9780199697403.

[161] Klaus Hueck et al. “Calibrating high intensity absorption imaging of ultracold atoms”. In: *Opt. Express* 25.8 (Apr. 2017), pp. 8670–8679. DOI: 10.1364/OE.25.008670. URL: https://opg.optica.org/oe/abstract.cfm?URI=oe-25-8-8670.

[162] S. S. Szigeti et al. “Feedback control of an interacting Bose-Einstein condensate using phase-contrast imaging”. In: *Phys. Rev. A* 82 (4 Oct. 2010), p. 043632. DOI: 10.1103/PhysRevA.82.043632. URL: https://link.aps.org/doi/10.1103/PhysRevA.82.043632.

[163] Anand Ramanathan et al. “Partial-transfer absorption imaging: A versatile technique for optimal imaging of ultracold gases”. In: *Review of Scientific Instruments* 83.8 (Aug. 2012), p. 083119. ISSN: 0034-6748. DOI: 10.1063/1.4747163. eprint: https://pubs.aip.org/aip/rsi/article-pdf/doi/10.1063/1.4747163/14829538/083119_1_online.pdf. URL: https://doi.org/10.1063/1.4747163.

[164] Fan Yang, Yong-Chun Liu, and Li You. “Atom-Photon Spin-Exchange Collisions Mediated by Rydberg Dressing”. In: *Phys. Rev. Lett.* 125 (14 Sept. 2020), p. 143601. DOI: 10.1103/PhysRevLett.125.143601. URL: https://link.aps.org/doi/10.1103/PhysRevLett.125.143601.

[165] Lu Qin et al. “Shock-wave generation and propagation in dissipative and nonlocal nonlinear Rydberg media”. In: *Phys. Rev. A* 110 (1 July 2024), p. 013703. DOI: 10.1103/PhysRevA.110.013703. URL: https://link.aps.org/doi/10.1103/PhysRevA.110.013703.

[166] H. P. Zahn et al. “Formation of Spontaneous Density-Wave Patterns in dc Driven Lattices”. In: *Phys. Rev. X* 12 (2 Apr. 2022), p. 021014. DOI: 10.1103/PhysRevX.12.021014. URL: https://link.aps.org/doi/10.1103/PhysRevX.12.021014.

[167] N. Behbood et al. “Real-time vector field tracking with a cold-atom magnetometer”. In: *Applied Physics Letters* 102.17 (Apr. 2013), p. 173504. ISSN: 0003-6951. DOI: 10.1063/1.4803684. eprint: https://pubs.aip.org/aip/apl/article-pdf/doi/10.1063/1.4803684/14273398/173504_1_online.pdf. URL: https://doi.org/10.1063/1.4803684.

[168] P. B. Wigley et al. “Non-destructive shadowgraph imaging of ultra-cold atoms”. In: *Optics Letters* 41.20 (Oct. 2016), pp. 4795–4798. DOI: 10.1364/OL.41.004795. URL: https://doi.org/10.1364/OL.41.004795.

[169] Plamen G. Petrov et al. “Nondestructive interferometric characterization of an optical dipole trap”. In: *Phys. Rev. A* 75 (3 Mar. 2007), p. 033803.

[170] David V. Sheludko et al. “State-selective imaging of cold atoms”. In: *Phys. Rev. A* 77 (3 Mar. 2008), p. 033401. DOI: 10.1103/PhysRevA.77.033401. URL: https://link.aps.org/doi/10.1103/PhysRevA.77.033401.

[171] Sayari Majumder and Saptarishi Chaudhuri. “All-Optical Broadband Atomic Magnetometer Utilizing Raman-Driven Spin Noise Spectroscopy”. In: *IEEE Transactions on Instrumentation and Measurement* 74 (2025), pp. 1–10. DOI: 10.1109/TIM.2025.3554278.

[172] Yuval Cohen et al. “A cold atom radio-frequency magnetometer”. In: *Applied Physics Letters* 114.7 (Feb. 2019), p. 073505. ISSN: 0003-6951. DOI: 10.1063/1.5084004. eprint: https://pubs.aip.org/aip/apl/article-pdf/doi/10.1063/1.5084004/14522954/073505_1_online.pdf. URL: https://doi.org/10.1063/1.5084004.

[173] Ryuta Yamamoto et al. “Site-resolved imaging of single atoms with a Faraday quantum gas microscope”. In: *Phys. Rev. A* 96 (3 Sept. 2017), p. 033610. DOI: 10.1103/PhysRevA.96.033610. URL: https://link.aps.org/doi/10.1103/PhysRevA.96.033610.

[174] Josiah Sinclair et al. “Observation of a large, resonant, cross-Kerr nonlinearity in a cold Rydberg gas”. In: *Phys. Rev. Res.* 1 (3 Dec. 2019), p. 033193. DOI: 10.1103/PhysRevResearch.1.033193. URL: https://link.aps.org/doi/10.1103/PhysRevResearch.1.033193.

[175] Nikolai A. Sinitsyn and Yuriy V. Pershin. “The theory of spin noise spectroscopy: a review”. In: *Reports on Progress in Physics* 79.10 (2016), p. 106501. DOI: 10.1088/0034-4885/79/10/106501. URL: https://doi.org/10.1088/0034-4885/79/10/106501.

[176] S. Liu et al. “Spin-noise spectroscopy of a spin-one system”. In: *Phys. Rev. A* 107 (2 Feb. 2023), p. 023527. DOI: 10.1103/PhysRevA.107.023527. URL: https://link.aps.org/doi/10.1103/PhysRevA.107.023527.

[177] Sebastian Starosielec and Daniel Hägele. “Ultrafast spin noise spectroscopy”. In: *Applied Physics Letters* 93.5 (Aug. 2008), p. 051116. ISSN: 0003-6951. DOI: 10.1063/1.2969041. eprint: https://pubs.aip.org/aip/apl/article-pdf/doi/10.1063/1.2969041/14399355/051116_1_online.pdf. URL: https://doi.org/10.1063/1.2969041.

[178] Tian-Jiao Sun et al. "Non-equilibrium spin noise spectroscopy of a single quantum dot operating at fiber telecommunication wavelengths". In: *Journal of Applied Physics* 131.6 (Feb. 2022), p. 065703. ISSN: 0021-8979. DOI: 10.1063/5.0078910. eprint: https://pubs.aip.org/aip/jap/article-pdf/doi/10.1063/5.0078910/16505218/065703_1_online.pdf. URL: https://doi.org/10.1063/5.0078910.

[179] M. A. Kristensen et al. "Sub-atom shot noise Faraday imaging of ultracold atom clouds". In: *Journal of Physics B: Atomic, Molecular and Optical Physics* 50.3 (Jan. 2017), p. 034004. DOI: 10.1088/1361-6455/50/3/034004. URL: http://dx.doi.org/10.1088/1361-6455/50/3/034004.

[180] P. D. Lett et al. "Observation of atoms laser cooled below the Doppler limit". In: *Journal of the Optical Society of America B* 6.11 (1989), pp. 2084–2107. DOI: 10.1364/JOSAB.6.002084.

[181] David W. Sesko, Thad G. Walker, and Carl E. Wieman. "Behavior of neutral atoms in a spontaneous-force optical trap". In: *Journal of the Optical Society of America B* 8.5 (1991), pp. 946–958. DOI: 10.1364/JOSAB.8.000946.

[182] Thad Walker, David Sesko, and Carl Wieman. "Collective Behavior of Optically Trapped Neutral Atoms". In: *Physical Review Letters* 64.4 (1990), pp. 408–411. DOI: 10.1103/PhysRevLett.64.408.

[183] S. D. Gensemer and K. Burnett. "Light-assisted collisional loss in a vapor-cell trap". In: *Physical Review A* 56.5 (1997), pp. 4055–4062. DOI: 10.1103/PhysRevA.56.4055.

[184] S. Falke et al. "The ^{39,40,41}K D-lines: absolute frequencies and hyperfine coupling constants". In: *Physical Review A* 74.3 (2006), p. 032503. DOI: 10.1103/PhysRevA.74.032503.

[185] S. Dutta et al. "Cooling and trapping of ^{39}K atoms with gray molasses". In: *Physical Review A* 94.6 (2016), p. 063408. DOI: 10.1103/PhysRevA.94.063408.

[186] M. Landini et al. "Sub-Doppler laser cooling of bosonic potassium isotopes". In: *Physical Review A* 84.4 (2011), p. 043432. DOI: 10.1103/PhysRevA.84.043432.

[187] Dipankar Nath et al. “Quantum-interference-enhanced deep sub-Doppler cooling of ^{39}K atoms in gray molasses”. In: *Physical Review A* 88.5 (2013), p. 053407. DOI: 10.1103/PhysRevA.88.053407.

[188] Vitali Zhaunerchyk. “Abel transform analysis of ion storage ring imaging data”. In: *Review of Scientific Instruments* 81.5 (May 2010), p. 053108. DOI: 10.1063/1.3422263. URL: https://doi.org/10.1063/1.3422263.

[189] K. R. Overstreet et al. “Multiple scattering and the density distribution of a Cs MOT”. In: *Optics Express* 13.24 (2005), pp. 9672–9682. DOI: 10.1364/OPEX.13.009672. URL: https://doi.org/10.1364/OPEX.13.009672.

[190] A.V. Rylov, A.S. Zakuskin, and T.A. Labutin. “Abel transform of laser-induced plasma image: Overcoming challenges of noisy and insufficient data for reliable reconstruction”. In: *Spectrochimica Acta Part B: Atomic Spectroscopy* 223 (2025), p. 107079. ISSN: 0584-8547. DOI: https://doi.org/10.1016/j.sab.2024.107079. URL: https://www.sciencedirect.com/science/article/pii/S0584854724002246.

[191] Sayari Majumder. *Sayari-GitHub/Abeltransform: v1.0.2 – Repository Content Fix (v1.0.2)*. Zenodo. Software, https://doi.org/10.5281/zenodo.15221094. Apr. 2025. DOI: 10.5281/zenodo.15221094. URL: https://doi.org/10.5281/zenodo.15221094.

[192] Chih-Chun Chien, Sebastiano Peotta, and Massimiliano Di Ventra. “Quantum transport in ultracold atoms”. In: *Nature Physics* 11.12 (2015), pp. 998–1004. DOI: 10.1038/nphys3531.

[193] Christian Gross and Immanuel Bloch. “Quantum simulations with ultracold atoms in optical lattices”. In: *Science* 357.6355 (2017), pp. 995–1001. DOI: 10.1126/science.aal3837.

[194] Dmitry Budker and Michael Romalis. “Optical magnetometry”. In: *Nature Physics* 3 (2007), pp. 227–234. DOI: 10.1038/nphys566.

[195] Klemens Hammerer, Anders Sørensen, and Eugene S. Polzik. “Quantum interface between light and atomic ensembles”. In: *Reviews of Modern Physics* 82 (2010), pp. 1041–1093. DOI: 10.1103/RevModPhys.82.1041.

[196] Mark Saffman, Thad G. Walker, and Klaus Mølmer. "Quantum information with Rydberg atoms". In: *Reviews of Modern Physics* 82 (2010), pp. 2313–2363. DOI: 10.1103/RevModPhys.82.2313.

[197] Loïc Henriet et al. "Quantum computing with neutral atoms". In: *Quantum* 4 (2020), p. 327. DOI: 10.22331/q-2020-09-21-327.

[198] Antoine Browaeys and Thierry Lahaye. "Many-body physics with individually controlled Rydberg atoms". In: *Nature Physics* 16 (2020), pp. 132–142. DOI: 10.1038/s41567-019-0733-z.

[199] Karen Wintersperger et al. "Neutral atom quantum computing hardware: performance and prospects". In: *EPJ Quantum Technology* 10.42 (2023). DOI: 10.1140/epjqt/s40507-023-00190-1.

[200] M. M. Glazov and V. S. Zapasskii. "Linear optics, Raman scattering, and spin noise spectroscopy". In: *Opt. Express* 23.9 (May 2015), pp. 11713–11723. DOI: 10.1364/OE.23.011713. URL: https://opg.optica.org/oe/abstract.cfm?URI=oe-23-9-11713.

[201] Konstantinos Mouloudakis et al. "Interspecies spin-noise correlations in hot atomic vapors". In: *Phys. Rev. A* 108 (2023), p. 052822. DOI: 10.1103/PhysRevA.108.052822.

[202] J. Delpy and et al. "Anomalous high-density spin noise in a strongly interacting rubidium vapor". In: *Phys. Rev. Research* 7 (2025), p. 013298. DOI: 10.1103/PhysRevResearch.7.013298.

[203] A. K. Vershovskii et al. "Projection Spin Noise in Optical Quantum Sensors Based on Thermal Atoms". In: *Technical Physics* 65.8 (2020), pp. 1193–1203. DOI: 10.1134/S1063784220080204.

[204] J.W.E. Fassbinder. "Magnetometry for Archaeology". In: *Encyclopedia of Geoarchaeology*. Ed. by A.S. Gilbert. Encyclopedia of Earth Sciences Series. Dordrecht: Springer, 2017. DOI: 10.1007/978-1-4020-4409-0_169.

[205] A. A. Fomin et al. "Spin alignment noise and nonlinear effects in atomic vapors". In: *Physical Review A* 108.4 (2023), p. 043109. DOI: 10.1103/PhysRevA.108.043109.

[206] P. Glasenapp et al. “Spin Noise Spectroscopy Beyond Thermal Equilibrium and Linear Response”. In: *Phys. Rev. Lett.* 113 (15 Oct. 2014), p. 156601. DOI: 10.1103/PhysRevLett.113.156601. URL: https://link.aps.org/doi/10.1103/PhysRevLett.113.156601.

[207] S. Lukashov, M. Bayer, and A. Greilich. “Two-photon spin-noise spectroscopy of Cs atoms”. In: *Phys. Rev. A* 112 (2 Aug. 2025), p. 023110. DOI: 10.1103/ngvk-b6sv. URL: https://link.aps.org/doi/10.1103/ngvk-b6sv.

[208] Rupak Bag et al. “Detection of long-range coherence in driven hot atomic vapors by spin noise spectroscopy”. In: *arXiv preprint arXiv:2509.18036* (2025). DOI: 10.48550/arXiv.2509.18036. arXiv: 2509.18036 [quant-ph]. URL: https://doi.org/10.48550/arXiv.2509.18036.

[209] Kevin Cox et al. “Measurements of the magnetic field vector using multiple electromagnetically induced transparency resonances in Rb vapor”. In: *Phys. Rev. A* 83 (1 Jan. 2011), p. 015801. DOI: 10.1103/PhysRevA.83.015801. URL: https://link.aps.org/doi/10.1103/PhysRevA.83.015801.

[210] Nicolás A. Nuñez Barreto, Martín Drechsler, and Christian T. Schmiegelow. “Three-laser coherent population trapping in a multi-Λ system: Theory, experiment, and applications”. In: *Phys. Rev. A* 106 (5 Nov. 2022), p. 053708. DOI: 10.1103/PhysRevA.106.053708. URL: https://link.aps.org/doi/10.1103/PhysRevA.106.053708.

[211] Guiying Zhang et al. “Spin-noise spectrum in a pulse-modulated field”. In: *Opt. Express* 28.11 (May 2020), pp. 15925–15933. DOI: 10.1364/OE.390771. URL: https://opg.optica.org/oe/abstract.cfm?URI=oe-28-11-15925.

[212] A. K. Mohapatra, T. R. Jackson, and C. S. Adams. “Coherent Optical Detection of Highly Excited Rydberg States Using Electromagnetically Induced Transparency”. In: *Phys. Rev. Lett.* 98 (11 Mar. 2007), p. 113003. DOI: 10.1103/PhysRevLett.98.113003. URL: https://link.aps.org/doi/10.1103/PhysRevLett.98.113003.

[213] Dixith Manchaiah, Rohit Kumar, and Raghavan K Easwaran. “Interplay of polarizations in a cascade EIT system in the presence of vortex coupling light in ^{87}Rb atomic vapor medium”. In: *New Journal of Physics* 25 (2023), p. 013013. DOI: 10.1088/1367-2630/acb0ef.

[214] James Keaveney et al. “Active narrowband filtering, line narrowing and gain using ladder electromagnetically induced transparency in an optically thick atomic vapour”. In: *Journal of Physics B: Atomic, Molecular and Optical Physics* 47.7 (2014), p. 075002. DOI: 10.1088/0953-4075/47/7/075002.

[215] S. Majumder et al. “Real-time local density probe for cold atoms utilising Raman driven spin noise spectroscopy”. In: *Applied Physics Letters* 127.4 (2025), p. 044004. DOI: 10.1063/5.0037169.

[216] Tara Fortier and Erin Baumann. “20 years of developments in optical frequency comb technology and applications”. In: *Communications Physics* 2 (2019), p. 153. DOI: 10.1038/s42005-019-0249-y. URL: https://doi.org/10.1038/s42005-019-0249-y.

[217] V. G. Lucivero et al. “Squeezed-light spin noise spectroscopy”. In: *Phys. Rev. A* 92.4 (2015), p. 043827. DOI: 10.1103/PhysRevA.92.043827.

[218] T. W. Hänsch and A. L. Schawlow. “Cooling of gases by laser radiation”. In: *Optics Communications* 13.1 (1975), pp. 68–69.

[219] D. J. Wineland and H. Dehmelt. “Proposed $10^{14}\Delta\nu/\nu$ laser fluorescence spectroscopy on Tl^+ mono-ion oscillator III”. In: *Bulletin of the American Physical Society* 20 (1975), p. 637.

[220] H. J. Metcalf and P. van der Straten. *Laser Cooling and Trapping*. Spring-Verlag, New York, 1999.

[221] D. J. Wineland and W. M. Itano. “Laser cooling of atoms”. In: *Physical Review A* 20.4 (1979), pp. 1521–1540.

[222] E. L. Raab et al. “Trapping of neutral sodium atoms with radiation pressure”. In: *Physical Review Letters* 59.23 (1987), pp. 2631–2634.

[223] J. Dalibard and C. Cohen-Tannoudji. “Laser cooling below the Doppler limit by polarization gradients: simple theoretical models”. In: *Journal of the Optical Society of America B* 6.11 (1989), pp. 2023–2045.

[224] P. J. Ungar et al. “Optical molasses and multilevel atoms: theory”. In: *Journal of the Optical Society of America B* 6.11 (1989), pp. 2058–2071.

विद्यया अमृतमश्नुते॥

“By knowledge one attains immortality.”